JUSTUS-LIEBIG-
UNIVERSITÄT
GIESSEN

Reduced Graphene Oxide Biosensors for Prostate Cancer Biomarker Detection

Dissertation to apply for the degree of

"**Doctor rerum naturalium**" (Dr. rer. nat.)

Submitted to the

Faculty 07 - Mathematics and Computer Science, Physics, Geography

September 10, 2018

Master of Science

Xiaoling Lu

Justus-Liebig-Universität Gießen
I. Physikalisches Institut
AG Prof. Dr. Martin Eickhoff
Nanotechnologische Materialien

REPORTERS:

1. Prof. Dr. Martin Eickhoff, I. Physikalisches Institut, Justus-Liebig-Universität Gießen, Germany
2. Prof. Dr. Sven Ingebrandt, Institute for Materials in Electrical Engineering, Rheinisch-Westfälische Technische Hochschule Aachen, Aachen, Germany

The following work was carried out between August 2013 and September 2018 under Prof. Dr. Sven Ingebrandt at the Biomedical Signalling group of University of Applied Sciences Kaiserslautern, Campus Zweibruecken, Germany.

Abstract

Prostate cancer (PCa) is a major mortality cause for men around the world and therefore there is a high demand for reliable diagnostic solutions. Prostate-specific antigen (PSA) is currently the representative biomarker for pre-screening of PCa, necessarily followed by biopsy examinations for confirmatory diagnosis. In the biomedical market, equipment to detect PSA in its relevant clinical concentration is already commercialized. These devices are accurate, but the bench-top systems are bulky, expensive, have a long response time, and rely on optical labels. To eliminate these drawbacks, point-of-care (POC) devices are under development, aiming at cost-effective, precise, portable, disposable and environmentally friendly designs with a fast response time. Most of the devices are utilizing conventional biosensing principles. However, the miniaturization of these approaches directly induces performance variations and a drastic decrease of the sensing accuracy. It is noteworthy that no biomarker is ideal, and no definite diagnostic decision can be based on a single biomarker. Thus, the detection of a combination of various biomarkers is recommended to provide multi-variable information for accurate diagnosis in the early stage of cancer development. Some biomarkers are more specific for PCa than others, but of a relatively low concentration in the clinical samples. Therefore, new biosensing concepts with multiplexing capability are under intensive investigation.

Graphene, as an atomic carbon lattice, possesses superior electronic, optical and plasmonic properties, which trigger a revolution in the microelectronics field. Graphene is of atomic thickness but mechanically ultra-strong, and the carrier transport is ballistic in the condition of high charge carrier concentrations. In addition, this material is highly heat resistant, cheap, environmentally friendly and biocompatible.

The aim of this thesis is to utilize graphene-based material for novel biosensors towards PSA detection. Graphene oxide (GO) and reduced graphene oxide (rGO), as derivatives of graphene, partially possess the promising properties of graphene. In addition, they provide diverse functionalization possibilities for immobilization of biomolecules and a wafer-scale preparation capability on arbitrary substrates. In the framework of this thesis, GO flakes were chemically exfoliated by a newly developed low-temperature exfoliation and desalination (LTEDS) method. The high-quality GO flakes were characterized intensively using scanning electron microscopy (SEM), transmission electron microscope (TEM), ultraviolet-visible (UV-VIS) spectroscopy, X-ray diffraction (XRD) and Fourier-transform infrared (FT-IR) spectroscopy. The graphene oxide and reduced graphene oxide ((r)GO) thin films were prepared in wafer-scale using the techniques of gas-phase silanization, spin-coating, followed

with patterning by photolithography and reactive ion etching. After a thermal reduction, electronic characterizations of rGO thin films were carried out using cyclic-voltammetry, current-voltage (I-V) characterizations and electrolyte-sensitive field-effect transistor (ESFET) measurements. These combined electronic and electrochemical characterizations aimed at analyzing the wafer-scale topographical completeness, uniformity, and field-effect mobility of the rGO thin films.

The rGO thin films were utilized as functional layers in different biosensor device configurations of surface plasmon resonance (SPR) spectroscopy, electrochemical impedance spectroscopy (EIS) and ESFET. The biosensing performances and the corresponding sensing mechanisms were analyzed and evaluated in detail. The bipolar property of the rGO thin films allowed a tuning effect of the SPR intensity. Concanavalin A (ConA) was detected using the rGO based SPR principle and a limit of detection (LOD) as low as $0.01\,\mu g\,ml^{-1}$ was achieved. Such a LOD was not attainable by the standard gold SPR chips. Besides, the electronic biosensing experiments were all carried out in a buffer solution with an ionic strength of 162 mM and a corresponding short Debye-screening length (0.76 nm), which were similar to physiological solutions (150 mM and 0.78 nm). The rGO based EIS and ESFET sensors exhibited the outstanding biosensing capability to detect PSA in its relevant clinical concentration range (4-10 $ng\,ml^{-1}$).

The rGO based biosensors as developed and optimized in this thesis work showed a highly sensitive PSA detection beyond the Debye-screening limitation and demonstrated a great potential towards real biosensor applications for future healthcare.

Zusammenfassung

Prostatakrebs (PCa) ist weltweit eine der Hauptursachen für Mortalität bei Männern. Daher besteht ein hoher Bedarf an zuverlässigen diagnostischen Verfahren. Prostataspezifisches Antigen (PSA) ist derzeit der repräsentative Biomarker für die PCa-Voruntersuchung, dem bei Auffälligkeiten für eine sichere Diagnose weitere Biopsieuntersuchungen folgen. Auf dem biomedizinischen Markt sind bereits Geräte zum Nachweis von PSA in klinisch relevanten Konzentrationen kommerziell erhältlich. Diese Systeme sind präzise, jedoch sind sie groß, teuer, haben eine lange Analysezeit und beruhen auf optischen Markern zur Detektion der Biomoleküle. Aktuell werden Point-of-Care (POC) Geräte entwickelt, die kostengünstig, präzise, tragbar und umweltfreundlich sind und dennoch eine schnelle Analysezeit besitzen. Die meisten dieser Geräte verwenden herkömmliche Biosensor-Prinzipien. Die Miniaturisierung der klassischen Prinzipien führt jedoch zu Ungenauigkeiten, die mit einer drastischen Verringerung der Zuverlässigkeit einhergehen. In diesem Zusammenhang ist festzustellen, dass kein Biomarker ideal ist und keine definitive diagnostische Entscheidung auf einem einzigen Biomarker basieren kann. Daher werden Anstrengungen unternommen, Kombinationen verschiedener Biomarker nachweisen zu können, um schon im Frühstadium der Krebsentwicklung multivariante Informationen für eine genauere Diagnose bereitzustellen. Dabei sind einige der neuen Biomarker spezifischer für PCa als andere, jedoch liegen sie alle nur in relativ geringen Konzentrationen in den klinischen Proben vor. Aus diesem Grund werden aktuell neue Biosensorkonzepte mit der Fähigkeit zur parallelen Detektion mehrerer Biomarker entwickelt.

Graphen besitzt als atomares Kohlenstoffgitter herausragende elektronische, optische und plasmonische Eigenschaften, die aktuell eine Revolution in der Mikroelektronik auslösen. Graphen ist nur eine Atomlage dick, jedoch mechanisch ultrastark und der Ladungsträgertransport ist bei hohen Ladungsträgerkonzentrationen ballistisch. Außerdem ist dieses Material sehr hitzebeständig, billig, umweltfreundlich und biokompatibel.

Das Ziel dieser Arbeit ist die Verwendung von graphenbasiertem Material in neuartigen Biosensorkonzepten für den PSA-Nachweis. Graphenoxid (GO) und reduziertes Graphenoxid (rGO), als Derivate von Graphen, besitzen zum Teil auch diese vielversprechenden Materialeigenschaften. Darüber hinaus bieten die funktionellen Gruppen im GO Material vielfältige Möglichkeiten für die Immobilisierung von Biomolekülen und erlauben zudem eine Wafer-skalige Herstellung von Sensoren auf beliebigen Substraten. Im Rahmen dieser Arbeit wurden GO-Flocken durch eine neu entwickelte Methode zur Niedertemperatur-Exfoliation von Graphit mit nachfolgender Entsalzung

(LTEDS) hergestellt. Die qualitativ hochwertigen GO-Flocken wurden mittels Rasterelektronenmikroskopie (SEM), Transmissionselektronenmikroskopie (TEM), UV-VIS-Spektroskopie, Röntgenbeugung (XRD) und Fourier-Transform-Infrarot (FT-IR) Spektroskopie intensiv charakterisiert. Die GO- und rGO-Dünnschichten wurden im Wafer-Maßstab unter Verwendung einer Gasphasen-Silanisierung der Wafer und Spin-Coating dünner Schichten hergestellt und mittels Photolithographie und reaktivem Ionenätzen strukturiert. Nach der thermischen Reduktion in leitfähige rGO-Dünnfilme und Strukturen wurden elektrische Charakterisierungen mittels zyklischer Voltammetrie, Strom-Spannungs (I-V)-Kennlinien und electrolytensensitiven Feldeffekt-Transistor (ESFET) Messungen durchgeführt. Diese kombinierten elektronischen und elektrochemischen Charakterisierungen zielten darauf ab, die topographische Qualität, Gleichmäßigkeit und Ladungsträgerbeweglichkeit der rGO-Dünnfilme im Wafermaßstab zu analysieren.

Die rGO-Dünnfilme wurden als funktionelle Schichten in verschiedenen Biosensorkonzepte wie Oberflächenplasmonenresonanzspektroskopie (SPR), elektrochemische Impedanzspektroskopie (EIS) und ESFET-Messungen verwendet. Die Eigenschaften dieser Biosensorkonzepte und die entsprechenden Sensormechanismen wurden analysiert und detailliert ausgewertet. Der bipolare Ladungsträgertransport innerhalb der rGO-Dünnfilme ermöglichte ein elektrisches Abstimmen der SPR-Intensität. Concanavalin A (ConA) wurde unter Verwendung des rGO-basierten SPR-Prinzips nachgewiesen, und eine Nachweisgrenze (LOD) von nur $0.01\,\mu g\,ml^{-1}$ wurde erreicht. Solch eine niedrige LOD war mit Gold-basierten SPR-Sensoren nicht erreichbar. Außerdem wurden alle elektronischen Biosensor Experimente in einer Pufferlösung mit einer Ionenstärke von 162 mM und einer daraus resultierenden, sehr kurzen Debye Abschirmungslänge (0.76 nm) durchgeführt, die einer physiologischen Lösung sehr ähnlich war (150 mM und 0.78 nm). Die rGO-basierten EIS- und ESFET-Sensoren zeigten dabei eine hervorragende Performance, um PSA im klinisch relevanten Konzentrationsbereich ($4\text{-}10\,ng\,ml^{-1}$) nachzuweisen.

Die in dieser Dissertation entwickelten und optimierten, rGO-basierten Biosensoren leisteten einen hochsensitiven PSA-Nachweis jenseits der typischen Limitierung durch die Debye-Abschirmung von Ladungen und zeigten dadurch ein sehr großes Potenzial für reale Biosensorkonzepte für die Gesundheitsversorgung der Zukunft.

List of Used Acronyms

AC	Alternating current
AFM	Atomic force microscopy
APS	3-aminopropylsiloxane
APTES	(3-aminopropyl) triethoxysilane
ATP	4-aminothiophenol
C-V	Capacitance-voltage
cDNA	Complementary DNA
CE	Counter electrode
ConA	Concanavalin A
CPE	Constant phase element
CTC	Circulating tumor cell
CVD	Chemical vapor deposition
DC	Direct current
DIW	De-ionized water
EDC	N-(3-dimethylaminopropyl)-N′-ethylcarbodiimide hydrochloride
EDL	Electrostatic double layer
EIS	Electrochemical impedance spectroscopy
ESFET	Electrolyte-sensitive field-effect transistor
FET	Field-effect transistor
FT-IR	Fourier-transform infrared
FWHM	Full width at half maximum
GO	Graphene oxide
HSA	Human serum albumin
I-V	Current-voltage
IBLG	Incommensurate bilayer graphene
IDE	Interdigitated electrode
IHM	Improved Hummers′ method
ISFET	Ion-sensitive field-effect transistor
LOD	Limit of detection

LTEDS	Low-temperature exfoliation and desalination
MCH	6-mercapto-1-hexanol
MOS	Metal-oxide-semiconductor
MOSFET	Metal-oxide-semiconductor field-effect transistor
NHS	N-hydroxysuccinimide
NP	Nanoparticle
PBS	Phosphate buffered saline
PBST	Phosphate buffered saline with tween-20
PCa	Prostate cancer
POC	Point-of-care
PSA	Prostate-specific antigen
PSAD	PSA density
PSADT	PSA double time
ProPSA	Pro-forms of PSA
PSAV	PSA velocity
fPSA	Free PSA
tPSA	Total (free and complexed) PSA
RE	Reference electrode
(r)GO	Graphene oxide and reduced graphene oxide
rGO	Reduced graphene oxide
RIU	Refractive index unit
RPA	Random-phase approximation
SEM	Scanning electron microscopy
SP	Surface plasmon
SPR	Surface plasmon resonance
ssDNA	Single-stranded DNA
TEM	Transmission electron microscope
TRP	Thermal reduction protocol
UV-VIS	Ultraviolet-visible
VDP	Van der Pauw
WE	Working electrode
XPS	X-ray photoelectron spectroscopy
XRD	X-ray diffraction

Contents

1 Introduction

Prostate cancer (PCa) [1–3] is the fifth leading cause of death from cancer in males around the world, according to the GLOBOCAN database 2012 [4]. An alveolar exocrine gland, the prostate is part of the male reproductive system responsible for producing alkaline fluids that are critical for maintaining suitable chemical environment for the sperms and also neutralize the acidity of the vaginal tract. PCa tends to develop in men over the age of fifty [5]. Its progress is often slow and patients with PCa may have no symptoms and eventually die of other unrelated causes. But in many cases, the patients who are diagnosed with PCa rapidly manifest life-threatening symptoms [6]. Therefore, it is highly necessary to carry out the PCa screening in order to discover the cancer in its early stage. Aiming to reduce the suffering as well as the mortality, the corresponding measures should be properly tailored for the patients, by balancing the potential benefit of treatments and the expected harms of the intervention. Meanwhile, the discussion with the patients about the pros and cons should be repeated along the treatment with the newest available information about the interventions.

The PCa progression is represented genetically and proteomically in and around the prostate by an overexpression of abnormal nuclear proteins, such as cell-cycle proliferation markers, structural proteins and some other molecules whose functions have yet to be addressed [7, 8]. To strengthen the protection against the pathological changes, antigens and specific inhibitors are activated. By examining and monitoring the abnormal molecules, so-called biomarkers, the PCa can be identified in its very early stage. This screening process is a critical challenge for pathologists, clinicians and biosensor researchers to precisely address the disease level.

PCa screening

Plenty of effort has been made to analyze PCa related biomarkers in serum, tissue and urine, which are summarized in table 1.1 [8]. The exact functional roles of these biomarkers in relation with the level, progression and aggressiveness of the PCa are still under investigation. Their sensitivity and specificity for diagnosing PCa must also be further evaluated and validated for real clinical utility.

Among all the biomarkers in table 1.1, prostate-specific antigen (PSA) is the most commonly used to identify the presence of PCa and to address the disease aggressiveness and relapse after treatment [9]. This biomarker is a type of glycoprotein produced by cells in the prostate gland (both normal cells and cancer cells). It is mostly found in semen, but a small amount can also be found in the blood. The serum PSA has been approved by the U.S. Food and Drug Administration since 1994 for

Table 1.1: Prostate-specific biomarkers in body fluids.

Body fluids	Prostate-specific biomarkers
Serum	PAP, tPSA, fPSA, ProPSA, PSADT, PSAD, PSAV, EPSA, EPSA-2
Tissue	GSTP1, AMACR, TMPRSS2-ETS gene rearrangement
Urine	DD3PCA3/UPM3

identifying PCa. Most healthy men have serum PSA levels under 4 ng ml^{-1}. However, the range 4-10 ng ml^{-1} of the serum PSA is regarded as a "gray zone", which implies further PCa diagnosis tests for the patients. Indeed, the elevation of serum PSA is frequently caused by benign prostatic hyperplasia, prostatitis, prostatic manipulation or medical interventions, for instance, cystoscopy. In addition, ethnicity, age, relative size of the prostate gland, dietary changes and physical activity of the patients have been found to make the PSA levels fluctuate [10–13]. These above-mentioned issues may induce an improper interpretation of the PCa screening, leading to false positive or false negative diagnoses and resulting in inadequate treatments. A false positive diagnosis means that a high PSA level is detected, but the patient has no cancer. A false negative diagnosis corresponds to a case where a patient with PCa shows low PSA levels. Therefore, in order to avoid diagnostic discrepancies with the use of PSA as a biomarker, it is proposed to examine additional parameters: PSA velocity (PSAV), defined as PSA changes over time (ng ml^{-1} per year); PSA density (PSAD), defined as PSA level divided by the sonographic prostate volume; PSA double time (PSADT), defined as the time for PSA level to double; the ratio of free PSA (fPSA) to total (free+complexed) PSA (tPSA); or the ratio of pro-forms of PSA (ProPSA) to fPSA. All these biomarkers were suggested after intensive investigation for accurate PCa screening.

State-of-the-art of PSA tests

At present, PSA is the most popular biomarker used for PCa screening. The typical sensing mechanism is making use of an immunoassay which generates an optical signal to identify the PSA level. The sensing range and response time are dependent on types, structures, and readout methods of the biosensor assay. The equipment supplied for the PSA tests in clinical laboratories can achieve the required sensitivity by covering the "gray zone" of PSA levels (4-10 ng ml^{-1}), but they are generally bulky and costly. In addition, the sample transportation and administration processes on the clinical laboratories side lead to extra costs and long waiting time. Therefore, the point-of-care (POC) devices are developed to provide portable, cost-effective and instant test results for the convenience of both patients and clinicians. The equipment available on the market for PSA tests for use in clinical laboratories and POC testing are listed in table 1.2 and table 1.3, respectively. Nevertheless, the PSA test results from POC devices are barely satisfactory, mainly because the PSA level is not perfectly addressed due to technical limitations. For instance, the measured PSA value may vary up to 20 % between two Tandem-R PSA assay from Hybritech company [14]. The portable device concile®Ω100 Reader was directly compared with the bulky clinical equipment: Immulite 2000®and Centaur®test systems from Siemens Healthcare Diagnostics. Although the PSA sensing range covers 0.5-25 ng ml^{-1}, it is suggested that the CancerCheck®PSA on this POC device is only appropriate for

detecting PSA concentrations below 2.5 ng ml^{-1} to identify the cases of low PCa risk. From PSA values of 10 ng ml^{-1}, the tests are proposed to be performed with the standard assays by bulky equipment, because the diagnostic precision of POC measurement is impaired [15].

Table 1.2: Commercialized equipment used in clinical laboratories for PSA tests.

Company	**Roche Diagnostics** [16, 17]	**Siemens Healthcare** [18]	**Ortho Clinical Diagnostics** [19, 20]	**Beckman Coulter** [21]	**Abbott Diagnostics** [22]
Country	Switzerland	Germany	USA	USA	USA
Equipment	COBAS analyzers	ADVIA Centaur, IMMULITE, Dimension systems	VITROS®ECiQ 3600 Immunodiagnostic Systems, VITROS®5600 Integrated Systems	Beckman Access/Access II Immunoassay system, Hybritech Total PSA assay	Architect, AxSYM, IMx
Principle	Electro-chemiluminesce immunoassay				
Biomarker	fPSA	tPSA,fPSA	tPSA, fPSA	tPSA	tPSA,fPSA
Range (ng ml^{-1})	0.01-100	0.001-150		0.1-150	0-100
Sample volume (µl)	20			25-175	
Time (min)	18				29

Table 1.3: Commercialized equipment for POC for PSA tests.

Company	**Mediwatch** [23]	**Sekisui Diagnostics** [24]	**concile** [15, 25]	**True Diagnostics** [26]
Country	UK	USA	USA	USA
Equipment	PSAwatch-Bioscan	FaskPack®IP Automated System	concile®Ω100	TrueDx Reader™
Principle	Au particles labeled immunoassay	Chemi-luminescent immunoassay	Au particle labeled chromatographic sandwich immunoassay	
Biomarker	tPSA	fPSA	tPSA/fPSA	PSA
Range (ng ml^{-1})	0.5-25		0.05-20	0.5-25
Sample volume (µl)	35			30
Time (min)	10	12	20	
Release year	2007		2014	

Being hindered by the insufficient specificity, the PSA test is necessarily combined with a biopsy to prognose the PCa screening. When the serum PSA reaches a level above 4 ng ml^{-1}, a further confirmatory diagnosis should be performed by digital rectal examination, transrectal ultrasound or pathological analysis of prostate needle biopsy [27]. For the biopsy, a tissue fragment is collected from the patient's prostate

by using a needle with a diameter of one millimeter. It cannot be guaranteed that the tissue sample is taken from the cancerous lesions and there is a 30 % probability of missing the cancer tissue. Although more advanced techniques, such as MRI-ultrasound fusion biopsy examination are developed to perform a precise tissue collection from the cancer lesion, it is still invasive, carries the risk of subsequent infections, and is another source of physiological and psychological suffering for the patients.

In order to avoid unnecessary biopsy, and reduce over-diagnosis and over-treatment of early detected PCa caused by inaccurate PSA levels [28], biomarkers that can diagnose PCa accurately are in high demand. There is a concerted effort to identify and develop the tests of highly specific biomarkers of PCa that are minimally invasive, using only body fluids such as blood, urine, and semen. These three general biomarkers matrices directly relate to circulating tumor cell (CTC), DNA, RNA/miRNA, prostasomes/exosomes, proteins and antigens, which are over expressed and responsible for the cancer cell proliferation and metastasis [7]. However, it is noteworthy that no biomarker is ideal. It is preferable to use a combination of biomarkers to provide multi-variable information about the status of PCa, leading to proper and precise treatments for the patients and avoiding under-estimation or over-diagnosis.

Biosensing mechanism and strategy

Many other PCa biomarkers potentially display superior specificity than PSA, but they are still being investigated to validate their utility for the real clinical application. Besides, the concentration of these biomarkers in body fluids is comparably low due to the presence of other unrelated matters. Therefore, new emerging sensing technologies focus on developing biosensors with multiplexing capability, which could be used for detecting several biomarkers simultaneously.

The typical biosensing principles, as described in figure 1.1, are based on thermodynamics, mechanics, optics and/or electrochemistry mechanisms, with a corresponding biosensing signal readout from calorimetry, micro-gravimetric analysis, photometry and electrochemical measurements.

To improve the biosensing selectivity, bio-recognition structures or molecules are typically immobilized on the transducer layers. The transducer elements can be cement based materials, piezo ceramics (*e.g.* quartz, zinc oxide (ZnO), lithium niobate $LiNbO_3$), nanoparticles (*e.g.* gold (Au)), metal (*e.g.* Au, platinum (Pt), palladium (Pd)), dielectric (*e.g.* silicon dioxide (SiO_2), silicon nitride (Si_3N_4), aluminium oxide (Al_2O_3), tantalum pentoxide (Ta_2O_5), aluminium anion (Al^-), borate anion (B^-), sodium (Na^-) silicates), crystalline (*e.g.* silver chloride (AgCl), silver bromide (AgBr), silver sulfide (Ag_2S), lanthanum trifluoride (LaF_3)), heterogeneous (*e.g.* ion-exchanger, polymers, ionophores) membranes, carbon based material (*e.g.* carbon nanotubes, graphene, graphene oxide and reduced graphene oxide ((r)GO) and other two dimensional materials (molybdenum disulfide (MoS_2)). Based on the above basic sensing mechanisms, plenty of biosensors have been investigated and corresponding development toward PSA detection before 2007 can be found in a review paper [33]. The most recent biosensors for PSA detection are summarized in table 1.4.

The label-based biosensing is the major transduction modality for PSA detection

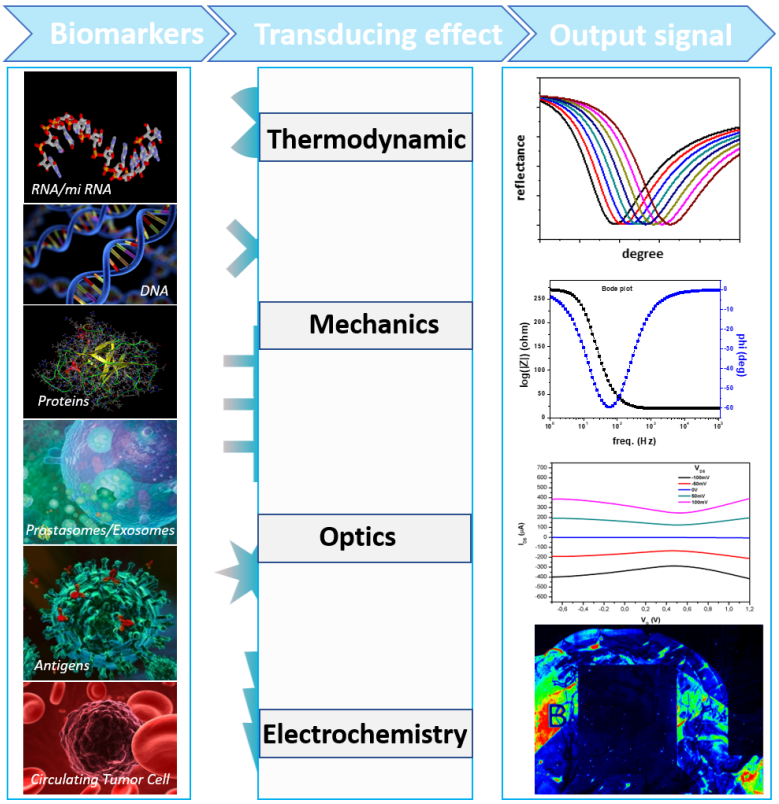

Figure 1.1: The over expressed biomarkers: CTC, DNA, RNA/miRNA, prostasomes/exosomes, proteins and antigens specifically bind with receptor biomolecules or structures on the surface of the transducer of a biosensor. The binding activities of these biomarkers are recognized and transformed by different formats transducing mechanisms into thermodynamic, mechanical, optical and electrochemistry readout signals. The images of CTC, DNA, prostasomes/exosomes and antigens are adpated from [29–32].

with optical readout signals, but this biosensing format has difficulties to realize multiplex sensing. The recent research is weighted in favor of label-free detection, making using of other transducing formats based on field-effect transistor (FET) [34–40], mechanical resonators [41], piezoelectric effect [36], surface acoustic wave [42], electrochemical impedance spectroscopy (EIS) [43], surface plasmon resonance (SPR) [44] and memristors [45].

An ideal biosensor is required to response linearly over the relevant concentration range, operate in complex media, have no or minimum cross-sensitivity, have no false positive and false negative results. In terms of design, they must be robust, reproducible, reliable, cost-effective, easy to handle, environmentally friendly, and disposable. Towards POC tests, it is also essentially required that the devices are of reduced sizes. Such a device miniaturization can be realized by taking advantages of micro- and nano-scale transducers as integral components of the biosensors. With size reduction, the size effect of nano-materials emerges [46] and leads to ultra-high sensitivities for biosensing applications [45, 47–50].

Table 1.4: Recent biosensors for PSA detection.

Sensing mechanism	**Transducer**	**Receptor structure**	**Detection range** ($ng\,ml^{-1}$)	**Buffer**	**Detection time** (min)	**Year Ref.**
Fluorenscence	Nanoparticle label		10^{-3}-1	0.05 M Tris-HCl buffer	> 180	2004 [51]
Fluorenscence	Fluropolymer microcapillary film		0.9-60	Blood	13	2015 [52]
Field-effect transistor	Si nanowires (NWs)	Nucleic acid	$> 9 \cdot 10^{-4}$	1 µM phosphate buffer	< 30	2005 [34]
Field-effect transistor	In_2O_3 NWs	Antibody	> 5	PBS	< 3	2005 [35]
Field-effect transistor	Single wall nanowires	Antibody	> 5	PBS	< 10	2005 [35]
Field-effect transistor	AlGaN/GaN	Antibody	10^{-2}-10^{3}	PBS	0.1	2007 [36]
Field-effect transistor	PEDOT:PSS polymer	Antibody labeled with Au NPs	10^{-3}-100	0.1 M PBS	1440	2010 [37]
Field-effect transistor	MoS_2	Antibody	10^{-3}-10^{-3}	PBS	10	2014 [38]
Field-effect transistor	Si NWs	Aptamer	10^{-2}-10^{3}	10 mM phosphate buffer	120	2018 [39]
Field-effect transistor	MOSFET	Molecularly imprinted cavity	10^{-3}-10^{-2}	Diluted human plasma	30	2016 [40]
Mechanical resonator	Si	Antibody	$1.5 \cdot 10^{-6}$-50	Serum	60	2007 [41]
Piezoelectric	Quartz	Antibody	1.5-40	150 mM PBS	> 40	2007 [36]
Surface acoustic wave	$LiTaO_3$	DNA aptamer	10-10^{3}	1 µM PBS	< 3.5	2015 [42]
Electrochemical enzymatic redox cycling	Au NPs/ MnO_2 NWs	Glucose oxidase (enzyme), TMB (redox terminator)	$1.2 \cdot 10^{-3}$-100	PBS	40	2014 [53]
Surface plasmon resonance	Au thin film	Antibody	8.9-825	PBST	3.5	2015 [44]
Electrochemical impedance spectroscopy	Au electrode	Aptamer-Molecularly imprinted cavity	0.1-100	Redox markers in 10 mM PBS		2016 [43]
Memristor	Si NWs	Aptamer	$> 0.76 \cdot 10^{-6}$	10 mM PBS	60	2016 [45]

Graphene, graphene oxide and reduced graphene oxide transducers for biosensing

Graphene and graphite have been studied theoretically since 1947 [54–56]. It was believed that graphene and graphite cannot exist in the free state due to the structure instability. Therefore, only theoretical models to describe the properties of various carbon-based materials have been established in the past [57, 58]. In 2004, Andre Geim and Konstantin Novoselov mechanically exfoliated the two dimensional material graphene from a highly ordered pyrolytic graphite using a scotch tape [59]. This discovery turned the illusion into reality and triggered a motion to employ graphene towards real applications in the field of biosensors.

The graphene exhibits promising electrical [59, 60], optical [61–66], mechanical [67], thermal [68] and biocompatible [69] properties. The bipolar property and high carrier mobility of graphene make it a suitable material for electrochemical biosensing applications. With the target biomolecules attached onto the graphene transducer layer, the carrier (holes or electrons) concentration (Fermi level) is tunable and the biosensing process is addressed in the form of a shift of the Dirac-point or a change in the bipolar characteristic curve. Due to the excellent electronic properties, graphene offers a promising sensitivity as a transducer layer in detecting single gas molecules [47]. In terms of optical properties, the signals are tunable and can be controlled by an external electric field. Such a method was applied by using infrared spectroscopy for biosensing with graphene coated nanoribbons [70]. Biomolecules of different sizes can be detected in the clinical concentration range. However, the carbon lattice of graphene only provides the binding by π-π stacking to attach the linker molecules for immobilizing the specific probe biomolecules. As a result, the binding strength and diversity of further surface functionalization is massively weakened and limited [71].

Two derivatives of graphene drew tremendous attention in recent years: graphene oxide (GO) [71, 72] and reduced graphene oxide (rGO) [73–75]. Both of them preserve the electronic and optical properties similar to graphene and can be cost-effectively prepared in wafer-scale [71]. Furthermore, the tertiary alcohols and ethers functional groups that remain on the carbon basal plane even after the reduction treatment, provide a high yield of covalent binding of receptor biomolecules. This is obtained by various means of chemical interactions to selectively capture the target analytes (PCa biomarkers) from different complex matrices.

A prerequisite for later commercialization of biosensors is a confirmed device robustness and reproducibility with reliable sensing results. In this work, the biosensing capability of the established (r)GO transducer layers in SPR, EIS and electrolyte-sensitive field-effect transistor (ESFET) configurations for PSA detection is addressed. The essential role of the rGO thin films in the biosensing processes is intensively investigated for further optimization of the exfoliation process of GO flakes, reduction treatments and configuration design of devices. This enables a straightforward detection of prostate-specific biomarkers in their clinical concentration ranges with reproducible and reliable readout signals.

This thesis is arranged as follows:

- In **Chapter 2**, a fabrication process flow of GO thin films on 4-inch wafers is described, using chemically exfoliated GO flakes as the source material. Various

state-of-the-art spectroscopy and microscopy techniques were carried out to illustrate the structural details of the produced GO thin films.

- In **Chapter 3**, the reduction methods to transform the insulating GO thin films into conductive rGO thin films are summarized. After a thermal reduction treatment, the uniformity of resistance as well as the field-effect mobility of the rGO thin films on 4-inch wafers were studied to understand the biosensing performances in later chapters. The reduction method was tested in order to protect the functional oxygen groups to a maximum degree.

- In **Chapter 4**, the (r)GO thin films are employed as functional layers on conventional Au based SPR devices to investigate their sensing mechanism and tunability of the SPR signals with and without externally applied electrical fields.

- In **Chapter 5**, the rGO thin films are utilized as the transducer layers on top of interdigitated electrodes (IDEs) in impedance spectroscopy. PSA-specific aptamers and antibodies served as receptor biomolecules in different buffer concentrations to analyze and address the essential role of the rGO thin films in the biosensing process for PSA detection.

- In **Chapter 6**, the rGO thin films are applied as transducer layers on top of IDEs in an ESFET configuration for PSA detection. The bipolar properties of rGO play a key role in the ESFET sensing. Moreover, the possibility of immobilizing metal nanoparticles were examined with their impact on the biosensing process.

- **Chapter 7** presents the conclusions and outlook. Novel findings and concepts elaborated in this thesis are discussed and related to latest findings in the field of biosensing with graphene based materials.

2 GO Based Devices: Material Synthesis and Nanofabrication

In this chapter, GO and rGO, which are utilized as a source material for the preparation of biosensor devices in this thesis, are presented. Firstly, the fundamental properties of pristine graphene are introduced as the predecessor of other carbon forms. The production methods of pristine graphene towards massive device production is reviewed. Secondly, the fundamental properties of GO and rGO flakes are introduced and the low-temperature exfoliation and desalination (LTEDS) synthesis method based on the improved Hummers' method (IHM) is discussed in detail. The GO flakes produced by LTEDS were characterized by scanning electron microscopy (SEM) and transmission electron microscope (TEM). Evidence of the upgraded process is shown by ultraviolet-visible (UV-VIS) spectroscopy, X-ray diffraction (XRD) and Fourier-transform infrared (FT-IR) spectroscopy characterizations. Thirdly, the preparation procedure of GO thin films via gas-phase silanization and a spin-coating technique is described and discussed. Afterwards, the spectroscopic ellipsometry was used to characterize the topography of the formed thin films, which are used after a reduction treatment as an alternative transducer layer for biosensing. Fourthly, a nanofabrication process of GO thin film based electronic devices is described and the obtained GO pattern was characterized by atomic force microscopy (AFM), SEM and optical microscopy.

2.1 Fundamentals of Graphene

Graphene was mechanically exfoliated for the first time from bulk graphite in 2004 [59]. It can be observed under an optical microscope on a 285 nm thick SiO_2 substrate, due to the optical contrast [61]. Graphene is a single atomic carbon lattice, in which the carbon bonds are sp^2 hybridized. The out-of-plane π bonds that contribute to a delocalized network of electrons, are responsible for the electrical conduction of graphene and lead to weak interactions among the graphene layers or between graphene and a substrate. Graphene exhibits extraordinary electronic properties [59], optical properties [61], mechanical properties [67], with a breaking strength of $42\,\mathrm{N\,m^{-1}}$ and a Young modulus value of 1.0 TPa, as well as high thermal stability up to 700 °C [68]. Possessing an ultra-high surface to volume ratio, various defects within the sheets and highest ratio of edgy carbon atoms compared to similar carbon materials such as nanotubes, graphene has an increased chemical reactivity, which results in a high potential of functionality. Nowadays, wafer-scale graphene is

generally produced by chemical vapor deposition (CVD) [76] or by high temperature decomposition [77]. Larger-scale fabrication has been realized by a roll-to-roll method [78]. With an extra step to transfer graphene to a target substrate, the application potentials based on graphene can be further realized [47, 79–84]. Since these properties promote graphene as a promising material for various applications, particularly as a transducer in biosensors, the intrinsic electronic and optical properties are introduced in detail in this section.

Massless Dirac Fermions

Intrinsic graphene acts as the mother of all graphitic forms by being wrapped up into 0D fullerenes, rolled into 1D nanotubes or stacked into three dimensional graphite [59]. It serves as the basis to study other allotropes of carbon, as shown in figure 2.1(a). Graphene is a two dimensional single layer of carbon atoms with a hexagonal packed structure, as shown in figure 2.1(b). The structural unit cell consists of two different atoms A and B which are arranged in a triangular lattice with a carbon-carbon distance $a \approx 1.42$ Å. The lattice can be defined by two vectors $\boldsymbol{a_1}$ and $\boldsymbol{a_2}$:

$$\boldsymbol{a_1} = \frac{a}{2}\left(3, \sqrt{3}\right), \quad \boldsymbol{a_2} = \frac{a}{2}\left(3, -\sqrt{3}\right) \tag{2.1}$$

For this periodic lattice, the Fourier transform can be applied to obtain the corresponding reciprocal space (also known as momentum space). The reciprocal lattice vectors can be written as:

$$\boldsymbol{b_1} = \frac{2\pi}{3a}\left(1, \sqrt{3}\right), \quad \boldsymbol{b_2} = \frac{2\pi}{3a}\left(1, -\sqrt{3}\right) \tag{2.2}$$

In the reciprocal lattice, the first Brillouin zone is a primitive cell which contains exactly one lattice point and it is used to define the properties of a lattice [85]. In the case of graphene, as shown in figure 2.1(c), the two points $\boldsymbol{K}$ and $\boldsymbol{K'}$, located at the corners of the graphene Brillouin zone, are the so-called Dirac points (also called Dirac cones) [60, 86]. Their positions in momentum space are as follows:

$$\boldsymbol{K} = \left(\frac{2\pi}{3a}, \frac{2\pi}{3\sqrt{3}a}\right), \quad \boldsymbol{K'} = \left(\frac{2\pi}{3a}, -\frac{2\pi}{3\sqrt{3}a}\right) \tag{2.3}$$

The other 4 Dirac cones can be obtained by adding some reciprocal lattice vectors to $\boldsymbol{K}$ and $\boldsymbol{K'}$. Considering that the electrons hop to the nearest and second nearest neighbor atoms, the energy bands derived from the tight-bonding Hamiltonian can be expressed as follows [54]:

$$\begin{aligned} E_{\pm}(\boldsymbol{k}) &= \pm t\sqrt{3 + f(\boldsymbol{k})} - t' f(\boldsymbol{k}) \\ f(\boldsymbol{k}) &= 2\cos\left(\sqrt{3}k_y a\right) + 4\cos\left(\frac{\sqrt{3}}{2}k_y a\right)\cos\left(\frac{3}{2}k_x a\right) \end{aligned} \tag{2.4}$$

where t is the nearest neighbor hopping energy and t' is the second nearest neighbor hopping energy, which represent the hopping between the different lattice and within the same lattice, respectively. The plus and minus signs apply to upper π and lower π^* bands, respectively.

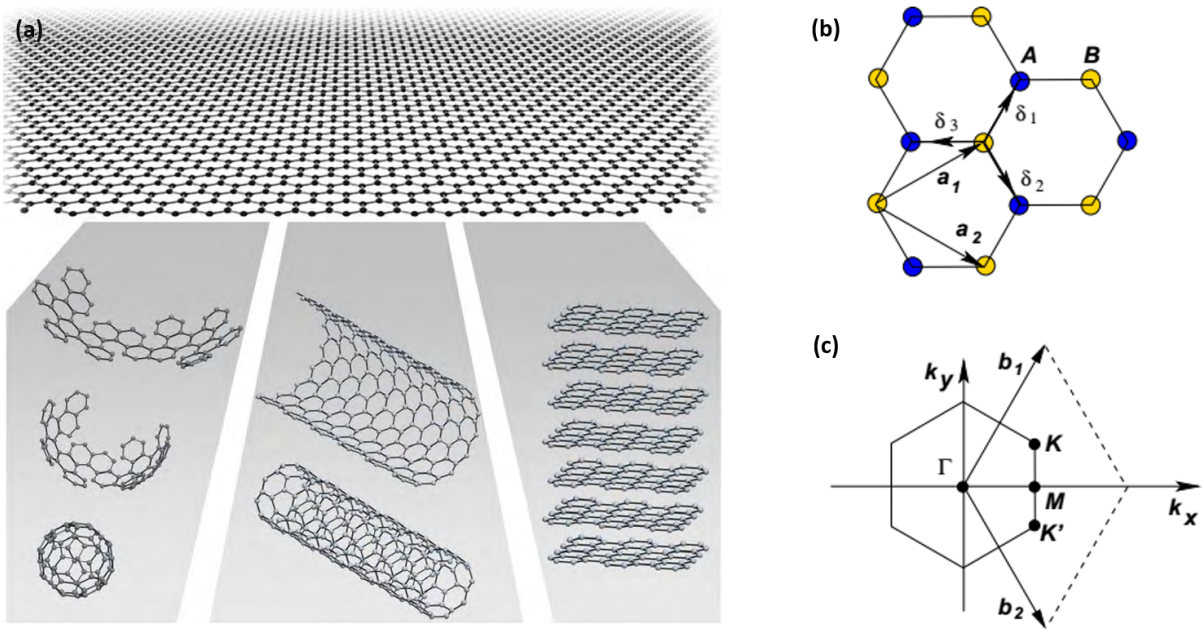

Figure 2.1: (a) On top, graphene, the mother of all graphitic forms [87]. Fullerene (left), nanotubes (center) and graphite (right) are obtained by cutting and folding graphene. (b) Lattice structure of graphene made of two interpenetrating triangular lattices. (c) First Brillouin zone of graphene lattice, where the Dirac cones are located at the $\boldsymbol{K}$ and $\boldsymbol{K'}$ points [60].

In condensed matter physics, a surface in the reciprocal space that separates occupied and unoccupied electron states is called a Fermi surface. In the case of graphene, the Fermi surface is defined by $\boldsymbol{K}$ and $\boldsymbol{K'}$. By expanding the full band structure (equation 2.4) close to the Dirac point $\boldsymbol{K}$ (or $\boldsymbol{K'}$) with the vector $\boldsymbol{k} = \boldsymbol{K} + \boldsymbol{q}$ while $|\boldsymbol{q}| \ll |\boldsymbol{K}|$, the dispersion relationship of energy and momentum can be obtained:

$$E_{\pm}(\boldsymbol{k}) \approx \pm v_F |\boldsymbol{q}| + \mathcal{O}\left((q/K)^2\right) \tag{2.5}$$

where q is the momentum relative to the Dirac points, and v_F is the Fermi velocity with the value:

$$v_F = 3ta/2 \simeq 1 \cdot 10^6 \,\mathrm{m\,s^{-1}} \tag{2.6}$$

Different from the free electron case with the $E(q) = q^2/(2m)$, the energy in graphene as shown in equation 2.5 has a linear relationship with the momentum of the particles. From the quantum mechanics point of view, these particles are defined as massless Dirac fermions. Within the semi-classical approximation, the cyclotron mass can be deduced as:

$$m^* = \frac{\sqrt{\pi}}{v_F}\sqrt{n} \tag{2.7}$$

where n is the electronic density. Experiments have confirmed the existence of such massless Dirac quasiparticles in graphene [88], while plenty of effort was made in order to comprehend their properties [59, 60, 63, 68, 87, 89–91].

Electronic Properties

The electron orbitals of the carbon atoms in graphene are s, p_x, p_y and p_z orbitals. The electron configuration for a single carbon atom in the ground state is $1s^2 2s^2 2p^2$. After forming the carbon lattice as graphene, the electron configuration of the carbon atom becomes $1s^2 2s^1 2p^3$ [92]. The $1s^2$ electrons are inert and plays no contribution for the chemical bonding formation. The $2s^1$ and two of the $2p^3$ electrons ($2p_x$ and $2p_y$) orbitals hybridize to form three in-plane sp^2 orbitals, corresponding to σ-bonds. The σ-bonds are responsible for maintaining the chemical bonding of carbon atoms and determine the mechanical properties of the graphene. The $2p_z$ orbitals are perpendicular to the plane of carbon lattice and responsible for most of the unusual electronic properties of graphene. Each p_z orbital contributes one electron per carbon atom. The p_z orbitals of carbon atoms combine to form the out-of-plane π bonds, which subsequently hybridize to form π bands and π^* bands [93]. In the π-π^* system, the cosine-like energy bands of the sublattices that are made of atoms A (or B) intersect at $E = 0$ and result in the conical sections of the energy spectrum as shown in figure 2.2(a). The minus band, as represented in equation 2.4, is fully occupied, while the plus band is empty. These two bands touch at the $\boldsymbol{K}$ points, which implies graphene is a zero-gap semiconductor. In a pronounced electric field, the Fermi level can be tuned towards either the valence or the conductance bands as shown in figure 2.2(b).

This electronic property of graphene is known as bipolar behavior, in contrast to conventional monopolar semiconductors. The bipolar property means that graphene can behave as either an n-type or a p-type semimetal with the assistance of an external electronic field, not requiring doping elements to offer mobile carriers. The concentration n of electrons and holes can be modulated continuously as high as $10^{13}\,\mathrm{cm}^{-1}$, with the mobility μ exceeding $15\,000\,\mathrm{cm}^2\,\mathrm{V}^{-1}\,\mathrm{s}^{-1}$, which is barely influenced by temperature [87]. The Dirac fermions in graphene are also insensitive to the defects in the graphene lattice. This implies that the carriers can travel freely thousands interatomic distances even at room temperature without being scattered, which is defined as ballistic transport on submicron scale (up to 0.3 µm at 300 K) [87].

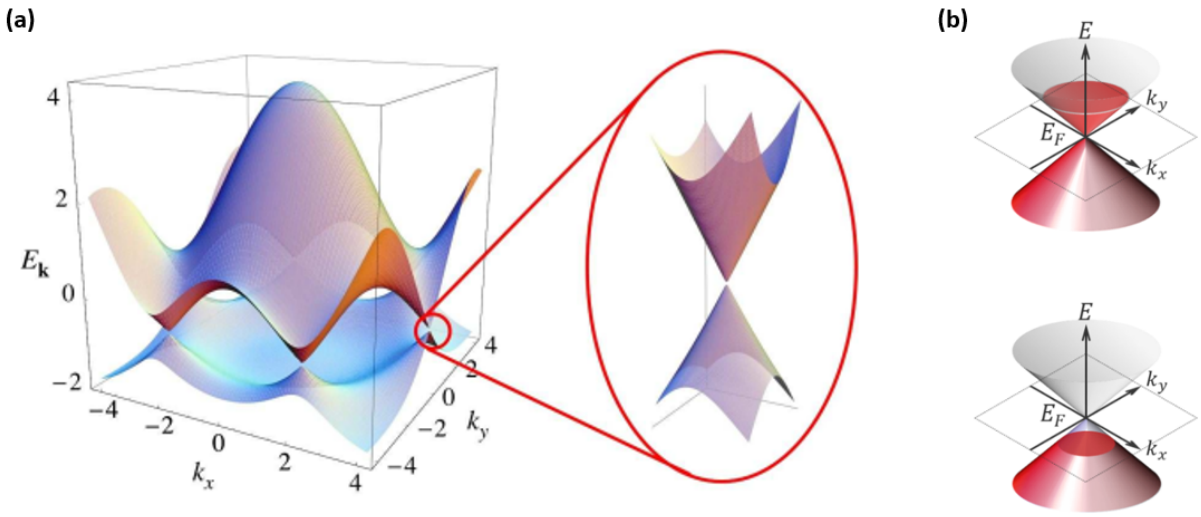

Figure 2.2: Energy landscape and Fermi level of graphene. (a) Energy landscape of graphene with $t = 2.7\,\mathrm{eV}$ and $t' = 0.2t$ [60] and a close-up of the energy bands at one of the Dirac points. (b) The Fermi level is tuned into conductance and valence bands by external applied voltages.

The energy spectrum and the electronic properties rapidly evolve with the number of layers and approach the three dimensional limit of graphite at 10 layers [94]. Only mono- and bilayer have a simple energy spectrum and behave as zero-gap semiconductors. For 3 and more layers, the spectrum becomes complicated, while several charge carriers appear, and the conduction and valence bands start overlapping [59, 94, 95]. Due to its structural and electronic flexibility, there are plenty of possibilities to tailor graphene by external metal atoms, molecules and interactions among the graphene layers. Such excellent electronic properties allow graphene to be utilized in various application fields.

Optical properties

The linear dispersion of the Dirac fermions determine the optical properties of graphene. These quasiparticles can completely transmit through a classical forbidden region without being localized, a fact known as the Klein paradox [96, 97]. The dynamic conductivity G_0 of Dirac fermions in graphene is a constant:

$$G_0 = \pi e^2/2h \approx 6.08 \cdot 10^{-5}\,\Omega^{-1} \tag{2.8}$$

while e is the charge of an electron and h is the Planck constant. This universal conductivity infers that the optical transmittance and reflectance are also constants:

$$T \equiv (1 + 0.5\pi\alpha)^{-2}, \quad R \equiv 0.25\pi^2\alpha^2 T \tag{2.9}$$

where $\alpha = G_0/\pi\varepsilon_0 c$ is the fine structure constant. As a result, the opacity of graphene is equal to:

$$1 - T \approx \pi\alpha = 2.3\,\% \tag{2.10}$$

This value was extracted experimentally with incident white light onto free-standing and undoped graphene [61, 62]. The absorption spectrum is flat from 300 nm to 2500 nm, with a peak (above 10 %) around 275 nm in the ultraviolet region due to resonant excitons which are induced by van Hove-like singularities [98, 99]. During the interband excitation generated by an ultrafast optical pumping, the carrier population in conductance and valence bands are in non-equilibrium states. The possible relaxation mechanisms, as depicted in figure 2.3(a), are generally associated with:

i) Carrier-carrier intraband and phonon emissions in the 100 femtosecond scale.

ii) Electron-hole interband recombination and cooling of hot phonons in the picosecond scale.

Furthermore, the linear dispersion of the Dirac electrons enables ultrawide band tunability in optics [100]. At the Dirac point, the electron energy is:

$$E \approx \hbar v_F k_{\parallel} \tag{2.11}$$

where k is the electron momentum. An external electrical field or chemical doping tend to tune the Fermi energy to:

$$E_F \approx \hbar v_F k_F \tag{2.12}$$

where $k_F = (\pi n)^{1/2}$, and n is the concentration of the injected or the doped carriers. Such a Fermi-level tuning effect induces immediately an optical gap of $2E_F$ for interband and intraband transitions as shown in figure 2.3(b). The Pauli blocking of photon absorptions in the case of graphene is shown in figure 2.3(c).

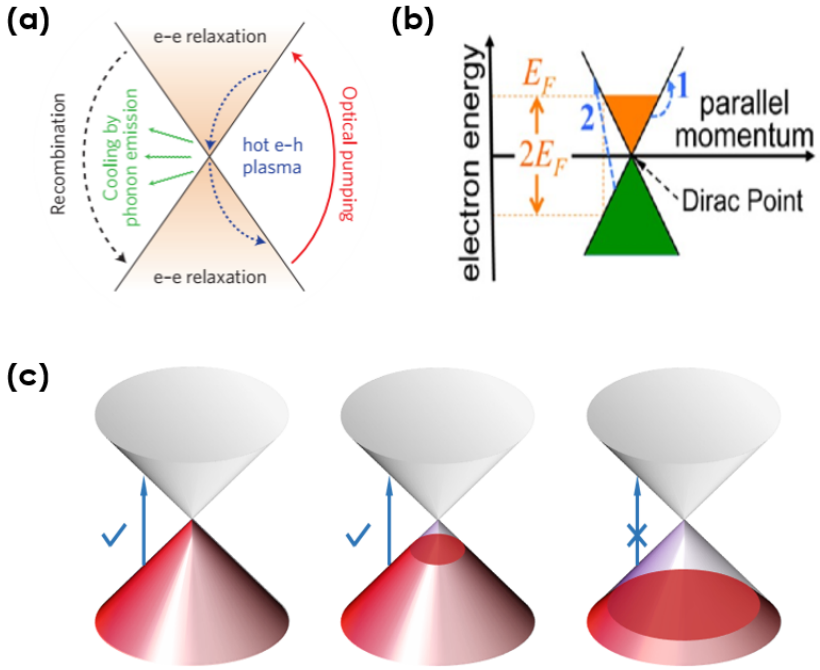

Figure 2.3: (a) Possible relaxation mechanisms for the non-equilibrium electron population [64]. (b) The Fermi level is raised up $E_F = \hbar v_F k_F$ by an external electronic field or chemical doping with $k_F = (\pi n)^{1/2}$, while n is the concentration of doped carriers. The optical gap of a size $2E_F$ is open. For an energy smaller than this value, the vertical transitions are forbidden [64]. (c) In graphene: Pauli blocking of photon absorptions.

The imaginary part $\Im\{r_p\}$ of the Fresnel reflection coefficient for p-polarized light describes the energy-loss probability as well as the wave vector $k_\parallel$ and the frequency ω dependent optical excitations, when graphene is excited by a fast electron [101]. The optical excitations include the emergence of a plasmon band. In an electrostatic view, r_p is given as:

$$r_p = \frac{1}{1 - \dfrac{j\omega}{2\pi k_\parallel \sigma}} \tag{2.13}$$

where σ is the graphene conductivity. In the event of finite graphene structures with a much larger size than the Fermi wavelength $\lambda_F = 2\pi/k_F$, the $k_\parallel$ dependence plays a negligible role such that the graphene conductivity can be expressed as random-phase approximation (RPA) conductivity [78, 102]:

$$\begin{aligned}\sigma(\omega) &\equiv \sigma\left(k_\parallel = 0, \omega\right) \\ &= \frac{-e^2}{\pi\hbar}\frac{j}{\omega + j\tau^{-1}} \int_{\infty}^{-\infty} \left[|E| \frac{df_E}{dE} + \frac{\dfrac{E}{|E|}}{1 - \dfrac{4E^2}{\hbar^2(\omega + j\tau^{-1})^2}} \right] dE\end{aligned} \tag{2.14}$$

where f_E is the electron distribution as a function of the energy E and τ is the finite electronic relaxation time. The first term inside the integral represents the intraband transition (marked as path 1) and the second term describes the interband transition (marked as path 2) across the optical gap $2E_F$ as shown in 2.3(b).

The plasmon dispersion relationship can be deduced by placing equation 2.14 into the pole of equation 2.13 ($k_{sp} = j\omega/(2\pi\sigma)$). The plasmon wavelength is obtained with:

$$\lambda_{sp} = \frac{2\pi}{\Re\{k_{sp}\}} = \lambda_0 \frac{4\alpha}{\varepsilon_1 + \varepsilon_2} \frac{E_F}{\hbar\omega} \tag{2.15}$$

where λ_0 is the wavelength of the incident light, α is the fine structure constant, ε_1 and ε_2 are the dielectric parameters of the materials on both sides of the graphene.

The plasmon dispersion relation only applies to the short in-plane wavelengths and the electron-hole excitations can be neglected between the induced charges with a separation distance larger than nanometers. The polarization of the interband transition generates a plasmon shift, which agrees with the description of local-RPA conductivity [64]. In recent years, graphene plasmons have become extraordinarily interesting, especially in the field of bio-plasmonic applications [63–66]. The surface plasmons (SPs) along graphene's surface are confined to a volume which is approximately 10^6 times smaller than the diffraction limit and in favor of strong light-matter interaction [103]. Based on the semimetallic characteristics of graphene [59, 60], the externally applied electric field can tune the Fermi level towards either the conductance band or the valence band, resulting in a sign switch of carrier type and a drastic change in carrier concentration. The aforementioned electric field has a strong tuning effect in the plasmon mode [104], the optical parameters [105], the quantum pathways of inelastic light scattering [106] and the band-gaps [107]. Moreover, the field enhancement [104] and interaction strength of SPs in graphene at the quantum level is increased by one degree, while the efficient decay rate exceeds the natural decay rate by six orders of magnitude with reduced dimensionality [103] and the resonant extinction cross section is much larger than the geometrical cross section of graphene. This electric field can be applied as a gating voltage or generated by the attachment of external molecules. With the assistance of an applied electric field, graphene electro-plasmonic, label-free biosensors achieve a tunable sensitivity in the mid-infrared regime [70]. Taking advantage of the above-mentioned powerful properties, graphene has been applied as a linker layer on Au based SPR based biosensor platforms. Its amplifying capability to boost the sensitivity during the detection of biomolecules has been verified [108].

2.2 Fundamentals of (Reduced) Graphene Oxide

The promising high field-effect mobility, excellent mechanical properties, high thermal stability and good biocompatibility enable graphene to be a competitive candidate comparable to silicon or III/V heterojunction based devices for biosensors and bioelectronic applications. However, the preparation of pristine graphene is generally highly expensive, a high-quality wafer-scale transfer of CVD graphene to arbitrary substrates is still challenging [109, 110] and probe molecule immobilization

on a pure carbon lattice is based on physi-absorption, which is not always effective. Therefore, chemically exfoliated GO [71, 72] and rGO [73–75] were intensively exploited due to their similarity to graphene and tested out as an alternative to overcome the dilemma that graphene is facing towards wafer-scale and robust device preparation.

The exfoliation methods [111–113] and their potential applications [114, 115] are still under discussion. Generally, the exfoliation process uses graphite as the starting material. Mono and/or multi atomic carbon layers are generated due to the degradation in the Van der Waals forces between the neighboring carbon layers. The sp^2 C−C bonds that build up the carbon hexagonal lattice are partially hybridized and tetrahedrally coordinated by sp^3 C−C and/or C−O bonds. It has been proven that the surface of GO flakes is covalently functionalized with the following chemical groups: ketones and phenols on the basal plane and carboxyl, anhydrates, lactones, lactols and pyrenes at the edges [73], as shown in figure 2.4.

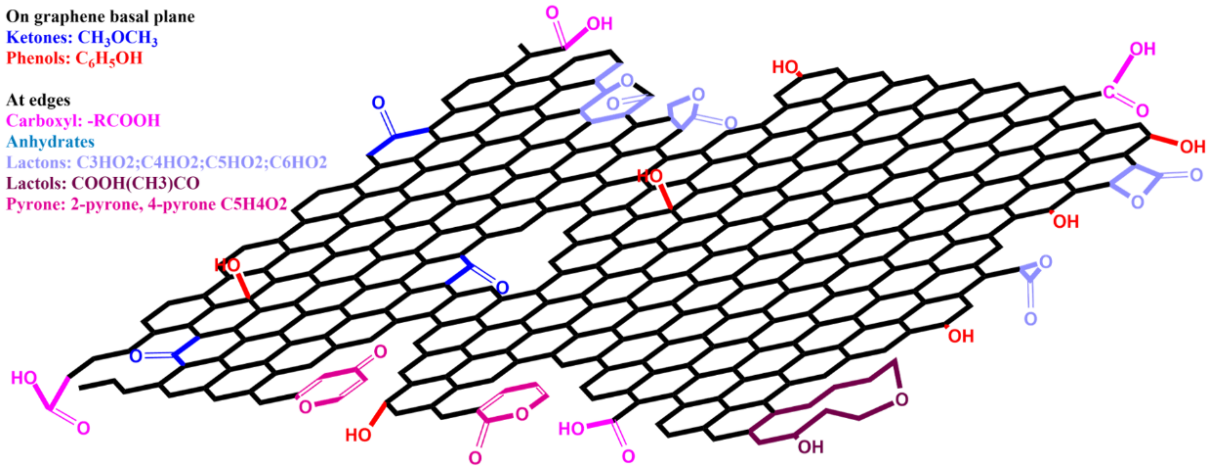

Figure 2.4: Schematic of a GO flake with various oxygen functional groups: ketones and phenols on the basal plane and carboxyl, anhydrates, lactones, lactols and pyrenes at the edges [73].

Thanks to the various functional groups, GO flakes are dispersible in various solvents for large-scale production of sensor devices on various substrates. In order to take advantage of the extraordinary electronic and mechanical properties of pristine graphene, the area of the pure carbon lattice network should be preserved as far as possible during the exfoliation process. Until now, the area size of the same fingerprint of graphene on GO flakes has reached nanoscale dimensions [112]. The electronic resistances of these GO flakes are comparably high because the carriers are not able to travel along the flake basal plane to realize conductivity within the microscale. Different reduction methods have been developed to remove the oxygen functional groups in order to enlarge the pure carbon lattice and smooth the carrier transport by transforming insulating GO into conductive rGO [75]. It was proven that the carbon lattice cannot be fully recovered to that of graphene [73]. The carriers can only hop among localized sp^2 states along the basal plane rather than traveling ballistically, due to the disordered carbon lattice and residual functional groups. However, thanks to these functional groups, the rGO surface can be functionalized with diverse metal nanoparticles and/or be covalently decorated with external functional molecules, resulting in a remarkable potential for molecular sensing. This is a powerful merit

of rGO compared to graphene in practical application fields. In this work, a GO dispersion was prepared by improving the process of IHM [111] and GO flakes of different sizes were subsequently selected for device fabrication. A wafer-scale fabrication method was developed to prepare rGO nano-film based devices which were further investigated in detail. Their potential application fields are highlighted in the next sections.

2.3 Low-Temperature Exfoliation and Desalination (LTEDS) Method

The work described from section 2.3 to section 2.5 was published as "Front-End-of-Line Integration of Graphene Oxide for Graphene-Based Electrical Platforms" [116]. The images used in this thesis are partially adapted from this paper with the journal's permission. This paper as well as experiments described in this chapter represent a shared work. Chemical synthesis and characterization of the GO material was done in a parallel thesis whereas patterning and electrical characterization was done in this thesis. For a better comprehension of this section, both parts are summarized.

The IHM as shown in figure 2.5(a) uses $H_3PO_4/H_2SO_4/KMnO_4$ instead of $HNO_3/H_2SO_4/KMnO_4$ to initially provide a water-free equilibrium condition. The ions SO_4^{2-} intercalate between the graphite layers and reduce the Van der Waals forces at the outer zone. Subsequently, the oxidant MnO_4^- reacts with the carbon lattice by predominantly breaking the in-plane sp^2 bonds and replaces them by out-plane sp^3 C−C, C=O, or C−O bonds. Stepwise, the matrices of monolayer, bilayer, and/or multi-layer GO flakes are chemically exfoliated. The generated oxygen functional groups are in the forms of ketones and phenols on the basal plane, while carboxyl, anhydrates, lactones, lactols and pyrenes can be found at the edges [73]. In order to use these final product GO flakes in application fields, full exfoliation is expected to generate mono- and/or multi-layer flakes rather than graphite-oxide flakes. Meanwhile, a gentle and slow process is also required to preserve as much of the carbon hexagonal lattice as possible, because the oxidation degree and the percentage of hybridized sp^3 carbon significantly restrict the transport of carriers along the carbon basal plane compared to pristine graphene [60, 63, 74, 117]. Mainly, the functionalization rate of the oxide groups, the generation rate of defects, and the formation of CO_2 within the carbon lattice can be suppressed by decreasing the process temperature [112]. Instead of using 50 °C as in the IHM protocol, the LTEDS developed in the framework of this thesis lowers the exfoliation temperature down to 20 °C (figure 2.5(b)). The very strong oxidant $KMnO_4$ is the most critical reactant for the exfoliation of graphite. In the highly acidic environment, MnO_4^- diffuses between the interlayer sheets and undergoes a redox reaction with the carbon atoms, so that the required manganese oxide gets formed. Considering all the reported GO synthesis protocols, there are currently no solutions to avoid the over-oxidation which creates irreversible structural defects inside of the carbon lattice. To protect the hexagonal honeycomb structure from this destructive effect, the key direction is minimizing the mass of $KMnO_4$, excessing the amount of graphite educts and lowering the reaction temperature. The advantage of a 20 °C reaction temperature, is that it maintains the

active efficiency of the exfoliation and realizes a trade-off between the generation rate of defects and the adequate percentage of functional groups.

After the exfoliation, the GO matrix contains highly-concentrated acids, which have to be removed by a sophisticated cleaning procedure. This is a critical part of the protocol because the residual ions and manganese oxide adhere to the GO flakes and influence their properties negatively. In the newly established LTEDS protocol, the cleaning procedure was upgraded to diminish this side effect and obtain a clearer fingerprint of the oxygen functional groups compared to the IHM. The LTEDS protocol contains the following precise steps:

i) The GO acid matrix was mixed with 400 ml milliQ water through a cone separatory funnel, followed by pipetting 4 ml hydrogen peroxide into the mixture to degas the CO_2 and to dissolve the manganese esters and other manganese-oxo-complexes. The milliQ water is a type of ultrapure water, which typically has a resistivity value of 18.2 MΩ cm at 25 °C. The solution can be generated by either the partial or complete hydrolysis of cyclo organo sulfate to organo sulfate [118]. All of the above processes were carried out at 8 °C to avoid a rapid temperature rise. Afterwards, the solution was allowed to sediment at room temperature for one day to obtain a rough GO matrix. The supernatant acid was removed and the bottom part was then mixed with fresh de-ionized water (DIW) again by stirring. The solution was then allowed to sediment again at room temperature for 5 days forming 3 distinct immiscible phases, as shown in figure 2.5(c). The middle phase was extracted for later-on-treatment because the bottom portion of the heavier products mainly consisted of graphite oxide flakes and the supernatant acid.

ii) For further treatment, the extracted solution was centrifuged at two different speeds, 100 rpm and 150 rpm sequentially for 60 min each and formed 3 distinct immiscible phases, as shown in figure 2.5(d). A large portion of the ions, primarily K^+, Mn_2^+, SO_4^{2-} and a lower amount of the PO_4^{3-}, were removed in this step.

iii) The middle phase was extracted and mixed again with DIW by stirring, followed up by centrifugation at 5000 rpm. With this procedure, the solution was separated into two phases. Removing the supernatant acid, the bottom GO layer was mixed again with DIW. This procedure had to be repeated two times until the pH range was within 2 to 4.4. Afterwards, the GO was mixed with hydrogen chloride 25 % and centrifuged at 5000 rpm for 50 min. To further clean away the residual ions, the GO was dissolved in DIW again and transferred into the dialyzing sack for one night, as shown in figure 2.5(e). After dialyzing, the final GO product was mixed with ethanol and centrifuged two times at 5000 rpm for 50 min. The GO product was redispersed in diethyl ether to remove ethanol completely and finally dried in the desiccator for 48 h. Afterwards, GO flakes were dissolved in DIW and centrifuged again two times at 1000 rpm. The supernatant was a GO flake dispersion with a final pH of around 2.9. This GO solution can be used for later preparation of GO thin films.

The images in figure 2.5(f)-(g) expose the differences of the final GO flakes synthesized by the IHM and the LTEDS protocols. In comparison to the IHM, the GO flakes

generated after LTEDS were capable of freeing the functional groups from the residual ions and CO_2. The improved quality of GO flakes by LTEDS was further verified by different characterization tools.

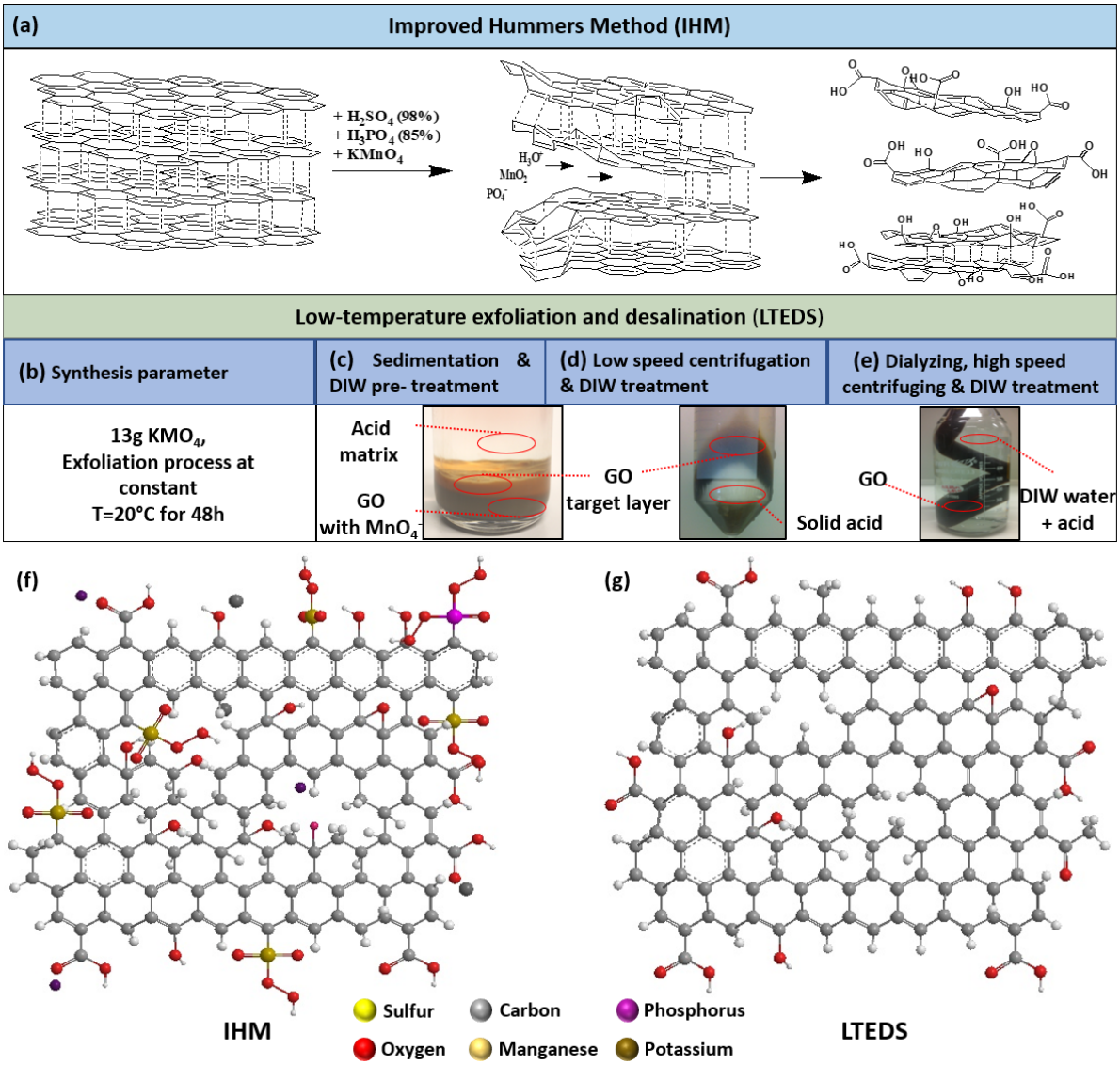

Figure 2.5: Synthesis procedure of GO flakes [116]. (a) The chemical exfoliation procedure of the IHM: with mesh graphite as source material, the H_2SO_4 and H_3PO_4 with the assistance of the oxidant $KMnO_4$ diffuse and intercalate between the carbon stack stepwise to realize the exfoliation. (b) The exfoliation temperature is maintained at 20 °C by a cooling system such that the lateral size of the carbon honeycomb lattice is preserved for a smooth carrier transport. (c)-(e) Additional cleaning steps after the chemical exfoliation were developed to remove the residual components resulting in an purer product. (f)-(g) Illustrative lattice images to compare the final GO flakes between the standard IHM process and the LTEDS process. The former image indicates that ions still remain within the oxidized functional groups on the GO flakes in the case of IHM. The latter image shows that in the LTEDS process the low exfoliation temperature suppresses the destructive power of the oxidants to restrict the size and density of defects in the GO lattice, meanwhile the additional cleaning steps provide better efficiency in removing residual ions.

2.4 Characterization of LTEDS

2.4.1 Topographical Characterization

The SEM image of the GO flakes exfoliated by LTEDS is shown in figure 2.6(a). To investigate and comprehend its potential for the wafer-scale applications, TEM characterizations were carried out by drop casting the GO flake solution onto a TEM grid to form a thin film. As it can be seen in figure 2.6(b), the exfoliated GO flakes are amorphous without periodic carbon lattice. According to the distinguishable contrast of the gray scale of the TEM image, the carbon amorphous thin film are formed with oval GO islands. It is however not a single complete mono-, double- or multi-layer, but it is decorated with small GO islands on its basal plane. As indicated by the distance of the discrete GO islands, the ballistic transport of the carriers should be limited to intervals of 25 nm or even larger.

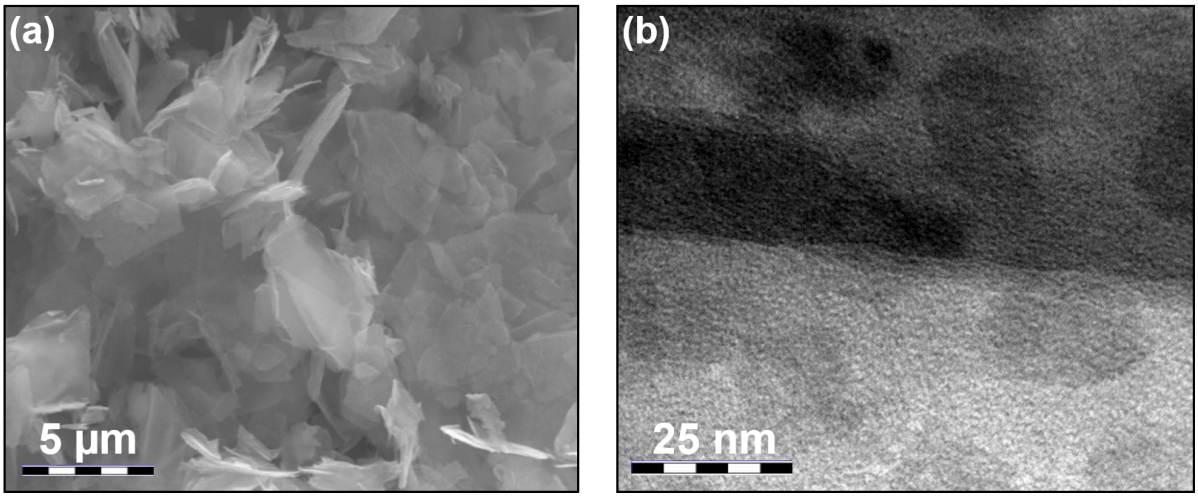

Figure 2.6: Topographical characterization of GO flakes [116]. (a) SEM image of GO flakes. (b) TEM image of a GO thin film.

2.4.2 UV-VIS Spectroscopy and Fluorescence Spectroscopy Characterizations

UV-VIS spectroscopy is a technique to measure the collective electronic transitions of the atoms and molecules from ground states to excited states in the UV-VIS spectral region. The absorption peaks provide the qualitative analysis of functional groups of molecules, impurities and conjugation of compounds. In molecules, there are four possible transitions σ-$\sigma^\star$, n-$\sigma^\star$, π-$\pi^\star$ and n-$\pi^\star$, for which the corresponding absorption energies are successively increasing. GO flakes generated by IHM and LTEDS were prepared in DIW of the same concentration and pH and characterized via UV-VIS spectroscopy. The obtained spectra are shown in figure 2.7(a). The black curve is the bulk spectrum of the original mesh graphite, which was also dissolved in DIW. For both GO flake solutions by IHM and LTEDS, there is a sub-shoulder at about 300 nm corresponding to n-$\pi^\star$ (plasmon peak) states which originate from carboxyl groups [111]. Moreover, an absorbance peak that appeared at 237 nm corresponds

to the electron transition between π-$\pi^\star$ states within a flake. The intensity of the absorption spectra is quantitatively proportional to the π-$\pi^\star$ and the σ-$\sigma^\star$ states within the amorphous carbon lattice. The peak broadening is related to the fact that the tetrahedral sp^3 states get formed during the high temperature treatment. Comparing the latter two spectra, the absorption intensity of the LTEDS GO solution at 237 nm was much higher and the peak was sharper. This was due to the fact that more sp^2 intact carbon lattices within GO flakes prepared by LTEDS were preserved in terms of higher rate of π-$\pi^\star$ vibrations states compared to those from the IHM. This is because the high process temperature of IHM favors the forming of MnO_4^-, which resides on the surface of the carbon sheets and reacts with the cyclo- manganese oxide and manganese oxide, resulting in more intrinsic defects tetrahedral sp^3 states and consequently decreases the amount of π-$\pi^\star$ states. The result confirmed that the IHM process, with its higher temperature, is fast but not effective enough to preserve the hexagonal carbon formation. The GO flakes produced by LTEDS present better characteristics in order to be utilized as a high-quality transducer material.

The GO flakes exfoliated by LTEDS were additionally characterized by fluorescence spectroscopy. The obtained excitation-emission matrix is shown in figure 2.7(b). The GO aqueous solution shows a very broad absorption spectrum. Dependent on the incident excitation wavelength, the emission energy is smaller (red-shift) than the excitation energy by following the so-called principle "Stokes shift". In other research works, both a blue-shift [119] and a red-shift [120] of GO fluorescence had been observed. The fluorescence of GO flakes with typical C:O ratio around 2 to 4 has been reported within the range from the visible to near infrared. Based on the semiconductor electronic band structure and molecular orbital concepts, the oxygen functional groups, sp^2 carbon lattice and some sp^3 oxidized sites of the GO flakes greatly contribute to the generation of the fluorescence. The fluorescence is present due to the electron-hole recombination from the bottom of the conductance band and surrounding localized electronic states to the valance band. More specifically, the emission species of visible fluorescence is generated from the non-oxidized atoms and the boundary of the oxidized carbon atoms [121]. Therefore, the fluorescence of GO flakes can be tuned in terms of the density of oxygen functional groups by different reduction methods and/or the distribution of carrier populations by external electronic fields.

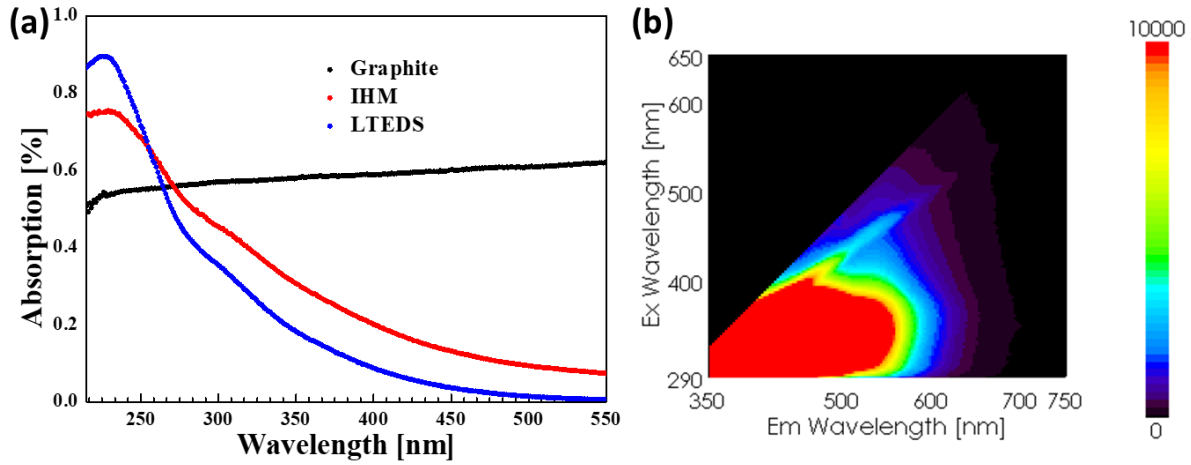

Figure 2.7: (a) UV-VIS spectroscopy characterization of GO flakes in DIW shows the absorption spectra for the original graphite and GO flakes exfoliated by IHM and LTEDS. (b) The excitation-emission matrix of the GO flakes in aqueous solution.

2.4.3 XRD and FT-IR Spectroscopy Characterizations

XRD is used to identify the crystallinity of materials. The X-rays interact with the crystal lattice by striking the electrons and the emanating secondary spherical waves from the electrons are formed. The destruction and construction of these waves generate the diffraction patterns. The crystallization of the measured sample can be deduced by analyzing the angle and intensities of the diffraction patterns. These diffraction patterns follow the Bragg's law: $2d \sin\theta = n\lambda$, where d is the spacing between diffracting planes, θ is the angle of incidence, n is an integer and λ is the wavelength of the incident X-ray. XRD is able to address the complete extent of the carbon lattice after the chemical exfoliation process. This characterization tool is used to compare the final flakes' quality between the two protocols, namely, the IHM and LTEDS. The results are shown in figure 2.8(a). The angle of incidence of the X-ray ranged from 5° to 70° and all of the curves are normalized. The shifts in the specific reflections and the overall diffraction patterns clearly prove a better synthesis-quality of GO flakes by LTEDS. The strong (002) peak at $2\theta = 26.5°$ corresponds to an interlayer spacing of approximately 0.34 nm in the graphitic layers. For both exfoliation protocols, the (001) peak that appeared at around $2\theta = 10.6°$ represents the exfoliated graphene oxide with an interlayer spacing of approximately 0.83 nm due to the presence of functional groups that bound on both sides of the carbon basal plane and physical-absorbed water molecules [114]. This value corresponds to other reported values, for example: the interlayer distance for a dry multi-GO flake was observed by XRD to be approximately 0.639 nm [122] and for a hydrate multi-GO flake the measured distance was 1.2 nm [123]. The vanishing (002) peak and the arise of the fingerprint at $2\theta = 32° - 37°$ for both IHM and LTEDS manifest that ordered carbon lattices of graphite were partially transformed into out-of-plane disordered carbon lattices. Diffraction peaks at $2\theta = 41° - 43°$ indicate the displacement degree of the sheets along the stacking direction for GO flakes. This implies that the basal plane in the mesh graphite had slipped out of the alignment. The residual ions remaining within the GO flakes by IHM lead to a broad peak at this position. LTEDS achieved sharper peaks, which indicate a better cleaning procedure of the amorphous carbon

material. More importantly, in comparison with other reported results, diffraction peaks of LTEDS GO emerged at $2\theta = 65°, 75°$ and 83°, which were clearly distinct and indicated that after the strong oxidation a larger portion of carbon lattice GO flakes were preserved by the low process temperature and advanced cleaning process.

In addition to XRD, FT-IR spectroscopy was used for a quantitative comparison of GO flakes synthesized by the IHM and the LTEDS protocols. This technique measures the IR absorption and transmission of the samples with incident infrared light. The obtained spectrum represents the molecular fingerprints of the sample. As shown in figure 2.8(b), the normalized spectra depict the influence of the additional parameters in combination with the cleaning procedures. In the standard IHM, the molecular vibration bounds were relatively weak and not clearly distinctive because of the residual impurities on the GO flakes after the cleaning procedure. After the first enhanced cleaning step using only the dialysis, this feature was improved minimally. The spectrum of the second cleaning step in LTEDS showed an improved purity of the exfoliated GO. The several washing described in the section 2.3 had a remarkable effect. The stretching vibration of the hydroxyl group O−H was confirmed at 3434.6 cm^{-1} and the stretching vibration of the carboxylic group was detected at 1720 cm^{-1}. Characteristic absorption bands could be clearly identified in the FT-IR spectrum of the GO, which could be attributed to the asymmetric C−O stretching vibration with a characteristic doublet state at 1050 cm^{-1} and 1100 cm^{-1}. Moreover, bands of medium intensity could be assigned to the symmetric and asymmetric C−H vibrations at 2912.4 cm^{-1} and 2850.1 cm^{-1}. The epoxide group could be identified by the weak band of the asymmetric C−H vibration of the epoxy ring at 2921.4 cm^{-1}. Additionally, the stretching vibration of the oxirane R−O−R functional was detected at around 1230 cm^{-1}. The systematic cleaning steps via LTEDS largely improved the quality of GO compared to the IHM. In addition, the carboxylic and hydroxyl functional groups of the high-quality GO by LTEDS were identifiable in the IR spectrum. This proves the efficiency for further chemical functionalization of the GO.

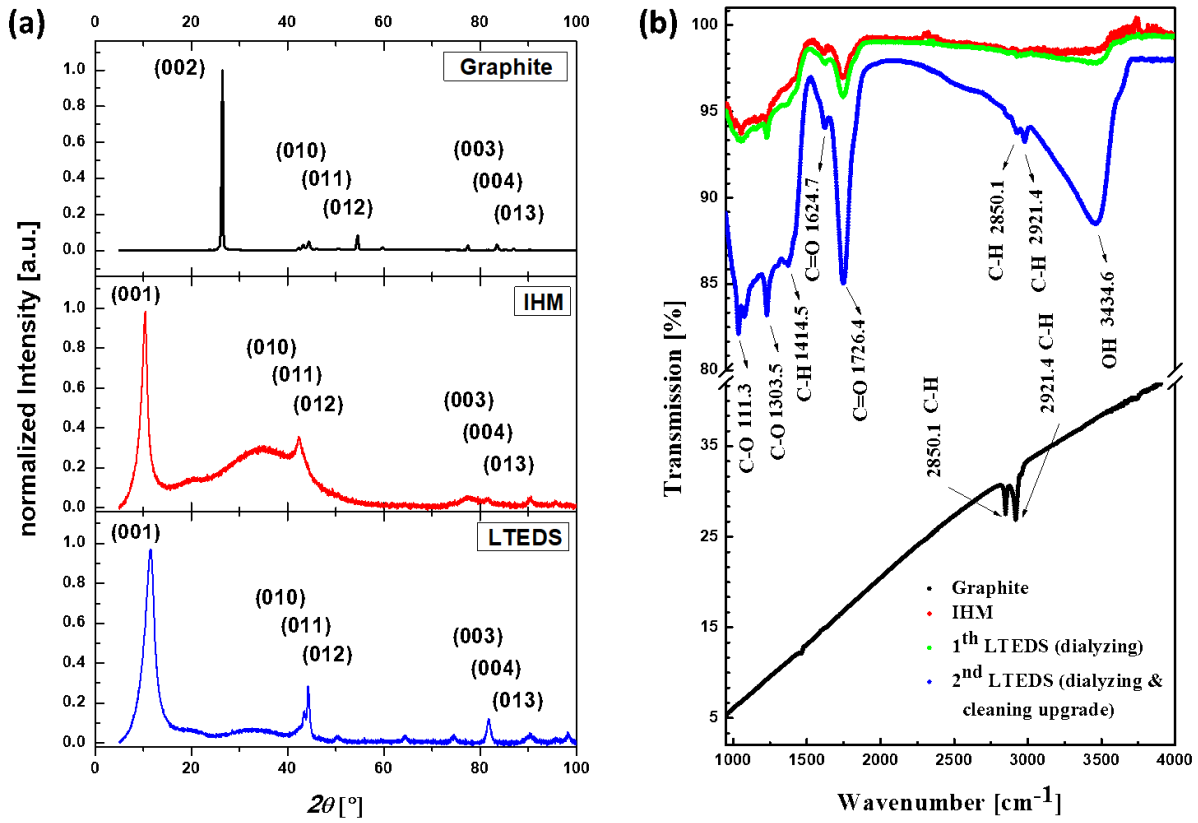

Figure 2.8: (a) XRD diffraction patterns of graphite and graphene oxide samples by IHM, pre-LTEDS and LTEDS within the diffraction angle range: 5° to 70° [116]. The shifts in the specific reflexes and the overall diffraction patterns clearly proves the synthesis enhancement of LTEDS. (b) FT-IR spectra of GO flakes prepared by IHM and LTEDS: the C−O vibration peaks clearly illustrate the uncovering of the doublet.

2.5 Wafer-Scale Fabrication of rGO Devices

2.5.1 GO Thin Films Preparation

Toward the purpose of wafer-scale fabrication, 4-inch glass or SiO_2/Si wafers were thoroughly cleaned with freshly prepared Caro's acid (H_2O_2 30 %). Afterwards, the wafers were activated by O_2 plasma ($t = 5$ min, 230 W) and functionalized by (3-aminopropyl) triethoxysilane (APTES) gas-phase silanization. The Au coated surface was positioned at an angle of about 85° with respect to the outlet valve of the desiccator to provide a maximum contact area between the substrate and the silane-saturated gas stream. Then, the pressure inside the desiccator was reduced to 130 mbar such that a continuous gas flow of the silane over the substrate was ensured. The reaction time was 2 h. In this process, the surface $-OH$ groups replace the $-O-CH_2-CH_3$ ethoxy-group by SN_2 reaction forming the corresponding 3-aminopropylsiloxane (APS) on wafer surface [124, 125]. After the silane coating, the wafer was washed with ethanol. The $-NH_2$ groups on the other end of the APS layer, which are freestanding in the ambient air, covalently immobilize GO flakes by reacting with the $-COOH$ groups. 5 ml GO solution $pH = 2.9$ prepared by LTEDS were applied and spin-coated onto the wafer surface.

The detailed process information is given in figure 2.9(a)-(d) and each process step was confirmed with a contact angle measurement. The static contact angle of a bare glass wafer is 30.5°. After being treated with O_2 plasma, the glass surface is functionalized by $-OH$ groups with a static contact angle below 10°. Uniform APTES molecules self-assemble all through the glass wafer surface by a gas-phase silanization technique. In this process, the $-OH$ groups on the glass surface covalently bond to the $-COOH$ groups of APTES in the manner of dehydration at 60 °C in a vacuum desiccator. The static contact angle of the formed APTES layer is 67.5°. An average of static contact angles is approximately 65° which indicates a successful formation of an APTES layer all through the 4-inch wafer. The freestanding $-CH_3$ groups of APTES molecules subsequently immobilize GO flakes by reacting with $-COOH$ groups of the carbon basal plane in the manner of dehydration at room temperature. The GO dispersion was adjusted to be acidic so that face-to-face interaction among flakes was dominant [126] with a pH value of 2.9 for the GO solution. The static contact angle of the formed GO thin film is 44.8°.

This spin-coating step was repeated multiple times to prevent pinholes within the GO layer. Because they were in hydrate states, the flakes were positively or negatively charged depending on the types of functional groups on the carbon basal plane. The amount, distribution and variety of functional groups on the carbon basal planes were random so that the positive- and negative-charge centers on a single flake were most probably separated. At least one layer of polar water molecules remained around these charge centers in the manner of electrostatic interaction. Consequently, the GO flakes, as dipoles, stacked up by Van der Waal interactions during the multi spin-coating process. In order to get rid of the water molecules, but not influence the thin film intrinsic properties, the GO on the substrate was baked in the ambient air at 90 °C for 30 s in between the sequential spin-coating steps.

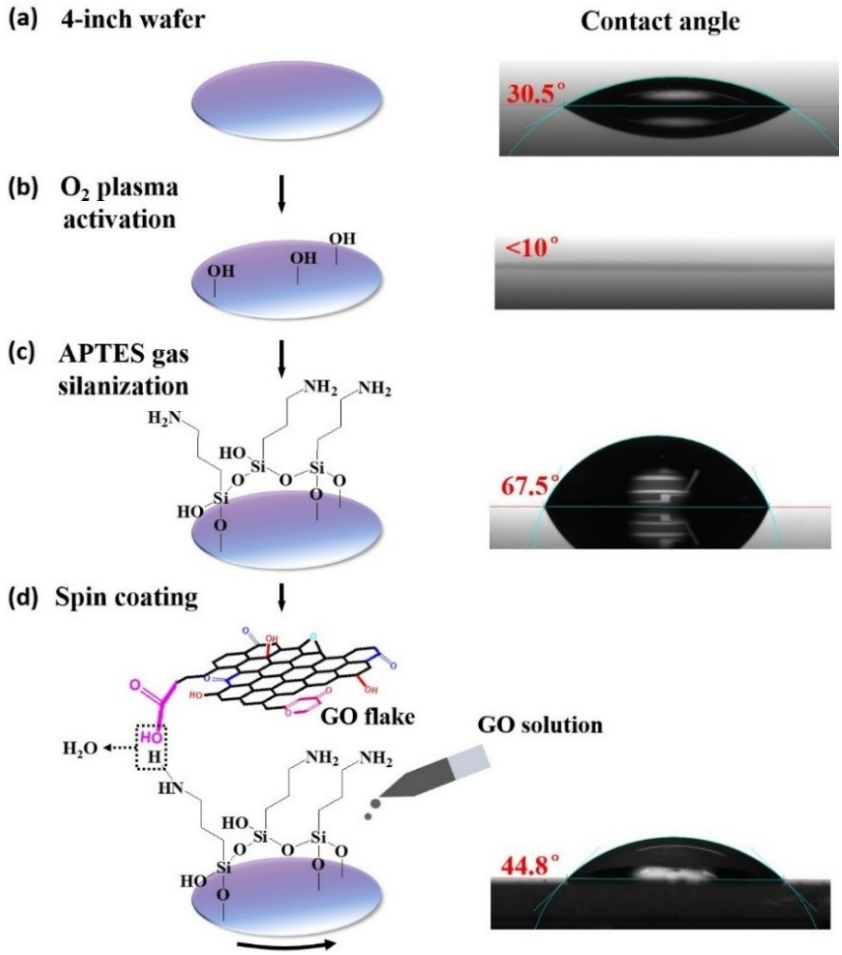

Figure 2.9: Schematics of the GO thin film preparation on glass substrate in wafer-scale. This protocol also applies to the Si/SiO_2 substrate [116]. (a) The static contact angle of a bare glass wafer is 30.5°. (b) After being treated with O_2 plasma, the glass surface is functionalized by $-OH$ groups with static contact angle below 10°. (c) Uniform APTES molecules self-assemble all through the glass wafer surface by a gas-phase silanization technique. In this process, the $-OH$ groups on the glass surface covalently bind to the $-COOH$ groups of APTES in condensation reaction at 60 °C in a vacuum desiccator. The static contact angle of the formed APTES layer is 67.5°. An average of static contact angles is approximately 65° which indicates a successful formation of an APTES layer all through the 4-inch wafer. (d) The freestanding $-CH_3$ groups of the APTES molecules subsequently immobilize GO flakes by reacting with the $-COOH$ groups on the carbon basal plane in a condensation reaction at room temperature, while the pH value of the GO solution is 2.9. The static contact angle of the formed GO thin film is 44.8°.

2.5.2 Wafer-Scale Ellipsometry Characterization

Unlike AFM characterization that provides information within the micro/nano- scale, ellipsometry is an effective and efficient tool to measure up to the millimeter scale and it is able to offer a macro view of the topographical uniformity of a thin film over a 4-inch wafer [127]. Ellipsometry is a contact-free optical technique, which is based on the change in polarization of the reflected light after interaction with the material. It is used for investigating the film thickness, refractive index, dielectric parameters, surface roughness, composition, crystallinity, uniformity and many other material properties. For spectroscopic ellipsometry, the wavelength of the incident light broadly ranges across the infrared, visible and ultraviolet regimes. As shown in

figure 2.10(a), the incident light upon the sample surface can be decomposed in its s-plane and p-plane components which are oscillating in a perpendicular and parallel direction to the plane of incidence. After being normalized to the initial amplitude of the s-plane and p-plane components of the incident light, the s-plane and p-plane components of the reflected light can be denoted as R_s and R_p. The output signal of the ellipsometry measurement is the reflectance ρ, defined as:

$$\rho = \frac{R_p}{R_s} = \tan(\Psi)\, e^{j\Delta} \tag{2.16}$$

in which $\tan(\Psi)$ and Δ are the amplitude ratio and phase difference of the s-plane and p-plane components of the reflected light, respectively. The thickness of APS and nano-GO thin films by different spin-coating times was determined subsequently by spectroscopic ellipsometry measurements [128] using the multi angle measurement method at 50°, 60° and 70°, as shown in figure 2.10(b).

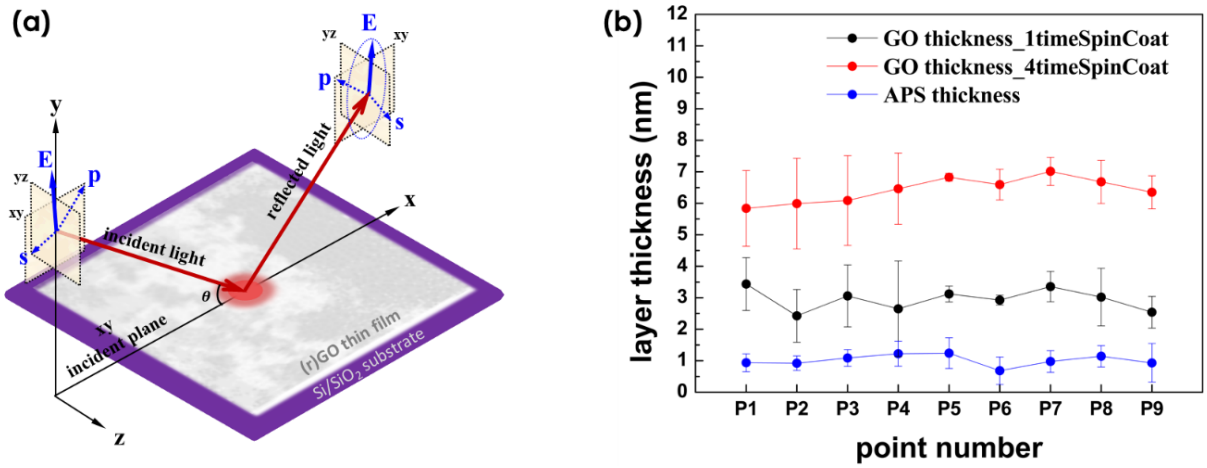

Figure 2.10: Characterization of GO thin film preparation on wafer-scale. (a) Ellipsometry setup: The incident light upon the sample surface can be decomposed into its s-plane and p-plane components which are oscillating perpendicular and parallel to the plane of incidence, respectively. The amplitude ratio $\tan(\Psi)$ and phase difference Δ of the reflected light are measured versus the incident wavelength at a set angle of incidence θ. (b) GO thin film thickness after 1 time spin-coating and 4 times spin-coating on a 4-inch wafer, which can be extracted from their ellipsometry measurements [116].

For both 1 time and 4 times spin-coating, 3 wafers with 9 points on each were measured geometrically along the wafer radium to extract the statistical values of the thicknesses of SiO_2, the APS layer and the GO thin film. The APS layer was about 1 nm, while the mean thicknesses of nano-GO thin films were 2.95 ± 0.35 nm and 6.43 ± 0.40 nm by 1 time and 4 times spin-coating, respectively. The thickness of mono-layer GO flakes was observed to range from 0.4 nm to 1 nm [74, 129–131], which was highly dependent on the oxidation functionalization of the carbon basal plane during the exfoliation process. From the ellipsometry results, it can be seen that the spin-coating technique formed a stack of GO. Additionally, the refractive indexes of each dielectric layer SiO_2, APS and nano-GO thin film were extracted by fitting them with the Cauchy equations:

$$\begin{aligned} n_\lambda &= n_0 + 10^2 \frac{n_1}{\lambda^2} + 10^7 \frac{n_2}{\lambda^4} \\ k_\lambda &= k_0 + 10^2 \frac{k_1}{\lambda^2} + 10^7 \frac{k_2}{\lambda^4} \end{aligned} \tag{2.17}$$

where λ is expressed in nanometers.

2.5.3 Nanofabrication of GO Devices

To characterize the electronic properties of the generated GO thin films, IDEs were prepared by standard photolithography, metal evaporation and a lift-off process on a 4-inch glass wafer, as shown in figure 2.11(a). The electrode was a bilayer stack: top layer was 270 nm Au and bottom was 30 nm Ti, which acted as an adhesion layer. Overall, there were 72 chips over the entire wafer. Each chip was 7 mm $\times$ 7 mm in size as shown in figure 2.11(b) and consisted of a set of 4×4 drain IDEs-array sharing a common source-electrode bar as shown in figure 2.11(c). The resistance and capacitance of each drain electrode were designed to be equal for an accurate comparison of measurement results amongst channels. The width and length of a single drain electrode was 5 µm and 100 µm, respectively, while the separation distance of the neighboring electrodes was 5 µm. In the case of the 10-finger electrodes, the effective channel length and width of the IDEs were 5 µm and 900 µm, respectively [132–134]. Following the same procedure as introduced in section 2.5.1, a GO thin film was formed on top of the prepared IDEs. Afterwards, the GO thin film was patterned by a second step of standard photolithography followed with O_2 etching. The detailed procedure is shown in figure 2.11(d)-(g). The photoresist patterns serve as masks to reserve the GO thin film during the O_2 reactive ion etching process, while the unprotected thin film was completely etched away.

After a thorough cleaning by acetone and isopropanol, the GO patterns fabricated from 2 times spin-coating were topographically characterized. The SEM image of the obtained GO-IDEs chip is shown in figure 2.12(a). A single GO-IDEs channel was characterized by optical microscopy and SEM, as shown in figure 2.12(b)-(c). The contrast of gray levels demonstrates that the surface was relatively smooth. Furthermore, the GO pattern was characterized by AFM, as shown in figure 2.12(d)-(e). The extracted thickness was 5.13 nm in average, which is coherent with the values obtained by the ellipsometry characterization after 1 and 4 times spin-coating. The roughness of the GO thin film was determined by means of the root mean square average of the height derivation $R_q = 1.39$ nm and the arithmetic average of the absolute values of the surface height derivation $R_a = 0.95$ nm.

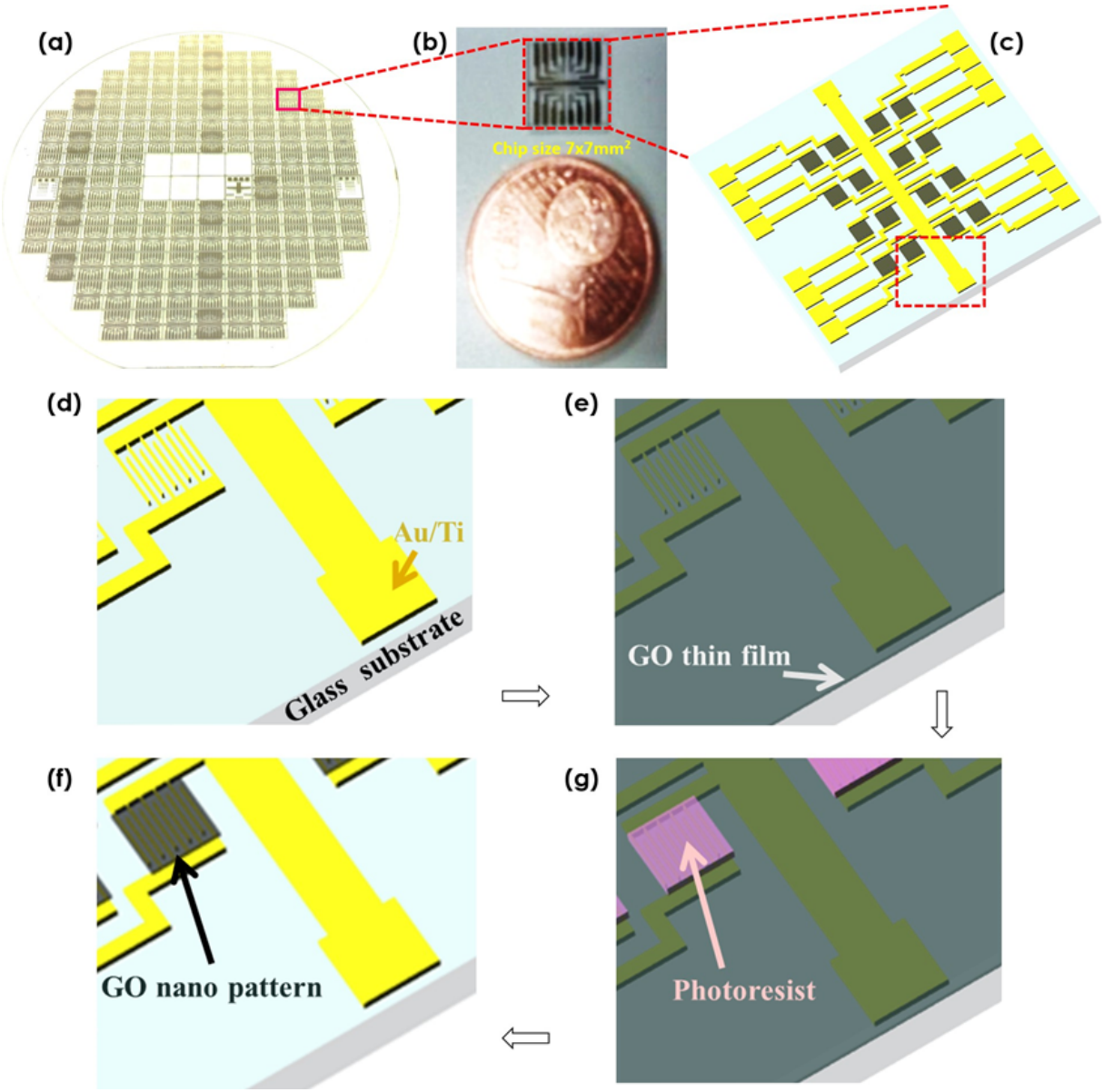

Figure 2.11: Preparation of GO devices. (a) GO devices on a 4-inch glass wafer. (b) The size of a single chip is 7 mm × 7 mm. (c) Schematic three dimensional illustration of interdigitated electrodes on a single chip: 16 channels share a common-source electrode, which is located in the middle of the chip. Each channel has 10 IDE fingers: the effective channel length and width are 5 µm and 900 µm, respectively. (d) IDEs consist of 30 nm Ti and 270 nm Au, and are prepared by standard photolithography, metal evaporation and lift-off processes on 4-inch glass wafers. (e) A GO thin film is formed by the spin coating technique. (f) Photoresist patterns serve as masks, which only cover IDEs fingers after a standard photolithography technique. (g) The GO thin film is preserved by the photoresist mask and the region without protection is etched away by O_2 plasma. The photoresist is removed by acetone and isopropanol later in the process.

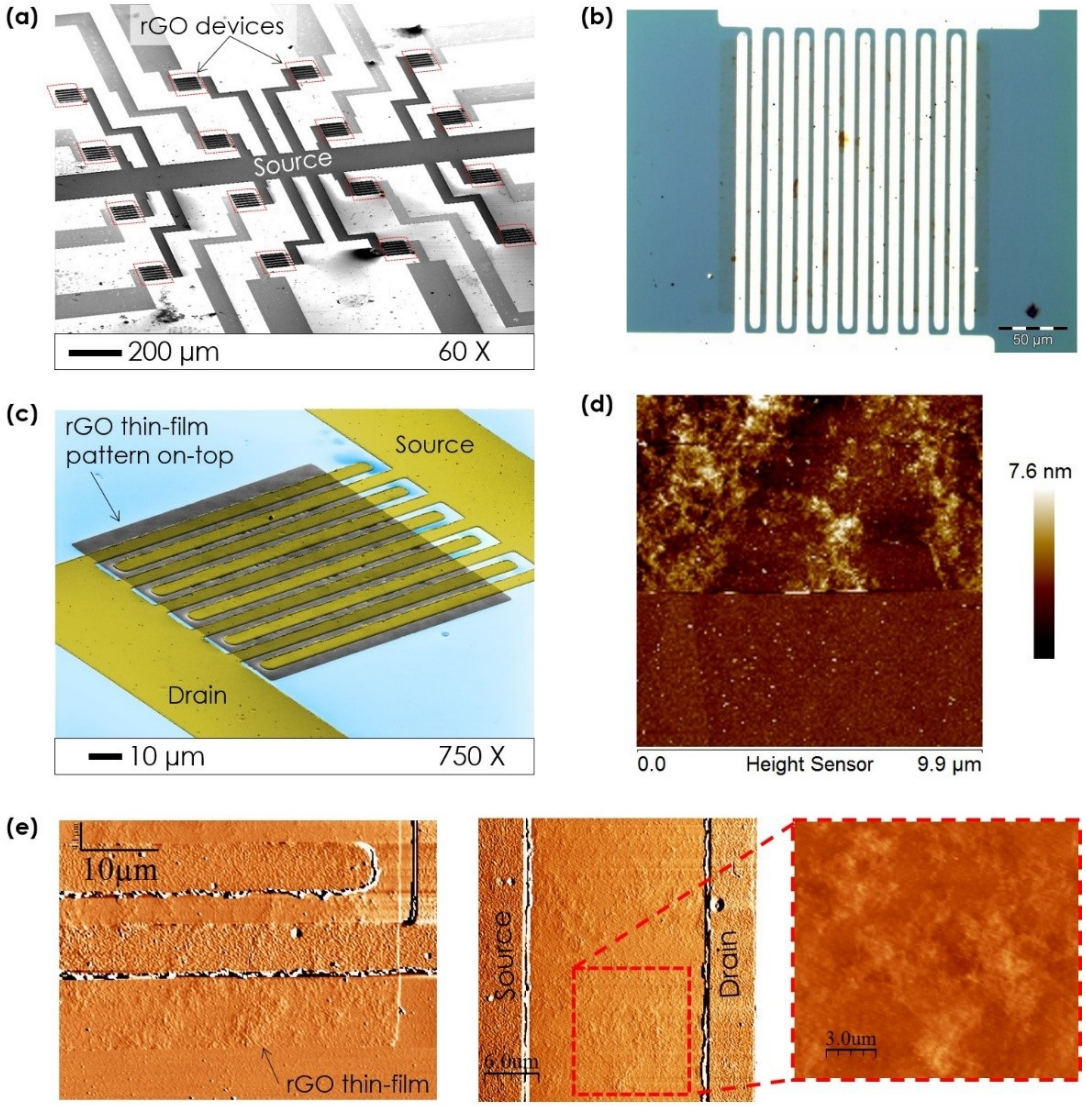

Figure 2.12: Topographical characterization of GO devices [116]. (a) SEM image of a GO-IDEs array on a single chip. (b) Microscopic image of a patterned GO thin film. (c) SEM image of a patterned GO thin film. (d) AFM characterization of a GO pattern (2 times spin-coating) indicates that the mean thickness of GO thin film is 5.13 nm with roughness $R_q = 1.39$ nm and $R_a = 0.95$ nm. (e) AFM characterization of a patterned rGO thin film over drain-source electrodes.

2.6 Conclusion

In this chapter, GO flakes were chemically exfoliated by a LTEDS method using low exfoliation temperature (20 °C) and additional desalination steps. The quality of GO flakes generated by LTEDS and conventional IHM were compared by UV-VIS, XRD and FT-IR characterizations. The UV-VIS characterization showed a higher absorption intensity at 237 nm for GO flakes by the LTEDS method, which is quantitatively proportional to the π-π^* vibration states. It indicated that a higher proportion of fine carbon lattice of GO flakes was preserved by the LTEDS method. The XRD characterization displayed a sharper diffraction peak at 41-43° for GO flakes by LTEDS. This result indicated larger displacements of atomic layers in the exfoliated GO flakes. The XRD peaks at 65°, 75° and 83° that appear in the case of the GO flakes produced by LTEDS were distinct features that manifest a higher density of oxidative functional groups and a more efficient removal of the physiosorbed ions from the carbon lattice. In addition, the FT-IR characterization results demonstrated more details of the fingerprints of oxygen functional groups after the exfoliation. The stronger IR adsorption at 3434.6 cm^{-1} ($-$OH stretching vibration), 1726.4 cm^{-1} (C$=$O stretching vibration), 2921.4 cm^{-1} and 2850.1 cm^{-1} (C$-$H symmetric stretching vibration) clearly proved that the ions were efficiently removed from the GO flakes by the LTEDS method. These characterization results concretely proved that the LTEDS method generated high-quality and clean GO flakes for device preparation.

A reproducible wafer-scale process for GO based devices was subsequently established, making use of gas-phase silanization, spin-coating, standard photolithography and O_2 reactive ion etching techniques. The GO thin films were formed on the bare Au and SiO_2/Si (or glass) substrates with APS as linker layers. Characterized by ellipsometry and AFM, the thickness of the linker layer APS was 1.01 ± 0.40 nm, while the thicknesses of the nano-GO thin films were 2.95 ± 0.35 nm and 6.43 ± 0.40 nm in the condition of 1 time and 4 times spin-coating, respectively. The ellipsometry results particularly proved that the GO thin film is topographically uniform at a 4-inch wafer-scale. This fabrication method is of significant importance for a massive, cost-effective production of GO thin films in the various application fields, especially towards biosensing.

3 Reduced Graphene Oxide (rGO) Devices

In this chapter, the electronic properties and surface characterizations of rGO thin films are investigated in detail. Firstly, the reduction methods, which transform the insulating GO thin films to conductive rGO, are summarized and commented. Secondly, a thermal reduction treatment was applied to the GO-IDEs devices which were described in the previous chapter. The electronic properties, such as the contact between the rGO thin films and the IDEs, the completeness of the rGO thin films, and the resistance uniformity over a 4-inch wafer-scale were verified by current-voltage (I-V) and cyclic voltammetry characterizations. Especially, the bipolar characteristics, the field-effect mobility and the sheet resistance of the rGO thin films extracted by FET and four-point measurements are studied. Thirdly, the reduction degrees were characterized and analyzed by Raman spectroscopy and X-ray photoelectron spectroscopy (XPS).

3.1 Reduction Methods

The oxygen functional groups on the carbon basal plane of chemically exfoliated GO allow the covalent immobilization of GO thin films on various substrates. However, the oxygen functional groups on the carbon basal plane of the thin films significantly obstruct the carrier hopping among the sp^2 localized carbon area, preventing advanced conductivity over microscale distances [59, 71]. To utilize GO as functional material, with a conductivity similar to that of the graphene, various reduction methods are summarized in this section. These reduction methods are utilized to remove the sp^3 oxygen functional groups, while preserving the carbon lattice as completely as possible. The principle of all reduction methods is to break down the sp^3 bindings existing in different forms and recover the sp^2 C−C bindings by the following routes:

- The chemical reduction makes use of different types of chemical reactants to remove oxygen groups, such as hydrazine [135–137], strong alkaline media [138], substituted borohydrides [139, 140], sulfuric acid [141], ascorbic acid [142], and alanine [143]. A chemical reduction is more functional in a liquid phase because the chemical reactions take place on both basal planes of the carbon lattice. However, this reduction method is not preferable because extra ions or molecules tend to attach onto the GO surface and act as contaminants or

dopants. This tends to influence the intrinsic properties of the carbon lattice [107].

- The optical reduction consists of irradiating GO with photons, whose energy is larger than the chemical bond energy between the oxygen functional groups and the carbon basal plane, thus restoring C−C bonds [144–146].
- The thermal reduction method works by annealing the carbon lattice [147, 148]. This method has been revealed to induce the formation of carbonyl and ether groups at the atomic level. Nevertheless, this method is able to reduce a bulky thin film composed of several carbon sheets.
- The hydrogen reduction consists of triggering a chemical reaction between the hydrogen and the functional oxygen groups under specific reaction temperatures. This causes the conjunction of the carbon lattices and the removal of the sp^3 oxygen groups [149]. The high efficiency of this reduction method has been proven [73]. Therefore, this method is of interest for researchers to generate rGO which behaves similarly to pristine graphene.

Considering the GO thin films are stacks of multiple GO flakes, the thermal treatment could be the optimal method to transform the insulating GO to conductive rGO thin films. Indeed, the thermal treatment is affecting the bulk of the thin films, whereas the other methods are limited to their surface.

During this process, the oxygen functional groups are removed from the carbon basal plane and subsequently decomposed as CO or CO_2. These gases are accumulating to form a relatively huge pressure between the neighboring GO sheets. The pressure values range from approximately 40 MPa at 300 °C to 130 MPa at 1000 °C [150]. As reported, the Young's modulus of pristine graphene is as high as 1 TPa [67] and the carbon lattice is thermally stable up to 700 °C [68]. Therefore, the pressure induced by CO or CO_2 has no destructive effect to the carbon lattice, but the reduction temperature must be kept below 700 °C. Since 400 °C is the maximum achievable temperature by the vacuum oven at disposition, a reduction temperature of 350 °C was chosen to carry out the thermal treatment to the GO devices. In this thesis, the thermal reduction at 350 °C for 10 h in the vacuum oven, followed by an annealing at 600 °C for 20 s in the ambient air, is defined as the thermal reduction protocol (TRP). The annealing is used to change the electrical contact between the thin films and the IDEs as explained in the next sections.

3.2 Electronic Characterization

To apply rGO thin films as transducers for electronic devices, their uniformity concerning electronic performance and device stability has to be clarified beforehand. The TRP was used as the reduction protocol. The device structures used for the electronic characterization is shown in figure 3.1(a), in which large-scale GO thin films were prepared on top of 10-finger IDEs without further patterning. The length of each finger electrode was 100 µm while the width of each electrode and the separation distance of neighboring electrodes were both 5 µm.

After the mild reduction at 350 °C for 10 h, the obtained rGO thin films formed a Schottky contact [151] with the IDEs beneath. This was deduced from the I-V curve, which was not linearly crossing the origin. In order to convert the Schottky contact into an ohmic contact, the devices were subsequently annealed at 600 °C for 20 s in ambient air. The ohmic contact is confirmed by linear I-V characteristic curves of all 16 channels as shown in figure 3.1(b), where the characteristic linear relation between the current I and voltage V is observed.

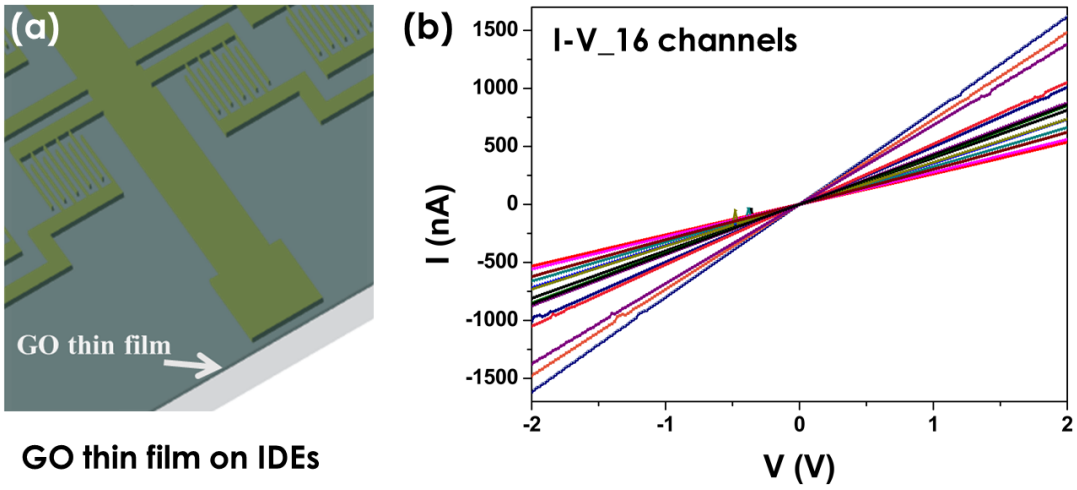

Figure 3.1: I-V characterization of a multi-layer rGO thin film (prepared by 8-times spin coating). (a) The configuration of the IDEs chip: in total 10 finger electrodes with a finger length of 100 µm, a finger width and a separation distance of neighboring electrodes of 5 µm. (b) The linear I-V characteristic of 16 channels of one IDEs chip shows that the ohmic contacts are formed between the rGO thin films and the IDEs after the thermal reduction at 350 °C for 10 h in the vacuum oven and subsequent annealing at 600 °C for 20 s in ambient air [116].

3.2.1 Cyclic Voltammetry Characterization

For the rGO thin films prepared by the TRP, cyclic voltammetry measurements were carried out to confirm the formation of complete rGO thin films without pinholes on the top of the IDEs. The measurements were performed with an Ivium potentiostat with a three-electrode configuration as shown in figure 3.2(a).

The rGO/IDEs or bare IDEs serve as working electrode (WE) while a Pt wire and an Ag/AgCl electrode are used as counter electrode (CE) and reference electrodes (REs), respectively. A series of sweeping voltages is applied to the WE against the RE and the output current is measured between the WE and the CE. The measured current represents the intensity of charges transferred between the redox markers K3/K4 ($K_3Fe(CN)_6/K_4Fe(CN)_6$) and the WE. It reflects the electrochemical properties on the WE surface [152, 153]. Therefore, the cyclic voltammetry measurement can be used as an electroanalytical technique to analyze the coverage quality of rGO thin films on top of the IDEs.

The electrolyte solution in the fluidic cell for the measurements was prepared by mixing 0.5 mM K3 with 0.5 mM K4 in 10 mM phosphate buffered saline (PBS). The PBS consisted of 0.01 M phosphate buffer, 0.0027 M KCl and 0.137 M NaCl with

a pH value 7.4, where 0.01 M phosphate buffer contained 0.0075 M Na_2HPO_4 and 0.0025 M NaH_2PO_4. The voltages were applied on the WE starting from -0.2 V and sweeping forwards and backwards between -0.2 V and 0.6 V with a scan rate of 50 mV s^{-1}. After 15 sweeping cycles, the results for rGO/IDEs and bare IDEs (Au) were summarized. An exemplary measurement is shown in figure 3.2(b). The results of the measurements show no peaks that correspond to Au electrodes for the rGO devices. This proves that the rGO thin film covers the IDEs completely without pinholes. It also confirms the topographic results obtained by AFM and SEM characterizations in chapter 2.

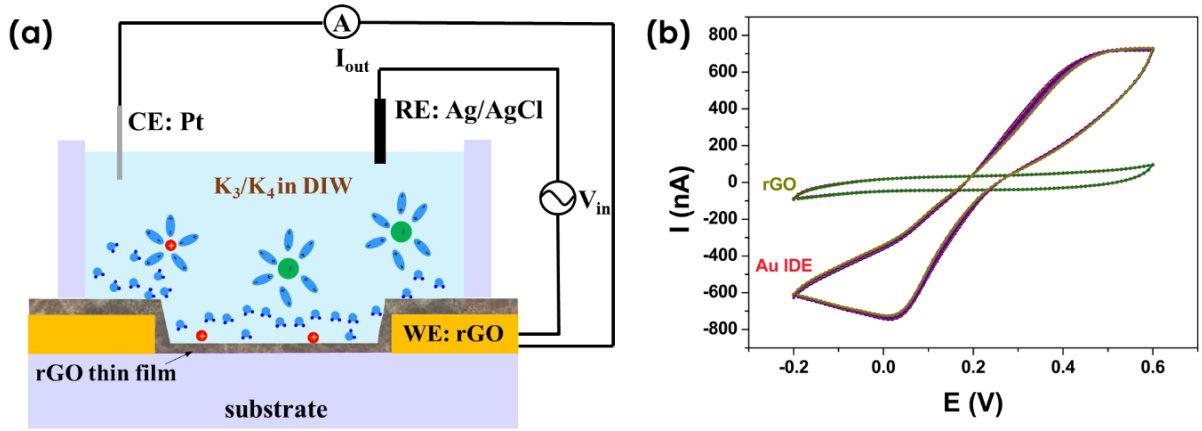

Figure 3.2: Cyclic voltammetry measurement of a rGO thin film. The rGO thin film was transformed from the prepared GO thin film with the TRP. (a) The measurement setup: the configuration of the electrodes was as follows: the WE of the impedance analyzer was connected to the common-source electrode and the drain electrode of the chip. An Ag/AgCl electrode and Pt electrode served as REs and CE. Both were immersed in the measurement cell filled with K3/K4 redox solution. (b) The scan ranged from -0.2 V to 0.6 V and started at -0.2 V with a scan rate of 50 mV s^{-1} [116]. The obtained result shows the difference between the rGO thin film and the bare IDEs. It indicates that the rGO thin film is compact and complete without pinholes.

3.2.2 Wafer-Scale Resistance Uniformity of rGO Thin Films

The uniformity of the resistance over a 4-inch wafer was investigated to ensure that the chips are reproducible and, hence, usable for biosensing. In total 10 chips with 16 channels each were measured. The obtained results are shown in figure 3.3(a) with the distribution of measured chips as shown in figure 3.3(b).

In total 11 channels showed defective IDEs and were therefore excluded from these measurements. There were 149 conductive channels with the following resistances:

- 16 channels ranged from $1.44 \cdot 10^4\,\Omega$ to $8.07 \cdot 10^5\,\Omega$ (10.8 %).
- 131 channels from $1.14 \cdot 10^6\,\Omega$ to $9.54 \cdot 10^6\,\Omega$ (87.9 %).
- 1 channel was $7.72 \cdot 10^8\,\Omega$ (0.7 %).
- 1 channel was $2.83 \cdot 10^9\,\Omega$ (0.7 %).

In conclusion, 93 % of the channels for this exemplary wafer were functional. Those defective channels were created during the metal microelectrode fabrication but were not caused by the nonuniformity of the rGO thin films. It is noteworthy that 87.9 % of the channels showed a resistance variation within one order of magnitude, which refers to a relative uniform rGO thin film with respect to electronic properties.

To have an overview of the impact of the reduction duration, another thermal reduction was carried out. The temperature was kept at 350 °C but the time was reduced from 10 h to 4 h in a vacuum oven. As for the first reduction, the samples were subsequently annealed at 600 °C for 20 s in the ambient air. The resistances of a single chip with 16 channels are shown in figure 3.3(c). This result reveals that the reduction for 10 h leads to a decrease in resistance of approximately 2 orders of magnitude. In addition a smoothing of the resistance derivation among channels is observed, compared to the reduction procedure for 4 h. This suggests that longer reduction times would produce even better electronic uniformity. Besides the duration of the reduction, further reduction tests can be carried out by applying different temperatures.

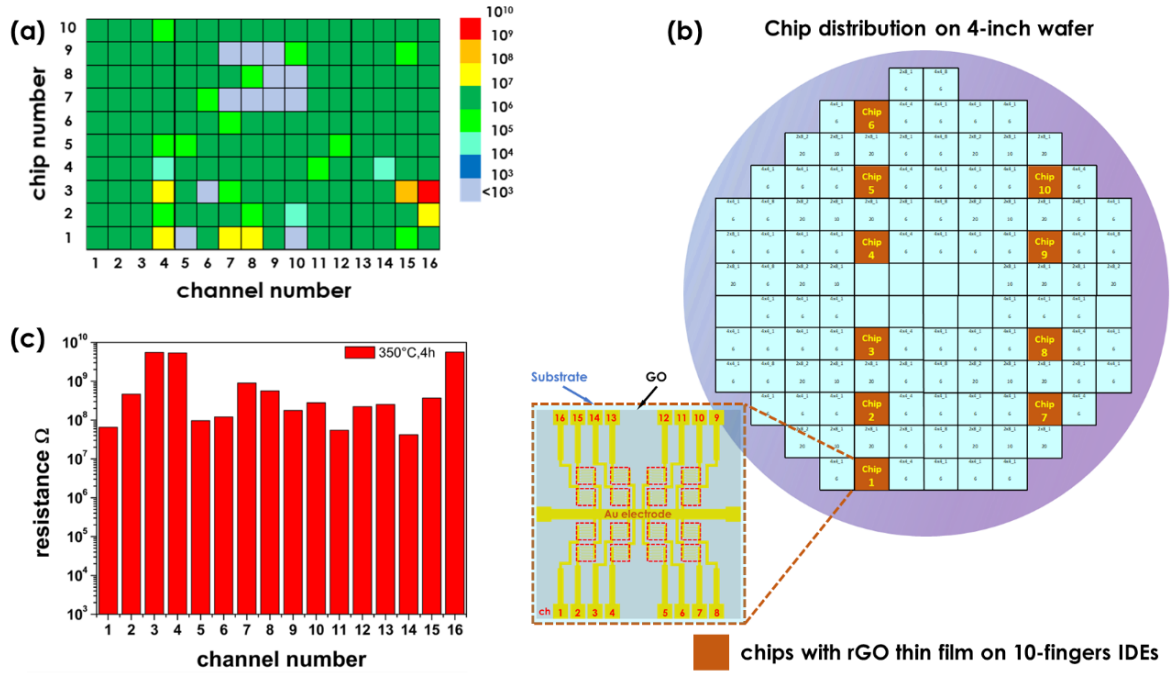

Figure 3.3: Resistance uniformity characterization of rGO thin films (8-times spin coating) with 10-finger IDEs configuration. (a) Resistance mapping of rGO thin films (160 channels) on a 4-inch wafer after TRP [116]. (b) The wafer-scale distribution of chips with rGO thin films on 10-fingers IDEs. (c) Resistance distribution of an rGO thin film (16 channels) after vacuum reduction at 350 °C for 4 h (against 10 h for the TRP) and subsequent annealing treatment at 600 °C for 20 s in ambient air.

3.2.3 rGO Thin Films Based ESFET

An ion-sensitive field-effect transistor (ISFET) device was firstly introduced by Piet Bergveld in 1970 [154]. The device proposed at that time combined a metal-oxide-semiconductor (MOS) transistor and a glass electrode to measure ion activities in electrochemical and biological environments. In line with the aim of

this thesis towards biosensing, the rGO thin films were employed as transducers in ISFET devices configuration which were operated in direct contact with the electrolyte solution. Such devices are denoted as ESFET in this thesis. The obtained bipolar characteristic curves for the rGO thin films provide a straightforward evaluation of the reduction method and its influence on the electronic properties of the rGO thin films.

3.2.3.1 Fundamentals of ESFET

The ESFET, as a potentiometric device, consists of drain, source and gate electrodes as shown in figure 3.4(a) [84, 155]. The transducer layer is located between the drain and source electrodes. An external Ag/AgCl electrode is placed above the transducer layer and immersed inside the buffer solution to apply a gate voltage through the electrolyte to the transducer layer. The critical function of the Ag/AgCl electrode is to maintain a constant potential which is independent from the ionic composition of the buffer solution. Similar to typical metal-oxide-semiconductor field-effect transistor (MOSFET), the Fermi level and the carrier concentration of the transducer layers can be modulated by the gate voltage V_{gs}, resulting in a current change I_{ds} in the drain-source channel.

The rGO-IDEs employed for the ESFET characterization were also thermally reduced by the TRP. The device consisted of 16 channels in a 4×4 array layout with a common-source electrode located in the middle of the chip. Each channel had 10 IDEs fingers, while the effective channel length and width were 5 µm and 900 µm, respectively. The separation distance of the neighboring fingers was 5 µm. The ESFET characterization measurements were carried out with a Keithley 4200-SCS parameter analyzer. The buffer solution was 10 mM PBS. The Ag/AgCl electrode served as the gate electrode to apply sweep voltages from -0.8 V to 0.8 V against the source electrode, while the step voltages were applied between the drain and source electrodes ranging from -0.1 V to 0.1 V with 0.1 V as the step size. The obtained bipolar characteristic curves are shown in figure 3.4(b). Since the Dirac points are located at the position where the valence and conductance bands meet, they correspond to the minimum on each I_{ds}-V_{gs} characteristic bipolar curve (blue and black curves). It can be seen that the Dirac points do not lie perfectly at $V_{gs} = 0$, but are slightly shifted to the right. This fact states that the rGO thin film is initially p-doped. The possible reason for this could be the impurity doping by the substrate and/or the modulation of the residual oxygen functional groups [84, 156]. The left and right arms of the bipolar curve correspond either to the holes or the electrons as the dominant carriers in rGO thin films which is not necessarily doped by impurity elements to realize the conductivity. The applied gate voltage tends to tune the Fermi level of the rGO thin film either into the conductance band or the valence band. This changes the type of carrier to electrons or holes respectively. The concentrations of the carriers increase when the difference between the Dirac point and the gate voltage increases. It is shown that electrons' concentration is increasing much faster than the holes' concentration by the gate voltages. As indicated in the bipolar curves, the concentrations of two carriers are highly dependent on the applied drain-source voltage. Furthermore, a stronger tuning effect is observed for a drain-source voltage $V_{ds} = -100$ mV compared to $V_{ds} = 100$ mV.

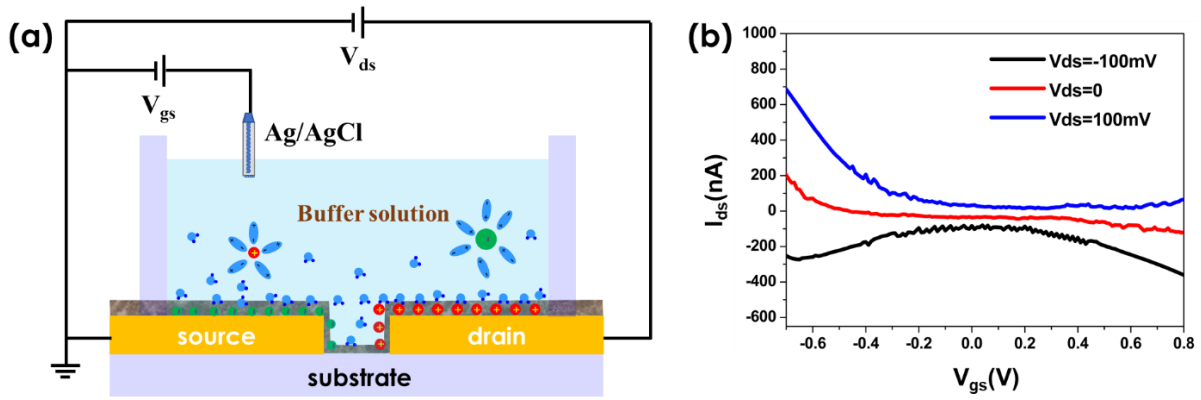

Figure 3.4: (a) Schematic of the ESFET configuration with an rGO thin film as a transducer layer and an Ag/AgCl RE immersed into the buffer solution as the electrolyte gate contact. (b) Bipolar characteristic curves of an rGO thin film in an ESFET device configuration.

In principle, each arm of the bipolar curve can be described in a first approximation by the characteristic equation of a MOSFET in its linear regime:

$$I_{ds} = C_g \mu \frac{W}{L} \left[\left(V_{gs} - V_t \right) V_{ds} - \frac{1}{2} V_{ds}^2 \right] \tag{3.1}$$

where C_g is the gate capacitance per unit area, μ is the field-effect mobility in the channel, L and W are the effective channel length and width, V_t is the threshold voltage in saturation mode. This equation can also be used as an alternative way to estimate the field-effect mobility of the rGO transducer layer [157–162].

3.2.3.2 Solid-Liquid Interface

In order to find the relationship between the drain-source current I_{ds} and the gate-source voltage V_{gs}, the condition at the interface of the rGO transducer layer and electrolyte has to be understood. In aqueous solutions, the rGO surface is negatively charged due to the oxygen functional groups being hydrolyzed by the water molecules. The ionic binding of the solute molecules are also broken, resulting in positive and negative charged ions. These ions are surrounded by the polar water molecules via electrostatic interactions. The charged rGO surface attracts the water-surrounded ions and forms an ionic layer. This layer acts as a barrier for the attractive force, which becomes too weak to attract further ions. This ionic layer is called the electrostatic double layer (EDL) as shown in figure 3.5 [163]. The surface potential Ψ decreases exponentially inside the EDL towards the bulk solution.

According to the Gouy-Chapman model, the EDL consists of a Stern layer and a diffuse layer in series. The Stern layer is formed by the non-mobile ions, which are strongly adsorbed by chemical binding on the rGO surface and are arranged in a condensed manner. Further away from the rGO surface, the ions are attracted by the Coulomb force and form a diffuse layer, in which the ions are mobile. The thickness of the EDL is the so-called Debye length, which depends on the solvent permittivity $\varepsilon_s = \varepsilon_0 \varepsilon_r$, the concentrations of the solute ions $n_{i,\infty}$ (m^{-3}) and the valence of the solute

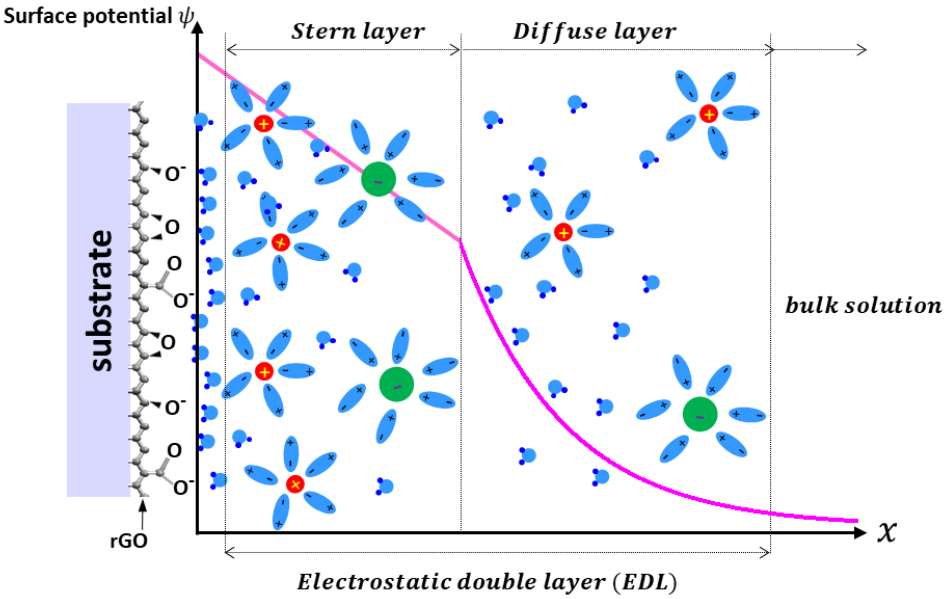

Figure 3.5: Descriptive schematic of the solid-liquid interface between rGO thin films and the buffer solution. The EDL is made of two layers, the so-called Stern layer and the diffuse layer, building up on the rGO surface.

ions Z_i by following the equation:

$$\kappa^{-1} = \sqrt{\frac{\varepsilon_s k_B T}{\sum_i n_{i,\infty} Z_i^2 e^2}} \tag{3.2}$$

The ionic strength of the solution is defined as:

$$I = \frac{1}{2} \sum_i \frac{n_{i,\infty}}{N_A} Z_i^2 \tag{3.3}$$

where N_A is the Avocadro constant. The ionic strength is a measure of the concentration of ions in that solution. As one of the main characteristics of a solution, the ionic strength significantly affects the dissociation constant and the solubility of different salts, the rate of reaction of the proteins, and the effects of ions on the zeta potential of biomolecules [164, 165].

The Debye length or the ionic strength can be used to calculate the capacitance of the EDL, which is formed at the interface of the rGO thin film and the buffer solution, using the following equation:

$$C_g = \frac{\varepsilon_0 \varepsilon_r A}{d} \tag{3.4}$$

with the vacuum permittivity $\varepsilon_0 = 8.854 \cdot 10^{-12}\,\mathrm{F\,m^{-1}}$, the relative permittivity of the solution, the area of rGO thin film A, and the thickness of the EDL d, the so-called Debye length.

3.2.3.3 Field-Effect Mobility in rGO Thin Films

Knowing the capacitance of the EDL and the geometrical parameters of the rGO-IDEs channel, the field-effect mobility μ of the rGO thin film can be estimated from the

obtained bipolar characteristic curve [166]. By rewriting equation 3.1, the field-effect mobility of holes and electrons can be deduced as the following equation:

$$\mu = \frac{\Delta I_{ds}}{\Delta V_{gs}} \frac{L}{W C_g V_{ds}} \tag{3.5}$$

where, I_{ds} is the drain-source current, V_{ds} is the drain-source voltage, L and W are the channel length and width, C_g is the gate capacitance, V_{gs} is the gate source voltage.

The field-effect mobility of rGO flakes and thin films prepared by different reduction treatments as described in the scientific literatures is summarized in the table 3.1.

The Debye length of the EDL formed at the interface of the rGO thin film and 10 mM PBS was approximately 0.76 nm, deducing from equation 3.2. Subsequently, the capacitance of the EDL can be obtained from equation 3.4: $C_g = 8.85\,\text{nF}$, using the relative permittivity of water $\varepsilon_r = 78$ and the area of the rGO thin film $A = 100\,\mu\text{m} \times 100\,\mu\text{m}$. The bipolar characteristic curves of an rGO thin film, shown in figure 3.4(b), provide the values of ΔV_{gs} and ΔI_{ds}. Therefore, the hole and electron mobility are calculated:

$$\begin{aligned} \mu_h &= \frac{\Delta I_{ds}}{\Delta V_{gs}} \frac{L}{W C_g V_{ds}} = 0.326\,\text{cm}^2\,\text{V}^{-1}\,\text{s}^{-1} \\ \mu_e &= 0.092\,\text{cm}^2\,\text{V}^{-1}\,\text{s}^{-1} \end{aligned} \tag{3.6}$$

with the channel length $L = 5\,\mu\text{m}$, the effective channel width $W = 900\,\mu\text{m}$, and the drain-source voltage $V_{ds} = 100\,\text{mV}$.

Table 3.1: Field-effect mobility of rGO flakes and thin film by different methods under different reduction treatments.

Material	Fabrication method	Thickness	Field-effect mobility $cm^2 V^{-1} s^{-1}$	Reduction condition	Measurement method	Publication year
rGO single flake (chemical exfoliation)		Lateral dimension: 100-5000 nm, height: 1.1-15 nm	2-200 [74]	24 h N_2H_4	Hall measurement	2007
rGO thin film (by octadecylamine-GO, lateral size of the flake: hundreds nm-1 µm)	Spin-coating/Printing	Monolayer (0.8 nm)-tens of µm	Hole/electron: 0.6/1.2 [157]	Thermal reduction 300 °C for 15 min	Extract from field effect measurement	2008
rGO thin film	Vacuum filtration (the formed thin film can be transfer to other substrates)	1-2 nm for 20 ml GO solution; 3-5 nm for 80 ml GO solution	Hole/electron: 1/0.2 [158]	Dimethylhydrazine vapor exposure 24 h and 200 °C in N_2 or vacuum oven 5 h	Extract from field effect measurement $\mu = \frac{\Delta I_{ds}}{\Delta V_{gs}} \frac{L}{W C_g V_{ds}}$	2008
rGO thin film (lateral size of the flake is hundreds of nm)	Spin-coating	6 nm	Hole/electron: 0.015/0.6 [159]	Thermal reduction: 150 °C for 260 min in the air		2010
rGO thin film (Hummer's method, more than 20 % GO flakes with lateral size above 25 µm)	Spin-coating (Au as electrodes)	Single layer: 0.5-0.8 nm	Hole/electron: 5.4/1.1 [160]	Thermal reduction at 1000 °C	Extract from field effect measurement $\mu = \frac{\Delta I_{ds}}{\Delta V_{gs}} \frac{L}{W C_g V_{ds}}$	2010
		Bilayer: 0.8-1.6 nm	Hole/electron: 50/10 [160]			

Continued on next page

Table 3.1 – continued from previous page

material	Fabrication method	thickness	Field-effect mobility $cm^2\,V^{-1}\,s^{-1}$	Reduction condition	Measurement method	Publication year
		Trilayer: 1.6-2.4 nm	Hole/electron: 92/51 [160]			
	Spin-coating/inject printing/drop casting (50-100 nm thick rGO as electrodes by inkjet printing/drop casting)	Trilayer: 1.6-2.4 nm	Hole/electron: 365/281 [160]	Thermal reduction at 1000 °C		
			Hole/electron: 5511/5479 with 1 M NaF [160]	Thermal reduction at 1000 °C. The device was measured in 1 M NaF		
rGO thin film	Vacuum filtration		Hole: 123[161]	$Na-NH_3$ for 1 min	Extract from field effect measurement $\mu = \frac{\Delta I_{ds}}{\Delta V_{gs}} \frac{L}{WC_g V_{ds}}$	2013
rGO thin film	Langmuir-Blodgett	Lateral dimension: several µm, height: ≈ 1 nm	Hall measurement: 270; Field effect measurement: Hole/-electron: 250/200 [112]	Hydriodic/trifluoroacetic acid at RT (5 min) and at 80 °C (10 min)	Hall and field effect measurement	2013

Continued on next page

Table 3.1 – continued from previous page

material	Fabrication method	thickness	Field-effect mobility $cm^2\,V^{-1}\,s^{-1}$	Reduction condition	Measurement method	Publication year
rGO flake		Lateral dimension: tens of µm, height: 1.1-15 nm	$>$ 1000 [162]	300 °C for 1 h in argon, then microwave reduction: 1000 W for 1 s/2 s pulses in argon	Extract from field effect measurement	2016
rGO thin film	Pulse laser deposition		372 [167]		Hall measurement	2017

3.2.4 Resistivity of rGO Thin Films

Van der Pauw (VDP) structures [168] were designed to extract the sheet resistivity of the rGO thin films. There are various types of VDP structures: circle, clover leaf, square, rectangle, Greek cross, and six- or eight-contacts Hall bars. Amongst these structures, the Greek cross shown in figure 3.6(a) is able to maintain the measurement error below 1 % with a sample geometry $a/w > 1.02$ [169]. Thus, the Greek cross structure was chosen for the sheet resistivity measurements with a geometry parameter $a/w = 1.1 > 1.02$. Considering the amorphous rGO thin films, the separation distance of the diagonal electrodes of the Greek cross is designed to be 5 µm, which is the same value as the separation distance of the IDEs used for the electronic biosensors. It is meant to supply a precise resistivity for analyzing the electronic biosensors.

The rGO thin film is patterned into the shape of the designed Greek cross by using the fabrication procedure described in chapter 2. The obtained rGO pattern was verified with SEM characterization and the result is shown in figure 3.6(b). The VDP measurement was carried out with a Keithley 4200-SCS semiconductor analyzer to extract the sheet resistivity [170]. This method involves applying a current bias and measuring the generated voltages using the 4 contacts of the designed Greek cross, with eight measurements as indicated in figure 3.6(c).

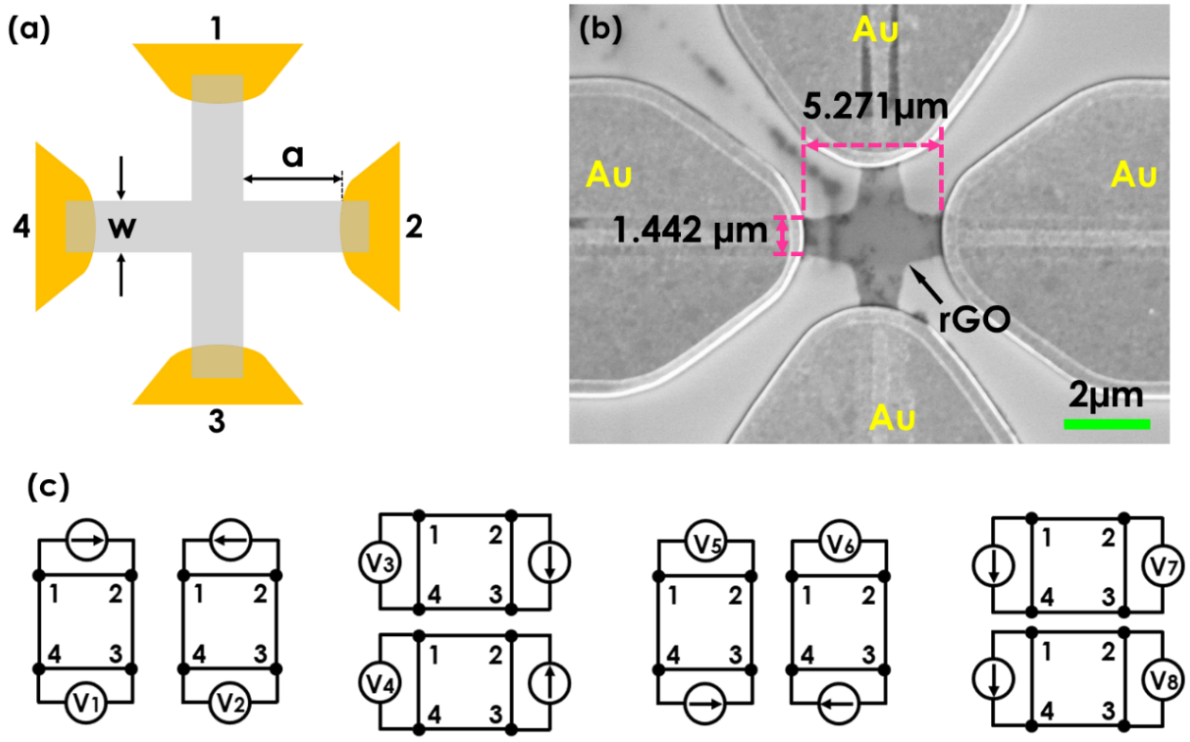

Figure 3.6: Sheet resistivity measurement of an rGO thin film. (a) Schematic of the rGO thin film patterned in the shape of a Greek cross, with the geometry parameter $a/w = 1.1 > 1.02$. (b) The SEM characterization which was used to extract the rGO thin film (8-times spin coated) resistivity by four-point measurement. (c) 8 VDP measurements to extract the sheet resistivity.

The 4 contacts are labeled clockwise as 1, 2, 3, 4. The measurements take place with the contact connection as follows:

1. Common ground.
2. Current bias supply with either positive or negative values.
3. Voltmeter.
4. The same setting parameters as contact 3.

The same procedure was repeated at every side of the rGO Greek cross and in total 8 voltages were collected: $V_1 - V_8$. The sheet resistivity can be calculated as follows:

$$\rho = \frac{\rho_A + \rho_B}{2} \tag{3.7}$$

with

$$\begin{aligned} \rho_A &= \frac{\pi}{\ln 2} f_A t_s \frac{V_1 - V_2 + V_3 - V_4}{4I} \\ \rho_B &= \frac{\pi}{\ln 2} f_B t_s \frac{V_5 - V_6 + V_7 - V_8}{4I} \end{aligned} \tag{3.8}$$

while t_s is the thickness of the rGO thin film, $V_1 - V_8$ are the voltages measured by a voltmeter, I is the current. The parameters f_A and f_B are the geometrical factors related to the two resistance ratios Q_A and Q_B:

$$\begin{aligned} Q_A &= \frac{V_1 - V_2}{V_3 - V_4} \\ Q_B &= \frac{V_5 - V_6}{V_7 - V_8} \end{aligned} \tag{3.9}$$

The relationship between Q and f is as follows:

$$\frac{Q-1}{Q+1} = \frac{f}{0.693} \operatorname{arccosh}\left(\frac{e^{0.693/f}}{2}\right) \tag{3.10}$$

To guarantee the measurement precision, the input current was 10 nA so that the voltage difference at two contacts was less than 100 mV. In this experiment, the thickness of the rGO thin film was 4.5 nm. The factors f_A and f_B are geometrical factors related to the sample symmetry. In the condition of near-perfect symmetry, such as with the Greek cross VDP structure, both factors can be considered as equal to 1 [170]. Based on the experimental results, the obtained sheet resistivity of rGO was calculated to be in the range of 0.03 Ω m to 0.06 Ω m after being treated by the TRP.

3.3 Reduction Characterization

To investigate the reduction degree after the thermal treatment, Raman spectroscopy and X-ray photoelectron spectroscopy were used to characterize the GO and rGO thin films. In this section, GO and rGO thin films were prepared on Si/SiO_2 substrates. The TRP was used as defined in the previous section, unless specified otherwise.

3.3.1 Raman Spectroscopy Characterization

Raman spectroscopy is an optical, non-destructive technique to quantitatively detect vibrations in molecules [171]. This technique is based on light scattering. Depending on the incident energy, the incident photons can be absorbed, scattered or completely transmitted, as shown in figure 3.7(a). The incident photons distort the electron clouds around the nuclei and excite the molecule into a short-lived, virtual energy state, which is determined by the frequency of the incident photons. When only the electron clouds are distorted, elastic Rayleigh scattering takes place where the energy of the incident photon matches the difference between the two energy levels. At the same time the energy of the scattered photon does not change compared to the incident photon energy, as shown in figure 3.7(b). Most of the photons are scattered based on Rayleigh scattering. Only one out of 10^6 to 10^8 scattered photons is scattered inelastically. This phenomenon is the so-called Raman scattering. In this scattering process, the motions of the nuclei (phonons) are induced such that the energy can be transferred from the molecule to the photon or *vice versa* (Stokes shift or anti-Stokes shift) as shown in in 3.7(b).

In principle, the incident light is monochromatic and the Rayleigh scattered light is filtered out. Only the Stokes-scattered (corresponding to Stokes shift) Raman light is recorded. The Raman spectrum is plotted with the number of the collected photons (y-axis) versus their energy shift referring to the incident energy (x-axis), which is labeled as Raman shift in the unit of Δcm^{-1}. In practice, the unit of Raman spectrum is labeled as cm^{-1} for the sake of convenience.

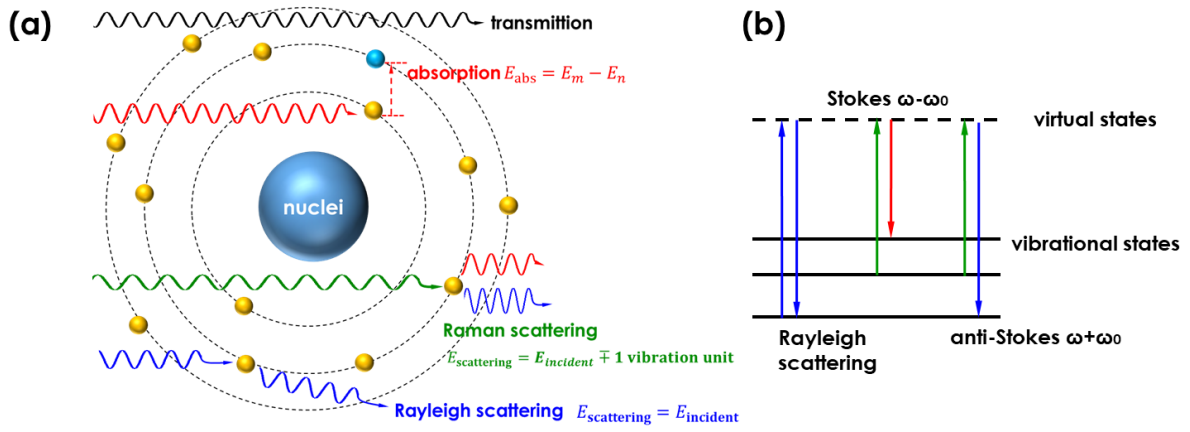

Figure 3.7: Principle of Raman spectroscopy. (a) Interaction types of incident photons with target atoms. (b) Two possibilities of Raman scattering: Stokes and anti-Stokes scatterings for emitted photons of energy smaller and larger than the energy of the incident photons, respectively. The vibrational state of the molecules can either absorb energy from the incident photons or transfer energy to the incident photons.

The Raman spectrum can reflect the evolution of the electronic structure as well as electron-phonon interactions [172, 173]. In graphene, there are six phonon branches named iLO, iTO, oTO, iLA, iTA, oTA as shown in figure 3.8(a) [174, 175]. Their name is defined based on three characteristics:

- The phonon branches can either be optical (O) or acoustic (A) phonons.

- One of each of these two kinds of phonons are out-of-plane (o) of the carbon lattice and the other four are in-plane (i).
- The direction of the zone-center mode of the phonons either vibrates along or perpendicular to the carbon-carbon bonds, which are known as transverse (T) and longitudinal (L) modes.

Mainly because the photon excited electrons interact with iTO and iLO, the phonon energies significantly disperse at the **Γ** and **K** points, as shown in figure 3.8(b). This effect induces the main characteristic Raman peaks of pristine graphene and defected graphene [175] as shown in figure 3.8(c)-(d). A detailed explanation about the Raman scattering process [176] is given in figure 3.8(e):

i) The **G** band is located at approximately $1580\,\mathrm{cm}^{-1}$. It is a doubly-degenerate in-plane sp^2 C−C stretching mode. The incident photons excite a virtual electron-hole pair, which is scattered by iTO or iLO of low momentum at the **Γ** point in the center of the first Brillouin zone. Subsequently, the electron and hole recombine and emit a photon, whose energy is smaller than the energy of the incident photon.

ii) The **2D** band is located at approximately $2700\,\mathrm{cm}^{-1}$. It originates from the in-plane breathing-like mode of the carbon lattice. The virtual electron-hole pair is created by an incident photon at the Dirac cone **K** point in the first Brillouin zone. The electron (or hole) is scattered by one iTO phonon to the **K'** point and scattered back to the **K** point by a second iTO phonon to recombine with a hole (or electron). This scattering routine is a so-called double resonant. Also, both electrons and holes can be scattered by iTO phonons from the vicinity of **K** point to **K'** point and recombine afterwards by emitting a photon. This scattering routine is a so-called triple resonant.

iii) The **D** band is located at approximately $1350\,\mathrm{cm}^{-1}$. It is induced by the disorders in the carbon lattice, such as sp^3 defects, grain boundaries, vacancy sites and edges, which are responsible for the momentum conversion. The photon-excited electron is scattered by an iTO around **K** point to **K'** point and scattered back by the above-mentioned defects. Since only one phonon participates in this process, the energy shift is half of the value compared to the **2D** band process.

iv) The **D'** band is located at approximately $1620\,\mathrm{cm}^{-1}$, normally observed as a shoulder peak of the **G** band. In contrast to the three bands mentioned above attributed to intervalley scattering, the **D'** band originates from intravalley scattering. It requires a defect for scattering and involves the electronic states around both **K** and **K'** points.

For chemically exfoliated GO, the carbon lattice consists of sp^3 oxygen functional groups and vacancy sites. This results from the destructive power of the gases generated during the chemical exfoliation process (CO and CO_2), which are formed in-between the neighboring carbon layers. These differences with pristine graphene can be evaluated through the Raman peaks of GO and rGO flakes. The Raman characteristic bands show the oxidation degree of the carbon lattice after the chemical

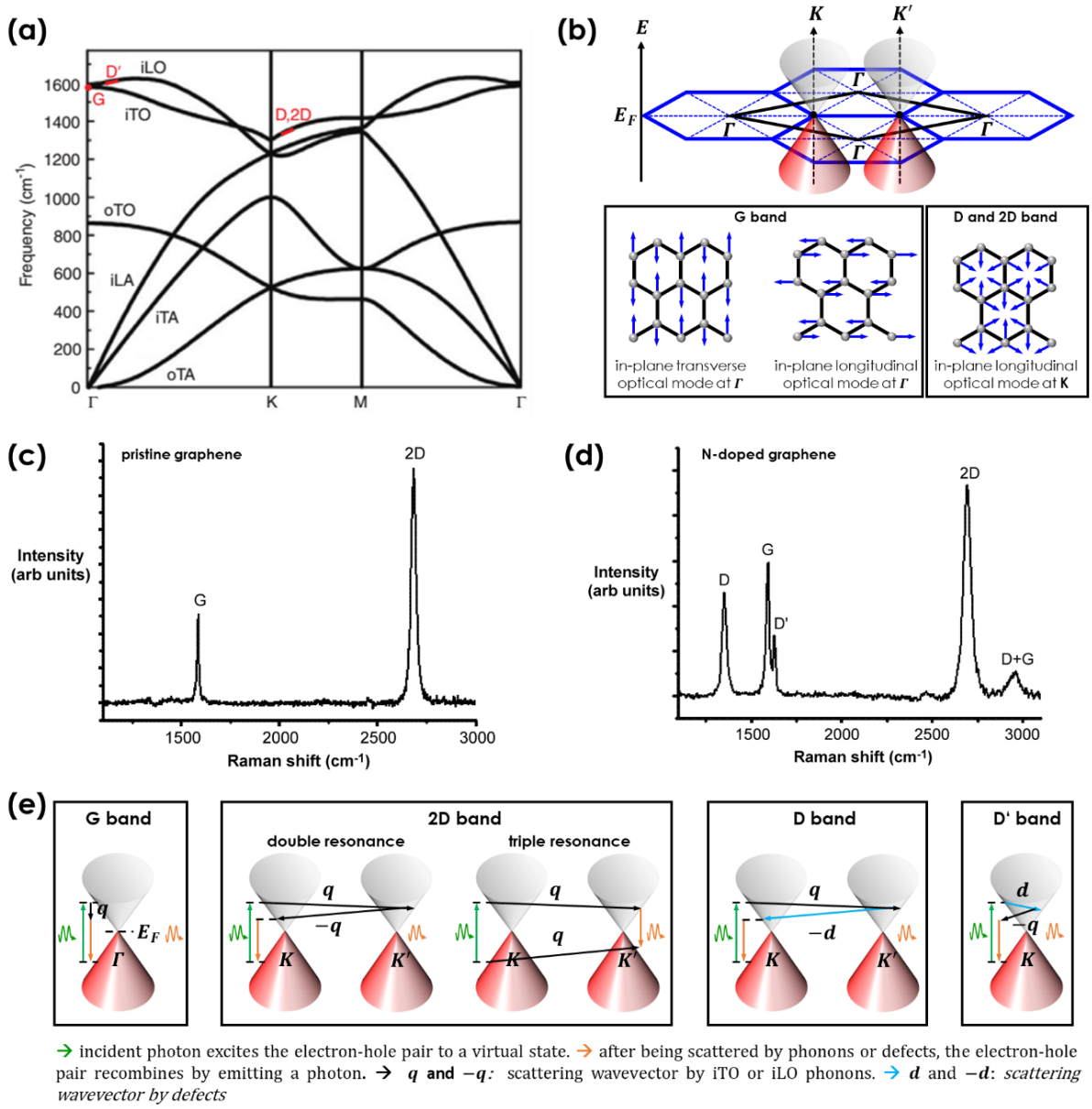

Figure 3.8: Principle of graphene Raman spectra: (a) Diagram of phonon dispersion in graphene [174]. (b) iTO and iLO phonons at **Γ** point in the center of Brillouin zone and at Dirac cone **K** (**K'**) points [174]. (c)-(d) Raman spectra of pristine graphene and n-doped graphene [177]. (e) Raman scattering processes that are responsible for the characteristic peaks: **G**, **D**, **D'** and **2D** bands [174].

exfoliation and how the reduction treatment helped recovering the carbon lattice. As depicted by the Raman scattering processes in graphene, the **D** and **D'** bands represent the disorder degree and the defect percentage of the carbon lattice. The **G** and **2D** bands describe the crystalline quality of the carbon lattice. The crystalline size of the carbon lattice, in the order of magnitude of nanometers, can be extracted by following the equation: $1/La = (I_D/I_G)$ [178]. It is also important to note that the flake stacking during the spin-coating process is also responsible for the introduction of additional Raman peaks for both GO and rGO thin films, which are discussed in the following.

In this work, the Raman characterizations of GO and rGO thin films were carried out with the excitation wavelength of 633 nm at room temperature. The obtained

Raman spectra for GO and rGO thin films are shown in figure 3.9(a)-(b). The detailed

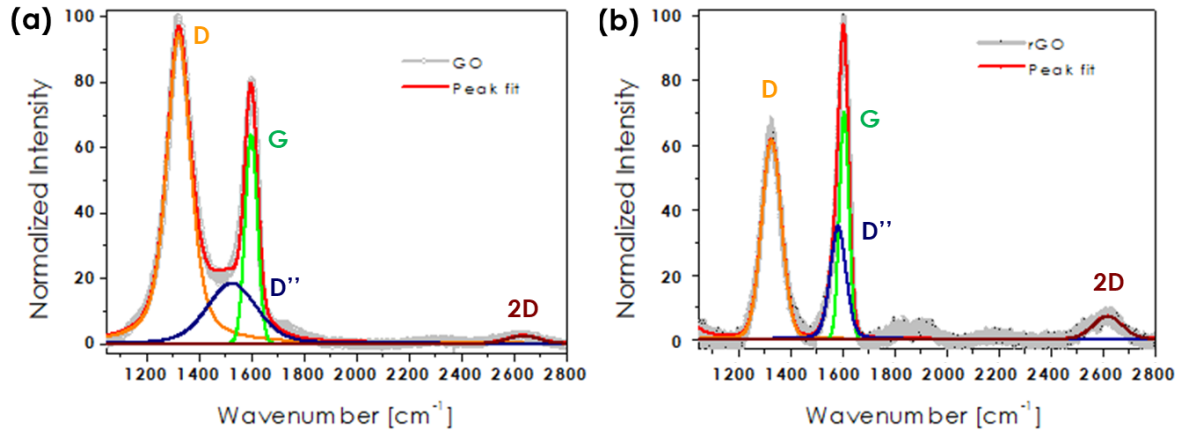

Figure 3.9: Raman spectra of (a) GO and (b) rGO thin films [116]. The evolution of the characteristic Raman peaks (**D** band, **G** band, **2D** band and **D″** bands) demonstrates how the carbon lattice is recovered with the thermal reduction. The GO thin film was prepared by gas-phase silanization and the spin-coating technique as described in chapter 2. The rGO thin film was transformed from the prepared GO thin film with the TRP.

information about the position, intensity and full width at half maximum (FWHM) of the characteristic Raman peaks for both GO and rGO thin films are summarized in table 3.2.

Table 3.2: Peak position, FWHM and intensity of Raman characteristic peaks for GO and rGO thin films.

	Peak position [cm^{-1}]		**FWHM**		**Intensity** [%]	
	GO	rGO	GO	rGO	GO	rGO
D	1325	1330	110	90	95.7	61.7
D″	1527	1581	207	76	18.1	28.4
G	1601	1608	56	44.5	64.5	76
2D	2638	2622	139	134.6	2.4	7

A Gaussian-Lorentzian algorithm was used for the spectrum deconvolution to extract the characteristic Raman peaks. For both GO and rGO thin films, three typical peaks **D**, **G** and **2D** bands appear with an extra **D″** band. The existence of the **D″** band can probably be attributed to the phonon density of states in the finite size crystals of graphite [179]. For GO, the **G** peak attributed to the in-plane sp^2 C−C stretching mode (E2g [180]) is located at 1601 cm^{-1} while the **2D** peak induced by the second-order overtone of different in-plane breathing-like mode is at 2638 cm^{-1}. The disorder induced **D** peak (A1g) is present as 1325 cm^{-1} and the **D″** band appears at 1527 cm^{-1}.

After thermal reduction, larger areas of sp^2 carbon lattices were recovered for rGO, so that the **G** peak, at 1608 cm^{-1} and the second order **2D**, at 2622 cm^{-1} show a stronger intensity compared to GO thin films. The intensity of the **D″** peak at 1581 cm^{-1} relates to the increase of phonon density states. The intensity of the **D** peak at 1330 cm^{-1}, which is disorder induced, drastically decreases. This is due to the removal

of sp^3 oxygen functional groups from the carbon basal plane by thermal reduction. Furthermore, the FWHM of the **G**, **D**, **2D** and **D"** bands become narrower for rGO thin films when compared to GO thin films after the reduction process [175, 181, 182]. In addition, more Raman peaks of rGO thin films gradually emerge within the spectral regime between 1690 cm^{-1} and 2150 cm^{-1}. They correspond to the **M**-band region and combination modes, which were observed in earlier reports for the case of few-layer graphene. This is due to the interlayer bonding and relaxation of the selection rules [183]. More pronounced combination modes were observed between 1800 cm^{-1} and 2150 cm^{-1}, which originate from the intravalley double resonance scattering processes in graphene. Such results indicate the strong commonalities between the quilted rGO thin films and other forms of graphene such as incommensurate bilayer graphene (IBLG) and stacked graphene layers [184, 185].

3.3.2 X-Ray Photoelectron Spectroscopy Characterization

XPS is an optical technique to analyze the surface chemistry of materials in ultra-high vacuum. X-rays stimulate the electrons in the irradiated atoms to let them escape from the analyzed material within a depth of less than 10 nm from the surface. These released electrons correspond to the binding energies of the electron configuration of the atoms and are collected by the XPS detector. The incident X-ray energy is known as $E_{\text{X-ray}} = 1486.7\,\text{eV}$, and the binding energies of the electrons is calculated with:

$$E_{\text{binding}} = E_{\text{X-ray}} - (E_{\text{kinetic}} + \phi) \tag{3.11}$$

where E_{kinetic} is the electron energy measured by the XPS detector and ϕ is the work function of the detector, which is attributed to the absorption of the photoelectrons.

The number of collected electrons versus their binding energies is plotted as XPS spectra, which are unique for each element. Therefore, the XPS spectrum can be used to characterize and identify the chemical compositions of the analyzed materials. Furthermore, the bonding energies of the electrons vary according to the chemical bonding environments. The resulting XPS spectrum can be used to distinguish the types of bindings within the same elements. Both GO and rGO are of the same chemical composition (C, O and H) but contain different portions of oxygen functional groups. The XPS is an ideal characterization tool to address and compare the amount of different oxygen functional groups in these two thin films in order to evaluate the influence of the thermal reduction treatments.

For GO and rGO, three characteristic XPS peaks are expected: the C−C bonds at 284.5 eV, the C−O bonds at 286.4 eV, and the C=O bonds at 288.3 eV [182, 186, 187]. The degree of reduction can be reflected by the C/O ratio, in terms of the intensity ratio of the sp^2 hybridized C (284.6 eV) and C−O groups (286.0 eV), carbonyl groups (287.8 eV) and carboxyl groups O=C−O (289.0 eV).

The XPS spectra as shown in 3.10(a)-(b) were obtained after the Shirley background correction referring to the binding energy of the C 1s electron (284.6 eV). It was observed that the amount of C−C bonds increased from 70.6 % to 74.4 %, which means that more of the sp^2 carbon lattice was restored after the thermal reduction. In addition, the amount of oxygen bonds C−O and C=O bonds decreases from 22.1 %

to 18.8 % and 7.3 % to 6.8 %, respectively. This shows that the amount of hybrid sp^3 oxygen functional groups was clearly diminished. These XPS results reveal that the thermal reduction was efficient to transform GO into rGO resulting in a larger area of the sp^2 carbon lattice and less sp^3 defects. In particular, it shows that rGO thin films still possess a certain amount of functional groups, which are in favor of biomolecule immobilization for biosensor applications.

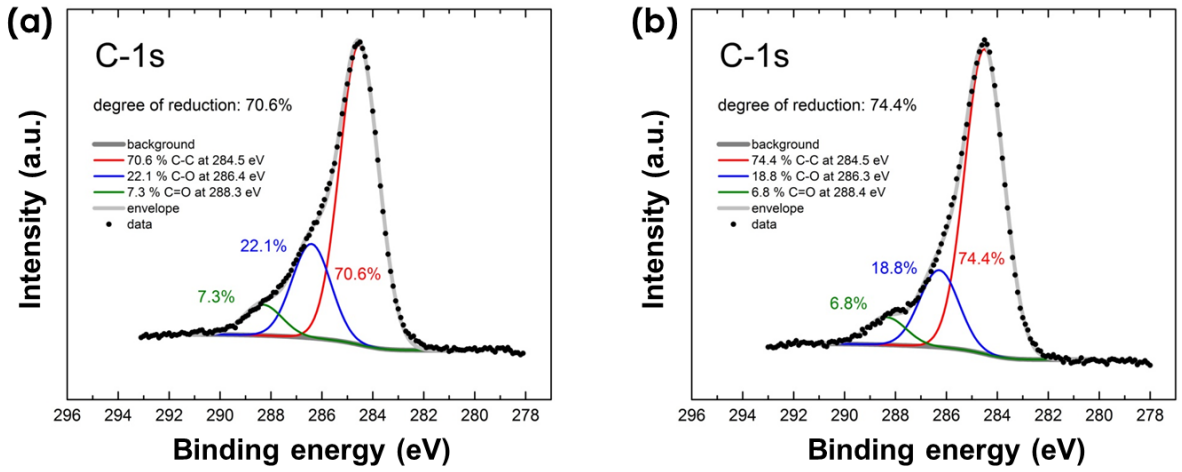

Figure 3.10: XPS spectra of GO and rGO thin films [116]. The GO thin film was prepared by gas-phase silanization and the spin-coating technique as described in chapter 2. The rGO thin film was transformed from the prepared GO thin film by the TRP.

3.4 Conclusion

In this chapter, the I-V and cyclic voltammetry characterizations proved that the rGO thin film obtained with the TRP formed an ohmic contact with the IDEs and that the rGO thin films were complete without pinholes. These two facts are the prerequisites so that the rGO thin films can be utilized into electronic devices. Furthermore, the TRP generated 98.7 % (147 channels out of 149 channels) of channels with a resistance between $1.44 \cdot 10^4\,\Omega$ and $9.54 \cdot 10^6\,\Omega$. Most importantly, the resistance value of 87.9 % of the conductive rGO channels were within only one order of magnitude. This result demonstrates the efficiency of the TRP. The established protocol shows a scalability for mass fabrication of rGO devices with further optimization.

The bipolar characteristic curves of the rGO thin film were measured in the ESFET device configuration. These curves provided the possibility to deduce the field-effect mobilities for holes and electrons with $0.326\,\mathrm{cm^2\,V^{-1}\,s^{-1}}$ and $0.092\,\mathrm{cm^2\,V^{-1}\,s^{-1}}$, respectively. In addition, the sheet resistivity was extracted by four-point measurements using Greek-cross VDP structures and is between $0.03\,\Omega\,\mathrm{m}$ and $0.06\,\Omega\,\mathrm{m}$. These parameters are important, because they characterize the reduction degree and serve as criteria to optimize the reduction conditions. The obtained bipolar characteristic curves, field-effect mobility and sheet resistivity indicated that the TRP removed the oxygen functional groups effectively and restored the sp^2 lattice partially. In addition, Raman spectroscopy and XPS characterizations were used to address the reduction degrees by TRP and confirmed that the reduction

was efficient. Therefore, the obtained rGO thin films were ready to be employed as transducers in the biosensor devices to detect PSA biomarkers.

4 rGO Based SPR Platforms

In this chapter, SPR biosensors with GO and rGO thin films as functional layers are presented. Firstly, the general principle of SPR is introduced and the state-of-the-art of graphene as a functional layer in SPR for biosensing is summarized. Secondly, (r)GO thin films were prepared on Au thin films with a glass wafer as substrate. These devices were employed as SPR biosensors with covalently immobilized PSA as the receptor biomolecules for detecting the target biomolecule lectin concanavalin A (ConA). The biosensing performance of the GO and rGO functional layers based SPR platforms in terms of SP enhancement are compared and discussed in detail. Thirdly, the rGO thin film based electronic SPR biosensors are investigated, and the tuning mechanism of the SPR signal by externally applied voltages is discussed.

4.1 State-of-the-Art of Graphene Based SPR Platforms

SPs are coherent, collective oscillations of charges at the interface of metals and dielectric materials [188]. They can be excited either by photons or electrons. SPR varies sensitively to dielectric changes in the vicinity of the interface, in a depth approximately half the wavelength of the incident light. This optical phenomenon enables label-free and real-time monitoring of the dynamic activity of biomolecular interaction. The real application SPR based biosensor was first demonstrated by Liedberg et al. in 1983 [189]. A typical SPR biosensor consists of a bilayer stack, namely a biorecognition layer and a metal thin film on a transparent substrate, as depicted in figure 4.1(a). Typically, a biorecognition layer is required to provide a high density of functional groups and a large three dimensional surface area for high-grade biomolecule immobilization. The biosensing process is addressed by the intensity changes of SPR, which is induced by the attachment of biomolecules. As depicted in figure 4.1(b), the angle of incident light to achieve a minimum value of reflectance is shifted by the change in dielectric parameter of the biomolecule layer $\Delta\varepsilon_{bio}$, which can be induced by the density and/or the type of biomolecules attached on the biosensor surface. This effect is utilized as SPR biosensing principle.

Graphene is utilized as a layer between the biorecognition element and the metal layer. This system shows improvements that are attributed to the promising optical and plasmonic properties of graphene. As a two dimensional atomic carbon lattice, graphene confines the SPs within a volume which is six orders of magnitude smaller than the diffraction limit of the light [87, 103]. In addition, the field enhancement [104] and the interaction strength of SPs in graphene at the quantum level is increased by one order of magnitude compared to conventional metal thin films. The resonant

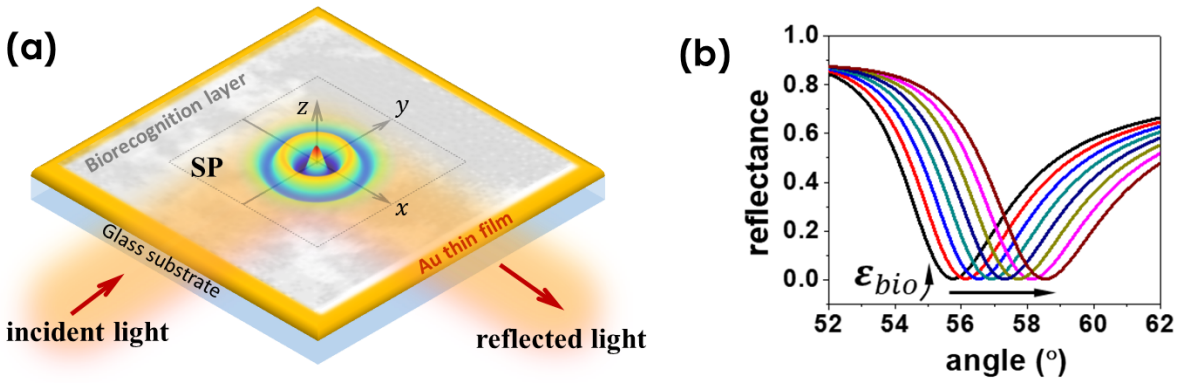

Figure 4.1: (a) Schematic of an SPR chip. A biorecognition layer is immobilized on an Au thin film with a glass as substrate. Through a prism, an incident light irradiates the glass side and stimulates SPs at the interfaces of the biorecognition layer and Au thin film. (b) A plot of the angle of incident light versus the SPR signal (reflectance), based on a typical five-layer system. The increase of dielectric parameter of biomolecule layer ε_{bio} leads to the shift of reflectance. The SPR biosensing principle is based on this effect.

extinction cross section is much larger than the geometrical cross section as well. These properties are all in favor of enhancing the strong light-matter interaction [103].

Especially, the bipolar property of graphene [59, 60] enables a tuning effect in the plasmon mode [104], the optical parameters [105], the quantum pathways of inelastic light scattering [106], and the band-gaps [107], with the assistance of externally applied bias voltages or the attachment of charged molecules. Therefore, graphene becomes prominent in the field of bio-plasmonic applications [64–66]. The amplifying capability of graphene as a functional layer on Au-based SPR biosensors was verified to boost the sensitivity for the detection of biomolecules [63, 68, 89–91, 108]. The sensing regime can be tuned by graphene based infrared spectroscopy with the assistance of an applied electric field in the mid-infrared regime [70].

However, graphene as a linker layer restricts the immobilization of probe biomolecules to π-π stacking. Unlike graphene, chemically exfoliated GO [71, 72] and its derivative product, rGO [73–75] possess oxygen functional groups on both sides of the carbon basal plane. This offers the possibility of (r)GO thin film formation on various substrates, but also enables the diverse and robust immobilization of biomolecules. Meanwhile, these two materials maintain a carbon lattice similar to pristine graphene in nanoscale [112] so that the previously mentioned plasmonic characteristics are partially preserved.

Plenty of effort is dedicated to investigate the biosensing performance of Au-based SPR using GO flakes or layers to enhance the SPR intensity [190–197]. These works proved that the sensitivity improved when compared to conventional Au based SPR platforms. GO flakes or layers as an insulating material are generally reduced to conductive rGO for the purpose of restoring the carbon lattice which also generates the opto-electro-plasmonic properties [111]. It was found that the optical properties of a few layers of rGO are similar to monolayer exfoliated graphene while also being tunable by the reduction treatment [198]. In addition, rGO exhibits an infrared-absorption which is highly superior to that of GO thin films [199]. This is due to the coupling of the electronic states and the asymmetric stretching mode of the

oxygen atoms aggregated at the edges of the defects. Such optically-active regimes of rGO include the infrared regime, in which the excitation wavelength of a typical SPR setup is located [200]. The comparison between the SPR enhancements of these two materials and the potential for simultaneous optical and electronic biosensing with (r)GO thin films as functional layers of SPR platform is of high interest.

4.2 (r)GO SPR Platforms

4.2.1 Preparation of (r)GO Based SPR Platforms

The (r)GO SPR chips were prepared as follows:

i) The glass wafers were thoroughly cleaned with freshly prepared Caro's acid to remove all contaminants and washed with DIW and dried under a nitrogen (N_2) flow. Afterwards, the glass wafers were directly transferred into an electron beam evaporator to deposit the metal layer, which consisted of 3 nm Ti and 47 nm Au thin films. A schematic of the obtained wafers is depicted in figure 4.2(a).

ii) 4-aminothiophenol (ATP) linker layers, as depicted in figure 4.2(b), were prepared on the Au surface by gas-phase silanization. This linker layer was used to covalently immobilize GO flakes to form a uniform thin film. Prior to the silanization process, the Au wafer was cleaned by O_2 plasma (230 W) for 5 min, in order to remove the adsorbates on the Au surface.

iii) The wafer was then transferred into a desiccator, which was inside a N_2 flooded glovebox to proceed to the gas-phase silanization. The silane ATP was placed onto a glass slide, which was then transferred inside of the preheated desiccator (60 °C). The Au wafer was positioned at an angle of about 85° with respect to the outlet valve of the desiccator to provide a maximum contact area between the substrate and the silane-saturated gas stream. Then, the pressure inside of the desiccator was reduced to 130 mbar, such that a continuous gas flow of the silane over the substrate was ensured. The process was carried out at 60 °C for 30 min and an ATP linker layer was formed on the Au surface, as shown in figure 4.2(b). Afterwards, the glass wafer was washed with ethanol (98 %) and DIW, and dried under a N_2 flow to remove physically absorbed impurities during the silanization process.

iv) The wafer with the silane ATP was then transferred into a second preheated desiccator to carry out a grafting procedure at 85 °C for 1 h to remove leaving groups. Eventually, the ATP linker layer was formed with the amino groups on the surface.

v) The GO flakes were chemically exfoliated by following the LTEDS technique presented in chapter 2.3 and the centrifugation speed in the last step was 500 rpm instead of 1000 rpm. The generated GO solution were applied by spin-coating onto the ATP-functionalized Au surface to form uniform GO thin films, as shown in figure 4.2(c).

vi) The rGO thin films were prepared following the TRP to remove the oxygen functional groups and partially restore the sp^2 hybridized carbon lattice of the GO thin films. In the following sections, the rGO thin films were reduced using this method unless specified otherwise.

After the preparation process, the 4-inch wafer was diced into chips of the size 1.25 cm × 1.25 cm which are suited for the commercial Reichert SPR setup for biosensing. To protect the (r)GO chips during cutting, a layer of photoresist was spin coated on the 4-inch wafer. Then, in order to remove the protective photoresist, the chips were first immersed in acetone for 30 min at room temperature, then in fresh acetone and afterwards in isopropanol for 5 min. Finally, the chips were dried by N_2.

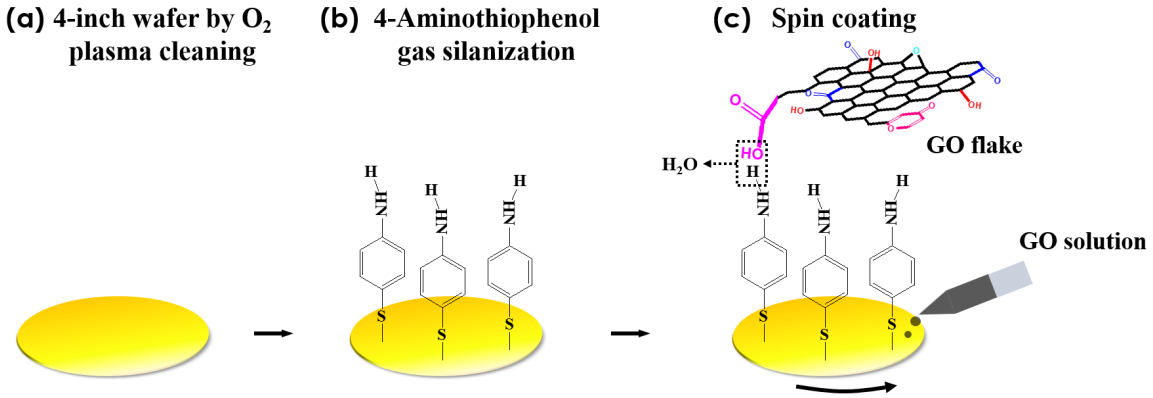

Figure 4.2: Schematics of a GO thin film preparation on Au surface with a glass wafer substrate. (a) The Au surface is cleaned by O_2 plasma to remove the impurities and adsorbates. (b) A uniform ATP layer is generated on the glass wafer surface by gas-phase silanization in a vacuum desiccator. In this process, the thiol (−SH) groups of ATP bind to the Au surface. (c) The freestanding $-NH_3$ groups of the ATP molecules bind to the GO flakes by reacting with the −COOH groups of the carbon basal plane in a condensation reaction at room temperature. The pH value of the GO solution is 2.9.

4.2.2 Fundamentals of (r)GO Based SPR Platforms

A Kretschmann configuration was used for the GO and rGO thin film based SPR biosensor platforms [201]. A six-layer system was established by adding a (r)GO layer into the typical five-layer system (prism, glass substrate, metal thin film, biomolecule layer and analyte solution), as shown in figure 4.3. The final six layers are:

- Layer 1: prism of refractive index n_p
- Layer 2: glass substrate of refractive index n_g.
- Layer 3: conductive gold layer of refractive index n_c.
- Layer 4: dielectric layer, GO or rGO, of refractive index n_d.
- Layer 5: biomolecule layer of refractive index n_{bio}.
- Layer 6: analyte solution of refractive index n_s.

The dielectric layer can immobilize PSA, which act as receptor biomolecules to detect the target biomolecule ConA. The objective of this section is to compare the performance of GO and rGO as functional layers in SPR biosensor platforms.

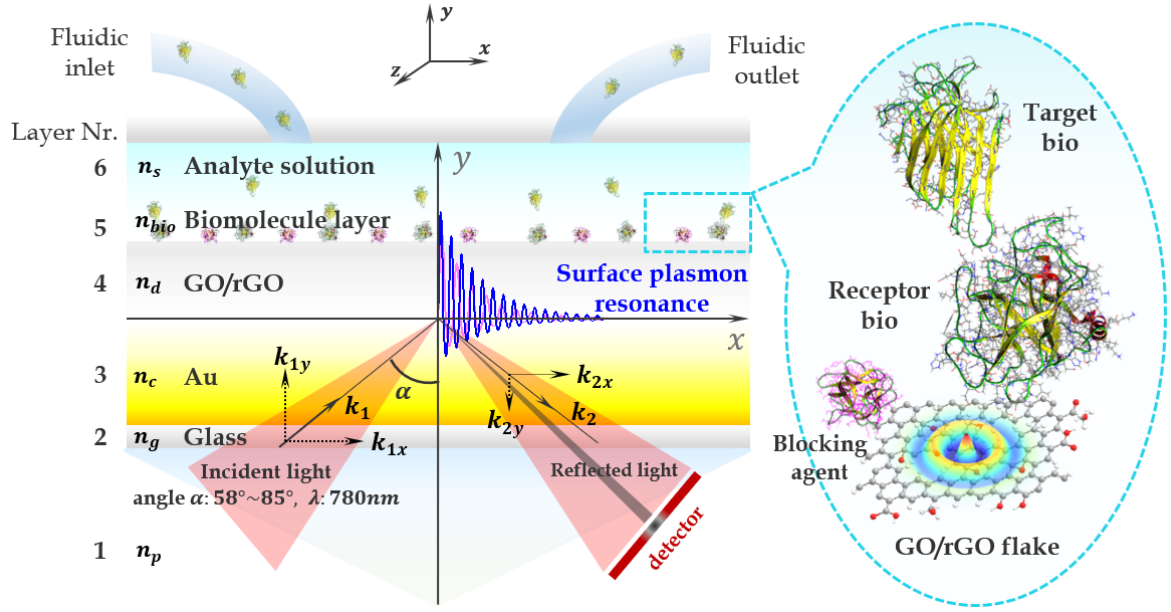

Figure 4.3: Schematic of the GO or rGO thin film based SPR biosensor platform. The typical five-layer system used for SPR sensing (prism, glass substrate, gold layer, biomolecule layer, analyte solution) is expanded by an additional layer from either GO or rGO coating, giving six layers: prism, glass substrate, conductive gold layer, dielectric layer (GO or rGO), biomolecule layer and analyte solution with refractive indices n_p, n_g, n_c, n_d, n_{bio} and n_s respectively. The wavelength of the incident light is 780 nm with an angle of incidence ranging from 58° to 85°.

In a typical SPR setup, a monochromatic plane-polarized light from a near-infrared LED illuminates the back surface of the biosensor chip, while the reflected light is detected by a diode array detector [202]. For the Reichert SPR setup used in this work, the incident wavelength λ was 780 nm and the angle of incidence α ranged from 58° to 85°. In a typical five-layer system, the incoming light E_i induces an evanescent wave E_r at the metal and dielectric interface with the wave vector k and an amplitude decaying exponentially, perpendicular into both medium sides [203]:

$$E_r = E_i \exp\left(j\omega t - jk_x x - jk_y y\right) \tag{4.1}$$

where E_i and ω are the amplitude and the angle frequency of the incident light, k_x and k_y are the wave vectors along the x and y axis at the interface plane, while the wave vector k_z along the z-axis is 0.

The SPR is activated by the evanescent wave at the metal and dielectric interface. The characteristic curve of the light angle of incidence α and the reflectance ($r_p = |E_r/E_i|^2$) is employed to address binding of biomolecules, which results in a change in the dielectric parameter of the biomolecule layer $\Delta\varepsilon_{bio}$ on the sensor surface. At a certain angle of incidence α, a minimum value of reflectance appears as a dark strip on the diode array detector. The SPR sensorgram is recording the change in α in real-time.

The relationship between α and $\Delta\varepsilon_{bio}$ can be described by an abstract multi-layer SPR system consisting of n_{lay} layers between the prism and the analyte solution. Each layer

has a specific dielectric constant ε, refractive index n ($\varepsilon \equiv n^2$), thickness d, and wave vector k_y along the y direction. The subscripts p, s, and i correspond to the prism, solution, and layer i, respectively. The reflectance r_p versus the angle of incidence α can be calculated with the following equation, which is obtained by repeatedly applying the Fresnel equations [203]:

$$r_p(\alpha) = \frac{\left(M_{11} + M_{12}\frac{k_{ys}}{\varepsilon_s}\right)\frac{k_{yp}}{\varepsilon_p} - \left(M_{21} + M_{22}\frac{k_{ys}}{\varepsilon_s}\right)}{\left(M_{11} + M_{12}\frac{k_{ys}}{\varepsilon_s}\right)\frac{k_{yp}}{\varepsilon_p} + \left(M_{21} + M_{22}\frac{k_{ys}}{\varepsilon_s}\right)} \tag{4.2}$$

where the factors M_{ij} are obtained from the transfer matrix M:

$$M = \prod_{i \in \{1, n_{lay}\}} M_i = \begin{bmatrix} M_{11} & M_{12} \\ M_{21} & M_{22} \end{bmatrix} \tag{4.3}$$

with each matrix M_i defined as:

$$M_i = \begin{bmatrix} \cos\left(k_{yi} d_i\right) & \frac{-j\varepsilon_i}{k_{yi}} \sin\left(k_{yi} d_i\right) \\ \frac{-jk_{yi}}{\varepsilon_i} \sin\left(k_{yi} d_i\right) & \cos\left(k_{yi} d_i\right) \end{bmatrix} \tag{4.4}$$

and the wave vector k_{yi} obtained with the Snell's law between layer i and $i-1$:

$$k_{yi}^2 = n_{i-1}^2 \left(\frac{2\pi}{\lambda}\right)^2 \left(\frac{n_i^2}{n_{i-1}^2} - \sin^2\alpha\right) \tag{4.5}$$

In the six-layer SPR system with an additional (r)GO thin film as functional layer on top of the Au metallic layer, M becomes:

$$M = M_{\text{glass}} \cdot M_{\text{Au}} \cdot M_{GO/rGO} \cdot M_{biolayer} \tag{4.6}$$

The sensitivity S of an SPR biosensor can be defined as the first derivation of the angle of incidence α for the minimum reflectance with respect to the dielectric parameter ε_{bio} of the bimolecule layer.

$$S = \left.\frac{d\alpha}{d\varepsilon_{bio}}\right|_{r_{p,\text{minimum}}} \tag{4.7}$$

The above deduction enables a comparison of the sensing performances of the SPR biosensor platforms with GO and rGO functional layers, in the condition of knowing the thicknesses and dielectric parameters of the (r)GO films $d_{(r)GO}$ and $\varepsilon_{(r)GO}$.

4.2.3 Biosensing Mechanism of (r)GO Based SPR Platforms

In this section, the thicknesses and dielectric parameters of the (r)GO thin films were extracted by AFM and ellipsometry measurements. Afterwards, the sensitivity corresponding to the binding activity of target biomolecule was simulated for both (r)GO SPR platforms based on the six-layer model established in section 4.2.2.

The AFM characterization was carried out to extract the thickness of the GO thin films. As shown in figure 4.4, the thickness of the thin films was approximately 8 nm. The GO flakes used to prepare the GO thin films for the SPR experiments were of larger lateral area and thickness, which lead to higher thin-film thickness compared to that obtained in chapter 3. Since the oxygen functional groups are partially removed by the thermal reduction, the rGO thin films tend to slightly collapse and their thickness should be smaller than 8 nm. The evanescent light propagates until approximately half of the incident light wavelength (390 nm) in the plane perpendicular to the conductive layers [203]. Therefore, both thin films are within the range of the evanescent light field and can be used to detect the target biomolecule bindings.

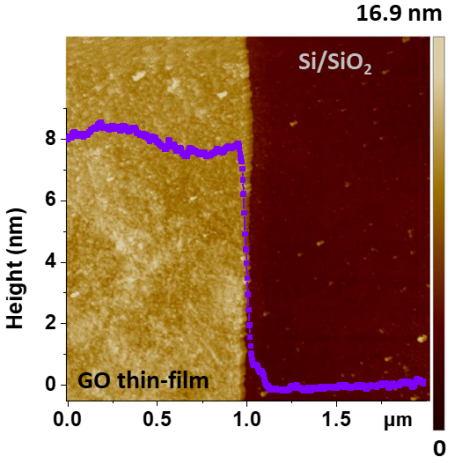

Figure 4.4: AFM characterization of a GO thin film showing an average thickness for the GO pattern of approximately 8 nm.

The dielectric parameters were extracted by ellipsometry. The principle of this characterization tool was introduced in chapter 2.5.2. The two parameters Ψ and Δ were directly measured versus the incident wavelength at a fixed angle of incidence θ. Ψ and Δ are the amplitude ratio and phase difference of the s-plane and p-plane components of the reflected light, respectively. In this study, the ellipsometry characterization was carried out with the incident wavelength ranging from 300 nm to 800 nm at multiple angles of incidence θ: 50°, 55°, 60°, 65° and 70°. Hereby, the measurements in multiple angles provided a more precise analysis than the measurement at a single angle. A proper layer model can be chosen to fit Ψ and Δ so that the dielectric parameters and thicknesses of both thin films can be extracted after the fitting.

A five-layer model was chosen for the fitting as shown in figure 4.5(a). It consists of a Si file layer (data in lookup table), a SiO_2 Cauchy layer, an APS Cauchy layer, a (r)GO thin film as Cauchy layer and air as a fixed dielectric constant layer. The fitting parameters of each layer are shown in figure 4.5(b).

The experimental and fitting curves of Ψ and Δ versus the incident wavelength are shown in figure 4.5(c)-(d). From the fitting data, the refractive indices ($\boldsymbol{n} = n + jk$) as well as the dielectric parameters ($\boldsymbol{\varepsilon} \equiv \boldsymbol{n}^2 = \varepsilon^{'} + j\varepsilon^{''}$) can be deducted. The dielectric parameter for Si substrate and air were $\boldsymbol{n}_{\mathrm{Si}} = 3.872 \pm 0.016j$ and $\boldsymbol{n}_{air} = 1$, respectively. The thickness of SiO_2 was measured to be $d_{\mathrm{SiO_2}} = 156.15 \pm 2.00\,\mathrm{nm}$ while its refractive index was $\boldsymbol{n}_{\mathrm{SiO_2}} = 1.464$. The thickness and refractive index of the APS layer was measured as $d_{APS} = 1.01 \pm 0.40\,\mathrm{nm}$ and $\boldsymbol{n}_{APS} = 1.422 \pm 0.0001j$ [204]. The thicknesses of GO and rGO thin film, obtained by AFM characterization, were $d_{GO} = 8\,\mathrm{nm}$ and $d_{rGO} = 6.8\,\mathrm{nm}$, respectively.

(a)

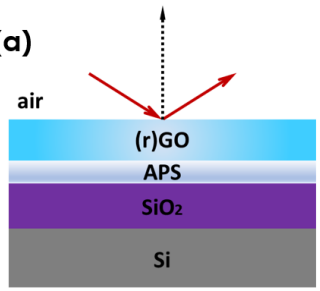

Layer type
nk layer
Cauchy layer
Cauchy layer
Cauchy layer
file layer

(b)

layer material	layer type	thickness	n	k
Si	file layer		3.872	0.016
SiO_2	Cauchy layer	156.15 ± 2 nm	1.464	
APS	Cauchy layer	1.01 ± 0.4 nm	1.422	0.0001
(r)GO	Cauchy layer	8 nm/6.8 nm	acquiring	
air	nk layer		1.00	

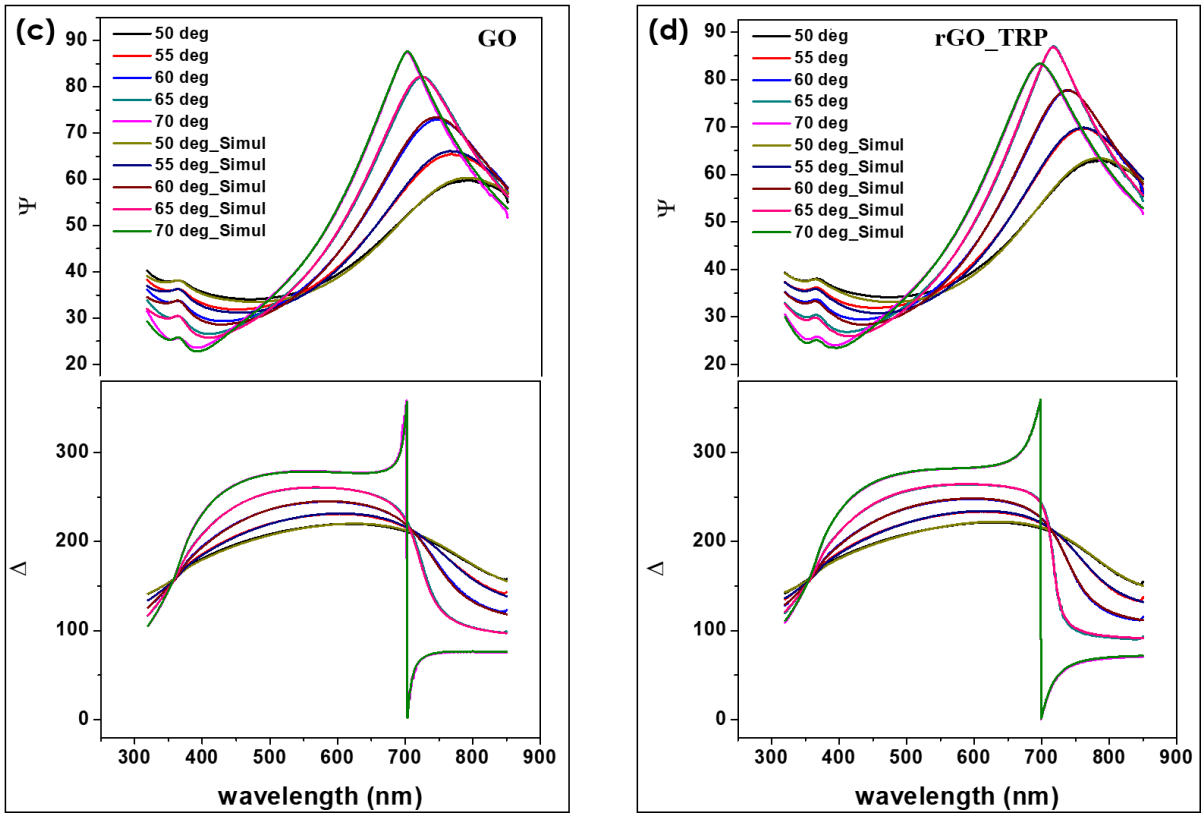

Figure 4.5: Ellipsometry measurements. (a) A layer model is chosen to extract the target material parameters. It consists of Si, SiO_2, APS, (r)GO thin film and air. The layer types are file layer, Cauchy layer, Cauchy layer, Cauchy layer and fixed dielectric constant layer (nk), respectively. (b) The fitting parameters of each layer used to extract the dielectric parameters and optical indices for (r)GO thin films. (c)-(d) Multi-angle ellipsometry characterization of the GO thin films (thickness 8 nm) and the rGO thin films (thickness 6.8 nm) after being treated by the TRP. The angles of incidence are 50°, 55°, 60°, 65° and 70°. The experimental ellipsometry results are fitted with the 5-layer model to extract the refractive indices and dielectric parameters of the (r)GO thin films.

The deduced dielectric parameters of (r)GO thin film are plotted in figure 4.6(a). This

result manifests a clear change in the complex dielectric parameters of the GO thin film after the TRP. At the incident wavelength 780 nm of the SPR setup, the dielectric parameters of GO and rGO thin films are: $\varepsilon_{GO} = 1.72 + 0.55j$, $\varepsilon_{rGO} = 1.59 + 1.10j$.

In the following, a simulation software "WinSpall" was used to analyze the SPR biosensor performance with (r)GO as functional layers, based on the layer structures shown in figure 4.6(b). For both cases, the sequential layers between the prism and water layers were glass substrate, Au thin film, (r)GO thin film and biolayer (ConA/PSA). All the parameters used for the simulation by WinSpall are listed in figure 4.6(c). The thicknesses and dielectric parameters of the prism ($d_{prism} = \infty$, $n_{prism} = 1.76$), glass ($d = \infty$, $\varepsilon_{glass} = 1.76$), Au ($\varepsilon_{\mathrm{Au}} = -12.45 + 1.3j$) and water ($d = \infty$, $\varepsilon_{water} = 1.78$) were adapted from the WinSpall tutorial materials. The Au thin film deposited by electron beam evaporation in this study was approximately 50 nm thick. The thicknesses and dielectric parameters for (r)GO thin films were the values obtained by the AFM and ellipsometry (at $\lambda = 780$ nm) characterizations. The performance of (r)GO based SPR biosensors were compared before and after the attachments of the ConA/PSA biolayer ($d_{ConA/PSA} = 10$ nm, $\varepsilon_{ConA/PSA} = 2.11$) [203]. The simulated results of the angle of incident light versus the SPR signal (reflectance) for (r)GO based SPR biosensors are shown in figure 4.6(d). It clearly manifests that the angle of incidence α corresponding to the minimum value of the reflectance shifts is larger for rGO SPR biosensing compared to the case of GO.

Furthermore, to predict the real biosensing process, the sensitivity as defined in equation 4.7 was compared for both biosensors with a variable thickness or dielectric parameters of the biolayer. The simulated results are shown in figure 4.7(a)-(b). It appears that the sensitivity is larger for rGO compared to GO based SPR biosensors in the condition of constant dielectric parameters and variable thickness of the biolayer or *vice-versa*.

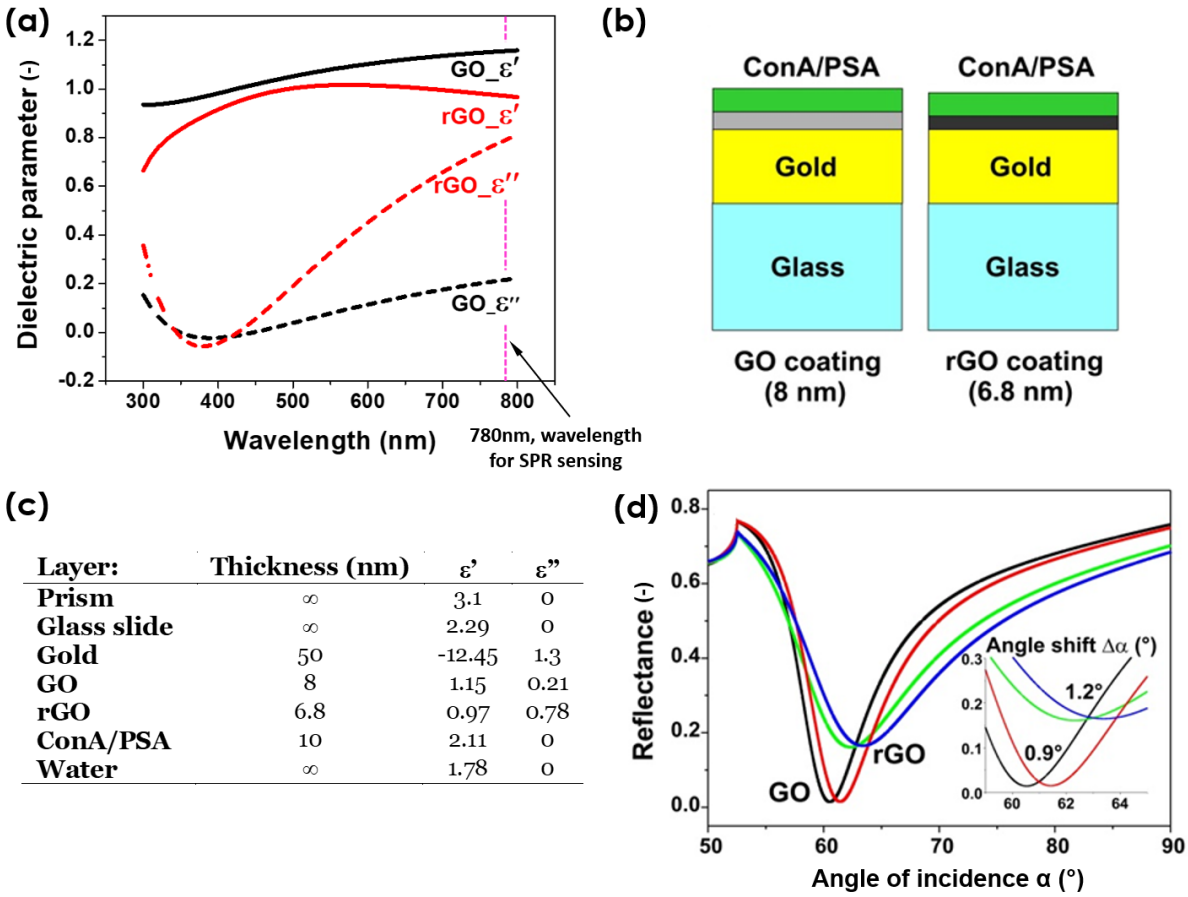

(c)

Layer:	Thickness (nm)	ε’	ε”
Prism	∞	3.1	0
Glass slide	∞	2.29	0
Gold	50	-12.45	1.3
GO	8	1.15	0.21
rGO	6.8	0.97	0.78
ConA/PSA	10	2.11	0
Water	∞	1.78	0

Figure 4.6: GO and rGO thin film based SPR biosensor. (a) The dielectric parameters of (r)GO thin films $\varepsilon = \varepsilon' + \varepsilon''$ are extracted by spectroscopic ellipsometry measurements. (b) The layer structures applied for the simulations. (c) All the parameters used for the simulation. (d) The simulated plots of the angle of incident light versus the SPR signal (reflectance) for (r)GO SPR biosensors.

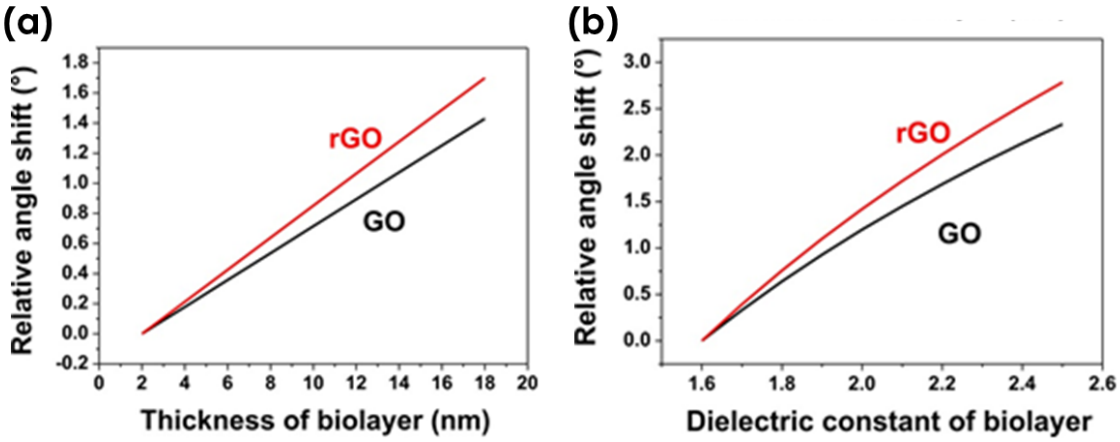

Figure 4.7: Simulated sensitivity of GO and rGO based SPR platforms (a) as a function of the thickness and (b) as a function of the dielectric parameter of the biolayer.

4.3 (r)GO Based SPR Platforms for Biosensing

The SPR setup for the biosensing experiments is shown in figure 4.8. The main components were an autosampler, a Y-valve, an SR7000DC SPR instrument, an electronic flow cell, a solvent reservoir and waste bottles. Prior to each biosensing process, the SPR was cleaned by six different substances in this sequence: DIW, 20 % ethanol, sodium dodecyl sulfate 0.5 %, glycin, DIW, 20 mM NaOH.

The autosampler maintained the temperature at 4 °C to preserve the activity of the agents. All the agents were degassed for 10 min before being injected into the flow cell. This was to avoid the formation of air bubbles, which would add strikes to the output SPR signals. In this study, both channels of the flow cell were used for the biosensing because the receptor biomolecules were incubated outside of the flow cell. The reference chips were used to extract the selectivity of (r)GO SPR biosensors.

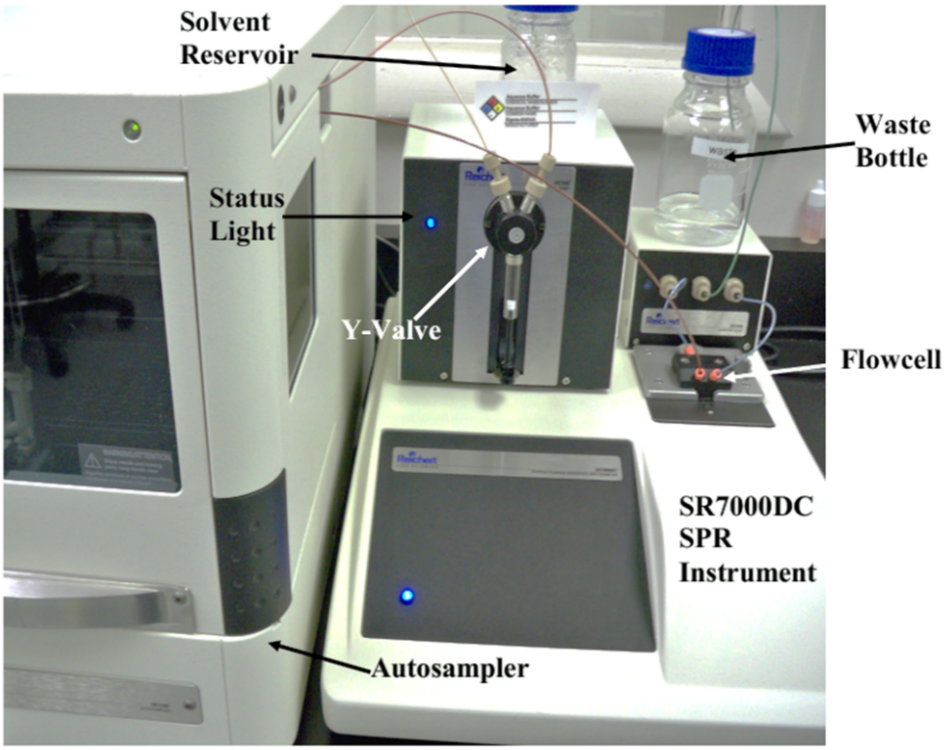

Figure 4.8: The SPR setup (Reichert, Inc.) consisted of an autosampler (maintained at 4 °C to preserve the activity of agents), a Y-valve, an SR7000DC SPR instrument, a flow cell, a solvent reservoir and waste bottles.

4.3.1 Non-Electronic (r)GO Based SPR Platforms for Lectin Detection

The biosensing process took place inside the flow cell. 1 µl matching fluid (refractive index: 1.515) was pipetted beforehand on the prism surface to reduce the reflection at the glass surface. Then the SPR chip was placed in the receptacle as shown in figure 4.9(a). Afterwards, the flow cell was clamped on top of the chip, with a schematic

sideview and a photo from the top shown in figure 4.9(b)-(c). A close-up of two channels is shown in figure 4.9(d). These two channels were used for the reagents passing through the surface of SPR chip.

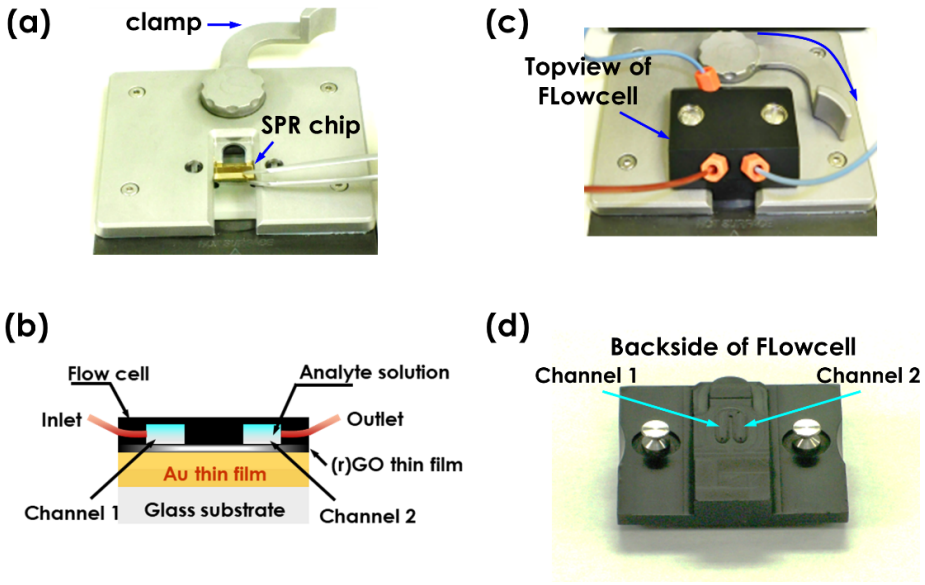

Figure 4.9: SPR flow cell (Reichert, Inc.). (a) The SPR chip is placed into the receptacle. (b)-(c) Sideview (schematic) and topview (photo) of the fluidics cell for biosensing. The target biomolecule, buffer solution, and agents to regenerate the biosensor surface are injected at the inlet and flow towards the outlet. The flow time and flow rates are controlled to optimize the biosensor performance. (d) The fluid cell contains 2 distinct channels and both serve as working channels in this study.

The (r)GO SPR platforms were prepared by the three following steps, while the detailed schematic of the preparation is shown in figure 4.10:

i) The $-$COOH groups on the surface of the (r)GO thin films were activated by mixed aqueous solutions of 100 mM N-(3-dimethylaminopropyl)-N'-ethylcarbodiimide hydrochloride (EDC) and 25 mM N-hydroxysuccinimide (NHS) for 30 min at room temperature. Afterwards, the chips were cleaned three times by DIW.

ii) The PSA receptor biomolecules were covalently immobilized on the surface of the (r)GO functional layers at 4 °C overnight. The concentration of PSA for the immobilization was 50 µg ml^{-1}, prepared in 10 mM acetate acid buffer solution, which was at a pH value of 5. This pH value was chosen to achieve the optimal surface charge of PSA for the immobilization [44]. The incubation of PSA was carried out outside of the flow cell overnight instead of a short-term injection in the flow cell, in order to achieve the maximum amount of $-$COOH on the surface.

iii) After the PSA incubation, the chip was mounted into the SPR setup and stabilized in phosphate buffered saline with tween-20 (PBST) for 2 h. 1 mM carbo-free blocking agent in 10 mM PBST was then injected for 10 min to saturate the freestanding $-$COOH groups.

The SPR biosensor platforms with (r)GO thin films as functional layers established with this protocol are called Au/GO/PSA and Au/rGO/PSA in the following sections.

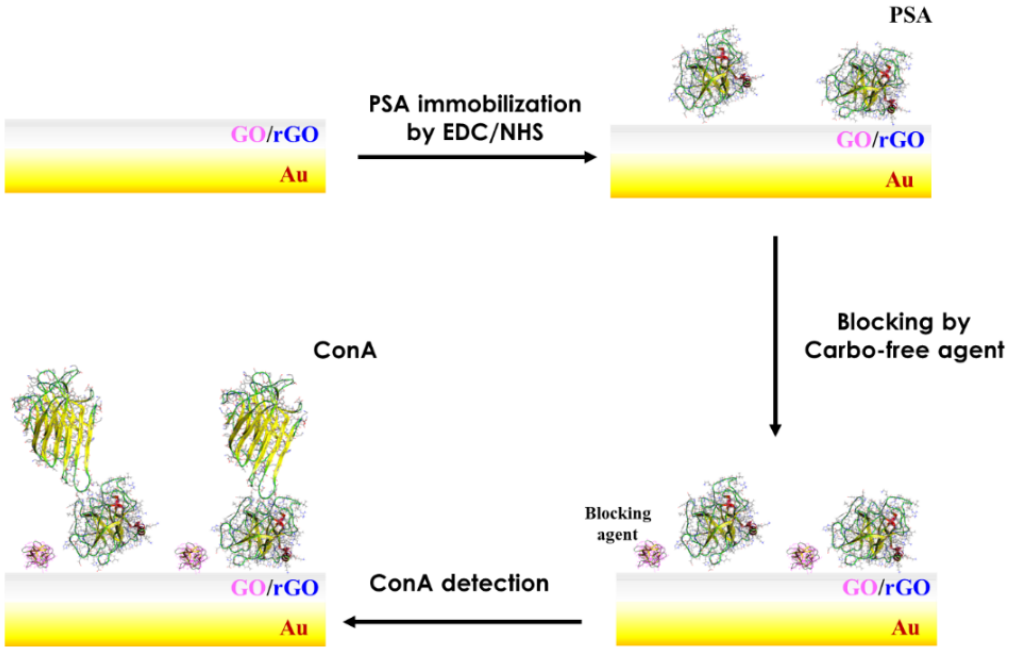

Figure 4.10: (r)GO thin film based SPR biosensor preparation. The −COOH groups of the (r)GO thin films are activated by EDC/NHS chemistry to covalently immobilize the PSA receptor biomolecules. Afterwards, the carbon-free blocking agents are applied to saturate the free-standing −COOH groups to prevent non-specific binding. The established biosensor is ready to detect target biomolecule: ConA lectin.

The specific test was carried out with a series of ConA concentrations: 0.5 µg ml^{-1}, 1 µg ml^{-1}, 5 µg ml^{-1}, 10 µg ml^{-1}, 50 µg ml^{-1} and 100 µg ml^{-1}. The detection overview of the SPR output signal for the ConA concentration experiments is shown in figure 4.11(a). Each concentration was injected 2 times in each channel. The measurements in the flow cell started from the addition of the carbo-free blocking agent, because the first two steps of the biosensor preparation took place outside the SPR setup. The figure 4.11(b) is a close-up showing the detection process of two specific ConA concentrations (50 µg ml^{-1} and 100 µg ml^{-1}).

The biosensing measurements are shown in figure 4.12(a). Between two subsequent ConA injections, 0.2 M NaCl and 10 mM NaOH were used to regenerate the sensor surface. For all the agents (ConA, NaCl and NaOH), the injection (also called association) started from the blue vertical line and terminated at the orange line. PBST cleaning (also called dissociation) followed up until the red line. Generally, between the red line and next blue line was also PBST cleaning so that the biosensor surface was cleaned and ready for the injection of the next agent. The exact values for the association and dissociation phases are summarized in figure 4.12(b).

The biosensing kinetics is represented by a sensorgram which displays the changes in refractive index unit (RIU) with respect to time. The relationship of refractive index unit and the angle shift $\Delta\alpha$ of the incident light which corresponds to the minimum reflectance follows: $0.1°\Delta\alpha = 1000$ µRIU. The obtained sensorgrams of the ConA concentrations for (r)GO based SPR platforms are given in figure 4.13(a)-(b). It is

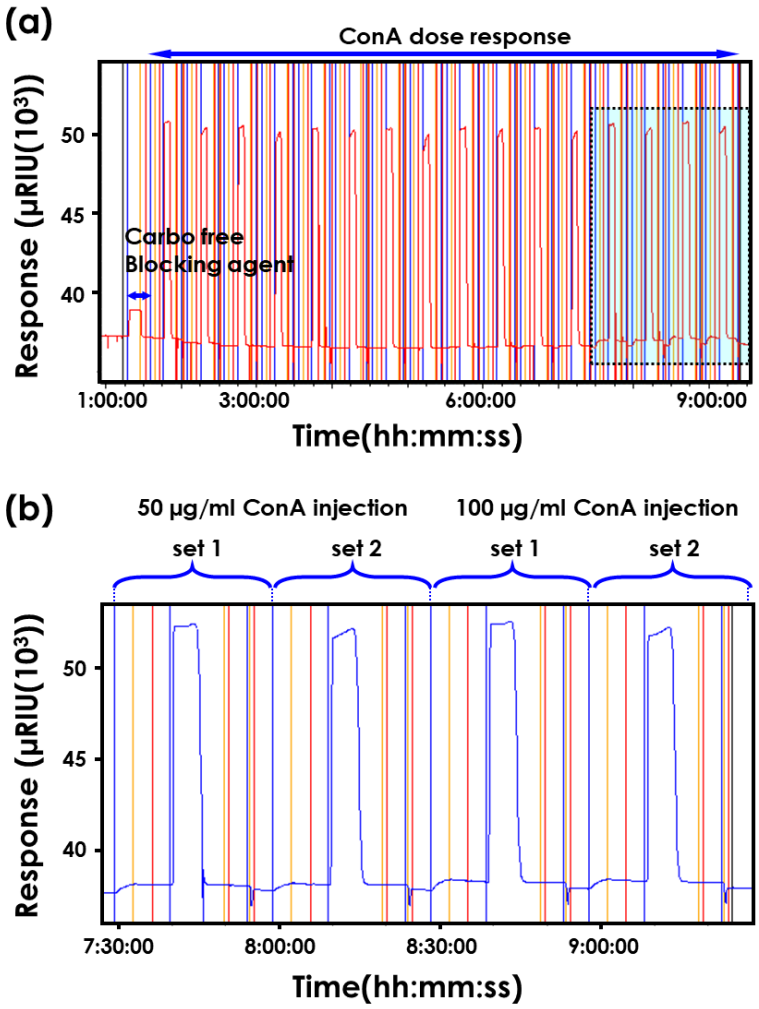

Figure 4.11: Output signal of the Reichert SPR setup. (a) Overview for ConA concentration experiments. The 1 mM carbo-free blocking agent was injected for 10 min to block the free-standing $-COOH$ groups. A series of ConA concentrations were detected. (b) A close-up of the detection of $50\,\mu g\,ml^{-1}$ and $100\,\mu g\,ml^{-1}$ ConA. Each concentration of ConA has been injected 2 times. Between measurements, the biosensor surface was cleaned by a regeneration agent.

shown that the rGO thin film enhances the SPR signal compared to the GO thin film. The amplification factor was 1.70 ± 0.25. This result confirms the SPs enhancement effect of rGO functional layers as already predicted by the simulation results in section 4.2.

Specific and non-specific tests were compared to analyze the sensing selectivity of the (r)GO based SPR platforms. The biosensor surface was prepared as described in figure 4.10 without PSA immobilization for non-specific tests. Each ConA concentration for specific and non-specific tests was injected three times on two different chips, so that the performance of both platforms could be investigated statistically. The obtained results were fitted by pharmacology DoseResp in origin software as shown in figure 4.14(a)-(b). The correlation of specific and non-specific bindings was analyzed by Student's unpaired t-test. It manifests the significant difference between specific and non-specific binding for the GO platform ($^{***}P < 0.001$, $^{****}P < 0.0001$, $n = 4 - 14$) and for the rGO platform ($^{**}P < 0.01$, $^{***}P < 0.001$, $n = 4 - 12$). The limit of detection

(a)

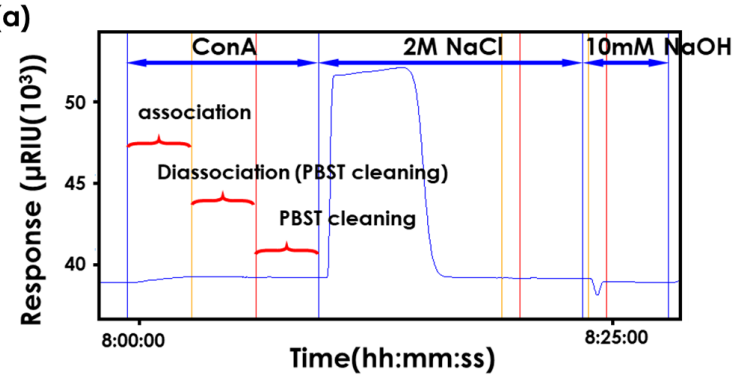

(b)

	Asso t (s)	Asso rate (μl/min)	Disso t (s)	Disso rate (μl/min)
10 mM Carbo-free	600	20	300	20
ConA	210	50	600	50
2 M NaCl	600	50	60	50
10 mM NaOH	10	50	60	50

Figure 4.12: SPR biosensing measurements and parameters. (a) A close-up of the detection of a single concentration of ConA (50 µg ml^{-1}). 0.2 M NaCl and 10 mM NaOH were used to regenerate the biosensor surface. For each agent (ConA, NaCl, and NaOH), three phases are observed: the injection (association), the PBST cleaning (dissociation) and the PBST cleaning so that the biosensor surface was cleaned for the injection of the next agents. (b) The flow time and rate of the association and dissociation phases for each agent: carbo-free blocking agent, ConA, NaCl and NaOH.

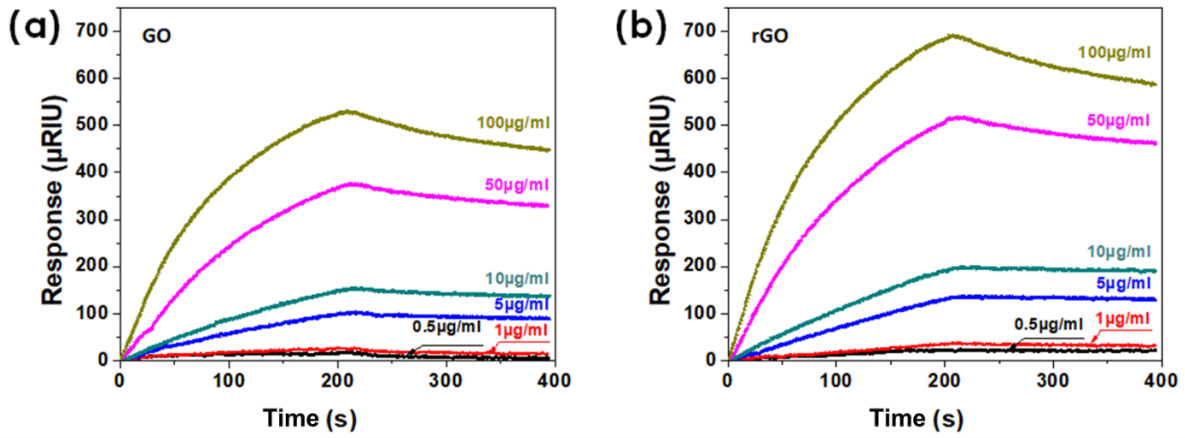

Figure 4.13: Sensorgrams of GO and rGO thin film based SPR biosensor platforms. PSA as receptor biomolecules were covalently immobilized on (r)GO thin film by EDC/NHS chemistry. To avoid non-specific binding, the freestanding −COOH groups were saturated by the carbo-free blocking agent. The target biomolecule ConA were detected with a concentration range of 0.01 µg ml^{-1} to 100 µg ml^{-1}.

(LOD) of the rGO biosensor platform was one order of magnitude lower than that of the GO based platform, with values of 0.5 µg ml^{-1} and 5 µg ml^{-1}, respectively. Moreover, the signal-to-noise ratio of the rGO platform was approximately three times larger than that for the GO platform with statistical values 6.56 ± 3.63 and 2.16 ± 1.64, respectively. When compared with GO thin films, rGO thin films restore a larger

area of the carbon lattice after the thermal reduction treatment. This enables the SPs to propagate over longer distances without being scattered. This could be responsible for the improved LOD and signal-to-noise ratio in the ConA biosensing process. These results indicate a significant influence of the thermal reduction on the SPR biosensors with GO and rGO as functional layers.

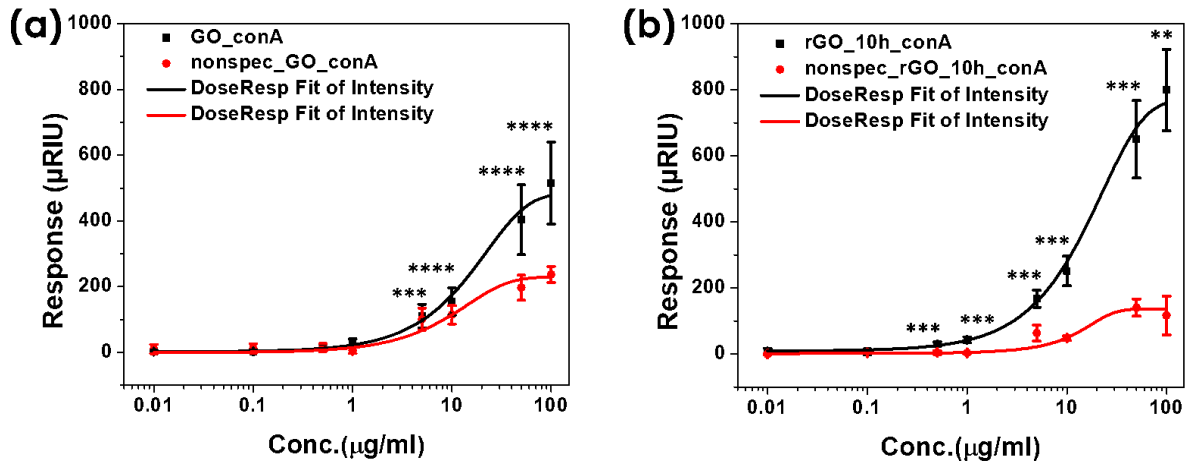

Figure 4.14: Statistical comparison of GO and rGO thin film based SPR biosensor performance for specific and non-specific detection of ConA. The results were analyzed using Student's unpaired t-test. Significant differences between specific and non-specific binding are shown for the GO platform ($^{***}P < 0.001$, $^{****}P < 0.0001$, $n = 4 - 14$), and for the rGO platform ($^{**}P < 0.01$, $^{***}P < 0.001$, $n = 4 - 12$).

4.3.2 Electronic rGO Based SPR Platforms

In this section, the tuning effect of SPR signals by external electronic fields is discussed for rGO thin film based SPR biosensor platforms. Prior to the biosensing process, the bipolar properties of the rGO thin films were characterized in an ESFET configuration, as shown in figure 4.15(a). The rGO thin film was prepared on IDEs by the fabrication process as described in chapter 2. The IDEs consisted of a common source electrode which is located at the center of the chip and is shared by 16 drain electrodes in a 4×4 array layout. There are 10 fingers for each channel with an effective channel length of 5 µm, an effective channel width of 900 µm and a separation distance between neighboring fingers of 5 µm. A SEM image of a close-up of a single channel with a patterned rGO thin film is shown in figure 4.15(b).

The ESFET measurements were carried out with a Keithley 4200-SCS parameter analyzer. To obtain the curves without any drifting, the rGO devices were stabilized beforehand in 10 mM PBS for 2 h at room temperature. An Ag/AgCl electrode immersed in 10 mM PBS served as the gate electrode to apply sweep voltages from -0.8 V to 0.8 V against the source electrode, while the step voltages are applied between the drain and source electrodes ranging from -0.1 V to 0.1 V with 0.1 V as the step size. The detailed explanation of the bipolar curve can be found in section 3.2.3. The measured bipolar characteristic curves are shown in figure 4.16. They indicate that the rGO thin film is initially n-doped, because the Dirac points are shifted to the left compared to $V_{gs} = 0$ V. Besides, a stronger tuning effect is observed for a drain-source

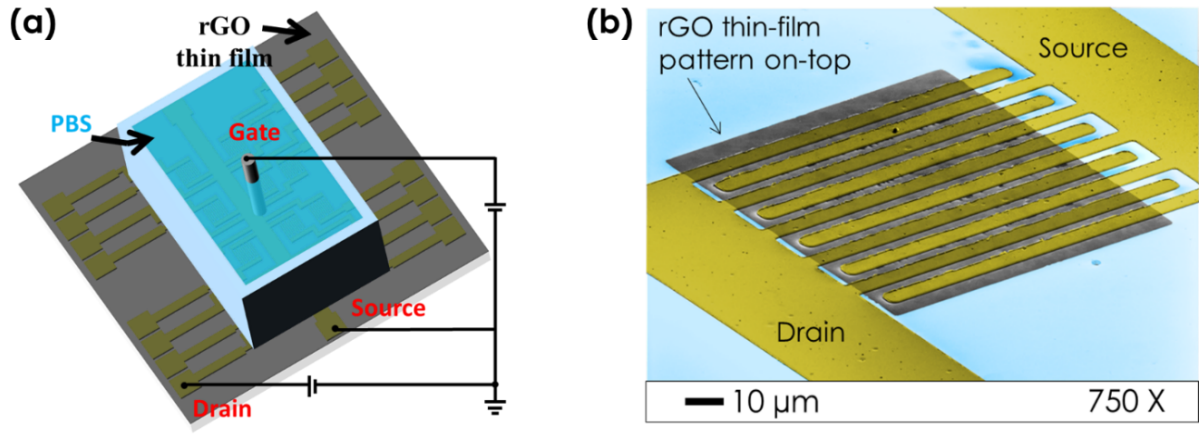

Figure 4.15: Electronic characterization of rGO thin films on IDEs. (a) Schematic of an ESFET configuration with the rGO thin film as a transducer layer. (b) SEM image of an rGO thin film on an IDEs structure used for ESFET characterization.

voltage $V_{ds} = -100\,\text{mV}$ compared to $V_{ds} = 100\,\text{mV}$. This bipolar property can be utilized for modulating the dielectric parameters of the rGO functional layers and, hence, possibly tune the sensitivity for rGO based SPR biosensors [205].

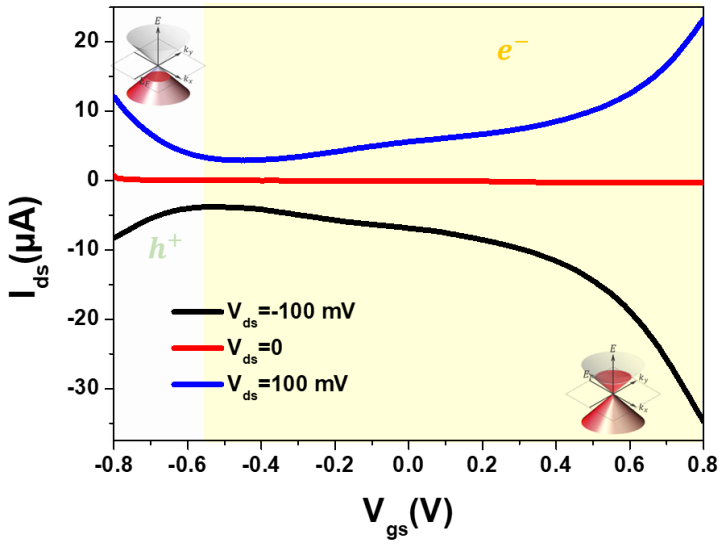

Figure 4.16: Bipolar characteristics of the rGO thin film as transducer layer in an ESFET configuration.

The electronic SPR measurements that intended to employ the bipolar property of rGO thin films were carried out in a flow cell, which is shown in figure 4.17(a)-(b). An Ag/AgCl electrode was immersed from the top of the flow cell into the analyte solution, while a metal pillar was in contact with the Au/rGO/PSA SPR biosensor surface. More details of this flow cell are given in the Reichert handbook [200, 206]. In this study, a bias voltage was applied to the Au/rGO/PSA biosensor surface through the metal pillar against the Ag/AgCl electrode. The close-up of this two-electrode configuration is depicted in figure 4.17(c).

The tuning effect was tested initially in the PBST buffer solution, by applying a voltage staircase to the rGO thin film: 0 V, 0.5 V, 0.8 V, 0 V, −0.5 V, −0.8 V and 0 V. Each voltage step was applied for 30 s. The corresponding SPR signals are shown in figure

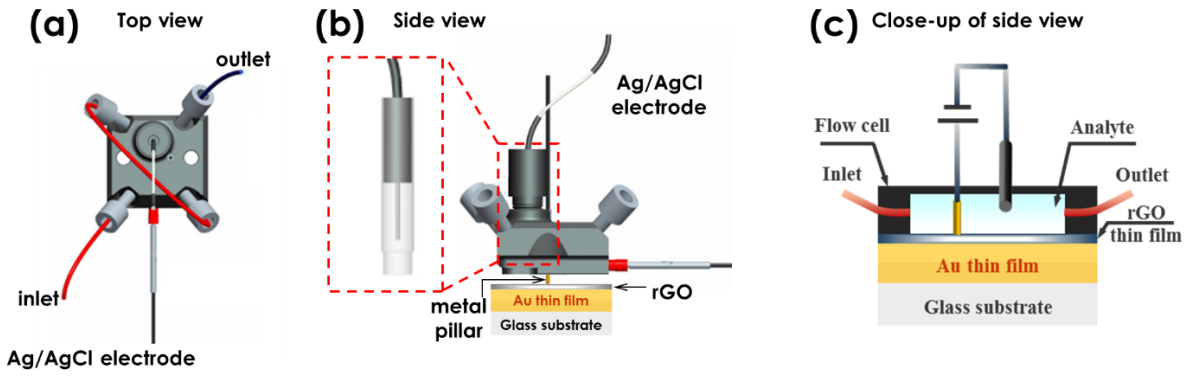

Figure 4.17: Flow cell setup for electronic SPR measurements. (a)-(b) Top view and side view of the electronic flow cell with an Ag/AgCl RE inserted from the top (the images are adapted from the user guide of the Reichert SPR setup [206]). (c) Close-up of the side view of the electronic flow cell: the voltage bias was applied to the rGO surface through a metal pillar (yellow color) against an Ag/AgCl electrode.

4.18(a). It demonstrates that only the positive but not the negative voltages modulate the SPR signals with a response delay time of 12-15 s. Then, the comparison of the SPR responses of Au/rGO/PSA biosensors and bare Au chips were carried out in PBST running buffer, by applying the sweeping voltages (0 V to 0.8 V to −0.8 V to 0 V) with a sweeping rate of 0.1 V s^{-1}. After compensating with a 12 s delay for the Au/rGO/PSA biosensor platform, the obtained voltage modulation curves were measured as shown in figure 4.18(b). The SPR signals of the Au/rGO/PSA chips showed no response to the applied negative voltages but they showed a response to the applied positive voltages (gray curve). This is consistent with the previously presented results in case of the applied voltage staircase. This result indicates that the running PBST buffer solution provides a stable baseline for the ConA detection when negative voltages are applied.

In contrast, the SPR signals of the bare Au chips are tuned with the applied voltages (orange curve) with a peak-to-peak delay between 8 s and 10 s. It is also seen that the modulation intensity of the SPR signals was slightly higher for the negative voltages than for the positive voltages. The reason for this might be due to the asymmetric modulation of the refractive indices [207], which is induced by cation or anion accumulations in the Helmholtz double layer [163], changes of charge density [208], and a reduction-oxidation process at the Au-liquid interface [209].

In the following, the tuning effect of the applied voltages on the biosensor performance to detect ConA was investigated. The voltages were applied to the Au/rGO/PSA SPR biosensor surface against the Ag/AgCl electrode, with a constant ConA concentration of 50 µg ml^{-1}.

- Positive voltages (0.4 V, 1 V and 1.6 V) were applied to the Au/rGO/PSA biosensor surface from $t = 0$ s for 210 s. It was observed that the maximum intensities of the output SPR signals increased proportionally with the positive voltages while the association time was longer than the injection time of 210 s, as shown in figure 4.19(a). This could be because the positive voltages polarized the PSA receptor molecules and ConA target molecules were still being attracted and bonded after the bias terminated. It is in a clear contrast with the reference

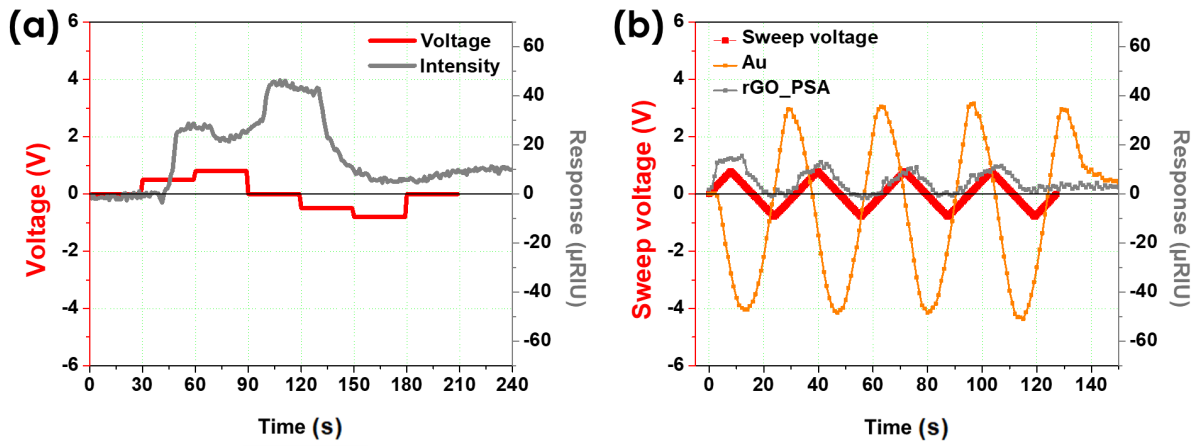

Figure 4.18: Electronically tunable SPR biosensor with an rGO thin film as a functional layer. (a) SPR response of an Au/rGO/PSA chip within PBST flow. The applied voltage staircase to the rGO thin film was 0 V, 0.5 V, 0.8 V, 0 V, −0.5 V, −0.8 V and 0 V and each step was lasting for 30 s. A response to positive voltages is observed with a delay of 12-15 s. (b) The sweeping voltages (0 V to 0.8 V to −0.8 V to 0 V, 4 cycles, red curve) were applied to an Au chip and an Au/rGO/PSA chip. The corresponding SPR response of the Au/rGO/PSA chip (gray curve) is displayed after compensating with a 12 s delay and can only be modulated by positive voltages. In contrast, the SPR response of an Au chip (orange curve) shows the voltage modulation corresponding to both positive and negative sweeping voltages.

test in PBST, during which the SPR signal intensity was also tuned by the applied positive voltage ($V = 1.6$ V) but dropped immediately when the voltage supply terminated at $t = 210$ s.

- With negative voltage modulations, the biosensing performance presented very distinctive characteristics. The SPR signal in figure 4.19(b) shows no influence of the PBST when negative voltages were applied. Therefore, the negative voltage was applied from 0 s to 630 s, which covers both association and dissociation periods. The baseline refers to the sensorgram which was measured in 10 mM PBST running buffer at $V = -0.8$ V. The sensorgrams for 50 µg ml^{-1} ConA injections were measured in the condition of the applied negative voltages of 0 V, −0.8 V and −1.6 V. The obtained results are shown in figure 4.19(b). As expected, the negative voltage introduces no SPs changes to the running PBST buffer solution. Therefore, it can be used as the baseline to analyze the tuning effect of the bipolar property of rGO thin film for detecting the target biomolecule. The SPR signals increased with the absolute value of the applied voltages, proving the tunability of the SPs on rGO based SPR biosensors with negative voltages.

In the following, the sensing limit of ConA biomolecules was investigated for the rGO based electronic SPR platform in three different conditions: no bias, positive bias ($V = 1.6$ V) and negative bias ($V = -0.8$ V). A concentration of 0.01 µg ml^{-1} ConA was chosen for the test, because it is not detectable by conventional Au SPR chips. The sensorgrams of 50 µg ml^{-1} ConA and PBST buffer solution serves as the references. The ConA injection was performed from 0 s to 630 s and the applied voltages were the same as described in the last session. The obtained results are shown in Figure 4.20(a)-(c).

- When no bias was applied on the rGO surface, there is no detection signal for the 0.01 µg ml^{-1} concentration.

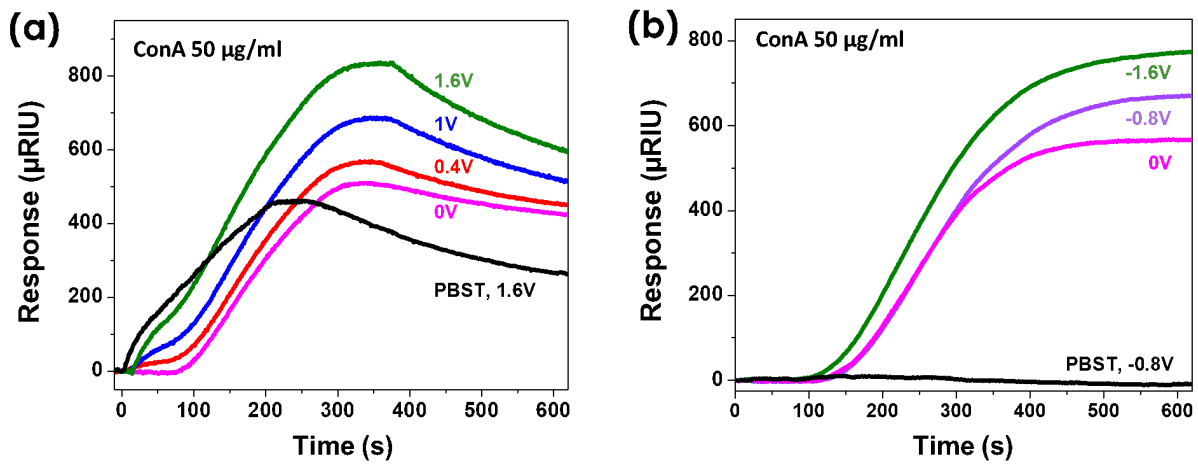

Figure 4.19: Biosensing performance of the electronically tunable SPR platform using rGO thin films as functional layers. (a) A ConA concentration of 50 µg ml^{-1} was detected while different bias voltages were applied on the Au/rGO/PSA sensor surface (0 V, 0.4 V, 1 V and 1.6 V). This confirmed the sensitivity increase. However, the SPR signal also responded to PBST as control experiment. (b) This can also be confirmed when 50 µg ml^{-1} ConA were detected when voltages of 0 V, −0.8 V and −1.6 V were applied on the Au/rGO/PSA sensor surface. The reference curve is given by 10 mM PBST at $V = -0.8$ V because the biasing into the negative direction generates a stable baseline for PBST.

- At a fixed positive voltage $V = 1.6$ V, the SPs intensity for 0.01 µg ml^{-1} is detectable with a lower intensity compared to that of PBST. The reason could be that the SPs intensity caused by the accumulated ions on the Au/rGO/PSA sensor surface in PBST is higher than that induced by the bound ConA molecules. In future, more detailed experiments are required to precisely clarify this issue.
- At a fixed negative voltage $V = -0.8$ V, the detection limit was as low as 0.01 µg ml^{-1} with the SPs intensity at 30 µRIU (as shown in the figure 4.20(d)), which can be distinguished from the baseline obtained from the pure PBST buffer solution.

These results show that the sensing LOD of rGO based SPR platforms can be improved by negative voltages applied to the thin films.

This electronic tuning effect with the application of negative biases makes the rGO thin films even more interesting compared to the GO thin films for SPR biosensing as previously shown (see performances in figure 4.13). The binding of incoming, negatively charged ConA (neutral pH of 6.3-7) onto the Au/rGO/PSA biosensor surface is equivalent to a negative bias, which tends to enhance the SPs intensity. Thereby, in a normal SPR setup without external bias, rGO based SPR platforms display a higher sensitivity compared to GO based SPR platforms.

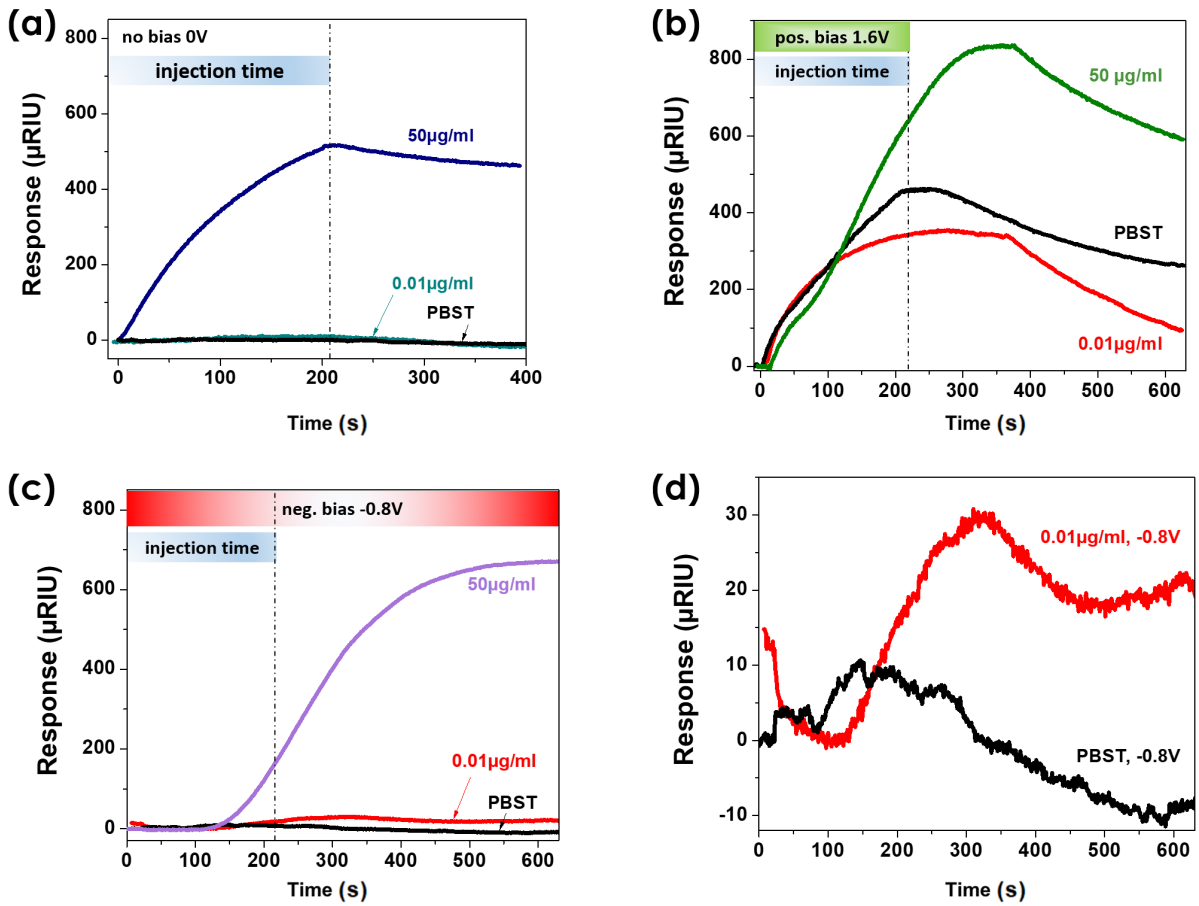

Figure 4.20: Sensitivity limit of the electronically tunable SPR biosensors using rGO thin films as functional layers. (a) When no bias voltage was set to the rGO thin film, the LOD was approximately $1\,\mu g\,ml^{-1}$. A concentration of $0.01\,\mu g\,ml^{-1}$ had no effect on the signal. (b) When biased with positive voltages, the SPR signal responded to a ConA concentration as low as $0.01\,\mu g\,ml^{-1}$. However, also a PBST flush as control showed a significant response. The bias voltage was fixed at $V = 1.6\,V$ while $0.01\,\mu g\,ml^{-1}$ and $50\,\mu g\,ml^{-1}$ ConA were detected. (c) When biasing with negative voltages, $0.01\,\mu g\,ml^{-1}$ caused a detectable response, which could be clearly distinguished from the PBST control. (d) A close-up of $0.01\,\mu g\,ml^{-1}$ ConA detection at $V = -0.8\,V$.

4.4 Conclusion

In this chapter, a wafer-scale method to prepare (r)GO based SPR biosensor platforms was successfully established, by using (r)GO thin films prepared with the LTEDS method and the TRP. Such a method is of a promising potential to allow a mass production of SPR devices towards commercialization due to its simplicity and robustness of the (r)GO coatings. The biosensing performance of these two SPR platform was simulated and compared with the WinSpall software. The required parameters, thicknesses and dielectric parameters of (r)GO thin films, were extracted by AFM and ellipsometry characterizations. The AFM characterization revealed that the thin-film thicknesses of GO were 8 nm and of rGO were 6.8 nm. The dielectric parameters extracted by ellipsometry measurement at a wavelength of 780 nm were $\varepsilon_{GO} = 1.72 + 0.55j$, $\varepsilon_{rGO} = 1.59 + 1.10j$.

The simulated results indicated that the rGO based SPR biosensors exhibited higher sensitivity than GO based devices. Experimentally, (r)GO based SPR biosensors were

prepared with PSA as receptor biomolecules to detect ConA target biomolecule. The experimental biosensing results concretely confirmed the simulation results. The specific and non-specific biosensing results demonstrated that rGO based devices exhibit improved LOD and signal-to-noise ratio compared to GO based ones. The LOD of the rGO biosensor platforms was one order of magnitude lower than that of the GO based platforms, with values of $0.5\,\mu g\,ml^{-1}$ and $5\,\mu g\,ml^{-1}$, respectively.

Moreover, the signal-to-noise ratio of the rGO platform was approximately three times larger than that of the GO platform with statistical values 6.56 ± 3.63 and 2.16 ± 1.64, respectively. This result implies that the thermal reduction effectively tuned the dielectric parameters of rGO thin films, which led to the enhanced SPR signals and reduced signal loss. More importantly, in contrast to the insulating GO thin films, the rGO devices showed bipolar characteristics. This electronic property allows influencing the dielectric parameters of the rGO thin films with the assistance of external bias voltages. This enables the SPs modulation and especially improved the LOD of the rGO based SPR platforms. Indeed, the LOD has been decreased significantly to $0.01\,\mu g\,ml^{-1}$, which is not attainable by conventional Au based SPR platforms.

Therefore, to achieve even better biosensing performance, the bipolar property of rGO thin films can be improved with a better restoration of the carbon lattice, either by employing initial GO flakes of higher quality or more efficient reduction methods. This study provides the basis and extends the frontiers of rGO as functional material for advanced SPR biosensing.

5 rGO Based Impedance Spectroscopy Biosensor

In this chapter, an impedimetric biosensor with an rGO thin film as transducer layer on IDEs structures is presented and discussed. This biosensor was used for the label-free detection of PSA. Firstly, the general principle and the state-of-the-art of impedance spectroscopy are introduced. Secondly, the out-of-line and in-line EIS with rGO thin films as transducers are presented. Theoretical equivalent circuits for both out-of-line and in-line EIS are proposed. Thirdly, the biosensing mechanism for the detection of PSA with rGO based in-line EIS is investigated. Based on a comparison of the biosensing performances with variable sizes of receptor molecules and different buffer concentrations, the sensing capability of rGO based in-line EIS in different frequency regimes is discussed in detail.

5.1 Fundamentals of EIS

Impedance spectroscopy is dedicated to the extraction of the complex impedance Z of a system within a pseudo-linear range. An alternating perturbation voltage $V(t)$ of small amplitude (generally in mV regime) in a certain frequency range is used as input and the alternating output current $I(t)$ is measured, as indicated in figure 5.1(a). The impedance is expressed as the quotient of the input voltage $V(t)$ and the output current $I(t)$:

$$Z(t) = \frac{V(t)}{I(t)} \tag{5.1}$$

In the polar form, the impedance is given by the impedance amplitude $|Z|$ and the phase change φ, and in Cartesian form by the real part Z_1 and the imaginary part Z_2, as shown in figure 5.1(b)-(c).

$$Z = |Z|e^{j\varphi} = Z_1 + jZ_2 \tag{5.2}$$

where

$$|Z| = \sqrt{Z_1^2 + Z_2^2}, \quad \varphi = \arctan\left(\frac{Z_2}{Z_1}\right) \tag{5.3}$$

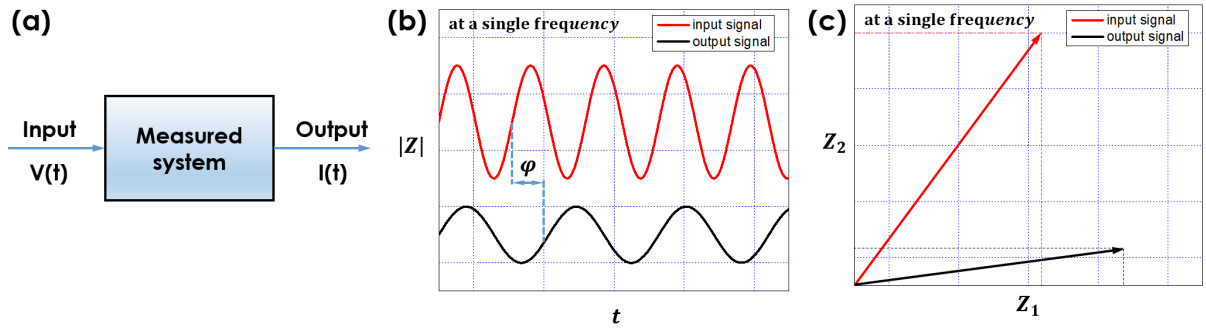

Figure 5.1: The basic principle of impedance spectroscopy. (a) The input signal of the measured system is the alternating current (AC) voltage $V(t)$ and the output signal is the AC current $I(t)$. (b)-(c) The impedance $Z(t)$ is defined as $V(t)/I(t)$. It can be represented in polar or cartesian form, which can be displayed in a Bode or Nyquist plot, respectively.

The EIS has been used to investigate the coating quality and the corrosion degree in the painting industry, to characterize the properties of products in the food industry, and to monitor the health status of human beings [210–215]. EIS is specially utilized as a sensitive, selective, and label-free biosensor platform to detect cells, microorganism, and various biomolecules [216]. The device configuration of a conventional EIS consists of an electrochemical cell with an aqueous RE, a CE and a WE immersed into an electrolyte solution. The RE is made of a metal encapsulated in a glass capillary, which is filled with an electrolyte solution to stabilize the metal. The potential of the RE is set at a fixed value. The CE is usually made of inert metals, for instance gold, stainless steel or platinum, which feeds current to the electrolyte solution. The WE is normally made up of metals, metal oxides, carbons and/or semiconductors. The size of the WE ranges from nano- to microscale. For biomolecules detection, either the WE or both the CE and WE can be further functionalized with biorecognition molecules. The biorecognition molecules can be antibodies, antigens, proteins, aptamers or single-stranded DNA (ssDNA). The target biomolecule should specifically bind to the biorecognition molecules in order to obtain a high biosensor selectivity.

For the two EIS approaches, either with only the WE or with both the CE and the WE for immobilizing the biorecognition molecules, the corresponding measurement setups are depicted in figure 5.2(a)-(b). A voltage $V(\omega)$ that is composed of an AC voltage V_{in_AC} and a constant voltage V_{in_DC} is applied through the WE against the RE to CE, while the output current between WE and CE is measured as $I(\omega)$. The impedance spectrum is plotted as $V(\omega)/I(\omega)$ along the frequency ω. The binding activity of biomolecules between the WE and CE is reflected by the impedance changes, therefore EIS can be utilized as a platform for biosensing.

EIS measurements can be carried out either in the faradaic mode or in the non-faradaic mode. For both of these modes, it is interesting to establish an equivalent circuit that reflects the behavior of the system. The final circuits are built from different elements, which model different physical phenomena and are described below.

In the faradaic mode, EIS measurements take place in an electrolyte solution containing a couple of redox markers. A typical couple is the ferri/ferrocyanide solution K3/K4 ($K_3Fe(CN)_6/K_4Fe(CN)_6$), also used for the cyclic voltammetry measurements presented in chapter 3. When a voltage is applied between the WE and the CE, the charge transfer takes places between the biosensor surface and the redox

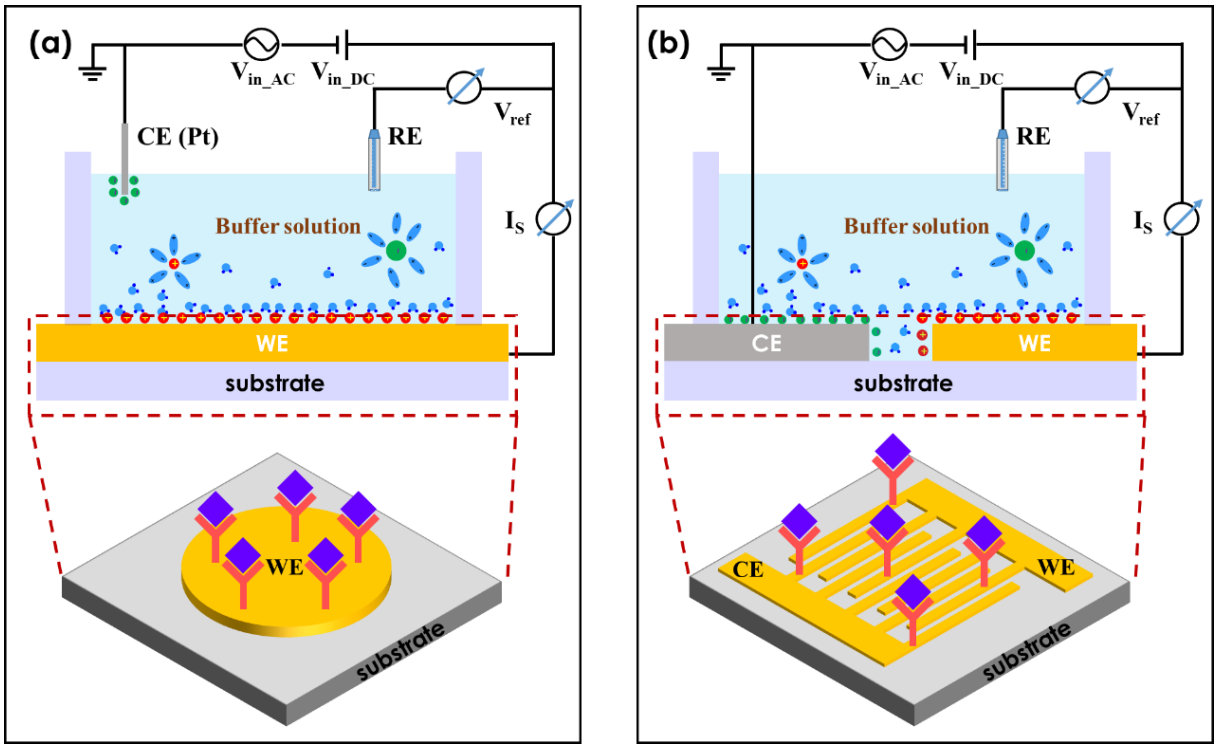

Figure 5.2: The typical three-electrodes configuration of the EIS measurement setups: $V(\omega)$ ($V_{in\_AC} + V_{in\_DC}$) is the input voltage, which is applied at the WE against the RE to CE, while the output current $I(\omega)$ is measured between WE and CE. (a) The CE is made of Pt and only the WE is functionalized with biorecognition molecules. The typical WE is an Au electrode of circular shape. (b) The two arms of IDEs can also serve as CE and WE. Both electrodes are functionalized with biorecognition molecules. This EIS configuration was used in this work.

markers. The charges must then pass through the electrolyte solution of resistance R_{sol}. When the potential is positive, the WE acts as an oxidant and the K4 is oxidized:

$$Fe(CN)_6^{4-} \longrightarrow Fe(CN)_6^{3-} + e^-$$

When the potential is negative, the WE acts as a reductant and the K3 is reduced:

$$Fe(CN)_6^{3-} + e^- \longrightarrow Fe(CN)_6^{4-}$$

The electrons go through the WE to the CE, resulting in the so-called faradaic current that relates to a charge transfer resistance R_{ct} given by:

$$\begin{aligned} R_{ct} &= \frac{RT}{nFi_0} \\ Z_R &= R_{ct} \end{aligned} \tag{5.4}$$

where T is the temperature; R and F are the gas and Faraday constants, respectively; n is the number of involved electrons; i_0 is the exchange current density. i_0 and R_{ct} vary corresponding to the electronic properties of the biosensor surface, which is influenced by the access area of the WE and the density of bound target biomolecules.

At the solid-liquid interface, the ions are attracted by the surface potential of the solid surface and this forms an EDL. A detailed explanation of the EDL and the calculation of the Debye length can be found in section 3.2.3.2. The EDL can be treated as an

ideal, parallel plates capacitor with a capacitance C_{int} and impedance Z_C. Its changes can also reflect the biosensing process.

$$\begin{aligned} C_{int} &= \frac{\varepsilon_0 \varepsilon_r A}{d} \\ Z_C &= \frac{1}{j\omega C} = \frac{1}{\omega C} e^{-j\pi/2} \end{aligned} \tag{5.5}$$

where ε_0 is the permittivity of free space; ε_r is the relative dielectric constant of the electrolyte solution; A is the surface area of the WE; d is the Debye length. When a potential is applied between the bulk analyte and the solid surface, the ions will flow along the electric field. This indicates that the EDL can be represented by a resistor R_{int} in direct current (DC) mode.

Additionally, an abstract constant phase element (CPE) is used to describe a non-ideal capacitor for the EIS measurement. This CPE is defined by its exponent n (dimensionless) and factor Q (in $s^n\,\Omega^{-1}$) and can be expressed with [211]:

$$Z_{CPE} = \frac{1}{j\omega^n Q} \tag{5.6}$$

Only when $n = 1$, this element is equivalent to an ideal capacitor. The CPE is a non-linear element and cannot be found in standard electronics.

A Warburg diffusion element, a special case of the CPE, can also be used to model the diffusion current from the bulk buffer solution to the solid-liquid interface, when the interface capacitor C_{int} is not ideal. The Warburg impedance W can be expressed as [211]:

$$W = \frac{\sigma}{\sqrt{\omega}}(1 - j) \tag{5.7}$$

with

$$\sigma = \frac{1}{\sqrt{2}} \frac{RT}{n_e^2 A F^2} \left(\frac{1}{c_O \sqrt{D_O}} + \frac{1}{c_R \sqrt{D_R}} \right) \tag{5.8}$$

where ω is the frequency of the input AC voltage; T is the temperature; R and F are the gas and Faraday constants; c_O and c_R are the concentrations of oxidant and reductant in the bulk solution; D_O and D_R are the diffusion coefficient of oxidant and reductant, respectively; A is the surface area of the WE; n_e is the number of involved electrons. The Warburg impedance is normally used in the faradaic EIS. At high frequencies, the diffusion speed of reactants cannot follow the frequency of the AC signal, resulting in a small Warburg impedance. In contrast, at low frequencies, they can follow and it generates a high Warburg impedance value.

With these different elements, it is possible to build different electrical circuits to model the spectra recorded in EIS. The faradaic EIS measurements can be described by the equivalent circuit shown in figure 5.3(a) using the above-mentioned electronic elements: the electrolyte solution resistance R_{sol}, the charge transfer resistance R_{ct} between the redox markers and the WE, the EDL capacitance C_{int} which is generated at the solid-electrolyte interface, and the Warburg element W, which represents

the diffusion activity between the bulk electrolyte solution and the solid-electrolyte interface. However, the usage of a redox system may limit the repeatability of the EIS measurements. For instance, the typical K3/K4 redox markers release the CN^- ions which tend to etch the gold electrodes even in the optimized experimental condition [217]. The etching process increases the surface roughness and surface area, resulting in inaccurate EIS measurements. Therefore, the EIS measurement in faradaic mode is not suitable for long-term monitoring of consecutive surface modification.

The non-faradaic mode of the EIS measurements are carried out in the absence of redox markers, so that no faradaic current is generated. These measurements are only based on the principle of capacitive biosensing, using the EDL built on the electrodes. In this case, the WE and CE may be two arms of an IDEs. The binding of target biomolecules to the biosensor surface lead to changes in the dielectric parameters and the charge distribution, and this can be measured [218, 219]. The corresponding equivalent circuit is built with a combination of different electronic elements shown in figure 5.3(b). The exact choice of elements must reflect the physical phenomena taking place during the EIS measurements. This newly built circuit replaces the equivalent circuit in faradaic mode marked with the red dashed square in 5.3(a).

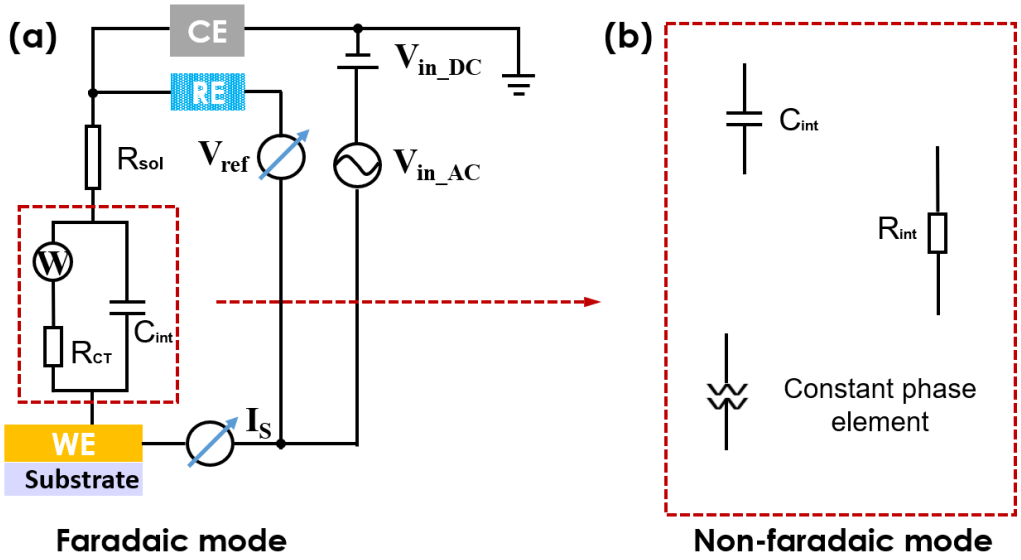

Figure 5.3: Equivalent circuits for EIS measurements: (a) Faradaic mode with redox markers. (b) Non-faradaic mode without redox markers. The equivalent circuits can be built by using a special combination of the shown electronic elements: a capacitor C_{int}, a resistor R_{int}, and/or a CPE.

For the faradaic mode, the typical equivalent circuit for the EIS measurements is given in figure 5.4(a). The corresponding Bode and Nyquist plots can be obtained when the parameters for the different electronic components are known. In the following, values were arbitrary chosen to compute typical Bode and Nyquist plots: solution resistance $R_1 = 20\,\Omega$, charge transfer resistance $R_2 = 250\,\Omega$, capacitance of the EDL $C = 40\,\mu F$ and the Warburg impedance $W = 150(1-j)\omega^{-1/2}$. The resulting plots are shown in figure 5.4(b)-(c). The 45° slope of the tail in the Nyquist plot (5.4(c)) is characteristic of the existence of a Warburg element in the equivalent circuit. For the non-faradaic mode, the equivalent circuit can be simplified as a resistor R and an EDL capacitor C in series as shown in figure 5.4(d). With a solution resistance $R = 20\,\Omega$ and an capacitance $C = 40\,\mu F$, the corresponding Bode and Nyquist plots are as

figure 5.4(e)-(f). In this case, the Nyquist plot is typically a straight line. When adding an EDL resistor $R_2 = 250\,\Omega$ in parallel to the EDL capacitor, as shown in figure 5.4(g), the Bode and Nyquist plots become as presented in figure 5.4(h)-(i). In this example, the Bode and Nyquist plots were drawn based on the values of the parameters. In the actual case, experimental data from EIS measurements are plotted and then the parameters are determined by fitting to equivalent circuits.

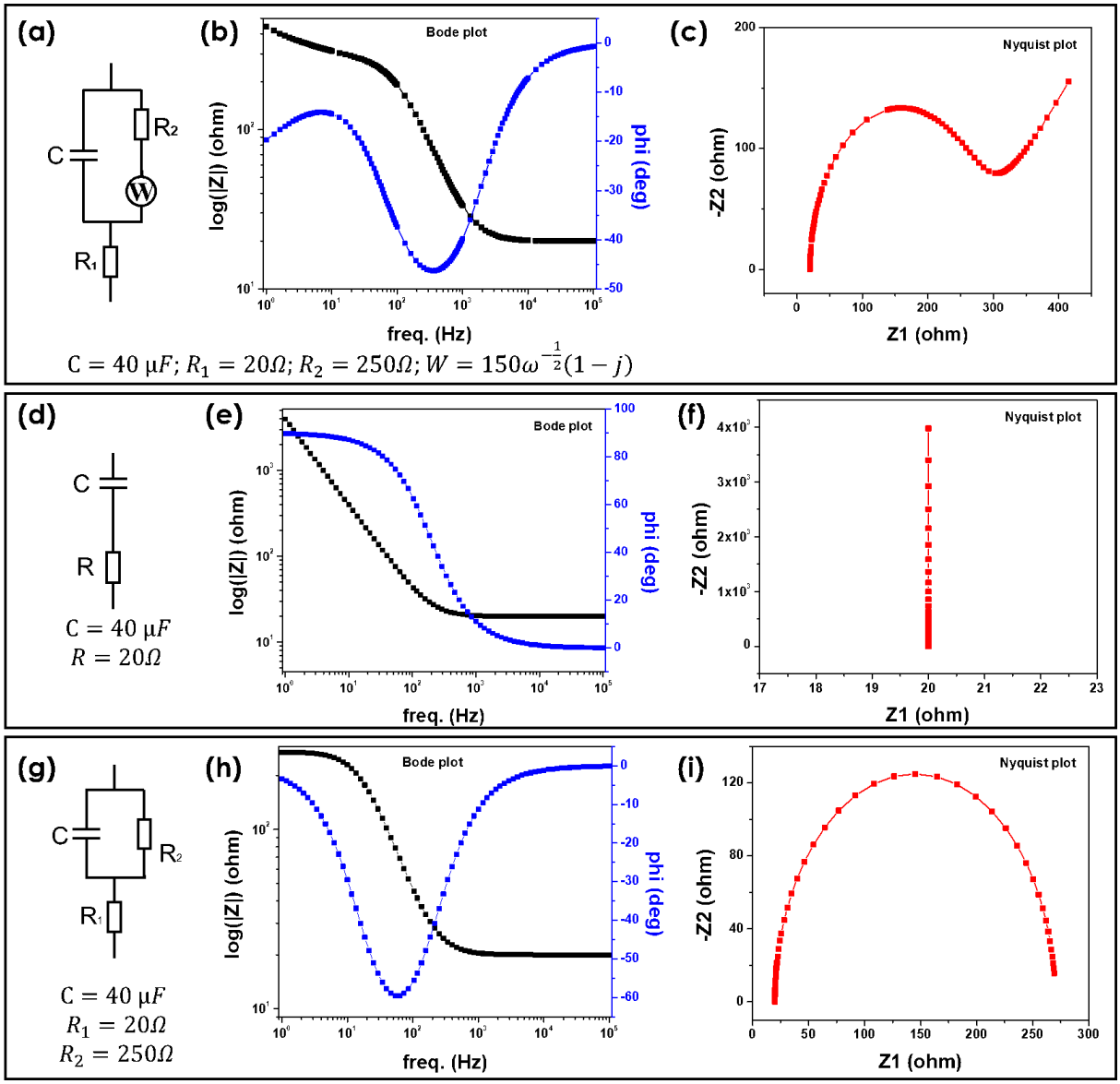

Figure 5.4: Typical Bode and Nyquist plots of the faradaic and non-faradaic EIS measurements. (a)-(c) Faradaic mode with redox markers, the values of the corresponding electronic elements are chosen arbitrarily: solution resistance $R_1 = 20\,\Omega$, charge transfer resistance $R_2 = 250\,\Omega$, EDL capacitance $C = 40\,\mu$F, Warburg impedance $W = 150(1-j)\omega^{-1/2}$. (d)-(f) Non-faradaic mode without redox markers. The electronic circuit contains a resistor $R = 20\,\Omega$ connecting with a capacitor $C = 250\,\Omega$ in series (arbitrary values). (g)-(i) Non-faradaic mode without redox markers. The electronic circuit is built up by adding an EDL resistor $R_2 = 250\,\Omega$ in parallel to the EDL capacitor in (d).

5.2 rGO Based EIS

The sensitivity of the faradaic and non-faradaic EIS based on bare electrodes for biosensing is often limited. To amplify the impedance signals and, hence, to increase the sensitivity, transducer layers can be deposited between the WE and CE. Such transducer layers can be, for example, a biomolecular or a polymer layer, a graphene or reduced graphene oxide thin film. Conventional EIS with rGO as transducer layer on macro-sized WE has been reported for biosensor applications to increase the sensing area [220, 221]. Besides, IDEs were used as capacitive biosensors with high sensitivity due to the locally confined electronic field [222–226]. In this section, a novel EIS device is presented by combining rGO thin films and IDEs structures. Its electronic performance was characterized with the non-faradaic mode (without redox markers) and the corresponding working mechanisms were investigated.

The GO thin films were prepared on top of IDEs on glass substrates and without being patterned by following the fabrication process described in chapter 2. The spin-coating times were eight and the obtained thickness of GO thin films was approximately 8 nm. The GO thin films were transformed into rGO thin films by the TRP presented in chapter 3. The device configuration is shown in figure 5.5. A fluidic setup was printed out by a 3D printer with a top and a bottom part. The top part had a container in the middle and a sealing rubber ring at its one side. The chip was clamped between these two parts, while the rGO array was exposed to the liquid [227]. All device characterizations, surface functionalizations and sensor measurements discussed in the following section were carried out in this fluidic cell.

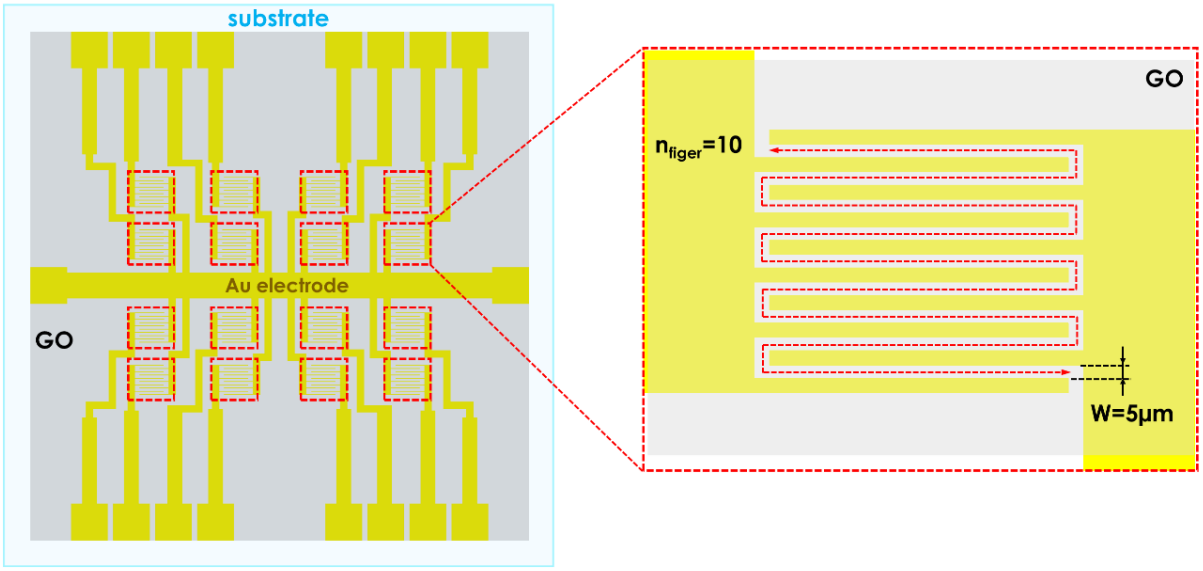

Figure 5.5: Device configuration for EIS measurements. GO thin films on top of 10-fingers IDEs to enhance the biosensing response in EIS.

The EIS measurements were carried out in two different configurations by connecting the electrodes to an impedance analyzer as shown in figure 5.6(a)-(b):

1. The drain electrode and the common-source electrode of the rGO-IDEs devices were connected to the WE, while an electrochemical Ag/AgCl electrode served as RE and a Pt wire as CE. This configuration is called out-of-line EIS (5.6(a)).

2. The drain electrode and the common source electrode were connected to the WE and the CE, respectively, while an electrochemical Ag/AgCl electrode served as RE. This configuration is called in-line EIS (5.6(b)).

The electronic performances of these two configurations in 10 mM PBS were compared under the following conditions: a DC offset potential and an AC signal were applied through the WE against a constant potential at the RE to CE, the standard potential of which is 230 mV in 3 M KCl at room temperature. The measurement started after 30 s to reach an equilibrium. The DC potential offset was 0.05 V while the AC input had an amplitude of 0.01 V and the frequency range was from 100 kHz to 0.1 Hz. The AC output $I_{out}(t)$ flowing from the WE to the CE was then measured.

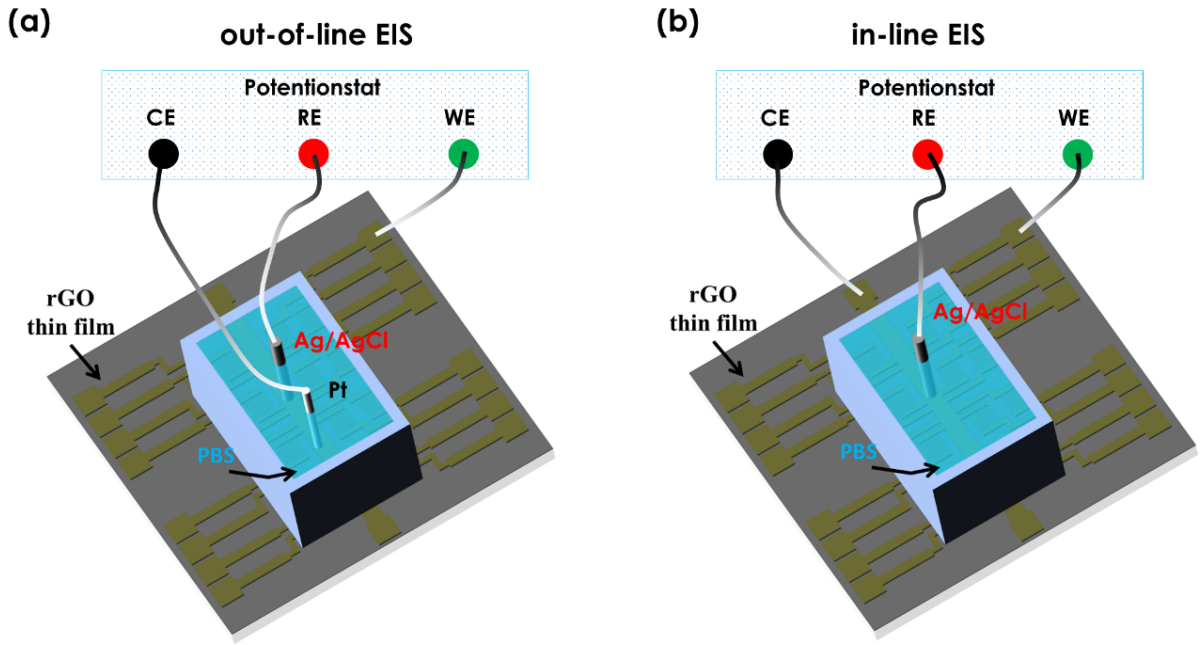

Figure 5.6: Electrode connections for the EIS measurements. (a) The out-of-line EIS configuration uses the drain IDEs arm as WE, a Pt wire as CE and an electrochemical Ag/AgCl electrode as RE. (b) The in-line EIS configuration uses the drain IDEs as WE, the source IDEs as CE and an electrochemical Ag/AgCl electrode as RE.

5.2.1 Out-of-Line rGO Based EIS

For the device configuration of the out-of-line EIS, the current travels from the WE through the EDL, modeled with a resistance R_{int} and a capacitance C_{int} in parallel at the solid-liquid interface. Then the current flows through the solution with a resistance R_{sol} to reach the CE. In the condition of a uniform EDL building on the WE, the equivalent circuit can be assumed as displayed in figure 5.4(g). However, the Bode and Nyquist plots of the rGO-IDEs devices in the out-of-line EIS configuration are shown in figure 5.7(a)-(b). Instead of a parabolic curve, the Nyquist plot appears as a straight line and its slope is not 45°. This result indicates that the combination of the EDL and the rGO thin film behaves neither as a pure capacitor nor as a Warburg element in the equivalent circuit.

An explanation could be that the more ions were accumulated around the oxygen functional groups than around the sp^2 C−C lattice. Therefore, the formed EDL was not uniformly distributed on the rGO surface, which is different from the typical EDL. Such behavior can be modeled with a more general CPE, and its two parameters Q and n, instead of a Warburg element. Therefore, an equivalent circuit was built up as represented in figure 5.7(c). The fitting was carried out with the software of Ivium COMPACTSTAT.e. Both Bode and Nyquist plots were fitted successfully by using this equivalent circuit within the 1 Hz to 10 kHz frequency range, which is the most interesting range for the later biosensing experiments. The corresponding values of the electronic elements are as follows: $R_{sol} = 2830\,\Omega$, $R_{int} = 2.685 \cdot 10^7\,\Omega$, $Q = 1.2 \cdot 10^{-6}$, $n = 0.7$. These parameters are also useful to describe the signal pass for the in-line EIS measurement as discussed in the following section.

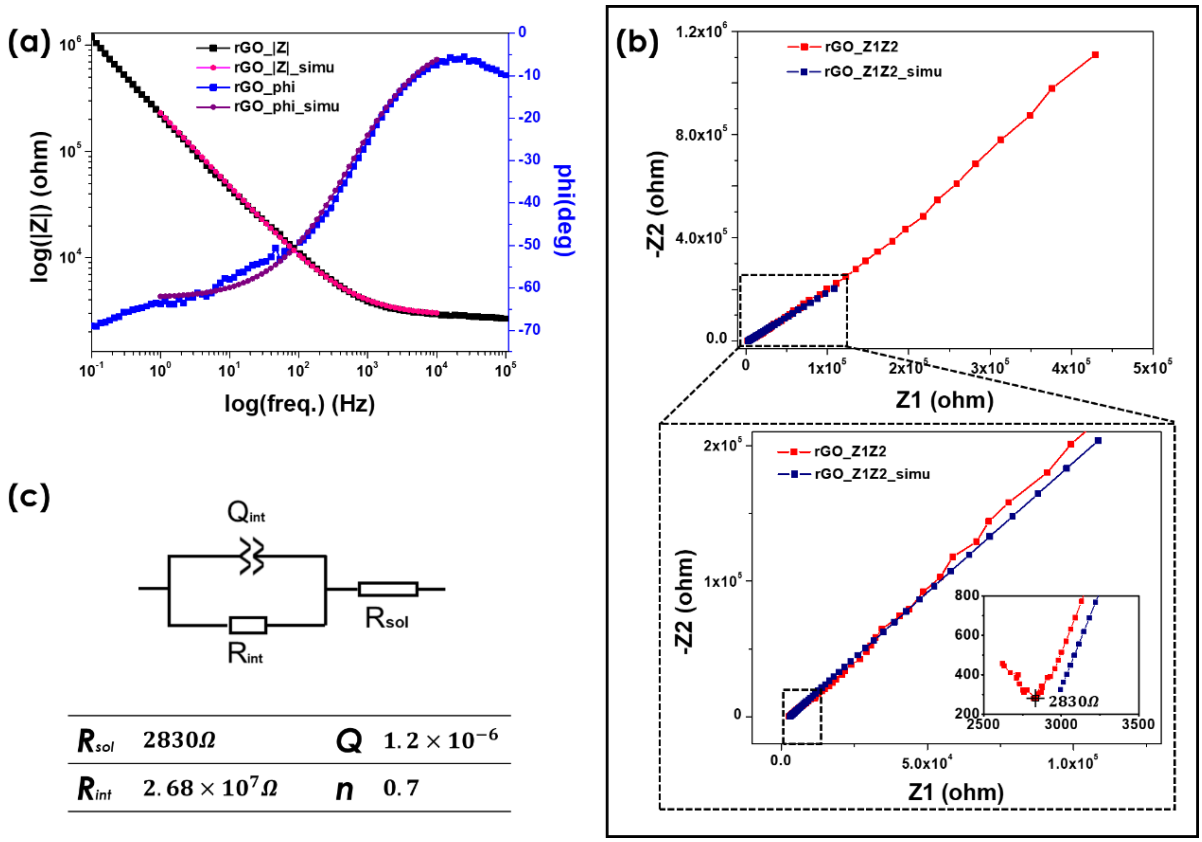

Figure 5.7: Out-of-line rGO based EIS measurement in PBS: (a)-(b) Nyquist and Bode plots, which were fitted by the equivalent circuit in the frequency range of 1 Hz to 10 kHz. (c) The equivalent circuits and the extracted values of the electronic elements.

5.2.2 In-Line rGO Based EIS

For the in-line EIS measurements, the stimulation signal travels from one IDEs arm to the other by passing through the buffer solution and the rGO thin film. To know the exact electronic elements of the rGO thin film, an I-V sweep in DC mode and capacitance-voltage (C-V) measurement in AC mode were carried out by a Keithley 4200-SCS parameter analyzer [228].

The exemplary I-V characteristic curve displayed in figure 5.8(a) shows that the rGO

thin film is in an ohmic contact instead of a Schottky contact with the IDEs structure. In DC mode, the rGO thin film acts as a resistor, whose conductivity comes from the charge carriers hopping along the restored carbon lattice. Afterwards, a C-V measurement in AC mode was carried out with the same rGO-IDEs channel.

For the AC mode measurement, the configuration is as shown in figure 5.8(b). Two signals, a small AC voltage (mV range) and a DC voltage, were simultaneously applied at the rGO thin film. The applied DC voltage allows sampling of the material at different depths in the rGO-IDEs device, while the AC voltage bias of small amplitude enables the capacitance measurement at a given depth in the device. The resulting current is measured and integrated over time to obtain the charges Q. Then, the capacitance is calculated by the quotient of the integrated charge and the applied voltage as follows:

$$C = \frac{\Delta Q}{\Delta V} \tag{5.9}$$

An AC signal with a fixed amplitude of 10 mV was applied at three different frequencies (1 kHz, 10 kHz and 100 kHz), while the DC voltage was swept from -1 V to 1 V. One exemplary result of a C-V measurement with the rGO-IDEs devices in dry status is shown in figure 5.8(c)-(d). For 1 kHz and 10 kHz, the noise was too high to properly read the capacitance value. At 100 kHz, the measured capacitance of the rGO thin film was approximately 4.2 pF.

Since the electronic biosensing experiments are performed in PBS, the rGO thin films were characterized after an overnight incubation in 10 mM PBS at room temperature. The incubation was done overnight in order to saturate and stabilize the rGO surface with ions from the buffer solution. The C-V measurements were done by applying an AC stimulation voltage with an amplitude of 10 mV at three different frequencies (1 kHz, 10 kHz and 100 kHz). The DC offset voltage was swept from -0.7 V to 0.7 V. The absolute value of the applied voltages need to be maintained below 0.7 V to avoid water electrolysis.

The measurements were carried out with an rGO-IDEs device in 10 mM PBS. The result obtained for the C-V characterization is shown figure 5.9(a). The average capacitance values were 44.38 ± 1.84 nF for 1 kHz, 10.79 ± 0.15 nF for 10 kHz, and 1.35 ± 0.02 nF for 100 kHz. The same rGO-IDEs channel was also characterized in 10 mM PBS by an I-V measurement with a dual sweep voltage, ranging from -0.7 V to 0.7 V. The obtained I-V curve, shown in figure 5.9(b) (green curve), passes through the origin point. However, the hysteresis behavior is typical for a capacitor with a charge/discharge happening over time. Additional experiments were conducted to further clarify the origin of the capacitor in or on the rGO thin films.

The same rGO-IDEs device was characterized in dry status after cleaning with DIW and drying with a N_2 flow. The experimental conditions of C-V and I-V measurements were the same as for the measurements in 10 mM PBS. The obtained C-V results are shown in figure 5.9(c)-(d). At the frequencies 10 kHz and 100 kHz, the capacitance of the rGO thin films was approximately 4-5 pF, which is in the same value range as for the rGO-IDEs devices before PBS incubation. The I-V characterization curve, shown in figure 5.9(b) (orange curve) is again linear. This means that the capacitor is caused by the ions on rGO thin films in the PBS and the non-capacitive behavior can be restored

by washing the device with DIW. The results obtained from the C-V characterizations prove that the signal path through rGO thin films in buffer solutions can be treated as a resistor R_{rGO} and a capacitor C_{rGO} in parallel in the EIS measurement. Such behavior could be attributed to the overlapping regions of the rGO flakes, which on the one hand enables the carrier transport but on the other hand also constrains its direction.

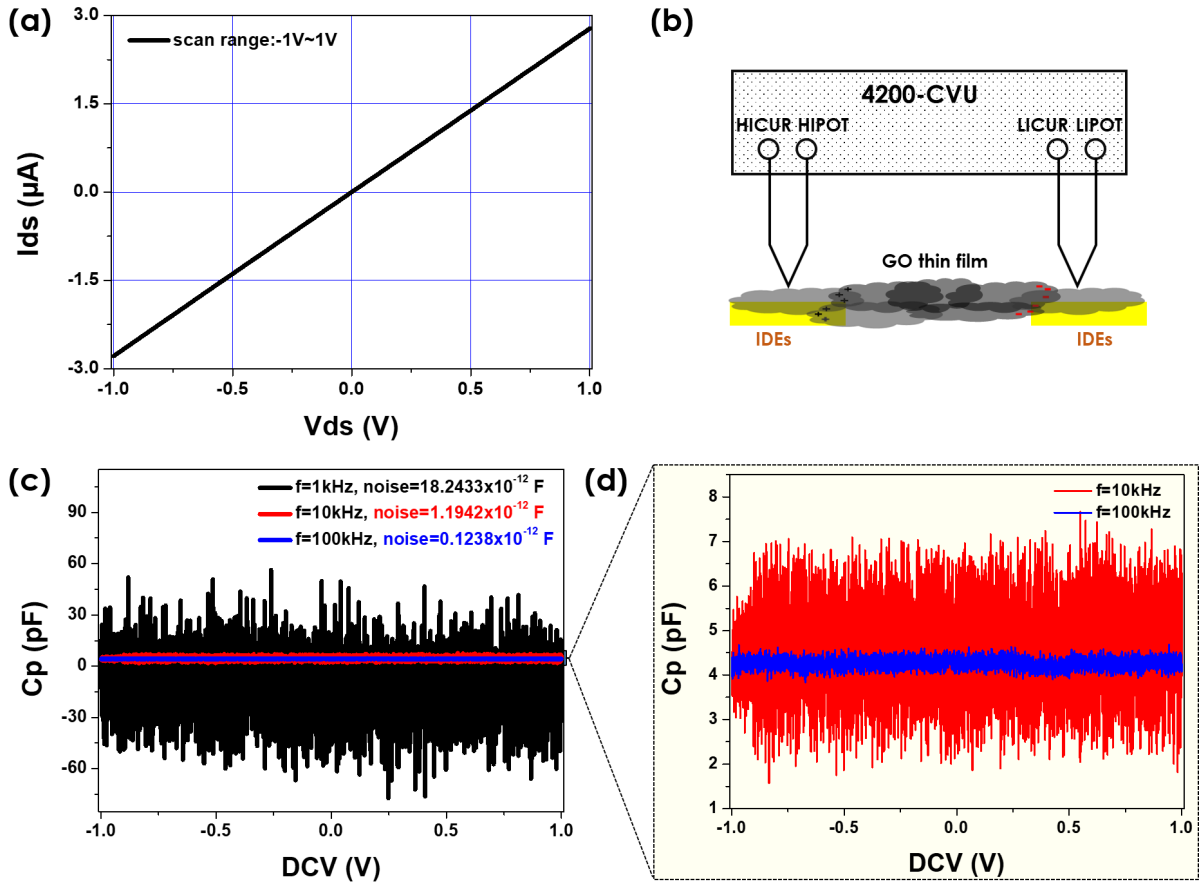

Figure 5.8: rGO thin films characterization in DC and AC mode achieved by I-V and C-V characterization in dry status. (a) The linear I-V characterization curve shows that the rGO thin films form an ohmic contact instead of a Schottky contact with the IDEs structures. (b) C-V measurement setup of rGO-IDEs devices in dry status. (c)-(d) The rGO-IDEs device shows a capacitive behavior at 100 kHz with a capacitance measured at 4.2 pF and a noise value of 0.1238 pF.

The focus of the previous discussion was on the modeling of the electronic elements of rGO thin films. With these elements determined, the in-line EIS measurements based on rGO-IDEs device were carried out. The WE and the CE were connected to the common source electrode and drain electrode of the rGO-IDEs device, respectively. The obtained Bode and Nyquist plots are shown in figure 5.10(a)-(b). The current flows through two distinct paths in parallel from WE to CE: path 1 is made of the two EDLs and the ohmic solution R_{sol} in series; path 2 consists only of the rGO thin film. As discussed for the out-of-line EIS, the EDL on the rGO surface is not an ideal capacitor. It can be represented by a CPE for both the WE and the CE. By including the resistance and the capacitance of the rGO thin films into the pre-developed circuits for bare IDEs [222], the equivalent circuit of rGO based in-line EIS can be extracted as presented in figure 5.10(c). Both Bode and Nyquist plots were fitted successfully by using this equivalent circuit for frequencies ranging from 1 Hz to 10 kHz. This is

the most interesting range for the biosensing processes and it is presented in the next section. The values of the same electronic elements were adapted from the out-of-line EIS fitting results. The corresponding values of additional electronic elements are: $R_{rGO} = 900\,\text{k}\Omega$, $C_{rGO} = 1.37\,\text{nF}$, $R_{int2} = 2.196 \cdot 10^7\,\Omega$, $Q_{int2} = 1.2 \cdot 10^{-6}$, $n_{int2} = 0.718$.

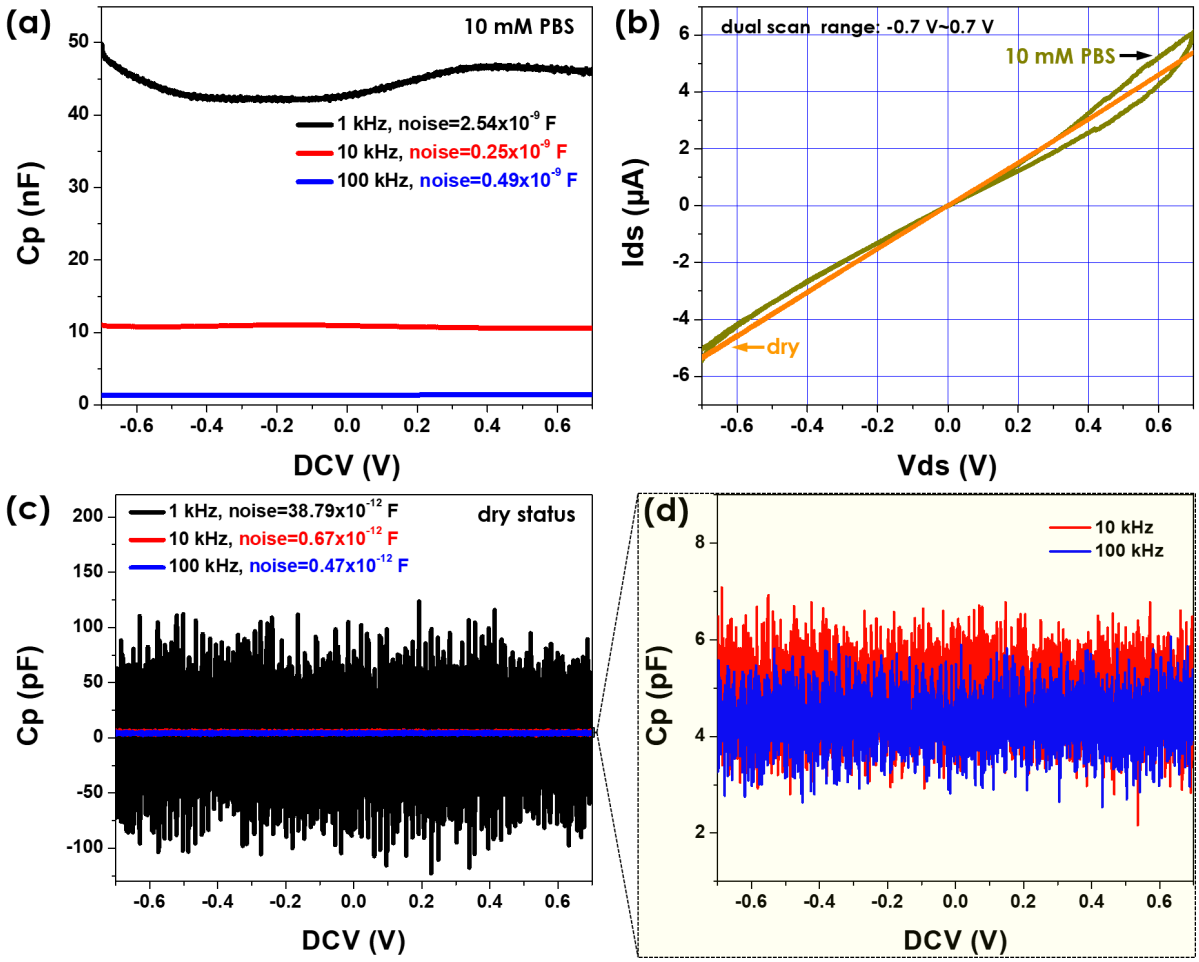

Figure 5.9: rGO thin films characterization by C-V and I-V measurements in PBS and in dry status. (a) C-V measurement after incubation overnight in 10 mM PBS. (b) I-V characterization was carried out with a dual sweep scanning from -0.7 V to 0.7 V. In 10 mM PBS, the I-V green curve shows a hysteresis behavior. In the dry status, the resistive behavior can be recovered. (c)-(d) C-V measurement in dry status, after cleaning by DIW and drying by N_2, the capacitance was similar to the value obtained before the 10 mM PBS overnight incubation.

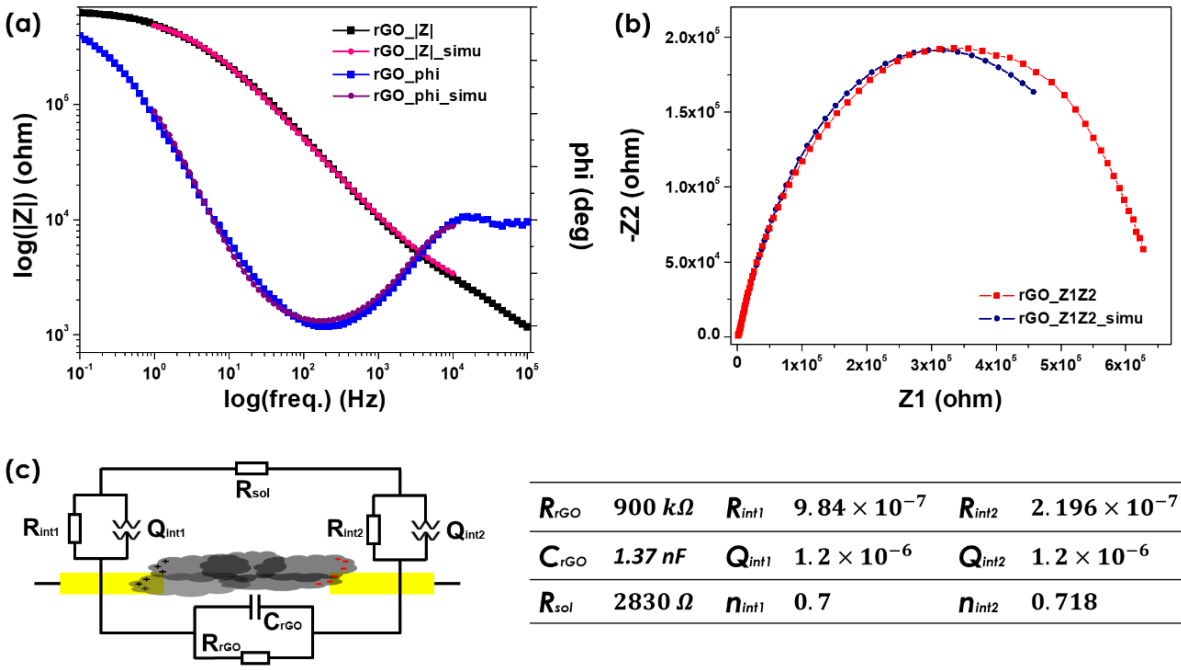

R_{rGO}	900 kΩ	R_{int1}	9.84×10^{-7}	R_{int2}	2.196×10^{-7}
C_{rGO}	1.37 nF	Q_{int1}	1.2×10^{-6}	Q_{int2}	1.2×10^{-6}
R_{sol}	2830 Ω	n_{int1}	0.7	n_{int2}	0.718

Figure 5.10: In-line rGO-IDEs based EIS measurement in PBS. (a)-(b) Nyquist and Bode plots can be fitted by the equivalent circuit in the frequency range of 1 Hz to 10 kHz. (c) The equivalent circuit and the computed values of the electronic elements.

5.3 rGO Based EIS for PSA Detection

After the electronic characterization, the rGO-IDEs devices were utilized in the in-line EIS configuration to detect the target biomolecule PSA. Two different impedimetric biosensor platforms were established, one with PSA-specific aptamers and the other with PSA-specific antibodies as receptor biomolecules. The PSA biosensing experiments were carried out in different buffer concentrations to compare the influence of different ionic strengths and the associated Debye lengths. In this section, the corresponding working mechanism is discussed in detail. The focus is set on the biosensing capability beyond the Debye-screening length in physiological buffer solution (ionic strength around 150 mM) towards the vision of future device commercialization.

5.3.1 rGO Based Biosensors Preparation

In the framework of this thesis, two types of receptor biomolecules, a PSA-specific DNA aptamer and PSA-specific antibody, were chosen to detect PSA. An aptamer usually consists of short oligonucleotide strands [229, 230]. It is of a small size, highly stable and cost-effective. The structure of aptamers is typically folded as a hairpin loop, because two complementary regions of the strand form local Watson-Crick base pairs. Such a structure provides a high affinity to bind specific target molecules like small organic compounds, proteins, or cells. In recent years, aptamers have been widely employed in the field of biosensing [231, 232] and also for PSA detection [233, 234]. In this study, the aptamer sequence was TTT TTA ATT AAA GCT CGC CAT CAA ATA GCT TT (5′ to 3′ direction). The 5′ end was modified by a 6-carbon

chain as a spacer and terminated with an amino group to enable a covalent binding to the sensor surface. The aptamer size is approximately 3-5 nm [235]. An antibody is a Y-shaped protein which recognizes a unique antigen [236, 237]. The size of an antibody is approximately 10 nm [238]. The PSA-specific antibody has also been popularly used in biosensor platforms for PSA detection [33].

The different steps of the bio-functionalization process to prepare the rGO-IDEs based biosensors are shown in figure 5.11. In all steps, a 10 mM PBS solution with pH 7.4 was used. The detailed biosensor preparation protocol was as follows:

i) The amino-terminated aptamers, not the antibodies, were treated as following to gain an optimum position to capture the PSA. This treatment started by taking the microcentrifuge tube, which contained 10 µl of 100 µM amino-terminated aptamer, out of the freezer. The tube stood at the room temperature for approximately 10 min until thawed. Fast spinning was applied for 5 s to centrifuge down the residual droplets from the sidewall. Then the microcentrifuge tube was immersed up to its half height into a flask containing milliQ water at 90 °C. When the temperature reached the room temperature naturally, the microcentrifuge tube was taken out and centrifuged for 5 s. Then the solution of 100 µM amino-terminated aptamer was diluted with 10 mM PBS to a final concentration of 2 µM.

ii) The rGO chips were incubated in 10 mM PBS overnight to stabilize the surface at room temperature. 80 mM EDC mixed with 20 mM NHS in milliQ water was used to activate the $-$COOH groups on the rGO surface and to ensure a robust immobilization of the receptor biomolecules [239]: amino-terminated aptamers and antibodies. 100 µl of EDC/NHS solution was applied onto the rGO surface for 30 min at room temperature.

iii) Immediately after the EDC/NHS activation, the chips were incubated in the solution of 2 µM receptor molecules overnight at 4 °C. Afterwards, the chips were cleaned 10 times by pipetting 100 µl of 10 mM PBS.

iv) For the aptamers case, 1 mM ethanolamine was prepared by diluting 10 mM ethanolamine ($pH = 8.5$) in 10 mM PBS and then applied on the rGO thin film for 30 min. For the antibodies case, 10 mM ethanolamine ($pH = 8.5$) was applied onto the rGO thin film for 1 h. This step was to saturate the freestanding $-$COOH groups on the rGO surface and to avoid the non-specific binding of target biomolecules.

v) The concentrations of PSA were prepared by diluting 100 µM stock solution in 10 mM PBS, with final concentrations of 33 fM, 330 fM, 3.3 pM, 33 pM, 330 pM, 3.3 nM, 33 nM and 330 nM in order to perform concentration-response measurements.

It must be noted that the 10 mM PBS ($pH = 7.4$) buffer solution should be the same for the overnight incubation of the devices and for the dilution of ethanolamine and PSA. This prevents the rearrangement of the ionic layer built on the rGO due to the difference in PBS. Otherwise, non-specific signals could be induced.

The concentration-response measurements started from the lowest concentration of PSA towards the highest concentration. The incubation of PSA for each concentration was done for 30 min at room temperature. After each incubation, the chips were cleaned 10 times with 10 mM PBS ($pH = 7.4$) by pipetting. It was then measured in the in-line EIS configuration by an Ivium COMPACTSTAT.e impedance analyzer. The biosensing mechanism of rGO-IDEs based in-line EIS biosensors for PSA detection is intensively studied in the following sections.

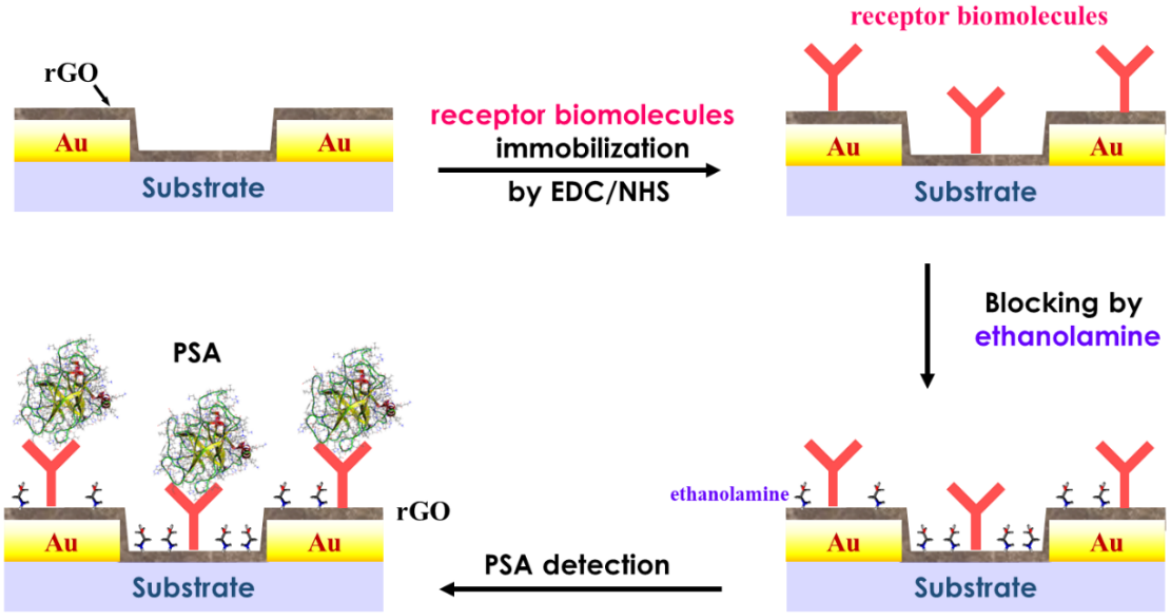

Figure 5.11: Preparation schematic for the rGO-IDEs based biosensors (clockwise). The $-$COOH groups on the rGO surface were activated by EDC/NHS chemistry, so that the amino-terminated receptor biomolecules can be immobilized. Afterwards, the free-standing $-$COOH groups were saturated by ethanolamine to avoid non-specific binding. The target biomolecule PSA was added and detected in the last step.

5.3.2 Aptamers as Receptor Molecules for PSA Detection

In this section, the PSA recognition process at the surface of rGO-IDEs based biosensor with PSA-specific aptamers as receptor biomolecules is discussed. The measurement setup was the in-line EIS configuration, as shown in 5.12(a). The two arms of the IDEs structures served as WE and CE, while an electrochemical Ag/AgCl electrode acted as RE. An AC signal of amplitude 10 mV, a frequency ranging from 1 Hz to 100 kHz and a DC bias voltage of 50 mV were applied through WE against the RE to the CE. PSA concentration-response experiments were carried out in 10 mM PBS ($pH = 7.4$). The resulting salt concentration (ionic strength) was 162 mM and the corresponding Debye length of EDL was approximately 0.76 nm. Both values are similar to that of physiological solutions. A detailed explanation of the EDL and the Debye length can be found in section 3.2.3.2. The Debye length and salt concentration (ionic strength) at room temperature for different PBS concentrations were calculated using the equations 3.2 and 3.3, as shown in the table 5.1. The target molecule PSA had a mass of 33 kDa and its corresponding size was approximately 4.5 nm, implying that the PSA biomolecules were located out of the Debye length of the EDL. The schematic

in figure 5.12(b) shows the principle of the PSA detection with aptamers as receptor biomolecules on a rGO thin film including the corresponding Debye length.

Table 5.1: PBS concentration, dilution, ionic strength, and Debye length

PBS concentration [mM] $pH = 7.4$	**PBS dilution**	**Salt concentration (ionic strength)** [mM]	**Debye length** [nm]
10	$1 \cdot PBS$	162	0.76
1	$0.1 \cdot PBS$	16.2	2.41
0.1	$0.01 \cdot PBS$	1.62	7.6
0.01	$0.001 \cdot PBS$	0.162	24.1

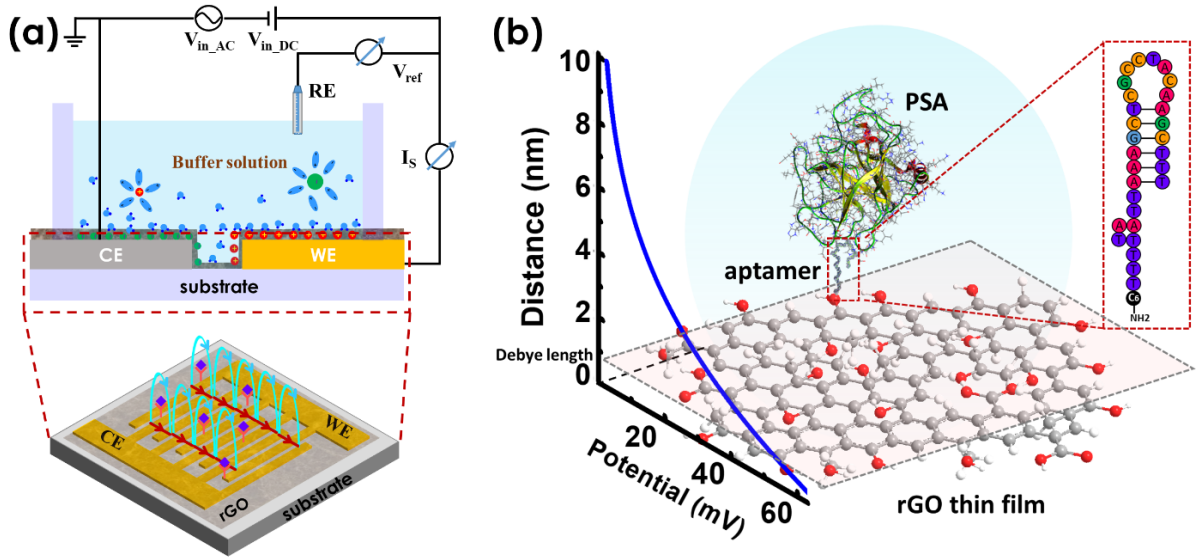

Figure 5.12: (a) Schematics of an rGO thin film in EIS configuration, where the two arms of the IDE structures and an electrochemical Ag/AgCl electrode served as WE, CE and RE. (b) Descriptive schematic of rGO based biosensor with aptamers as receptor biomolecules for PSA in 10 mM PBS. The corresponding Debye length was 0.76 nm. The diameters of the aptamers and PSA were 3-5 nm and approximately 10 nm. In theory, both biomolecules should be located outside of the Debye length.

The baselines of biosensors should be measured to prove the device stability before the PSA concentration-response experiments. For this purpose, the channels of rGO-IDEs based biosensors were measured in 10 mM PBS ($pH = 7.4$) 1 time after switching the connection cables of the measurement setup and 3 times after changing the PBS solution. The baselines of biosensors were statistically obtained according to these 4 measurements. Afterwards, the PSA concentrations 33 fM, 330 fM, 3.3 pM, 33 pM, 330 pM, 3.3 nM, 33 nM and 330 nM were sequentially measured. The PSA concentration-response curves of an exemplary channel obtained using the in-line EIS configuration are shown in figure 5.13(a)-(b). The results show that the output impedance sensitively varied with the PSA concentration at the frequencies of 1-10 Hz and 1 kHz, compared to the baseline (black curve). The close-up of the real and imaginary parts of the output impedance around 1-10 Hz is given in figure 5.13(c)-(d). At low frequencies, the resistive path through the rGO thin film mainly contributes to the output impedance signal. As indicated by the experimental results, the real part of the impedance increased with an increase of the PSA concentration. The amplitude and phase of the output impedance at 1 kHz, figure 5.13(e)-(f), indicate

that the phase is decreasing with increasing PSA concentration, while the amplitude shows no clear tendency of PSA biosensing. In this case, the capacitive path from one IDEs arm to another through the buffer solution plays a dominant role for the output impedance signal. In contrast to the conventional IDEs based capacitive biosensor [226], the capacitive path of rGO-IDEs sensor is measuring the biomolecular layer between the CE and the WE. The capacitive detection of PSA with rGO-IDEs seems to be more pronounced at a frequency of 1 kHz.

To confirm the biosensing mechanism of rGO-IDEs based in-line EIS devices in low frequency regime, the PSA concentration-response experiments were also carried out by performing an I-V dual characterization, which can be considered as an ESFET measurement with a zero gate voltage. The sweeping voltage was applied between the two arms of IDEs from -0.8 V to 0.8 V. The results are shown in figure 5.14(a). It can be seen that the binding of PSA leads to a resistance increase in the rGO thin film. This result is in agreement with the biosensing tendency of PSA concentration-response curves obtained using the in-line EIS device configuration. This is explained considering that the isoelectric point of PSA is 6.9-7.2 [240], so PSA is negatively charged in 10 mM PBS with a pH 7.4. The attachment of PSA onto the rGO thin films is equivalent to an additional negative voltage. The modulation effect of the negative voltage to the rGO thin films can be explained in the ESFET configuration, in which rGO thin films serve as transducers, as shown in figure 5.14(b). The corresponding bipolar characteristic curves are given in figure 5.14(c). The ESFET measurements were performed as follows: the sweeping voltages were applied to the gate electrode against the source electrode and ranged from -0.8 V to 0.8 V, while the step voltages were applied between the drain and source electrodes ranging from -0.1 V to 0.1 V with a step size of 0.1 V. The Dirac points in the bipolar curves were shifted to the left compared to the axis $V_{gs} = 0$, therefore the rGO thin films were initially n-doped. The negative voltage, that is caused by the PSA attachment, tended to modify the Fermi level and carrier concentrations within the rGO thin film. During the biosensing, the voltage applied by the gate electrode on the rGO thin film was zero. The negatively charged PSA biomolecules were equivalent to a negative voltage applied on the rGO thin film. As indicated in figure 5.14(b), the drain-source current I_{ds} decreased while a negative gate voltage V_{gs} was applied, and the drain source voltage V_{ds} maintained constant. Therefore, an increase of PSA molecules led to a larger negative gate voltage, which induced a decrease of the conductivity and an increase of the resistance.

In the application field of biosensors, the concentration of an unknown sample is extracted by comparing to a calibration curve which is obtained from concentration-response experiments. The calibration curves of the rGO based biosensors were generated for the amplitude of the impedance at 1 Hz and the phase of the impedance at 1 kHz from the PSA concentration-response experiments with 5 channels. The corresponding results are displayed in figure 5.15(a)-(b). For the amplitude calibration curve, the LOD the rGO-IDEs biosensor was 33 pM, while it was 33 fM for the phase calibration curve. The clinically relevant PSA concentration range of 4-10 ng ml^{-1}, which corresponds to a concentration range of 115-290 pM, is completely covered by the linear response regime of these two calibration curves. Besides, the results also indicate that it is possible to detect even lower concentrations with the presented biosensor. This makes the platform also interesting and promising

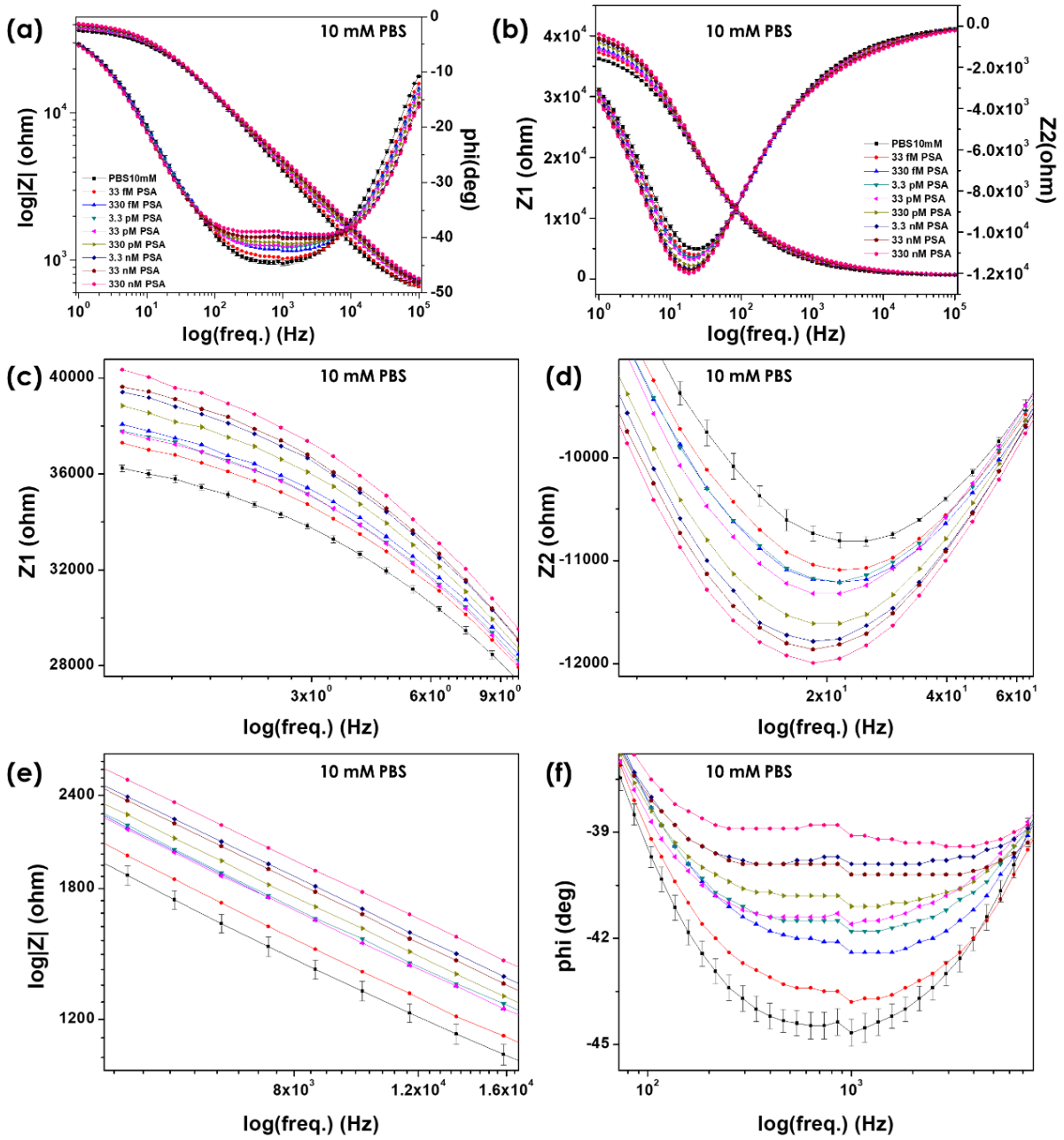

Figure 5.13: PSA concentration-response experiments with aptamers as receptor molecules, using rGO thin film based in-line EIS configuration. The measurements were carried out in 10 mM PBS. An input AC signal of 10 mV amplitude in a frequency range of 1 Hz to 100 kHz and a DC offset of 50 mV were applied. Before PSA detection, the baseline (black curve) of the biosensors was obtained by measuring the devices 4 times in 10 mM PBS ($pH = 7.4$) (1 time after switching the connection cables of the measurement setup and 3 times after changing the 10 mM PBS solution). (a)-(b) Plots of amplitude, phase, real part and imaginary part of the output impedance from PSA concentration-response experiments. (c)-(d) Real part and imaginary part of the output impedance for 1-10 Hz. (e)-(f) Amplitude and phase of the output signal impedance around 1 kHz.

for applications to detect smaller concentration of target molecules.

Additionally, non-specific control experiments were carried out to detect 1 µM human serum albumin (HSA) instead of PSA. 1 µM HSA was prepared by diluting the 100 µM stock solution in 10 mM PBS ($pH = 7.4$). The 100 µM HSA was beforehand filtered by a filter with pore size 0.2 µm. The sensor surface was prepared as described for the

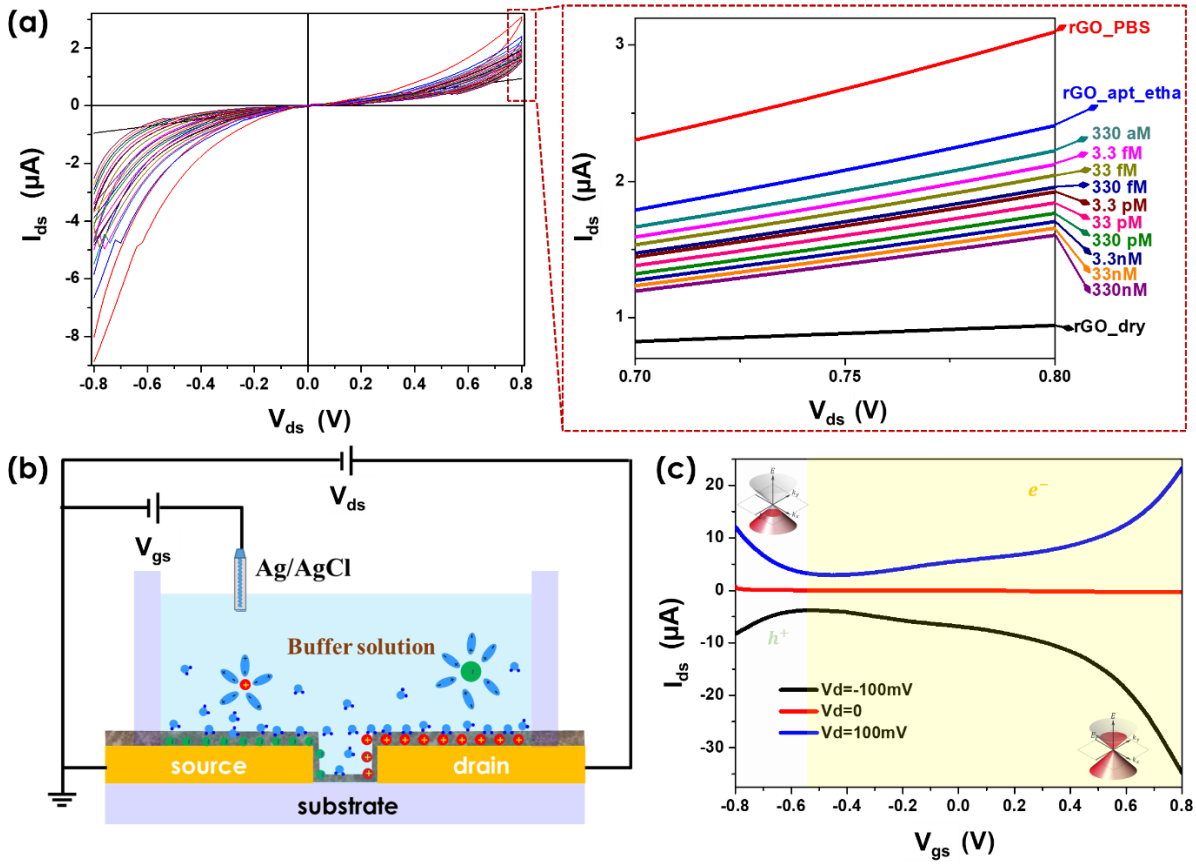

Figure 5.14: (a) PSA concentration-response measurements by I-V dual sweep. A sweeping voltage from −0.8 V to 0.8 V was used as bias between source and drain electrodes. (b) Schematic of the ESFET based on rGO thin film IDEs device. (c) Electronic characterization of the rGO thin film IDEs biosensor platform: bipolar characteristic curves of ESFET with rGO thin film as transducer layer in 10 mM PBS.

aptamer immobilization. Then the sensor was incubated with 1 µM HSA for 30 min at room temperature. The baseline was determined as reported before. After the HSA incubation, 3 channels were measured 2 times to obtain the non-specific control signal. As one can see in figure 5.15, the incubation with 1 µM HSA led to no significant signal change, which means that only the PSA is selectively bound to the aptamers.

To prove that the resistive path at 1 Hz is caused by the tuning effect of the Fermi level of the rGO thin film, a higher PBS concentration of 200 mM was chosen to carry out the PSA concentration-response experiments. The corresponding Debye length in this case is only 0.17 nm. The experimental condition for the in-line EIS measurements was the same as for the previous experiments in 10 mM PBS. The baseline of rGO-IDEs based biosensors was statistically obtained by measuring the channels in 200 mM PBS ($pH = 7.4$) 1 time after switching the connection cables of the measurement setup and 3 times after changing the PBS solution. The rGO-IDEs device incubation, aptamer immobilization and ethanolamine blocking process were all carried out in 200 mM PBS. Because of solubility issues, the PSA concentrations were measured only from 33 fM to 3.3 nM. The obtained plots of the amplitude, phase, real part and imaginary part of the output impedance are shown in figure 5.16(a)-(b). The results indicate that there was no response in the amplitude, real and imaginary parts of the output impedance for the low frequency range from 1-10 Hz. The resistive path through the rGO thin film was screened out due to the Debye length of only 0.17 nm. This means

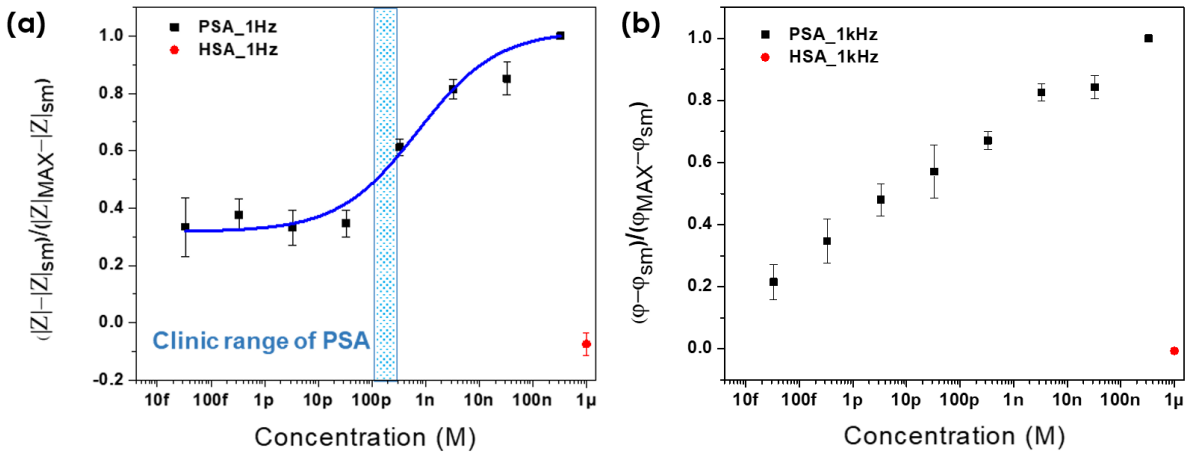

Figure 5.15: (a)-(b) Amplitude and phase calibration curve of PSA concentration-response experiments by rGO based in-line EIS with aptamers as receptor molecules in physiological 10 mM PBS (channel number $n = 5$). In red, the non-specific binding of 1 µM HSA is shown as a control.

that the surface potential of the rGO thin film is completely compensated by the ions from buffer solution. The PSA molecules were located farther than the Debye length of the EDL and their charge were not able to induce an effective voltage to the rGO thin film. Therefore, there is no change in the channel resistance. In contrast, the impedance amplitude and phase around 1 kHz, shown in figure 5.16(c)-(d), is changed after binding of the analyte, which indicates the PSA sensing capability. This means that the capacitive path from one IDEs arms to the other seems to be modulated by the attached PSA charges in such a high buffer concentration. It could be that the capacitive biosensing of PSA took place within the electric field depth, which equaled to the finger separation distance of the IDEs 5 µm.

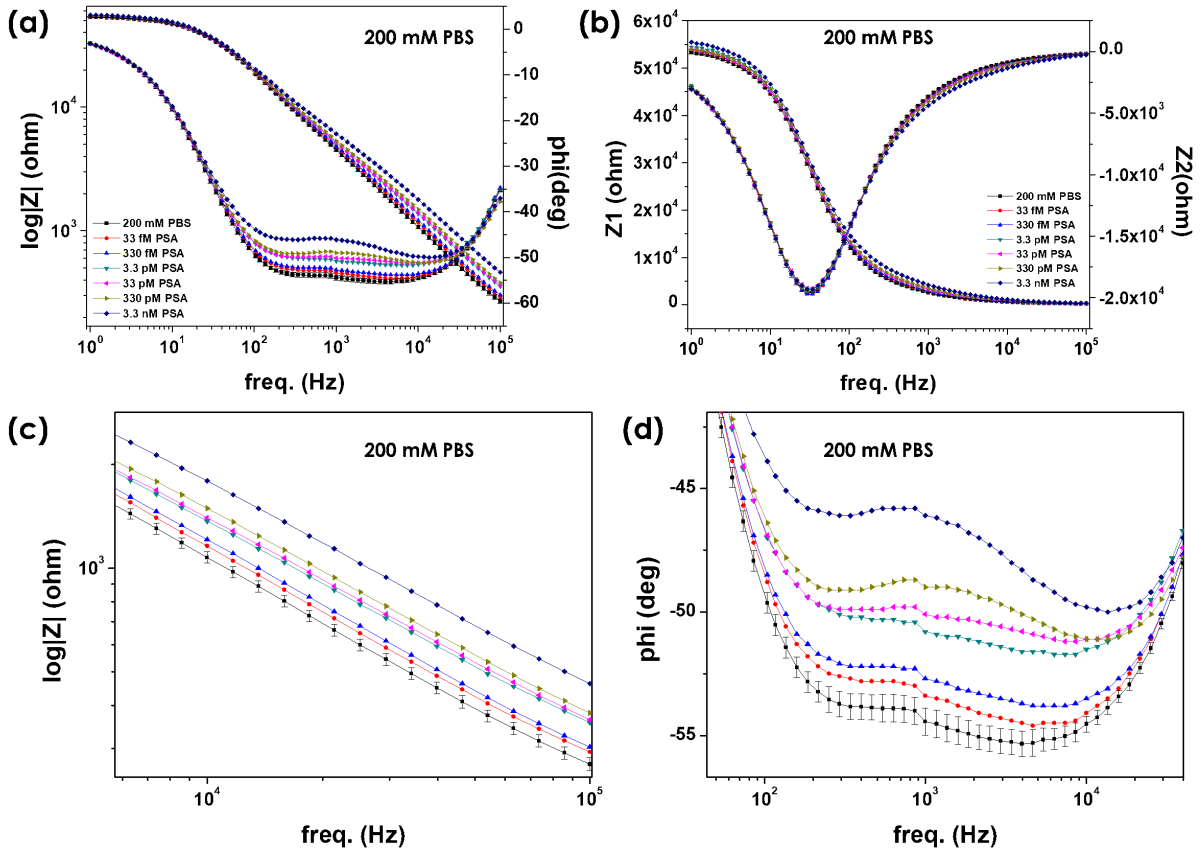

Figure 5.16: PSA concentration-response experiments with aptamers as receptor molecules, using rGO thin film based in-line EIS configuration. The measurements were carried out in a high ionic strength solution of 200 mM PBS. An input AC signal of 10 mV amplitude in a frequency range from 1 Hz to 100 kHz and a DC offset of 50 mV were applied. Before PSA detection, the baseline of rGO-IDEs based biosensors was statistically obtained by measuring the channels in 200 mM PBS ($pH = 7.4$) 1 time after switching the connection cables of the measurement setup and 3 times after changing the PBS solution. (a)-(b) Plots of amplitude, phase, real part and imaginary part of the output impedance from the PSA concentration-response experiments. (c)-(d) Amplitude and phase of the output impedance around 1 kHz.

5.3.3 Antibodies as Receptor Molecules for PSA Detection

In this section, antibodies instead of aptamers were used as receptor biomolecules to detect PSA. The biosensors were prepared by following the process introduced in section 5.3.1. The aim of these experiments was to reveal if the capacitive sensing is positively influenced by the rGO transducer layer compared to the sole effect of bare IDEs structures. The descriptive schematic of an antibody-based biosensor is shown in figure 5.17.

The experimental procedure for the rGO-IDEs based in-line EIS measurements and the baseline determination of PSA concentration-response experiments were the same as in the case with aptamers as receptor biomolecules in 10 mM PBS ($pH = 7.4$). The obtained plots of amplitude, phase, real part and imaginary part of the output impedance from the PSA concentration-response experiments in 10 mM PBS ($pH = 7.4$) are shown in figure 5.18(a)-(b). The corresponding Debye length is 0.76 nm. The Bode plot indicates that the capacitive sensing effect around 1 kHz was completely screened out. The diameter of the antibodies (10 nm) is bigger than that of the

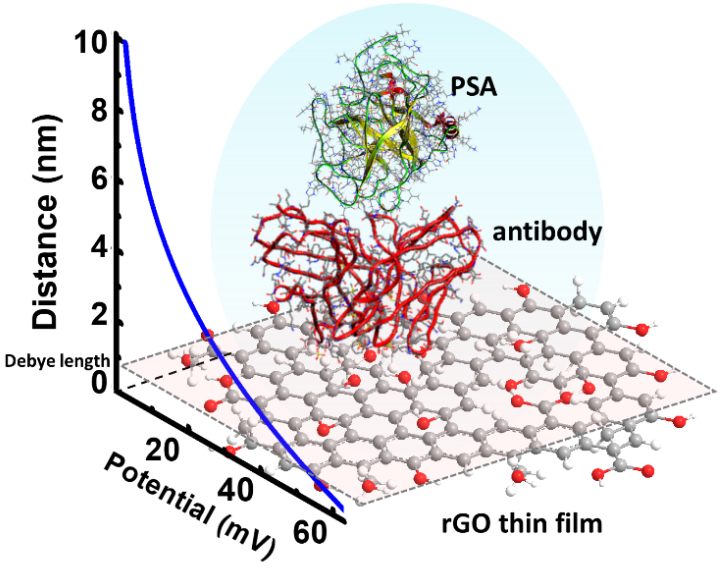

Figure 5.17: Descriptive schematic of an rGO-based biosensor with antibodies as receptor biomolecules in 10 mM PBS. The corresponding Debye length is indicated by the dashed plane.

aptamers (3-5 nm). Eventually, in the case of antibodies, the PSA biomolecules were located out of the vertical range of the effective electrical field, which is created between the rGO covered IDEs arms. Therefore, the capacitance change might not be sensible and cannot be used for the measurements. These results demonstrated that the depth of the electric field induced by IDEs and rGO thin films should be less than 10 nm, which was much smaller than that of the bare IDEs. However, the biosensors still responded to the PSA attachment in the low frequency range from 1-10 Hz, as shown in figure 5.18(c)-(d). The real part of the output impedance increased with the increasing PSA concentration. This result indicates that the resistive path through the rGO thin films is responsible for sensing the PSA, even with a Debye length of 0.76 nm.

In summary, the rGO-IDEs based in-line EIS biosensor is capable to detect PSA in 10 mM and even in very high ionic strength buffer 200 mM PBS with a similar or even higher Debye length as typical physiological solutions. The presented results concretely confirm that the established biosensor device with aptamers or antibodies overcomes the Debye-screening effect, which is the major challenge for charge based label-free biosensing towards clinical applications.

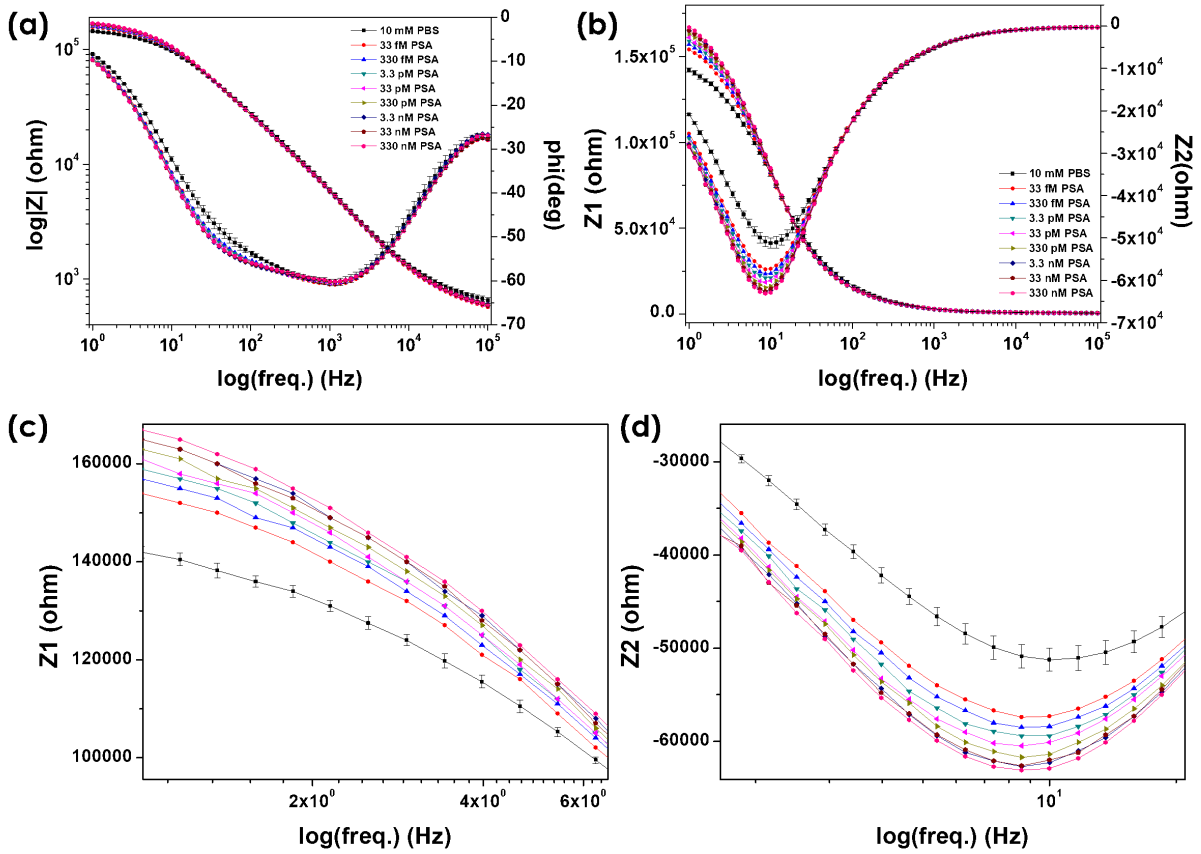

Figure 5.18: PSA concentration-response experiments with antibodies as receptor molecules, using rGO thin film based in-line EIS configuration. The measurement was carried out in physiological 10 mM PBS. An input AC signal of 10 mV amplitude in a frequency range from 1 Hz to 100 kHz with a DC offset of 50 mV was applied. Before PSA detection, the baseline of rGO-IDEs based biosensors was statistically obtained by measuring the channels in 10 mM PBS ($pH = 7.4$) 1 time after switching the connection cables of the measurement setup and 3 times after changing the PBS solution. (a)-(b) Plots of amplitude, phase, real part and imaginary part of the output impedance from the PSA concentration-response experiments. (c)-(d) Real and imaginary parts of the output impedance at low frequencies from 1 Hz to 10 Hz.

5.4 Conclusion

In this chapter, the equivalent circuits for rGO-IDEs based out-of-line and in-line EIS were established. The results imply that the interface of the rGO thin film and the electrolyte solution can be represented by a resistor connected to a CPE in parallel, instead of a perfect capacitor.

The biosensing mechanisms with rGO as transducer layer on IDEs were investigated by using PSA-specific aptamers (length 3-5 nm) and antibodies (diameter 10 nm) as receptor biomolecules to detect PSA (diameter 4.5 nm) target biomolecules in PBS of different ionic strengths and, hence, different Debye lengths. In the case of aptamers as receptor biomolecules, the sensing in 10 mM PBS was visible in the impedance amplitude and phase in Bode plots. At around 1 Hz, an increase of the impedance amplitude was observed with PSA concentrations from 33 pM to 330 nM. At around 1 kHz, a decrease of the impedance phase was observed for PSA ranging from 33 fM to 330 nM. Such biosensors with the aptamers as receptor molecules can directly detect PSA target molecules in their clinical concentration range in 10 mM PBS,

where the ionic strength (162 mM) and Debye length (0.76 nm) are similar to the values of physiological buffer solution (150 mM and 0.78 nm). Even in rather high concentrations of 200 mM PBS, the impedance phase still displays sensing capability at 1 kHz. Also, the biosensors with antibodies as receptor biomolecules in 10 mM PBS still displayed biosensing capability.

These results demonstrate that both resistive and capacitive mechanisms are most likely responsible for the biosensing in different frequency regimes. It could be attributed to the sp^2 hybridized carbon lattice of rGO thin films, because the electrochemical functionalization of graphene was proven to change the surface charge and result in capacitance and resistance changes [241]. The sensing performance was not influenced by the so-called Debye-screening effect, which is the major challenge that conventional charge-based label-free biosensing devices are facing towards their clinical implementation. The rGO-IDEs based biosensors developed in this thesis concretely demonstrated their biosensing capability beyond the Debye-screening effect. Therefore, they have a great potential to directly analyze real clinic samples, with no need of sample pretreatment.

6 rGO Based ESFET

In this chapter, ESFET biosensors based on rGO thin films for label-free detection of PSA are presented and discussed. Firstly, the state-of-the-art of ESFETs for biosensing is introduced. The characteristics of the ESFETs with rGO thin films as transducers are discussed. Secondly, Au nanoparticles (NPs) were immobilized onto the surface of the rGO thin films in order to immobilize thiol-terminated aptamers. The biosensing performance of ESFET aptasensors for PSA detection is presented and analyzed in detail. Thirdly, Cu NPs were grown on the rGO thin films by a chronoamperometry technique. The modulation effect of Cu NPs on the electronic characteristics of rGO thin films is investigated.

6.1 rGO Based ESFET

The principle of the ESFETs biosensor is utilizing FETs to detect biomolecules in a buffer solution. The transducing channel of the FETs, used to detect ions or biomolecules, can be doped Si [242], GaN [243], poly polystyrene sulfonate (PEDOT:PSS polymer) [244] and other semiconducting materials. Since the discovery of graphene in 2004, graphene-based materials drew tremendous attention and have been extensively investigated as transducer layers in ESFETs for biosensing [245–251].

In this section, the GO thin films were prepared using GO aqueous solutions, which were chemically synthesized by following the LTEDS method without the centrifugation in the last step. This results in a GO solution with larger flake sizes. The details are given in section 2.3. The preparation process of GO thin films was the same as introduced in section 2.5.1. The GO thin films were transformed into rGO thin films after following the TRP. The obtained rGO thin films were utilized as transducer layers on the top of IDEs in the ESFET configuration to detect PSA, as depicted in figure 6.1(a). The two arms of the IDEs act as source and drain electrodes, while an electrochemical Ag/AgCl RE is placed above the rGO thin film and immersed inside the buffer solution to apply a gate voltage through the electrolyte to the rGO thin film. A single rGO-IDEs chip consists of 16 channels in a 4×4 array layout with a common-source electrode located in the middle of the chip. Each channel has 10 IDEs fingers, while the effective channel length and width are 5 µm and 900 µm, respectively. The separation distance of the neighboring fingers is 5 µm. The structure of a single channel is shown in figure 6.1(b).

The ESFET characterization measurements were carried out in 10 mM PBS using a Keithley 4200-SCS parameter analyzer. The gate voltage V_{gs} was swept from -0.7 V to

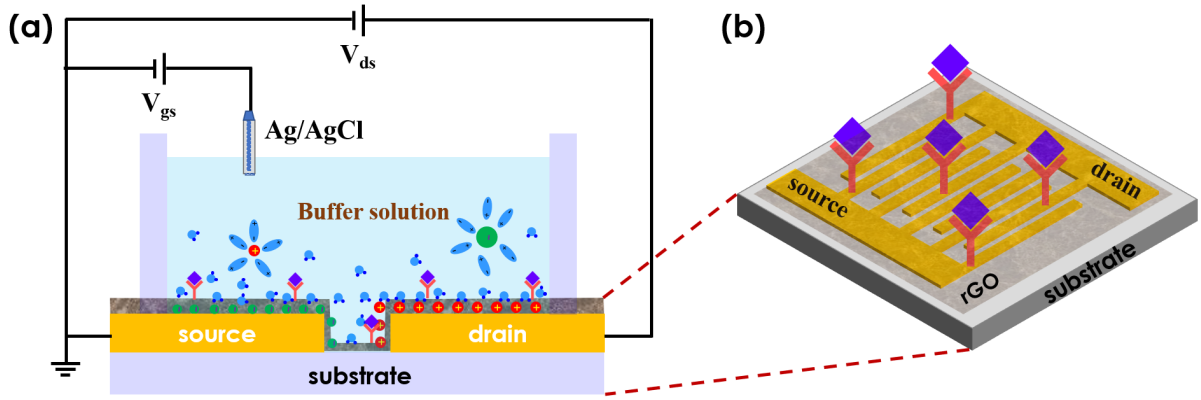

Figure 6.1: (a) Schematic of ESFET configuration with an rGO thin film as a transducer layer and an Ag/AgCl RE immersed into the buffer solution as the electrolyte gate contact. (b) A single chip consists of 16 channels in a 4×4 array layout with a common-source electrode located in the middle of the chip. Each channel has 10 IDEs fingers, while the effective channel length and width are 5 µm and 900 µm, respectively. The separation distance of the neighboring fingers is 5 µm.

1.2 V and the drain-source step voltage V_{ds} was varied from -100 mV to 100 mV with a 50 mV step size. The obtained characteristic curves, figure 6.2(a), show that the rGO thin films of the exemplary device preserve the bipolar property similar to pristine graphene and intrinsically possess electrons and hole as carriers. This is a promising property compared to typical monopolar materials, which can be conductive in the means of doping with either electrons or hole as the carriers. The right side and left side of the Dirac point (detailed explanation can be found in sections 2.1 and 3.2.3) in the bipolar characteristic curves correspond to the carrier type as electron and hole in the rGO thin films, respectively. The I_{ds} drastically increases when the difference between the gate voltage and the Dirac points increases. It is because the higher V_{gs} shifts the Fermi level deeper into the conductance (or valence) band, resulting in a higher carrier concentration and a larger drain-source current I_{ds}.

Ideally, for a fixed drain-source voltage V_{ds}, the drain-source current I_{ds} of each bipolar characteristic curve reaches its minimum at zero gate voltage ($V_{gs} = 0$ V). This minimal I_{ds} corresponds to the Dirac point where the valence and conductance bands meet. However, the obtained bipolar characteristic curves show that the Dirac point is shifted away from the zero gate voltage ($V_{gs} = 0$ V) and slightly varies with the applied drain-source voltage V_{ds}. The detailed information is summarized in figure 6.2(b) for this exemplary device. The minimal I_{ds} of each I_{ds}-V_{gs} characteristic curves with $V_{ds} = -100$ mV, -50 mV, 50 mV and 100 mV correspond to $V_{gs} = 0.47$ mV, 0.46 mV, 0.5 mV and 0.53 mV, respectively. This result is possibly due to impurity doping induced by the substrate, surface contaminations and/or the modulation of the residual oxygen functional groups [84, 156]. In principle, each arm of the bipolar curve can be described in a first approximation by the characteristic equation of a MOSFET in its linear regime [252], as given in equation 3.1 of section 3.2.3.1.

In the biosensing process, the binding of target biomolecules onto the sensing area of ESFET lead to changes of the characteristic curves [155]. This is due to the charges of the target biomolecules, which modulate the capacitance on the transducer layer. This leads to a change in the source-drain current I_{ds}. As indicated by the equation 3.1, a higher change in capacitance C_g induces a bigger change in I_{ds}. The concentration of incoming target biomolecules is directly correlated to the changes of I_{ds}. Therefore,

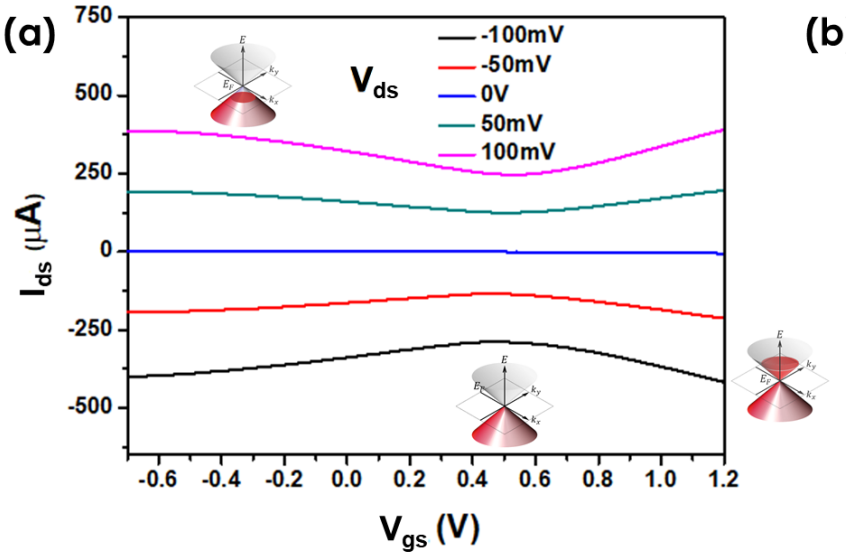

(b)

V_{ds} (mV)	Dirac point (V_{gs}_mV,I_{ds}_μA)	
-100	0.47	-287.8
-50	0.46	-134.8
0	--	--
50	0.5	-125.4
100	0.53	-246.3

IDEs: Channel width L=900μm,length W=5μm, Leakage current I_{gs}=hundreds of nA

Figure 6.2: The characteristic properties of rGO thin films as the transducer layers of an ESFET device. (a) The bipolar behavior of rGO thin films shows high similarity to that of the pristine graphene. This ESFET measurement was carried out in 10 mM PBS. The gate-source voltage V_{gs} was swept from -0.7 V to 1.2 V and the drain-source voltage V_{ds} was varied from -100 mV to 100 mV with a 50 mV step. (b) The table lists the corresponding V_{gs} of Dirac points at different V_{ds}. These values were extracted from the bipolar characteristic curves as shown in (a).

the sensitivity of the biosensing process is defined as the transconductance g_m, which is the first derivative of I_{ds} with respect to V_{gs} for a constant V_{ds}. It corresponds to the slope of the characteristic curve I_{ds}-V_{gs}. Deduced from equation 3.1, g_m is expressed as the product of the capacitance per unit area of the gate structure C_g, the field-effect mobility of the transducer layer μ, the ratio of effective width W and length L of the gate area, and the gate-source voltage V_{ds}:

$$g_m = \left.\frac{\partial I_{ds}}{\partial V_{gs}}\right|_{V_{ds}=\text{const}} = \mu C_g \frac{W}{L} V_{ds} \tag{6.1}$$

A high sensitivity of an ESFET biosensor device is represented by a high g_m. For the above exemplary rGO ESFET, the geometry factor W/L and gate capacitance per area C_g are constants so that g_m is linearly proportional to the field-effect mobility of the transducer layer μ and V_{ds}. For the bipolar rGO thin film, the slope (g_m), as seen from the curves in figure 6.2(a), are different for both sides of a bipolar curve in the condition of a constant V_{ds}. This result shows that the g_m is dependent on the type of the carriers, because the field-effect mobilities of electrons and holes are different. Besides, the slopes on either side of the bipolar curves at different V_{ds} are distinctly different. This demonstrates that g_m is influenced by the applied drain-source voltage V_{ds} as well. Before performing the biosensing experiments, the voltages V_{ds} and V_{gs} corresponding to the maximum g_m were selected and used as the working point of the rGO based ESFET biosensor. During the biosensing, the capacitance of the gate C_g is a critical parameter to influence the biosensing performance, since the other parameters V_{ds}, V_{gs}, μ, W , and L are constant at this working point.

For a typical ESFET, the capacitance C_g is dominantly modulated by the attachment of the biomolecules and directly related to the ionic layer EDL (details can be found in

section 3.2.3.2). In a buffer solution, the gate surface of the ESFET is typically charged and the ions are accumulating on the gate surface to form the EDL. As demonstrated in equation 3.2, the thickness of the EDL (so-called Debye length) is dependent on the solvent permittivity, concentration of the solution ions and valence of solute ions. The Debye length influences the biosensing performance of the ESFET. Indeed, only the attachment of the biomolecules that takes place within the Debye length can lead to a change in the characteristic curves of the ESFET, because the charged biomolecules beyond the Debye length are not sensitive to the electrostatic field generated by the charged gate surface. Therefore, the charges of the biomolecules outside of the Debye length have no influence on the capacitance of the surface of the gate area, resulting in no change in I_{ds} of the ESFET. This effect is the so-called Debye-screening effect. The typical charge-based FET biosensor are restricted by this effect towards real applications [253]. Since the clinical fluid sample is of high ionic strength (150 mM) and the corresponding Debye length is approximately 0.8 nm, a pre-dilution of the clinical fluid sample is required. This enables the detection of the biomolecules (of diameter larger than several nanometers) in a lower buffer concentration with a higher Debye length. The PSA biosensing capability of rGO based ESFET related to the Debye-screening effect is of great interest and is investigated in the following sections.

6.2 rGO Based ESFET for PSA Detection

In this section, rGO based ESFET devices were prepared with aptamers as receptor biomolecules towards PSA detection. Au NPs were proposed to be functionalized onto the surface of rGO thin films to increase the surface area. Thus, thiol terminated aptamers were chosen as receptor biomolecules to bind onto Au NPs. A descriptive schematic of the aptasensors preparation process is shown in figure 6.3. In this study, the aptamer sequence used for PSA detection was TTT TTA ATT AAA GCT CGC CAT CAA ATA GCT TT (5′ to 3′ direction). The 5′ end was modified by a 6-carbon chain as a spacer and terminated with a thiol group. The detailed preparation of a biosensor was as follows:

i) A mixture solution containing 80 mM EDC and 20 mM NHS in milliQ water was used to activate the $-$COOH groups on the surfaces of the rGO thin films for 30 min.

ii) The ATP linker molecules with a concentration of 2 mg ml^{-1} in ethanol were incubated on the rGO surfaces for 30 min. In this process, the amino groups of the ATP linker molecules covalently bound to the $-$COOH groups of the rGO thin films, while the thiol groups of ATPs were standing towards the ambient air.

iii) Au NPs (Gold (III) chloride hydrate, $HAuCl_4 \cdot x\,H_2O$)) diluted in milliQ water were incubated overnight at 4 °C to bind to the thiol groups of ATP.

iv) The microcentrifuge tube which contained 10 µl of 100 µM thiol-terminated aptamers was taken out of the freezer and left at the room temperature for approximately 10 min until thawed. Fast spinning was applied for 5 s to centrifuge down the residual droplets from the sidewall.

v) Then the microcentrifuge tube was half-immersed into a flask containing milliQ water at 90 °C. When the milliQ water temperature returned to the room temperature naturally, the microcentrifuge tube was taken out and fast spun for 5 s.

vi) A stock solution 10 mM 6-mercapto-1-hexanol (MCH) was prepared in ethanol. Then a solution 50 µM MCH was prepared in 10 mM PBS with the stock solution. Finally, the solution 100 µM thiol-terminated aptamers was mixed with the solution 50 µM MCH to obtain 1 µM aptamers.

vii) This prepared solution was subsequently incubated on the rGO device for 4 h at 4 °C to immobilize the thiol-terminated aptamer on the Au NPs. In this step, the concentration of MCH was chosen to obtain an optimized arrangement of the aptamers [254].

viii) The rGO device was incubated for 1 h at 4 °C in a blocking solution, which contains 1 mM MCH and 10 % ethanol (volume percentage) in 10 mM PBS. This step was to block the free space on the Au NPs to avoid non-specific bonding. The established rGO aptasensor was stabilized in 10 mM PBS overnight at 4 °C as a final step before PSA detection.

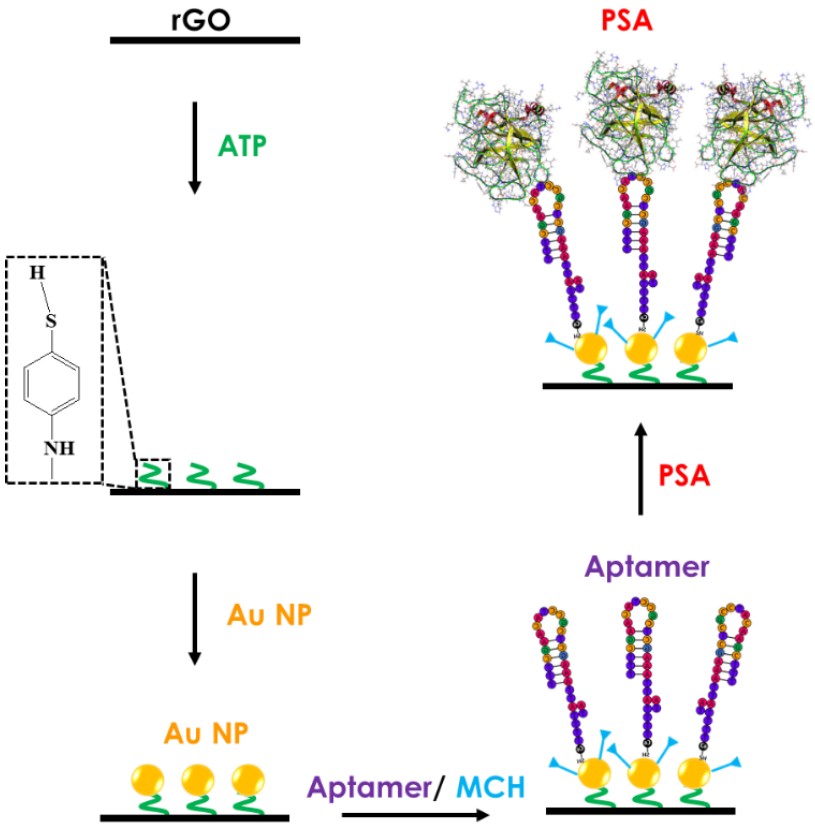

Figure 6.3: Descriptive schematic of the biosensor preparation protocol with thiol-terminated aptamers as receptor biomolecules. The rGO surface was functionalized with ATP linker molecules via EDC/NHS chemistry to immobilize Au NPs, to which afterwards thiol-terminated aptamers are binding. The free sites on Au NPs were blocked by MCH molecules. These aptasensors were established to detect PSA target biomolecules by the ESFET transducing mechanism with an increased density of receptor biomolecules.

Different PSA concentrations were prepared in 10 mM PBS. The concentration-response measurements started by incubating the chip in 100 µl PSA with a concentration of 33 fM for 30 min. Afterwards, the chip was cleaned 10 times with 10 mM PBS using pipette and measured by an Agilent 4156C semiconductor analyzer. The same process was repeated by adding different PSA concentrations on the rGO aptasensor surface: 330 fM, 3.3 pM, 33 pM, 330 pM, 3.3 nM, 33 nM and 330 nM.

The gate voltage V_{gs} was swept from -0.8 V to 0.8 V for a constant drain-source step voltage $V_{ds} = 100$ mV. The obtained bipolar characteristic curves are shown in figure 6.4(a). The results clearly show that a higher concentration of PSA molecules leads to a smaller drain-source current I_{ds}. This indicates an increase of resistance within the rGO sensing area with the attachment of PSA. The cause is that the PSA target biomolecules are negatively charged and an equivalent negative voltage is applied on the rGO thin films. Indeed, the Dirac points are left-shifted away from the axis $V_{gs} = 0$ V and the right arm of the bipolar curve indicates that the electrons, as the majority of carriers, are responsible for the detection. Thus, the higher negative gate voltage generated on the rGO biosensor surface suppresses the Fermi level to lower levels in conductance band, resulting in a lower carrier concentration in the rGO thin films and a higher resistance.

To verify the specificity of the rGO biosensing performance, 1 µM non-specific HSA biomolecules were tested on the established rGO biosensor surface. The drain-source current I_{ds} showed no change induced by 1 µM HSA, as indicated in figure 6.4(b). These measurements of specific binding of PSA and non-specific binding of HSA demonstrate an outstanding selectivity of the rGO aptasensor platform.

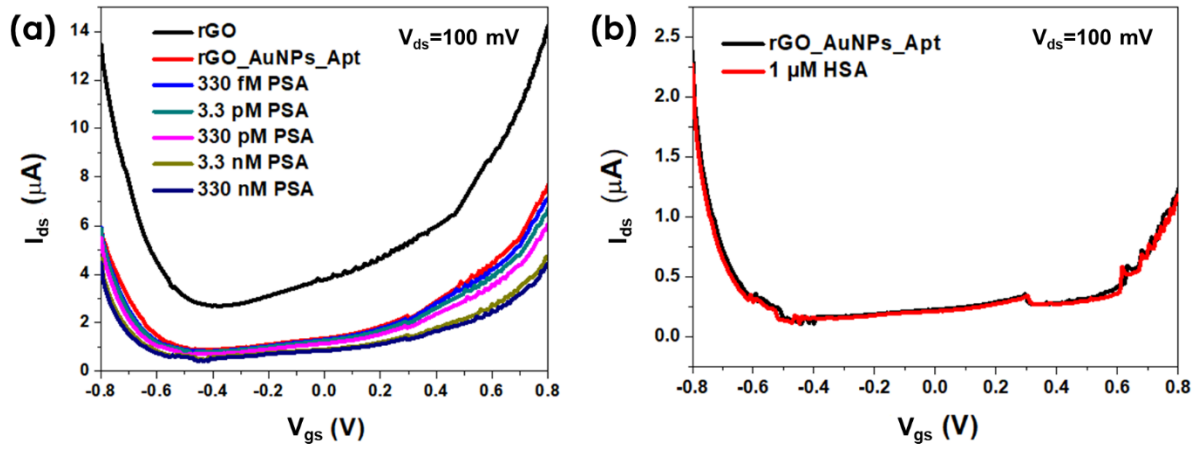

Figure 6.4: (a) PSA concentration-response curves measured for an exemplary rGO based ESFET. (b) A high concentration of HSA (1 µM) was used as a non-specific control.

It is noteworthy that the concentration-response were carried out in 10 mM PBS. The corresponding Debye length is 0.76 nm, which is much smaller than the total diameter of the aptamer (3-5 nm) and the PSA (10 nm). Also in this approach, the rGO based ESFETs exhibit an outstanding sensing capability beyond the Debye-screening effect. It could be because of the attachment of biomolecules which influenced the ion arrangement on the rGO transducer layer and induced the changes of I_{ds}.

6.3 Modification of rGO Based ESFET Devices with Cu Nanoparticles

6.3.1 Growth of Cu Nanoparticles

The oxygen functional groups on the surface of carbon basal plane of rGO thin films offer various possibilities for receptor biomolecules immobilization. The rGO thin films can be functionalized with Cu NPs, which serve as catalysts of a click chemistry NPs [255–257] to immobilize alkyne terminated receptor biomolecules for detecting prostate-specific biomarkers. A three-electrodes electrochemical configuration connected with an Ivium potentiostat was used to grow Cu NPs on the rGO surfaces. Electrodeposition methods are a typical way to synthesize nanoparticles, nanorods, nanowires and nanoclusters metals [258]. Chronoamperometry, one type of electrodeposition, is generally used to apply step voltages on a WE, while the resulting faradaic current is monitored over time. This technique can be utilized for Cu NPs growth [259]. In this study, Cu NPs were deposited onto rGO thin films by using the chronoamperometry technique. The conversion solution used was prepared by mixing 10 mM copper acetate and 100 mM lithium chloride with a volume ratio 1:5. Both solutions were prepared in DIW. The used chronoamperometry setup is shown in figure 6.5(a). The WE was connected to the common source of the rGO chip. A Pt wire, which acted as a CE, was twisted and placed around the inner wall along the bottom of the electrochemical cell. An electrochemical Ag/AgCl electrode acted as RE. A chronoamperometry voltage of -1.1 V was applied to the WE for 10 s. It is noteworthy that the lithium ions were used to increase the solution conductivity as well as precisely control the size, shape and size distributions of the Cu NPs [260]. The Cu NPs density can be modified by the concentrations, the growth time, and the volume ratio of the copper acetate and lithium chloride. A descriptive schematic of Cu NPs growth on rGO thin films is given in figure 6.5(b)-(c).

The applied negative potential on the WE reduced the Cu^{2+} into Cu NPs at the defective sites of the rGO thin films. The Cu NPs formation process is monitored with the current values across the rGO thin films dropping from microampere to nanoampere. The rGO thin films, before and after Cu growth, were characterized by SEM and shown in figure 6.6(a)-(b). This indicates that the Cu NPs were successfully grown with a high density and a uniform distribution.

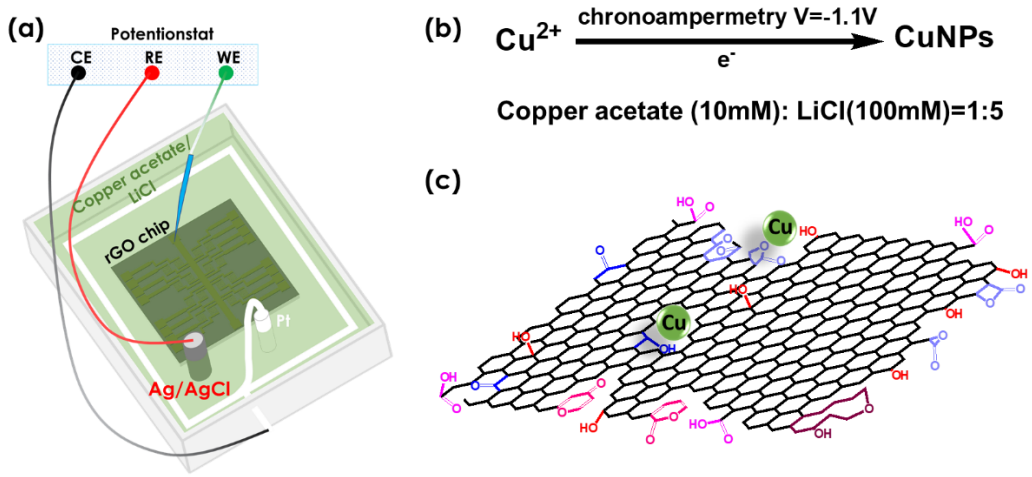

Figure 6.5: Cu NPs growth on rGO thin films. (a) The experimental setup for the Cu NPs growth using an Ivium potentiostat. The WE was connected to the common source bar of the rGO chip while the Pt wire in the chemical cell served as CE and the electrochemical Ag/AgCl as RE. (b) The chronoamperometry condition for Cu NPs growth in the conversion solution, which consisted of copper acetate and lithium chloride. The applied voltage on the WE was $V = -1.1\,\mathrm{V}$ for 10 s. (c) Schematic of the Cu NPs on a rGO thin film.

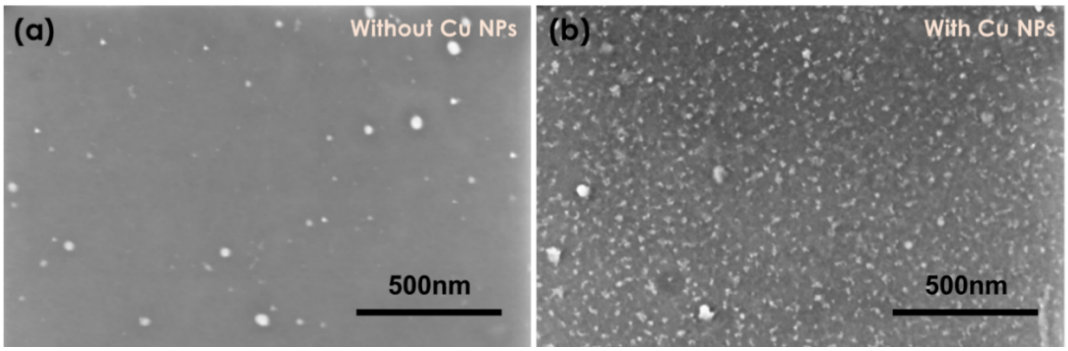

Figure 6.6: (a)-(b) SEM characterizations of the rGO thin films before and after the Cu NPs growth.

6.3.2 Electronic Characterization of rGO Based ESFET with Cu Nanoparticles

The bipolar characteristic curves of the rGO ESFETs were measured in 10 mM PBS before and after the growth of Cu NPs. The results are shown in figure 6.7(a)-(b). The measurements were carried out with the gate-source voltage V_{gs} sweeping from $-0.7\,\mathrm{V}$ to $1.2\,\mathrm{V}$ and the drain-source voltage V_{ds} from $-100\,\mathrm{mV}$ to $100\,\mathrm{mV}$ with a 50 mV step size. The obtained results show that the drain-source current I_{ds} decreased after the Cu NPs growth. This is most likely caused by a scattering effect of the carriers induced by Cu NPs on the rGO thin films. The transconductance g_m, that represents the sensitivity of the rGO ESFET, is calculated from the bipolar curves before and after the growth of the Cu NPs. The results are shown in figure 6.7(c)-(d), in which g_m for electrons (the right arm of the bipolar curves) is generally higher when comparing to the holes (the left arm of the bipolar curves). In addition, it shows that the maximum value of g_m with electrons as majority carrier on the right arm of bipolar curves are slightly enhanced after Cu NPs modification, while the maximum value of g_m

decreases in the case of the holes.

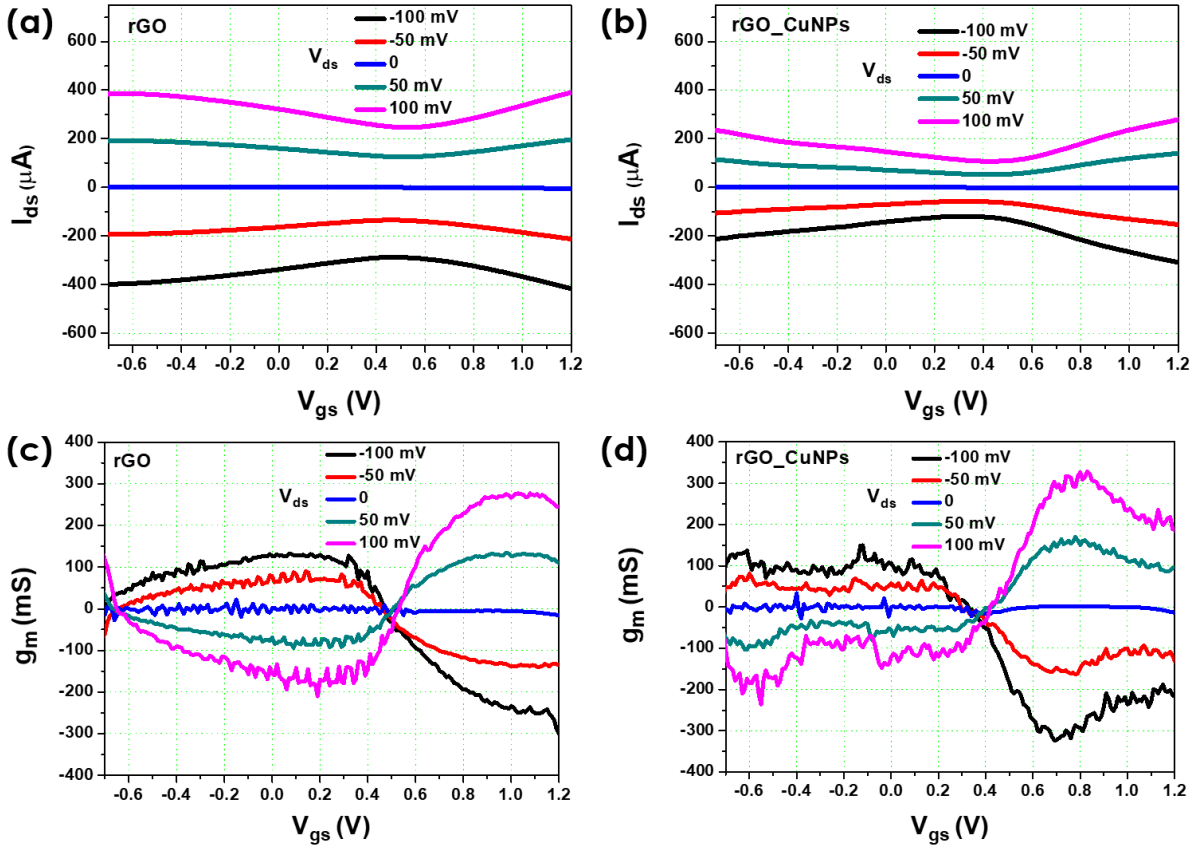

Figure 6.7: Characterization curves of rGO ESFETs before and after the growth of Cu NPs. (a)-(b) Bipolar characteristic curves. (c)-(d) The transconductance g_m.

Taking a closer look at the bipolar curve of $V_{ds} = 100\,\text{mV}$, it can be observed that the Dirac point is left-shifted after Cu NPs decoration, as shown in figure 6.8. This is because the Cu NPs act as electron donors for the rGO thin films and modulate the Femi-level even deeper into the conductance band.

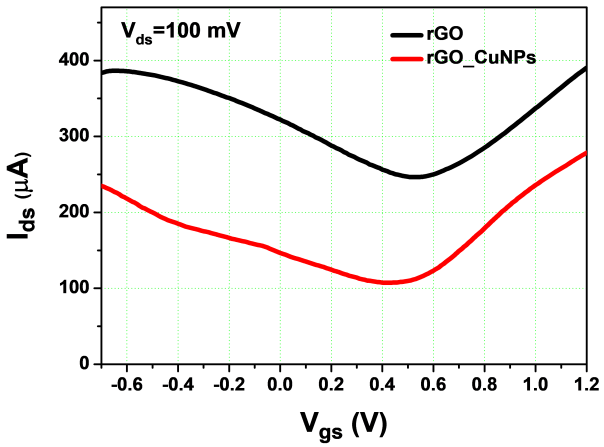

Figure 6.8: Close-up of the bipolar curve of an exemplary rGO ESFET before and after Cu decoration, in the condition of $V_{ds} = 100\,\text{mV}$. The Dirac point is left-shifted and the transconductance g_m is increasing with electrons as the major carriers.

The performances of the rGO ESFETs were highly dependent on the treatment of

the GO aqueous solution for the rGO thin films preparation. As an experimental comparison, the GO aqueous solution used for GO thin film preparation was treated with the last centrifugation step of LTEDS protocol. This only selected GO flakes of smaller sizes for the formation of rGO thin films. After the same reduction condition in TRP, the characteristic curves of rGO based ESFET are shown in figure 6.9(a)-(b). The I_{ds} is one thousand times smaller than that of the devices prepared by GO aqueous solution without the last centrifugation step. Nevertheless, for both rGO ESFET devices, the enhancement effect of the Cu NPs on the bipolar curves was consistent.

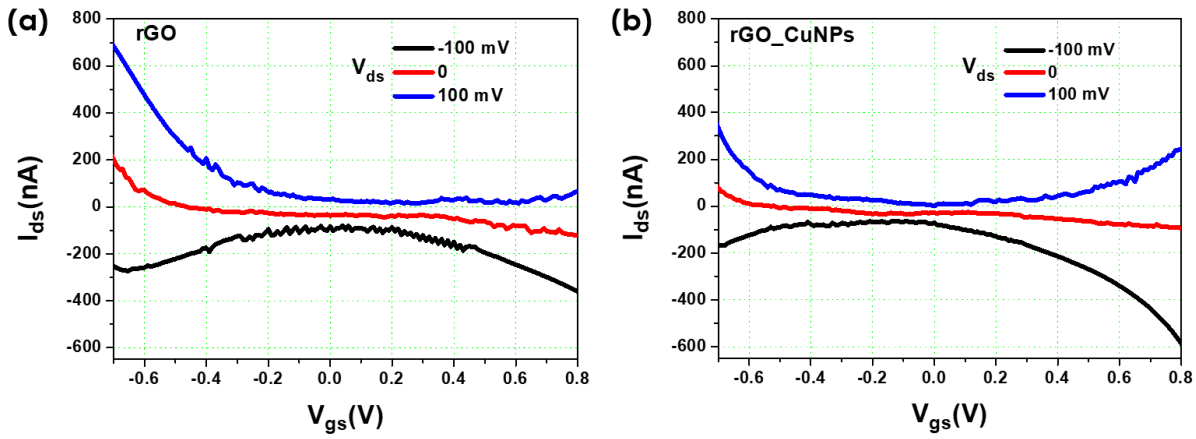

Figure 6.9: The rGO device was prepared with mesh graphite as original material. In the preparation protocol the last centrifugation step was used. Close-up of the bipolar curve of rGO ESFET before and after Cu decoration, with V_{ds} $=-100\,\text{mV}$, $0\,\text{mV}$ and $100\,\text{mV}$. The current is here expressed in nanoampere against microampere previously (figure 6.7(a)-(b).)

Towards biosensing, azide molecules can be initially anchored on the surface of rGO thin films. The receptor biomolecules are terminated with alkyne groups to react with the azide, while the grown Cu NPs serve as catalysts. This reaction is so-called click chemistry. It is fast and quantitative as well as biocompatible. The reaction process is easy to handle, since it can happen in various solutions, such as buffers, dimethyl sulfoxide, and water. A wide range of pH value from 1 to 4 can be used. Furthermore, it takes place only between azide and alkyne terminated components and does not react with other organic groups, which are contained in native biomolecules, for instance amino and carboxyl groups. Therefore, this immobilization mechanism of receptor biomolecules is of high specificity and can be investigated to detect prostate-specific biomarkers in a future work.

6.4 Conclusion

The GO thin films that were prepared using GO solutions by the LTEDS method without the centrifugation in the last step showed a superior bipolar property and a higher transconductance g_m compared to the case of the GO solution with the centrifugation step. This result demonstrates the bigger GO flakes preserve more similar electronic properties to the pristine graphene. Remarkably, with the immobilized Au NPs on the rGO thin films, the rGO based ESFET biosensor can detect

PSA with thiol-terminated aptamers as receptor biomolecules in 10 mM PBS which has a similar ionic strength (162 mM) and corresponding Debye length (0.76 nm) as physiological solutions. The concentration-response curves of an exemplary device exhibit PSA detection with a wide sensing range from 33 fM to 330 nM, beyond the Debye-screening effect.

Additionally, Cu NPs were successfully grown on the surface of rGO thin films by chronoamperometry technique. rGO transducer layer with Cu NPs functionalization showed improved transconductance g_m of the rGO ESFETs. Click chemistry could be used with Cu NPs as catalysts for assisting the immobilization of alkyne-terminated ssDNA receptors to detect prostat-specific complementary DNA (cDNA) sequences. This immobilization mechanism of receptor biomolecules needs to be further optimized to conclude quantitatively about the biosensing capability.

7 Conclusions and Outlook

Conclusions

In conclusion, the newly developed LTEDS synthesis process, which is an upgraded version of the IHM with lower process temperature and additional purification steps, offers a unique opportunity to preserve larger areas of carbon lattice with less defects and contaminations from ions and molecules. The chemically exfoliated GO flakes synthesized by the LTEDS process were utilized as the source material to establish a wafer-scale flow process of GO thin films. Afterwards, thermal reduction treatments were chosen to transform the insulating GO to conductive rGO thin films. The (r)GO thin films were utilized as transducers in the SPR ((r)GO), EIS (rGO) and ESFET (rGO) based biosensor platforms for PSA detection. In the following, the properties of (r)GO flakes and thin films as well as the sensing mechanisms and performance of (r)GO based biosensor platforms are summarized, compared and discussed. In addition, the potential applications of these biosensor platforms are assessed.

Wafer-scale fabrication of GO devices
The properties of GO flakes produced by the LTEDS synthesis process were characterized by SEM, TEM, UV-VIS spectroscopy, fluorescence spectroscopy, XRD and FT-IR spectroscopy. Low exfoliation temperature and additional purification steps of the LTEDS method proved to generate GO flakes of high quality in terms of larger and cleaner carbon lattice. With the GO aqueous solution as the original material, a top-down wafer-scale fabrication process of GO thin films was established, making use of gas-phase silanization, spin-coating, photolithography and O_2 reactive etching techniques. The GO thin films were formed on 4-inch SiO_2/Si (or glass) substrates with APS as linker layers, which were of thicknesses 1.01 ± 0.40 nm. Characterized by ellipsometry spectroscopy and AFM, the thickness of the wafer-scale GO thin films were 2.95 ± 0.35 nm and 6.43 ± 0.40 nm in the condition of 1 time and 4 times spin-coating, respectively. The results indicated that GO thin films were topographically uniform in wafer-scale and their thicknesses were controllable by the number of spin-coating.

Electronic properties after reduction treatments
To characterize the electronic properties on wafer-scale, the GO thin films were prepared on top of IDEs, which consisted of a bilayer stack of 30 nm Ti and 270 nm Au. Each IDEs channel had a total of 10 finger electrodes with a finger length of 100 µm, a finger width and a separation distance of neighboring electrodes of 5 µm. The TRP

with a reduction at 350 °C for 10 h in a vacuum oven and subsequent 600 °C for 20 s in ambient conditions was used throughout this thesis to obtain rGO thin films.

Confirmed by cyclic voltammetry measurements and I-V characterizations, the generated rGO thin films were dense and complete without pinholes and formed ohmic contacts with the IDEs. After the TRP, approximately 98.7 % of the working channels of an exemplary 4-inch wafer were conductive with a resistance ranging from $10^4\,\Omega$ to $10^7\,\Omega$. More remarkably, 87.9 % of all the conductive rGO channels showed a uniform electrical resistance varying within only one order of magnitude ($1.14 \cdot 10^6\,\Omega$ to $9.54 \cdot 10^6\,\Omega$). The resistance uniformity demonstrated that the formed rGO thin films can be integrated into electronic devices for further applications. Four-point measurements were carried out to extract the sheet resistivity from Greek-cross VDP structures with a diagonal electrodes' distance of 5 µm. The obtained sheet resistivities ranged from $0.3\,\Omega\,\mathrm{m}$ to $0.06\,\Omega\,\mathrm{m}$. In addition, bipolar characteristic curves of rGO based ESFET devices in 10 mM PBS were used to deduce the field-effect mobility: $0.326\,\mathrm{cm^2\,V^{-1}\,s^{-1}}$ for holes and $0.092\,\mathrm{cm^2\,V^{-1}\,s^{-1}}$ for electrons. Furthermore, the evolution of the functional groups on the carbon basal plane were revealed by Raman spectroscopy and XPS characterization. These results showed the reduction degree of rGO thin films by TRP and can serve as an important reference for the further optimization of reduction treatments.

(r)GO based SPR biosensor

The rGO based SPR chips were prepared by metal evaporation and gas-phase silanization techniques. With the metal evaporation technique, bilayer stacks of 3 nm Ti and 47 nm Au were prepared in sequence on top of 4-inch glass wafers. Afterwards, the Au thin films were functionalized with ATP linker molecules by the gas-phase silanization technique to covalently immobilize GO flakes, which formed uniform GO thin films. The obtained GO thin films were then transformed into rGO thin films using the TRP. The (r)GO thin films were utilized as the functional layers on conventional Au based SPR chips for PSA detection while ConA served as receptor biomolecule. The biosensing mechanism and capability of rGO based SPR biosensors were analyzed and cross-checked by simulations, using a standard WinSpall software to simulate the SPR spectra. The simulation principle was to repeatedly apply the Fresnel equations to the established six-layer stack, namely prism, glass substrate, Au thin film, (r)GO thin film, ConA/PSA biomolecule layer and analyte solution. From this perspective, the sensitivity of the (r)GO based SPR biosensor is dependent on the thin film thickness and dielectric parameters of (r)GO. The AFM characterizations revealed that the thin-film thickness of GO was 8 nm and rGO was 6.8 nm. The dielectric parameters extracted by ellipsometry measurements at a wavelength of 780 nm were $\varepsilon_{GO} = 1.72 + 0.55\mathrm{j}$, $\varepsilon_{rGO} = 1.59 + 1.1\mathrm{j}$. By substituting these parameters into the established layer model, the simulated data demonstrated that rGO thin films as functional layers lead to a higher sensitivity than GO thin films for SPR biosensing.

The real-time biosensing results manifested that the SPR signal intensities were amplified by a factor of 1.70 ± 0.25 for the rGO compared to the GO layers. Moreover, the statistical results from the specific and non-specific biosensing data showed that the signal-to-noise ratio for the rGO functional layers was approximately 3 times higher than that of the GO functional layers, with exact values of 6.56 ± 3.63 for rGO and 2.16 ± 1.64 for GO. The rGO thin films as transducers in SPR device exhibited

superior biosensing capability than GO thin films, which was concretely confirmed with the simulation results. Besides, the LOD was reduced to 0.01 µg ml^{-1} PSA when negative voltages were applied across the rGO thin films-liquid interface. This is attributed to the bipolar characteristic of the rGO thin films, which enables a Fermi level modulation to tune the SPs. Such a tuning effect is not reachable by conventional Au based SPR platforms.

rGO based impedance spectroscopy biosensor

The rGO thin films prepared on top of IDEs were utilized as the transducer layers of in-line EIS biosensors, in which the two arms of IDEs acted as CE and WE with electrochemical Ag/AgCl electrode as RE. The input signal was a DC signal of 0.05 V combined with an AC signal of an amplitude 0.01 V while the frequency was swept from 100 kHz to 0.1 Hz. The biosensing activity was revealed by the changes of the amplitude, phase, real part and imaginary part of the output impedance. The biosensing mechanisms with rGO thin films as transducer layers on IDEs were investigated by using PSA-specific aptamers (diameter 3-5 nm) and antibodies (diameter 10 nm) as receptor biomolecules to detect PSA (diameter 4.5 nm) target biomolecules in PBS of different ionic strengths and Debye lengths. Besides, the influence of the rGO thin films on the electric field across the IDEs fingers was evaluated.

With PSA-specific aptamers as receptor molecules, the PSA detection was carried out in 10 mM PBS with an ionic strength of 162 mM and a Debye length of 0.76 nm. The biosensing activity was indicated by the impedance amplitude and phase in the Bode plots. Around 1 Hz, an increase in the impedance amplitude was observed with the PSA concentration increasing from 33 pM to 330 nM. The charges of bound PSA biomolecules are equivalent to a variable voltage on the bipolar rGO thin film which can tune the Fermi level, carrier mobility and channel resistance. Therefore, the bindings of PSA lead to an increase in the impedance amplitude. This tendency was confirmed by the experimental results of dual I-V sweep concentration-response. At around 1 kHz, a decrease in the impedance phase was observed with the PSA concentration increasing from 33 fM to 330 nM. The differences in the response frequency regimes of impedance amplitude and phase indicate that the corresponding electronic elements for biosensing are different. As a control, non-specific binding experiments were carried out to detect HSA in 10 mM PBS. The result showed almost no signal and thus demonstrated the excellent selectivity of this biosensor platform. Therefore, the biosensors, that were utilizing rGO thin films as transducer layers on IDEs and aptamers as receptor biomolecules, were capable of detecting PSA in buffer solution with an ionic strength of 162 mM and a corresponding Debye length of 0.76 nm, which is similar to physiological solutions (150 mM and 0.78 nm). This result indicated that the rGO based EIS biosensors overcame the Debye-screening effect which significantly obstructs the charged based label-free biosensing devices towards real clinical applications.

To understand the sensing mechanism of rGO thin films for biosensing, the same experiments were carried out in 200 mM PBS, with a corresponding Debye length of 0.17 nm. The difference in the impedance amplitude around 1 Hz vanished because the target biomolecules were bound beyond the Debye length. The rGO thin films were not able to sense the charges of the binding PSA biomolecules. As a result, the

Fermi level, the carrier concentration, and the channel resistance were also not altered. In contrast, the impedance phase still displayed a sensing capability around 1 kHz. A decrease in impedance phase was observed with PSA concentration increasing from 33 fM to 3.3 nM. This biosensing activity is attributed to the existing electric field confined by the IDEs and rGO thin films. The recognition process of PSA biomolecules on rGO thin films was reflected by a capacitance change between the IDEs.

Technically, the electric field decays perpendicularly away from the plane of bare IDEs structures, with a depth approximately equal to the finger width of the IDEs, which is 5 µm. In our case, rGO thin films were prepared on top of the IDEs and most likely significantly reduced the depth of the electric field created by the IDEs to only a few nm. To estimate the value of this parameter, the PSA detections were carried out in the 10 mM PBS and antibodies, larger than the aptamers in terms of diameter, were used as receptor biomolecules. The results showed that both impedance amplitude and phase exhibit no sensing behavior throughout the whole tested frequency regime. The PSA molecules bound to the antibodies with large diameters, and as a result the charged PSA biomolecules were outside the Debye-screening length and outside the electric field created by the IDEs and rGO thin films. The resistive path (real part of the output impedance) at 1 Hz was altered with the increased PSA concentration. However, the capacitive path across IDEs at 1 kHz showed no response for the PSA binding. These results demonstrated that the depth of the electric field induced by IDEs and rGO thin films should be less than 10 nm, which was much smaller than that of the bare IDEs.

rGO based ESFET biosensor

The rGO thin films prepared on top of IDEs were utilized as the transducer layers of ESFET biosensor platforms. The two arms of IDEs acted as drain and source electrodes with an electrochemical Ag/AgCl electrode as RE. The drain-source voltage V_{ds} was swept within a range from -0.7 V to 1.2 V. In this experiment, the GO flakes used for the GO thin films were prepared without the last centrifugation step of the LTEDS protocol. Thus, the thin films contained a larger portion of bigger flakes. The GO thin films were transformed into rGO thin films using the TRP. The obtained field-effect characteristic curves demonstrated that the bipolar properties were very promising with high transconductances g_m for both carriers: electrons and holes. A right shift of the Dirac point in the firstly prepared devices indicated that the rGO thin films were p-doped, which is opposite to the case of rGO thin films (n-doped) quilted with the GO flakes prepared by the complete LTEDS protocol.

With the assistance of ATP linker molecules, Au NPs were functionalized on the rGO transducer layer to immobilize the thiol terminated aptamers as receptor biomolecules for PSA. The concentration-response (33 fM to 300 nM) in 10 mM PBS buffer solution demonstrated that the binding activity of PSA led to a decrease in the channel current and an increase in the resistance of the rGO thin films. This result was also in accordance with the concentration-response experiments of I-V and EIS measurements. Also, the biosensing was not obstructed by the Debye-screening effect. In addition, Cu NPs were successfully grown by a chronoamperometry technique. They could serve as the catalysts for click chemistry, which should facilitate the immobilization of the alkyne terminated receptor biomolecules to detect PSA.

Remarkably, the Cu NPs improved the transconductance g_m of rGO based ESFET devices and thus were capable to enhance the sensitivity of biosensing.

Outlook

Properties of (r)GO flakes and thin films
In a future work, even lower exfoliation temperature could be applied to restore the carbon lattice of GO flakes, in favor of further tuning their properties as similar to the pristine graphene as possible. However, the decreased exfoliation temperature directly reduces the yield of GO flakes. The trade-off between the flake quality and yield is an important issue that needs to be addressed during the later optimization of the exfoliation process. Besides, more efficient reduction treatments of GO is another path worth exploring to restore larger areas of the carbon lattice. It would be interesting to combine both thermal and hydrogen reductions to remove the oxygen functional groups and restore the carbon lattice simultaneously, such that the electronic and optical properties of the rGO thin films can be substantially improved.

As one of the important electronic parameter, the Hall mobility of rGO thin films can be further extracted by Hall measurements [168] to confirm the field-effect mobility deduced from the field-effect measurement as discussed in chapter 3. Continuing from the section 3.2.4, the Hall mobility μ can be calculated by the following equations:

$$\mu = \frac{|R_H|}{\rho} \tag{7.1}$$

where ρ is the magnetoresistivity and R_H the hall coefficient expressed by:

$$R_H = \frac{t}{B} \frac{V^+_{31,42}(+B) - V^-_{31,42}(+B) + V^-_{31,42}(-B) - V^+_{31,42}(-B)}{I^+_{31}(+B) - V^-_{31}(+B) + V^-_{31}(-B) - V^+_{31}(-B)} \tag{7.2}$$

with the thickness of the material t and the applied magnetic field B.

Even larger rGO based Greek cross and 8-arms Hall bar structures (shown in figure 7.1(a)-(b)) were designed and fabricated to investigate the carrier mobilities and electronic performance of the ESFET devices with different channel lengths after different reduction treatments. It is noteworthy that the 8-arms VDP structures are capable to provide more precise measurements of carrier mobilities. The above-mentioned measurements require a specific Hall effect setup, which was not available during the course of this thesis.

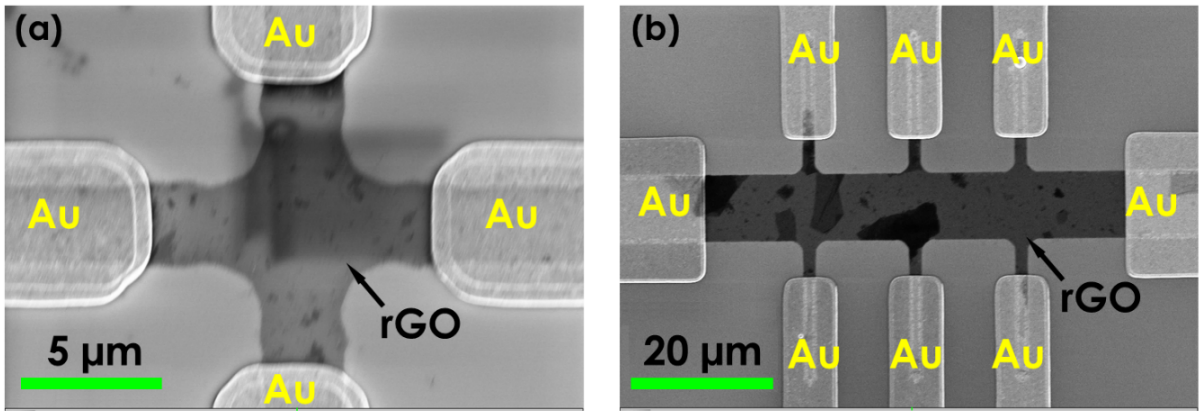

Figure 7.1: SEM images of VDP structures realized in this thesis: (a) Greek cross. (b) 8 arms Hall bar structure.

(r)GO based biosensors

The wafer-scale fabrication and patterning technique established in this work enable (r)GO thin films to act as transducers in SPR, EIS and ESFET based biosensors. All proof of concept experiments showed promising biosensing capability towards PSA detection. For rGO based SPR biosensors, the above two aspects in optimizing the exfoliation process and reduction conditions can be further investigated to generate a better bipolar property to enhance the SPR signals. The related electro-optical tuning effect of the rGO thin films can be elaborated precisely by combining a more sophisticated theoretical layer configuration. For both rGO based in-line EIS and ESFET based biosensors, the sensing mechanism of rGO thin films beyond Debye-screening effect should be further investigated and discussed with the support of better modeling and simulations.

In terms of improving the reliability and reproducibility of (r)GO based biosensors, surface activation protocols of (r)GO thin films should be employed in an optimized manner to specifically immobilize receptor biomolecules or structures. The click chemistry, as well as other functionalization possibilities of NPs, provides an alternative approach to immobilize higher density of receptor biomolecules and it can be further investigated in a future work. For instance, the grown Cu NPs can function as catalysts of click chemistry, assisting the immobilization of prostate-specific receptor ssDNA sequences for biosensing. The detailed steps to establish the biosensor surface are described in figure 7.2(a)-(d) and as follows:

i) After the growth of Cu NPs, the $-$COOH groups were activated by EDC for 1 h to functionalize the rGO thin films with azide molecules. The concentration of EDC and azide were 15 mM and 50 nM prepared in milliQ water, respectively.

ii) The residual $-$COOH groups after coupling with EDC and azide were blocked by 10 nM ethanolamine for 20 min.

iii) With the grown Cu NPs as catalysts, 10 nM alkyne-terminated receptor biomolecules were immobilized on the chip surface for 30 min.

This protocol is a first proposal and was tested with inconclusive results in the biosensing experiments. It is believed that different chemicals and concentrations

could improve the biosensing performances. This proposed biosensing scheme could be an alternative approach to the EDC/NHS chemistry to immobilize the prostate-specific ssDNA sequences.

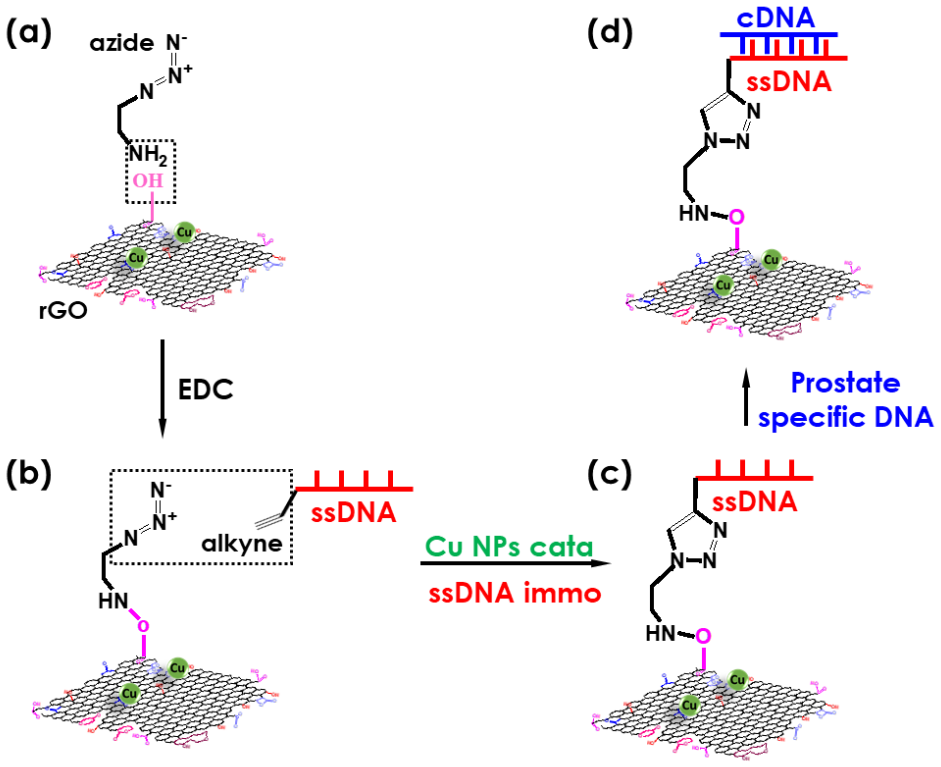

Figure 7.2: The working principle of the click chemistry protocol to immobilize the prostate-specific receptor molecules after Cu NPs growth on rGO thin films (anticlockwise). (a) Azide molecules bind to the $-$COOH groups on the rGO thin films, which are beforehand activated by EDC. The free $-$COOH groups are blocked by ethanolamine molecules. (b)-(c) The alkyne at the 5′ end of ssDNA receptors reacts with the azide, forming a triazole ring with the Cu NPs as catalysts. (d) The prostate-specific cDNA can theoretically be detected by the established rGO biosensor surface.

In an overall view, this thesis represents an elementary work to comprehend the basic properties of GO and rGO thin films. The established biosensor platforms based on the (r)GO thin films are all very promising towards the label-free detection of PSA. In a future work, combined with a microspotter technique, a multiplexing array with various receptor biomolecules on the same rGO based biosensor could be developed to offer multi-variable information of the biosensing results. The biosensing mechanism of the rGO based biosensors can be further analyzed and provide an opportunity for future healthcare applications, especially for future POC devices.

A | (r)GO Based Devices Preparation

A.1 Preparation of the Electrodes

The bottom IDEs are fabricated by standard photolithography (negative photoresist ARU4030), metal evaporation and lift-off process on 4-inch substrate, for instance SiO_2/Si or glass. The electrode is a bilayer stack: top layer is 270 nm Au and bottom 30 nm Ti as an adhesion layer.

Chip cleaning (note: this process can be applied to clean the wafers for preparing SPR chips):

- Spin dry: DIW, 700 rpm/3 min+2000 rpm/4 min, N_2
- Caro's acid tank: H_2SO_4 (98 %), H_2O_2(30 % by weight, 20-40 ml), 115 °C, 10 min
- DIW cleaning, 2-3 min
- Spin dry: DIW, 700 rpm/3 min + 2000 rpm/4 min, N_2
- Plasma stripper, 40 % O_2, 350 W, 5 min

Cr/Au Bottom electrodes: negative photoresist patterning

- 3 ml photoresist ARU4030, spin coat 100 rpm/7 s + 2000 rpm/60 s
- Soft bake 85 °C/120 s, 10 min cool down in the air
- Hard contact mode, exposure 10 s, UV energy dose 6.5 mW
- Post bake 115 °C/5 min, 10 min cool down in the air
- Development, AR300-26: DIW = 1:3, 15 s
- Spin-dry, 3000 rpm/30 s
- Microscope, check the structures

Cr/Au evaporation

- 270 nm Cr/Au evaporation (Au, 5 Å s^{-1}, Power 51 %)

Lift-off process

- In container, lift off in Acetone/20 min,
- In container, fresh Aceton/1 min
- In container, isoproponal/1 min
- Clean the wafer with DIW
- Spin-dry machine, program 1, 700 rpm/3 min; DIW; 200 rpm/4 min; N_2
- O_2 stripper, 40 % O_2, 350 W, 5 min

A.2 Gas-Phase Silanization

4-inch SiO_2 and glass wafer surface activation:

- Plasma stripper: 2.5 min, 240 W, 40 % O_2
- Or Piranha acid: H_2SO_4(95-97 %)/20 ml+H_2O_2(30 %)/1 ml, clean the wafer with pipette/5 min

4-inch SiO_2 and glass wafer APTES silanization

- After surface activation, immediately transfer the wafer to glove box, 2 µl APTES in petri dish/60 °C/2.5 h, the contact angle is around 60-70 °C

A.3 GO Spin-Coating

- $pH \approx 2.9$ GO solution
- 500 rpm/90 s or 100 rpm/120 s+2000 rpm/60 s, 90 °C/60 s between each spin coating

A.4 Etching of GO Thin-Films

GO patterning

- Positive photoresist ARU4030, spin coat 500 rpm/30 s+2000 rpm/60 s
- soft baking 85 °C/120 s
- contact mode, exposure 10 s, UV energy does 6.5 W
- Development, AR300-26: DIW = 1:3, 15 s
- O_2 plasma etching, 33 sccm O_2, 10 Pa chamber pressure, 10 W, 250

A.5 Wafer Dicing

Chip dicing (note: this process can be applied to dice the wafers for preparing SPR chips):

- Spin coat positive photoresist ARU4030, spin coat 500 rpm/30 s+2000 rpm/60 s
- Cut 4-inch wafer in to 7 mm $\times$ 7 mm chips (SPR chip size: 1.25 cm $\times$ 1.25 cm)

Chip cleaning:

- Aceton/5 min
- Fresh aceton/5 min
- Isoproponal/5 min
- N_2 dry

B | Equipment List

Table B.1: Equipment list.

Equipment	Model	Company	Country
Spin coater/Hot plate	Delta 30 T2	Süss	Germany
Mask aligner	MA/BA 6	Süss	Germany
Reactive ion etching (RIE)	SI 591 M	SENTECH Instruments GmbH	Germany
Plasma stripper	300-E	Technics Plasma	USA
Electron Beam Evaporator	BAK500	Oerlikon Balzers	Liechtenstein
High temperature oven	DS-3900-PC-150	INOTHERM	Germany
Vacuum oven	VT5042 EKP	Heraeus	Germany
Wafer dicing saw	DAD-2H/6T	Disco	Japan
Optical microscopy	Olympus BX51	Olympus	UK
Atomic Force Microscopy (AFM)	DEMENSION icon with ScanAsyst	Bruker Corporation	Germany
Scanning Electron Microscopy (SEM)	Zeiss Supra 40 SEM	Carl Zeiss AG	Germany
Transmission Electron Microscopy (TEM)	JEOL JEM 2010	Michigan TECH	USA
Fluorescence spectroscopy	FP 8300	Jesco Corporation	Japan
Ultraviolet-visible (UV-VIS) spectroscopy	PerkinElmer Lambda 40	PerkinElmer	USA
X-ray diffraction (XRD)	PANanlytical X'Pert PRO MPD Diffractometer	Philips	Netherland
Fourier-transform infrared spectroscopy (FTIR)	PerkinElmer Frontier	PerkinElmer	USA
Goniometers	Contact angle system OCA	Dataphysics	Germany
Spectroscopic Ellipsometer	SE850	SENTECH Instruments GmbH	Germany
Raman spectroscopy	LabRAM HR Evolution	Horiba	Japan
X-ray photoelectron spectroscopy (XPS)	D8Advance	Bruker AXS GmbH	Germany

Continued on next page

Table B.1 – continued from previous page

Equipment	Model	Company	Country
Surface Plasmon Resonance (SPR) system	SR7000DC	Reichert Technologies	USA
Semiconductor analyzer	Keithley 4200-SCS	Keithley Instruments	USA
Semiconductor analyzer	Agilent 4156C	Keysight Techologies	USA
Impedance analyzer	Ivium COMPACTSTAT.e	Ivium Techologies	Netherland
Silver/Silver chloride (Ag/AgCl) RE	DRIREF-2SH	World Precision Instruments	Germany
Three-dimensional (3D) material printer	Objet350 Connex	Stratays Ltd.	Israel
Localized Surface Plasmon Resonance (LSPR) system	Home-made equipment	University of Bath	UK

C | Chemical List

Table C.1: Chemical list.

Name of chemical	Company	Country
Graphite	Alfa Aeser	Germany
(3-Aminopropyl) triethoxysilane (APTES)	Sigma Aldrich	Germany
4-aminothiopheol (4-ATP)	Sigma Aldrich	Germany
$K_3Fe(CN)_6/K_4Fe(CN)_6$ (K3/K4)	Sigma Aldrich	Germany
Phosphate buffered saline (PBS)	Sigma Aldrich	Germany
Phosphate buffered saline with Tween 20 (PBST)	Sigma Aldrich	USA
Glycin	Sigma Aldrich	USA
NaOH	Sigma Aldrich	Germany
N-(3-Dimethylaminopropyl)-N'-ethylcarbodiimide hydrochloride (EDC)	Sigma Aldrich	Germany
N-Hydroxysuccinimide (NHS) Carbo-free blocking agent	Sigma Aldrich	Germany
Concanavalin A (ConA)	Vector Laboratories	USA
Maackia Amurensis lectin ii (MAA ii)	Vector Laboratories	USA
Biotin labeled MAA ii	Vector Laboratories	USA
PSA (SPR experiments)	Fitzgerald Industries International	USA
PSA specific aptamer (amino-, thiol terminated)	Sigma Aldrich	Germany
Anti-PSA antibody	Abcam	UK
Ethanolamine	Sigma Aldrich	Germany
Human serum albumin (HSA)	Sigma Aldrich	UK
PSA (all experiments except SPR)	Merck	USA
Au NPs (Gold (III) chloride hydrate, $HAuCl_4 \cdot x\,H_2O$)	Sigma Aldrich	UK
6-mercapto-1-hexanol (MCH)	Sigma Aldrich	UK
Ethanol	Sigma Aldrich	UK
Copper acetate	Sigma Aldrich	Germany
Lithium chloride	Sigma Aldrich	Germany
200 stainless sieves	Spoerl OHG	
25.4 mm dialysis membrane	Th. Geyer GmhH&Co.KG	

References

[1] A. W. Hsing, L. Tsao, and S. S. Devesa. "International trends and patterns of prostate cancer incidence and mortality". In: *International journal of cancer* 85.1 (2000), pp. 60–67.

[2] M. A. Dall'Era et al. "Active surveillance for early-stage prostate cancer: review of the current literature". In: *Cancer: Interdisciplinary International Journal of the American Cancer Society* 112.8 (2008), pp. 1650–1659.

[3] M. A. Dall'Era et al. "Active surveillance for prostate cancer: a systematic review of the literature". In: *European urology* 62.6 (2012), pp. 976–983.

[4] *GLOBOCAN 2012: Estimated Cancer Incidence, Mortality and Prevalence Worldwide in 2012*. URL: http://globocan.iarc.fr/Pages/fact_sheets_cancer.aspx.

[5] P. D. Baade, D. R. Youlden, and L. J. Krnjacki. *International epidemiology of prostate cancer: Geographical distribution and secular trends*. 2009.

[6] S. I. Berndt et al. "Two susceptibility loci identified for prostate cancer aggressiveness". In: *Nature communications* 6 (2015), p. 6889.

[7] V. M. Velonas et al. "Current Status of Biomarkers for Prostate Cancer". In: *Int. J. Mol. Sci.* 14 (2013).

[8] D. V. Makarov et al. "Biomarkers for Prostate Cancer". In: *Annu. Rev. Med.* 60 (2009), pp. 139–151.

[9] J. A. V. Antenor et al. "Preoperative PSA and progression-free survival after radical prostatectomy for Stage T1c disease". In: *Urology* 66.1 (2005), pp. 156–160.

[10] D. A. Armbruster. "Prostate-specific antigen: biochemistry, analytical methods, and clinical application." In: *Clinical chemistry* 39.2 (1993), pp. 181–195.

[11] E. P. DeAntoni et al. "Age-and race-specific reference ranges for prostate-specific antigen from a large community-based study". In: *Urology* 48.2 (1996), pp. 234–239.

[12] P. D. Loprinzi and M. Kohli. "Effect of physical activity and sedentary behavior on serum prostate-specific antigen concentrations: results from the National Health and Nutrition Examination Survey (NHANES), 2003-2006". In: *Mayo Clinic Proceedings*. Vol. 88. 1. Elsevier. 2013, pp. 11–21.

[13] W. Demark-Wahnefried et al. "Pilot study of dietary fat restriction and flaxseed supplementation in men with prostate cancer before surgery: exploring the effects on hormonal levels, prostate-specific antigen, and histopathologic features". In: *Urology* 58.1 (2001), pp. 47–52.

[14] R. E. Link et al. “Variation in prostate specific antigen results from 2 different assay platforms: clinical impact on 2,304 patients undergoing prostate cancer screening”. In: *The Journal of urology* 171.6 (2004), pp. 2234–2238.

[15] S. Rausch et al. “Assessment of a new point-of-care system for detection of prostate specific antigen”. In: *BMC Urol.* 16.1 (2016).

[16] *Elecsys ® free prostate specific antigen (free PSA)*. Tech. rep. Roche Diagnostics Ltd., 2011, pp. 1–2.

[17] *total PSA*. Tech. rep. Roche, 2010, pp. 7–10.

[18] S. healthineers. *Prostate cancer*.

[19] Cardinal Health. *Clinical Chemistry*. Tech. rep. 2016.

[20] *VITROS ® Assay Menu*. Tech. rep. Ortho Clinical Diagnostics, 2018.

[21] K. Hutchinson. *Hybritech Prostate Specific Antigen (PSA) on the Beckman Access*. Tech. rep. 2002.

[22] *Total PSA ARC system Abbott Diagnotics*. Tech. rep. 2007.

[23] O. Karim et al. “Point-of-care PSA testing: An evaluation of PSAwatch”. In: *Prostate Cancer Prostatic Dis.* 10.3 (2007), pp. 270–273.

[24] *Seikisui Diagnostics PSA Point-of-Care testing*.

[25] *POINT-OF-CARE TESTING WITH concile® Ω100*. Tech. rep. concile GmbH, 2014.

[26] *True Diagnostics PSA Point-of-Care testing*.

[27] A. W. Partin et al. “The use of prostate specific antigen, clinical stage and Gleason score to predict pathological stage in men with localized prostate cancer”. In: *The Journal of urology* 150.1 (1993), pp. 110–114.

[28] C. H. Bangma, S. Roemeling, and F. H. Schröder. “Overdiagnosis and overtreatment of early detected prostate cancer”. In: *World J Urol* 25 (2007), pp. 3–9.

[29] S. C. Williams. “Circulating tumor cells”. In: *Proceedings of the National Academy of Sciences* 110.13 (2013), pp. 4861–4861.

[30] M. Landon, ed. *Biology: Understanding Living Matter*. The Study of Science Series (2015).

[31] C. Thã. *Exosome Explosion*. July 2011. URL: https://www.the-scientist.com/features/exosome-explosion-42253.

[32] A. Simeonov. *Defenders Against Death*. 2014. URL: https://www.genengnews.com/gen-exclusives/defenders-against-death/77900097.

[33] D. A. Healy et al. “Biosensor developments: application to prostate-specific antigen detection”. In: *TRENDS in Biotechnology* 25.3 (2007), pp. 125–131.

[34] G. Zheng et al. “Multiplexed electrical detection of cancer markers with nanowire sensor arrays”. In: *Nature biotechnology* 23.10 (2005), p. 1294.

[35] C. Li et al. “Complementary detection of prostate-specific antigen using In2O3 nanowires and carbon nanotubes”. In: *Journal of the American Chemical Society* 127.36 (2005), pp. 12484–12485.

[36] B. Zhang et al. “A novel multi-array immunoassay device for tumor markers based on insert-plug model of piezoelectric immunosensor”. In: *Biosensors and Bioelectronics* 23.1 (2007), pp. 19–25.

[37] D.-J. Kim et al. “Organic electrochemical transistor based immunosensor for prostate specific antigen (PSA) detection using gold nanoparticles for signal amplification”. In: *Biosensors and Bioelectronics* 25.11 (2010), pp. 2477–2482.

[38] J. Lee et al. “Two-dimensional layered MoS 2 biosensors enable highly sensitive detection of biomolecules”. In: *Scientific reports* 4 (2014), p. 7352.

[39] D. Rani et al. “Top-Down Fabricated Silicon Nanowire Arrays for Field-Effect Detection of Prostate-Specific Antigen”. In: *ACS omega* 3.8 (2018), pp. 8471–8482.

[40] V. K. Tamboli et al. “Hybrid synthetic receptors on mosfet devices for detection of prostate specific antigen in human plasma”. In: *Analytical chemistry* 88.23 (2016), pp. 11486–11490.

[41] P. S. Waggoner, M. Varshney, and H. G. Craighead. “Detection of prostate specific antigen with nanomechanical resonators”. In: *Lab on a Chip* 9.21 (2009), pp. 3095–3099.

[42] F. Zhang et al. “A microfluidic love-wave biosensing device for PSA detection based on an aptamer beacon probe”. In: *Sensors* 15.6 (2015), pp. 13839–13850.

[43] P. Jolly et al. “Aptamer–MIP hybrid receptor for highly sensitive electrochemical detection of prostate specific antigen”. In: *Biosensors and Bioelectronics* 75 (2016), pp. 188–195.

[44] P. Damborskỳ et al. “Surface plasmon resonance application in prostate cancer biomarker research”. In: *Chemical Papers* 69.1 (2015), pp. 143–149.

[45] I. Tzouvadaki et al. “Label-free ultrasensitive memristive aptasensor”. In: *Nano letters* 16.7 (2016), pp. 4472–4476.

[46] E. Roduner. “Size matters: why nanomaterials are different”. In: *Chemical Society Reviews* 35.7 (2006), pp. 583–592.

[47] F. Schedin et al. “Detection of Individual Gas Molecules Adsorbed on Graphene”. In: *Nat. Mater.* 6 (2007), pp. 652–655.

[48] J. York et al. “Single-molecule detection of DNA via sequence-specific links between F 1-ATPase motors and gold nanorod sensors”. In: *Lab on a Chip* 8.3 (2008), pp. 415–419.

[49] Z.-Y. Li and Y. Xia. “Metal nanoparticles with gain toward single-molecule detection by surface-enhanced Raman scattering”. In: *Nano letters* 10.1 (2009), pp. 243–249.

[50] S. S. Acimovic et al. “Plasmon near-field coupling in metal dimers as a step toward single-molecule sensing”. In: *ACS nano* 3.5 (2009), pp. 1231–1237.

[51] Z. Ye et al. “Preparation, characterization, and time-resolved fluorometric application of silica-coated terbium (III) fluorescent nanoparticles”. In: *Analytical Chemistry* 76.3 (2004), pp. 513–518.

[52] A. I. Barbosa et al. “Portable smartphone quantitation of prostate specific antigen (PSA) in a fluoropolymer microfluidic device”. In: *Biosensors and Bioelectronics* 70 (2015), pp. 5–14.

[53] L. Li et al. “Growth of gold-manganese oxide nanostructures on a 3D origami device for glucose-oxidase label based electrochemical immunosensor”. In: *Biosensors and Bioelectronics* 61 (2014), pp. 76–82.

[54] P. R. Wallace. “The band theory of graphite”. In: *Phys. Rev.* 71.9 (1947), pp. 622–634.

[55] M. P. Sharma, L. G. Johnson, and J. W. McClure. “Diamagnetism of graphite”. In: *Phys. Lett. A* 44.7 (1973), pp. 445–446.

[56] J. C. Slonczewski and P. R. Weiss. “Band structure of graphite”. In: *Phys. Rev.* 109.2 (1958), pp. 272–279.

[57] F. D. M. Haldane. “Model for a quantum hall effect without landau levels: Condensed-matter realization of the "parity anomaly"”. In: *Phys. Rev. Lett.* 61.18 (1988), pp. 2015–2018.

[58] G. W. Semenoff. “Condensed-Matter simulation of a three-Dimensional anomaly”. In: *Phys. Rev. Lett.* 53.26 (1984), pp. 2449–2452.

[59] K. S. Novoselov et al. “Electric Field Effect in Atomically Thin Carbon Films”. In: *Science* 306 (2004), pp. 666–669.

[60] A. H. Castro Neto et al. “The electronic properties of graphene”. In: *Rev. Mod. Phys.* 81.1 (Jan. 2009), pp. 109–162.

[61] R. R. Nair et al. “Fine Structure Constant Defines Visual Transperency of Graphene”. In: *Science* 320.June (2008), p. 2008.

[62] K. F. Mak et al. “Measurement of the optical conductivity of graphene.” In: *Phys. Rev. Lett.* 101.19 (2008), p. 196405.

[63] J. Baringhaus et al. “Exceptional ballistic transport in epitaxial graphene nanoribbons”. In: *Nature* 506.7488 (Feb. 2014), pp. 349–354.

[64] F. Javier García de Abajo. “Graphene plasmonics: Challenges and opportunities”. In: *ACS Photonics* 1.3 (2014), pp. 133–152.

[65] A. N. Grigorenko, M. Polini, and K. S. Novoselov. “Graphene plasmonics”. In: *Nat Phot.* 6.11 (Nov. 2012), pp. 749–758.

[66] T. J. Constant et al. “All-optical generation of surface plasmons in graphene”. In: *Nat. Phys.* 12.2 (Feb. 2016), pp. 124–127.

[67] C. Lee et al. “Measurement of the Elastic Properties and Intrinsic Strength of Monolayer Graphene”. In: *Science* 321.18 July 2008 (2008), pp. 385–388.

[68] Y. H. Kahng et al. “Thermal stability of multilayer graphene films synthesized by chemical vapor deposition and stained by metallic impurities.” In: *Nanotechnology* 23.7 (2012), p. 75702.

[69] A. Bendali et al. “Purified Neurons can Survive on Peptide-Free Graphene Layers”. In: *Adv. Healthc. Mater.* 2 (2013), pp. 929–933.

[70] D. Rodrigo et al. “Mid-infrared plasmonic biosensing with graphene”. In: *Science* 349.6244 (2015), pp. 165–168.

[71] D. R. Dreyer et al. “The chemistry of graphene oxide”. In: *Chem. Soc. Rev.* 39.1 (2010), pp. 228–240.

[72] G. Eda and M. Chhowalla. "Chemically derived graphene oxide: towards large-area thin-film electronics and optoelectronics". In: *Adv. Mater.* 22.22 (2010), pp. 2392–2415.

[73] A. Bagri et al. "Structural evolution during the reduction of chemically derived graphene oxide". In: *Nat. Chem.* 2.7 (2010), pp. 581–587.

[74] C. Gomez-Navarro et al. "Electronic Transport Properties of Individual Chemically Reduced Graphene Oxide Sheets". In: *Nano Lett.* 7.11 (2007), pp. 3499–3503.

[75] S. Pei and H.-M. M. Cheng. "The reduction of graphene oxide". In: *Carbon N. Y.* 50.9 (2012), pp. 3210–3228.

[76] X. Li et al. "Evolution of graphene growth on Ni and Cu by carbon isotope labeling". In: *Nano Lett.* 9.12 (2009), pp. 4268–4272.

[77] K. V. Emtsev et al. "Towards wafer-size graphene layers by atmospheric pressure graphitization of silicon carbide". In: *Nat. Mater.* 8.3 (2009), pp. 203–207.

[78] P. N. David Pines. *The Theory of Quantum Liquids: Normal Fermi liquids*. W.A. Benjamin, 1966.

[79] K. S. Kim et al. "Large-scale pattern growth of graphene films for stretchable transparent electrodes". In: *Nature* 457.7230 (Feb. 2009), pp. 706–710.

[80] X. Li et al. "Transfer of Large-Area Graphene Films for High-Performance Transparent Conductive Electrodes". In: *Nano Lett* 9 (2009), pp. 4359–4363.

[81] M. Dankerl et al. "Graphene Solution-Gated Field-Effect Transistor Array for Sensing Applications". In: *Adv. Funct. Mater* 20 (2010), pp. 3117–3124.

[82] A. Venugopal et al. "Effective mobility of single-layer graphene transistors as a function of channel dimensions". In: *J. Appl. Phys.* 109.10 (2011).

[83] S. J. Park et al. "Ultrasensitive Flexible Graphene Based Field-Effect Transistor (FET)-Type Bioelectronic Nose". In: *Nano Lett.* 12.10 (2012), pp. 5082–5090.

[84] L. H. Hess, M. Seifert, and J. A. Garrido. "Graphene Transistors for Bioelectronics". In: *Proc. IEEE* 101.7 (July 2013), pp. 1780–1792.

[85] S. Reich et al. "Tight-binding description of graphene". In: *Physical Review B* 66.3 (2002), p. 035412.

[86] T. Jacqmin et al. "Direct observation of Dirac cones and a flatband in a honeycomb lattice for polaritons". In: *Physical review letters* 112.11 (2014), p. 116402.

[87] A. K. Geim and K. S. Novoselov. "The rise of graphene". In: *Nat. Mater.* 6 (2007), pp. 183–191.

[88] R. S. Deacon et al. "Cyclotron resonance study of the electron and hole velocity in graphene monolayers". In: *Phys. Rev. B - Condens. Matter Mater. Phys.* 76.8 (2007).

[89] K. S. Novoselov et al. "A roadmap for graphene". In: *Nature* 490.7419 (Oct. 2012), pp. 192–200.

[90] P. Y. Huang et al. "Grains and grain boundaries in single-layer graphene atomic patchwork quilts". In: *Nature* 469.7330 (Jan. 2011), pp. 389–392.

[91] S. De and J. N. Coleman. "Are There Fundamental Limitations on the Sheet Resistance and Transmittance of Thin Graphene Films?" In: *ACS Nano* 4.5 (2010), pp. 2713–2720.

[92] J.-N. Fuchs and M. O. Goerbig. "Introduction to the physical properties of graphene". In: *Lecture notes* (2008).

[93] N. Peres. "Graphene, new physics in two dimensions". In: *Europhysics News* 40.3 (2009), pp. 17–20.

[94] B. Partoens and F. M. Peeters. "From graphene to graphite: Electronic structure around the K point". In: *Phys. Rev. B - Condens. Matter Mater. Phys.* 74.7 (2006).

[95] S. V. Morozov et al. "Two-dimensional electron and hole gases at the surface of graphite". In: *Phys. Rev. B - Condens. Matter Mater. Phys.* 72.20 (2005).

[96] A. Calogeracos and N. Dombey. "History and physics of the Klein paradox". In: *Contemp. Phys.* 40.5 (1999), pp. 313–321.

[97] C. Itzykson and J.-B. Zuber. *Quantum field theory*. Courier Corporation, 2006.

[98] L. Van Hove. "The occurrence of singularities in the elastic frequency distribution of a crystal". In: *Physical Review* 89.6 (1953), p. 1189.

[99] A. N. Grigorenko, M. Polini, and K. S. Novoselov. "Graphene plasmonics - optics in flatland". In: *Condens. Matter* (2013), pp. 1–25.

[100] F. Bonaccorso et al. "Graphene Photonics and Optoelectronics". In: *Nat. Photonics* 4.9 (2010), pp. 611–622.

[101] F. J. García De Abajo. "Multiple excitation of confined graphene plasmons by single free electrons". In: *ACS Nano* 7.12 (2013), pp. 11409–11419.

[102] S. Thongrattanasiri, A. Manjavacas, and F. J. García De Abajo. "Quantum finite-size effects in graphene plasmons". In: *ACS Nano* 6.2 (2012), pp. 1766–1775.

[103] F. H. L. Koppens, D. E. Chang, and F. J. García De Abajo. "Graphene plasmonics: A platform for strong light-matter interactions". In: *Nano Lett.* 11.8 (2011), pp. 3370–3377.

[104] J. Chen et al. "Optical nano-imaging of gate-tunable graphene plasmons." In: *Nature* 487.7405 (2012), pp. 77–81.

[105] Z. Q. Li et al. "Dirac charge dynamics in graphene by infrared spectroscopy". In: *Nat. Phys.* 4.July (2008), pp. 6–9.

[106] C.-F. F. Chen et al. "Controlling inelastic light scattering quantum pathways in graphene". In: *Nature* 471.7340 (2011), pp. 617–620.

[107] S. M. Kozlov, F. Viñes, and A. Görling. "Bandgap engineering of graphene by physisorbed adsorbates". In: *Adv. Mater.* 23.22-23 (2011), pp. 2638–2643.

[108] L. Wu et al. "Highly sensitive graphene biosensors based on surface plasmon resonance". In: *Opt. Express* 18.14 (2010), pp. 15458–15463.

[109] J. W. Suk et al. "Transfer of CVD-Grown Monolayer Graphene onto Arbitrary Substrates". In: *ACS Nano* 5.9 (Sept. 2011), pp. 6916–6924.

[110] X. Liang et al. "Toward Clean and Crackless Transfer of Graphene". In: *ACS Nano* 5 (2011), pp. 9144–9153.

[111] D. C. Marcano et al. “Improved Synthesis of Graphene Oxide”. In: *ACS Nano* 4.8 (2010), pp. 4806–4814.

[112] S. Eigler et al. “Wet Chemical Synthesis of Graphene”. In: *Adv. Mater.* 25.26 (2013), pp. 3583–3587.

[113] W. S. Hummers and R. E. Offeman. “Preparation of Graphitic Oxide”. In: *J. Am. Chem. Soc.* 80.6 (1958), pp. 1339–1339.

[114] H. Bi et al. “Ultrahigh humidity sensitivity of graphene oxide”. In: *Sci. Rep.* 3 (Sept. 2013), p. 2714.

[115] H. A. Becerril et al. “Evaluation of Solution-Processed Reduced Graphene Oxide Films as Transparent Conductors”. In: *ACS Nano* 2.3 (2008), pp. 463–470.

[116] X. Lu et al. “Front-End-of-Line Integration of Graphene Oxide for Graphene-Based Electrical Platforms”. In: *Adv. Mater. Technol.* 1700318 (2018), p. 1700318.

[117] X. Du et al. “Approaching Ballistic Transport in Suspended Graphene”. In: *Nat Nano* 3.8 (Aug. 2008), pp. 491–495.

[118] S. Eigler, C. Dotzer, and A. Hirsch. “Visualization of defect densities in reduced graphene oxide”. In: *Carbon N. Y.* 50.10 (2012), pp. 3666–3673.

[119] C. T. Chien et al. “Tunable photoluminescence from graphene oxide”. In: *Angew. Chemie - Int. Ed.* 51.27 (2012), pp. 6662–6666.

[120] Z. Luo et al. “Photoluminescence and band gap modulation in graphene oxide”. In: *Appl. Phys. Lett.* 94.11 (2009).

[121] J. Shang et al. “The Origin of Fluorescence from Graphene Oxide”. In: *Sci. Rep.* 2 (Nov. 2012), p. 792.

[122] T. Szabó, O. Berkesi, and I. Dékány. “DRIFT study of deuterium-exchanged graphite oxide”. In: *Carbon N. Y.* 43.15 (2005), pp. 3186–3189.

[123] A. V. Talyzin et al. “The structure of graphene oxide membranes in liquid water{,} ethanol and water-ethanol mixtures”. In: *Nanoscale* 6.1 (2014), pp. 272–281.

[124] M. Schmitt. “Analysis of silanes and of siloxanes formation by Raman spectroscopy ”. In: *RSC Adv.* 4.4 (2014), pp. 1907–1917.

[125] M. Schmitt et al. “Statistical approach for contact angle determination on inclining surfaces: "slow-moving" analyses of non-axisymmetric drops on a flat silanized silicon wafer”. In: *J. Adhes. Sci. Technol.* 29.17 (2015), pp. 1796–1806.

[126] L. Wu et al. “Aggregation Kinetics of Graphene Oxides in Aqueous Solutions: Experiments,Mechanisms,and Modeling”. In: *Langmuir* 29.49 (2013), pp. 15174–15181.

[127] N. I. Kovtyukhova et al. “Layer-by-Layer Assembly of Ultrathin Composite Films from Micron-Sized Graphite Oxide Sheets and Polycations”. In: *Chem. Mater.* 11.3 (1999), pp. 771–778.

[128] F. A. Jenkins, H. E. White, and D. G. Brukhard. “Fundamentals of Optics”. In: *Am. J. Phys.* 26.4 (1958), p. 272.

[129] J. Zheng et al. “High quality graphene with large flakes exfoliated by oleyl amine”. In: *Chem. Commun.* 46.31 (2010), pp. 5728–5730.

[130] S. Gilje et al. “A Chemical Route to Graphene for Device Applications”. In: *Nano Lett.* 7.11 (2007), pp. 3394–3398.

[131] S. Stankovich et al. “Synthesis of graphene-based nanosheets via chemical reduction of exfoliated graphite oxide”. In: *Carbon N. Y.* 45.7 (June 2007), pp. 1558–1565.

[132] M. C. Zaretsky, L. Mouayad, and J. R. Melcher. “Continuum Properties from Interdigital Electrode Dielectrometry”. In: *Electr. Insul. IEEE Trans.* 23.6 (Dec. 1988), pp. 897–917.

[133] N. F. Sheppard, R. C. Tucker, and C. Wu. “Electronic conductivity measurement using microfabricated interdigitated electrodes”. In: *Anal. Chem.* 65.9 (1993), pp. 1199–1202.

[134] R. Igreja and C. J. Dias. “Analytical evaluation of the interdigital electrodes capacitance for a multi-layered structure”. In: *Sensors Actuators A Phys.* 112.2–3 (May 2004), pp. 291–301.

[135] D. Li et al. “Processable aqueous dispersions of graphene nanosheets”. In: *Nat. Nanotechnol.* 3.2 (2008), pp. 101–105.

[136] S. Park et al. “Hydrazine-reduction of graphite- and graphene oxide”. In: *Carbon N. Y.* 49.9 (2011), pp. 3019–3023.

[137] C. K. Chua and M. Pumera. “The reduction of graphene oxide with hydrazine: elucidating its reductive capability based on a reaction-model approach”. In: *Chem. Commun.* 52.1 (2016), pp. 72–75.

[138] S. D. Perera et al. “Alkaline deoxygenated graphene oxide for supercapacitor applications: An effective green alternative for chemically reduced graphene”. In: *J. Power Sources* 215 (2012), pp. 1–10.

[139] C. K. Chua and M. Pumera. “Reduction of graphene oxide with substituted borohydrides”. In: *J. Mater. Chem. A* 1.5 (2013), pp. 1892–1898.

[140] Z.-z. Yang et al. “A simple method for the reduction of graphene oxide by sodium borohydride with CaCl2 as a catalyst”. In: *New Carbon Mater.* 30.1 (2015), pp. 41–47.

[141] W. I. Hayes et al. “Production of reduced graphene oxide via hydrothermal reduction in an aqueous sulphuric acid suspension and its electrochemical behaviour”. In: *J. Solid State Electrochem.* 19.2 (2014), pp. 361–380.

[142] M. J. Fernández-Merino et al. “Vitamin C is an ideal substitute for hydrazine in the reduction of graphene oxide suspensions”. In: *J. Phys. Chem. C* 114.14 (2010), pp. 6426–6432.

[143] J. Wang, E. C. Salihi, and L. Šiller. “Green reduction of graphene oxide using alanine”. In: *Mater. Sci. Eng. C* 72 (2017), pp. 1–6.

[144] S.-J. Choi, S.-J. Kim, and I.-D. Kim. “Ultrafast optical reduction of graphene oxide sheets on colorless polyimide film for wearable chemical sensors”. In: *NPG Asia Mater.* 8.9 (2016), e315.

[145] S.-H. Park and H.-S. Kim. “Environmentally benign and facile reduction of graphene oxide by flash light irradiation”. In: *Nanotechnology* 26.20 (2015), p. 205601.

[146] Y. H. Ding et al. “A green approach to the synthesis of reduced graphene oxide nanosheets under UV irradiation”. In: *Nanotechnology* 22.21 (2011), p. 215601.

[147] W. Gao et al. “New insights into the structure and reduction of graphite oxide”. In: *Nat. Chem.* 1.5 (2009), pp. 403–408.

[148] S. H. Huh. “Thermal Reduction of Graphene Oxide”. In: *Phys. Appl. Graphene - Exp.* (2011), pp. 73–90.

[149] D. Pan et al. “Hydrothermal route for cutting graphene sheets into blue-luminescent graphene quantum dots”. In: *Adv. Mater.* 22.6 (2010), pp. 734–738.

[150] M. J. McAllister et al. “Single Sheet Functionalized Graphene by Oxidation and Thermal Expansion of Graphite”. In: *Chem. Mater.* 19.18 (2007), pp. 4396–4404.

[151] B. Sharma. *Metal-semiconductor Schottky barrier junctions and their applications*. Springer Science & Business Media, 2013.

[152] P. T. Kissinger and W. R. Heineman. “Cyclic voltammetry”. In: *J. Chem. Educ.* 60.9 (Sept. 1983), p. 702.

[153] G. A. Mabbott. “An introduction to cyclic voltammetry”. In: *J. Chem. Educ.* 60.9 (Sept. 1983), p. 697.

[154] P. Bergveld. “Development of an ion-sensitive solid-state device for neurophysiological measurements”. In: *IEEE Transactions on Biomedical Engineering* 1 (1970), pp. 70–71.

[155] P. Bergveld. “Thirty years of ISFETOLOGY: What happened in the past 30 years and what may happen in the next 30 years”. In: *Sensors Actuators B Chem.* 88.1 (2003), pp. 1–20.

[156] T. Wehling et al. “Molecular doping of graphene”. In: *Nano letters* 8.1 (2008), pp. 173–177.

[157] S. Wang et al. “Band-like transport in surface-functionalized highly solution-processable graphene nanosheets”. In: *Adv. Mater.* 20.18 (2008), pp. 3440–3446.

[158] G. Eda, G. Fanchini, and M. Chhowalla. “Large-area ultrathin films of reduced graphene oxide as a transparent and flexible electronic material”. In: *Nat. Nanotechnol.* 3.5 (2008), pp. 270–274.

[159] H. Chang et al. “Thin film field-effect phototransistors from bandgap-tunable, solution-processed, few-layer reduced graphene oxide films”. In: *Adv. Mater.* 22.43 (2010), pp. 4872–4876.

[160] S. Wang et al. “High mobility, printable, and solution-processed graphene electronics”. In: *Nano Lett.* 10.1 (2010), pp. 92–98.

[161] H. Feng et al. “A low-temperature method to produce highly reduced graphene oxide”. In: *Nat. Commun.* 4 (2013), pp. 1537–1539.

[162] D. Voiry et al. “High-quality graphene via microwave reduction of solution-exfoliated graphene oxide”. In: *Science* 353.6306 (2016), pp. 1413–1416.

[163] K. Graf and M. Kappl. *Physics and chemistry of interfaces*. John Wiley & Sons, 2006.

[164] W. Koppenol. "Effect of a molecular dipole on the ionic strength dependence of a biomolecular rate constant. Identification of the site of reaction". In: *Biophysical journal* 29.3 (1980), pp. 493–507.

[165] S. Salgin, U. Salgin, and S. Bahadir. "Zeta potentials and isoelectric points of biomolecules: the effects of ion types and ionic strengths". In: *Int. J. Electrochem. Sci* 7.12 (2012), pp. 12404–12414.

[166] G. Eda and M. Chhowalla. "Graphene-based Composite Thin Films for Electronics". In: *Nano Lett.* 9.2 (2009), pp. 814–818.

[167] A. Bhaumik et al. "Reduced Graphene Oxide Thin Films with Very Large Charge Carrier Mobility Using Pulsed Laser Deposition". In: *J. Mater. Sci. Eng.* 06.04 (2017).

[168] W. Härdle and L. Simar. "Appendix A". In: *Technometrics* 47.4 (2003), p. 486.

[169] J. M. David and M. G. Buehler. "A numerical analysis of various cross sheet resistor test structures". In: *Solid. State. Electron.* 20.6 (1977), pp. 539–543.

[170] Fridman. "Measurements with the Model 4200-SCS". In: *Appl. Note* 2475 (2007), pp. 2005–2007.

[171] E. Smith and G. Dent. *Modern Raman Spectroscopy - A Practical Approach*. 2005, pp. 1–210.

[172] A. C. Ferrari et al. "Raman spectrum of graphene and graphene layers". In: *Physical review letters* 97.18 (2006), p. 187401.

[173] A. C. Ferrari. "Raman spectroscopy of graphene and graphite: disorder, electron–phonon coupling, doping and nonadiabatic effects". In: *Solid state communications* 143.1-2 (2007), pp. 47–57.

[174] L. M. Malard et al. *Raman spectroscopy in graphene*. 2009.

[175] A. C. Ferrari and D. M. Basko. "Raman spectroscopy as a versatile tool for studying the properties of graphene". In: *Nat. Nanotechnol.* 8.4 (2013), pp. 235–246.

[176] R. Beams, L. Gustavo Cançado, and L. Novotny. "Raman characterization of defects and dopants in graphene". In: *J. Phys. Condens. Matter* 27.8 (2015), p. 083002.

[177] Z. Yan and A. R. Barron. "Characterization of Graphene by Raman Spectroscopy". In: *OpenStax-CNX* (2010), pp. 1–4.

[178] J. Ribeiro-Soares et al. "Structural analysis of polycrystalline graphene systems by Raman spectroscopy". In: *Carbon N. Y.* 95 (2015), pp. 646–652.

[179] R. J. Nemanich and S. A. Solin. "First- and second-order Raman scattering from finite-size crystals of graphite". In: *Phys. Rev. B* 20.2 (1979), pp. 392–401.

[180] F. Tuinstra and J. L. Koenig. "Raman spectrum of graphite". In: *The Journal of Chemical Physics* 53.3 (1970), pp. 1126–1130.

[181] S. Claramunt et al. "The importance of interbands on the interpretation of the raman spectrum of graphene oxide". In: *J. Phys. Chem. C* 119.18 (2015), pp. 10123–10129.

[182] D. Yang et al. “Chemical analysis of graphene oxide films after heat and chemical treatments by X-ray photoelectron and Micro-Raman spectroscopy”. In: *Carbon N. Y.* 47.1 (2009), pp. 145–152.

[183] C. Cong et al. “Second-order overtone and combination raman modes of graphene layers in the range of 1690-2150 cm-1”. In: *ACS Nano* 5.3 (2011), pp. 1600–1605.

[184] R. Rao et al. “Effects of layer stacking on the combination raman modes in graphene”. In: *ACS Nano* 5.3 (2011), pp. 1594–1599.

[185] P. Tan, S. Dimovski, and Y. Gogotsi. “Raman scattering of non-planar graphite: arched edges, polyhedral crystals, whiskers and cones”. In: *Philos. Trans. R. Soc. A Math. Phys. Eng. Sci.* 362.1824 (2004), pp. 2289–2310.

[186] L. E. Delle et al. *Impedimetric immunosensor for the detection of histamine based on reduced graphene oxide*. 2015.

[187] G. Beamson and D. Briggs. “High Resolution XPS of Organic Polymers: The Scienta ESCA3000 Database”. In: *J. Chem. Educ.* 70.1 (1993), A25.

[188] H. Raether. *Surface plasmons on smooth and rough surfaces and on gratings*. Vol. 111. Berlin: Springer, 1988.

[189] B. Liedberg, C. Nylander, and I. Lunström. “Surface plasmon resonance for gas detection and biosensing”. In: *Sensors and actuators* 4 (1983), pp. 299–304.

[190] J. Zhang et al. “A novel surface plasmon resonance biosensor based on graphene oxide decorated with gold nanorod-antibody conjugates for determination of transferrin”. In: *Biosens. Bioelectron.* 45.1 (2013), pp. 230–236.

[191] I. V. Lightcap, T. H. Kosel, and P. V. Kamat. “Anchoring semiconductor and metal nanoparticles on a two-dimensional catalyst mat. storing and shuttling electrons with reduced graphene oxide”. In: *Nano Lett.* 10.2 (2010), pp. 577–583.

[192] C.-F. Huang et al. “Graphene oxide and dextran capped gold nanoparticles based surface plasmon resonance sensor for sensitive detection of concanavalin A.” In: *Biosens. Bioelectron.* 50 (2013), pp. 305–310.

[193] P. Subramanian et al. “Lysozyme detection on aptamer functionalized graphene-coated SPR interfaces”. In: *Biosens. Bioelectron.* 50 (2013), pp. 239–243.

[194] N. F. Chiu and T. Y. Huang. “Sensitivity and kinetic analysis of graphene oxide-based surface plasmon resonance biosensors”. In: *Sensors Actuators, B Chem.* 197 (2014), pp. 35–42.

[195] T. Xue et al. “Surface plasmon resonance technique for directly probing the interaction of DNA and graphene oxide and ultra-sensitive biosensing”. In: *Biosens. Bioelectron.* 58 (2014), pp. 374–379.

[196] S. Szunerits et al. “Recent advances in the development of graphene-based surface plasmon resonance (SPR) interfaces”. In: *Anal. Bioanal. Chem.* 405.5 (2013), pp. 1435–1443.

[197] Y. V. Stebunov et al. “Highly Sensitive and Selective Sensor Chips with Graphene-Oxide Linking Layer”. In: *ACS Appl. Mater. Interfaces* 7.39 (2015), pp. 21727–21734.

[198] Y. Shen et al. “Optical investigation of reduced graphene oxide by spectroscopic ellipsometry and the band-gap tuning”. In: *Appl. Phys. Lett.* 99.14 (2011).

[199] M. Acik et al. “Unusual infrared-absorption mechanism in thermally reduced graphene oxide.” In: *Nat. Mater.* 9.10 (2010), pp. 840–845.

[200] *Reichert SR7000DC System User Guide Version 2*.

[201] E. Kretschmann. “Decay of non radiative surface plasmons into light on rough silver films. Comparison of experimental and theoretical results”. In: *Optics Communications* 6.2 (1972), pp. 185–187.

[202] C. Guiducci. *Surface Plasmon Resonance Based Systems*. Tech. rep., pp. 1–28.

[203] G. Electric and E. Pessimist. “Handbook of surface plasmon resonance”. In: (2003).

[204] W.-M. Munief et al. “Silane deposition via gas-phase evaporation and high-resolution surface characterization of the ultra-thin siloxane coatings”. In: *Langmuir* (2018).

[205] J. Kim et al. “Electrical Control of Optical Plasmon Resonance with Graphene”. In: *Nano Lett.* 12.11 (2012), pp. 5598–5602.

[206] L. In and O. Products. “Reichert Electrochemical Flow Cell User Guide Version 2”. In: *Science* November (2010), pp. 1–6.

[207] V. Lioubimov et al. “Effect of varying electric potential on surface-plasmon resonance sensing.” In: *Appl. Opt.* 43.17 (2004), pp. 3426–3432.

[208] H. Ohshima and K. Furusawa. *Electrical phenomena at interfaces: fundamentals: measurements, and applications*. Vol. 76. CRC Press, 1998.

[209] V. Lioubimov et al. “Effect of varying electric potential on surface-plasmon resonance sensing”. In: *Applied optics* 43.17 (2004), pp. 3426–3432.

[210] J. R. Macdonald. “Impedance spectroscopy: old problems and new developments”. In: *Electrochim. Acta* 35.10 (1990), pp. 1483–1492.

[211] E. Barsoukov and J. R. Macdonald. *Impedance Spectroscopy: Theory, Experiment, and Applications, 2nd Edition*. WILEY, 2005.

[212] J. R. Macdonald. “Impedance spectroscopy: Models, data fitting, and analysis”. In: *Solid State Ionics* 176.25-28 (2005), pp. 1961–1969.

[213] M. E. Orazem and B. Tribollet. *Electrochemical Impedance Spectroscopy*. WILEY, 2011.

[214] B.-Y. Chang and S.-M. Park. “Electrochemical impedance spectroscopy”. In: *Annual Review of Analytical Chemistry* 3 (2010), pp. 207–229.

[215] G. Tsekenis. “Studies towards the development of label-free AC impedimetric immunosensors for healthcare and food quality control”. PhD thesis. 2008.

[216] F. Lisdat and D. Schafer. “The use of electrochemical impedance spectroscopy for biosensing”. In: *Anal. Bioanal. Chem.* 391.5 (2008), pp. 1555–1567.

[217] S. Vogt et al. “Critical View on Electrochemical Impedance Spectroscopy Using the Ferri/Ferrocyanide Redox Couple at Gold Electrodes”. In: *Anal. Chem.* 88.8 (2016), pp. 4383–4390.

[218] M. Bart et al. “On the response of a label-free interferon-γ immunosensor utilizing electrochemical impedance spectroscopy”. In: *Biosens. Bioelectron.* 21.1 (2005), pp. 49–59.

[219] C. Laborde et al. “Real-time imaging of microparticles and living cells with CMOS nanocapacitor arrays”. In: 10.August (2015).

[220] A. Bonanni, A. H. Loo, and M. Pumera. “Graphene for impedimetric biosensing”. In: *TrAC - Trends Anal. Chem.* 37 (2012), pp. 12–21.

[221] A. Bonanni, A. Ambrosi, and M. Pumera. “Nucleic acid functionalized graphene for biosensing”. In: *Chem. - A Eur. J.* 18.6 (2012), pp. 1668–1673.

[222] D. Berdat et al. “Label-free detection of DNA with interdigitated micro-electrodes in a fluidic cell”. In: *Lab Chip* 8.2 (2008), pp. 302–308.

[223] D. Berdat et al. “DNA biosensor using fluorescence microscopy and impedance spectroscopy”. In: *Sensors Actuators, B Chem.* 118.1-2 (2006), pp. 53–59.

[224] L. Yang, Y. Li, and G. F. Erf. “Interdigitated Array Microelectrode-Based Electrochemical Impedance Immunosensor for Detection of Escherichia coli O157:H7”. In: *Anal. Chem.* 76.4 (2004), pp. 1107–1113.

[225] D. Berdat et al. “Biosensor for the Detection of Specific DNA Sequences by Impedance Spectroscopy”. In: *Solid-State Sensors, Actuators Microsystems Conf. 2007. TRANSDUCERS 2007. Int.* 2007, pp. 951–954.

[226] C. Berggren, B. Bjarnason, and G. Johansson. “Capacitive biosensors”. In: *Electroanalysis* 13.3 (2001), pp. 173–180.

[227] R. Lanche et al. “Reduced graphene oxide-based sensing platform for electric cell-substrate impedance sensing”. In: *Phys. Status Solidi Appl. Mater. Sci.* 211.6 (2014), pp. 1404–1409.

[228] Keithley. “C-V Testing for Components and Semiconductor Devices”. In: *Appl. Guid.* (2014), pp. 1–105.

[229] S. Tombelli, M. Minunni, and M. Mascini. “Analytical applications of aptamers”. In: *Biosensors and Bioelectronics* 20.12 (2005), pp. 2424–2434.

[230] D. H. Bunka and P. G. Stockley. “Aptamers come of age–at last”. In: *Nature Reviews Microbiology* 4.8 (2006), p. 588.

[231] C. K. O’Sullivan. “Aptasensors–the future of biosensing?” In: *Analytical and bioanalytical chemistry* 372.1 (2002), pp. 44–48.

[232] S. Song et al. “Aptamer-based biosensors”. In: *TrAC Trends in Analytical Chemistry* 27.2 (2008), pp. 108–117.

[233] P. Jolly et al. “Label-free impedimetric aptasensor with antifouling surface chemistry: A prostate specific antigen case study”. In: *Sensors Actuators, B Chem.* 209 (2015), pp. 306–312.

[234] N. Formisano et al. “Optimisation of an electrochemical impedance spectroscopy aptasensor by exploiting quartz crystal microbalance with dissipation signals”. In: *Sensors Actuators B Chem.* 220 (2015), pp. 369–375.

[235] D. J. Javier et al. “Aptamer-targeted gold nanoparticles as molecular-specific contrast agents for reflectance imaging”. In: *Bioconjugate chemistry* 19.6 (2008), pp. 1309–1312.

[236] R. Rhoades and R. Pflanzer. *Human physiology*. Pacific Grove, Calif. : Thomson Learning ; South Melbourne : Nelson Thomson, 2003.

[237] G. W. Litman et al. "Phylogenetic diversification of immunoglobulin genes and the antibody repertoire." In: *Molecular biology and evolution* 10.1 (1993), pp. 60–72.

[238] M. Reth. "Matching cellular dimensions with molecular sizes." In: *Nat. Immunol.* 14.8 (2013), pp. 765–7.

[239] S. Roy et al. "Graphene oxide for electrochemical sensing applications". In: *Journal of Materials Chemistry* 21.38 (2011), pp. 14725–14731.

[240] W.-M. Zhang et al. "Purification and characterization of different molecular forms of prostate-specific antigen in human seminal fluid." In: *Clinical chemistry* 41.11 (1995), pp. 1567–1573.

[241] L. Zuccaro et al. "SI:Tuning the isoelectric point of graphene by electrochemical functionalization". In: *Sci. Rep.* 5 (2015), p. 11794.

[242] N. Moser et al. *ISFETs in CMOS and Emergent Trends in Instrumentation: A Review*. 2016.

[243] C.-H. Chu et al. "Beyond the Debye length in high ionic strength solution: direct protein detection with field-effect transistors (FETs) in human serum". In: *Sci. Rep.* 7.1 (2017), p. 5256.

[244] P. Lin, F. Yan, and H. L. Chan. "Ion-sensitive properties of organic electrochemical transistors". In: *ACS applied materials & interfaces* 2.6 (2010), pp. 1637–1641.

[245] B. Zhang and T. Cui. "Suspended graphene nanoribbon ion-sensitive field-effect transistors formed by shrink lithography for pH/cancer biomarker sensing". In: *Journal of Microelectromechanical Systems* 22.5 (2013), pp. 1140–1146.

[246] I.-Y. Sohn et al. "pH sensing characteristics and biosensing application of solution-gated reduced graphene oxide field-effect transistors". In: *Biosensors and Bioelectronics* 45 (2013), pp. 70–76.

[247] J.-L. Her et al. "Label-free detection of alanine aminotransferase using a graphene field-effect biosensor". In: *Sensors and Actuators B: Chemical* 182 (2013), pp. 396–400.

[248] B. Wang et al. "Oxide-on-graphene field effect bio-ready sensors". In: *Nano Research* 7.9 (2014), pp. 1263–1270.

[249] T. K. Truong et al. "Reduced graphene oxide field-effect transistor with indium tin oxide extended gate for proton sensing". In: *Current Applied Physics* 14.5 (2014), pp. 738–743.

[250] A. Tarasov et al. "Gold-coated graphene field-effect transistors for quantitative analysis of protein–antibody interactions". In: *2D Materials* 2.4 (2015), p. 044008.

[251] T.-C. Lin et al. "A high sensitivity field effect transistor biosensor for methylene blue detection utilize graphene oxide nanoribbon". In: *Biosensors and Bioelectronics* 89 (2017), pp. 511–517.

[252] T. Ytterdal, Y. Cheng, and T. A. Fjeldly. “MOSFET device physics and operation”. In: *Device Modeling for Analog and RF CMOS Circuit Design* (2003), pp. 1–45.

[253] C.-S. Lee, S. K. Kim, and M. Kim. “Ion-sensitive field-effect transistor for biological sensing”. In: *Sensors* 9.9 (2009), pp. 7111–7131.

[254] S. D. Keighley et al. “Optimization of DNA immobilization on gold electrodes for label-free detection by electrochemical impedance spectroscopy”. In: *Biosensors and Bioelectronics* 23.8 (2008), pp. 1291–1297.

[255] H. C. Kolb, M. G. Finn, and K. B. Sharpless. “Click chemistry: Diveverse chemical funtion from a few good reactions”. In: *Angew. Chemie - Int. Ed.* 40 (2001), pp. 2004–2021.

[256] W. Wang et al. “Sulfated ligands for the copper(I)-catalyzed azide-alkyne cycloaddition”. In: 49.18 (2009), pp. 1841–1850.

[257] S. Sun et al. “Click chemistry as a route for the immobilization of well-defined polystyrene onto graphene sheets”. In: *J. Mater. Chem.* 20.27 (2010), p. 5605.

[258] U. Mohanty. “Electrodeposition: a versatile and inexpensive tool for the synthesis of nanoparticles, nanorods, nanowires, and nanoclusters of metals”. In: *Journal of applied electrochemistry* 41.3 (2011), pp. 257–270.

[259] D. Grujicic and B. Pesic. “Electrodeposition of copper: the nucleation mechanisms”. In: *Electrochimica Acta* 47.18 (2002), pp. 2901–2912.

[260] K.-D. Jang et al. “Effect of Lithium Ions on Copper Nanoparticle Size, Shape, and Distribution”. In: *J. Nanotechnol.* 2012 (2012), pp. 1–6.

List of figures

List of tables

Publications

[1] X. Lu, W.-M. Munief, F. Heib, M. Schmitt, A. Britz, S. Grandthyl, F. Müller, J.-U. Neurohr, K. Jacobs, H. M. Benia, R. Lanche, V. Pachauri, R. Hempelmann, S. Ingebrandt, Adv. Mater. Technol. 2018, 3, 1700318.

[2] X. Lu, P. Damborsky, W.-M. Munief, J. K. Law, V. Pachauri, J. U. Neurohr, S. Grandthyll, K. Jacobs, F. Müller, J. Katrlik, X. Chen, S. Ingebrandt, ACS Appl. Mater. Interfaces 2017, submitted.

[3] X. Lu, A. Miodek, W.-M. Munief, P. Jolly, V. Pachauri, X. Chen, P. Estrela, S. Ingebrandt, Biosens. Bioelectron. 2018, submitted.

[4] W. Munief, X. Lu, T. Teucke, J. Wilhelm, F. Hempel, M. Schwartz, J. K. Y. Law, R. Lanche, A. Britz, S. Grandthyll, F. Mueller, J. Neurohr, K. Jacob, M. Schmitt, R. Hempelmann, V. Pachauri, S. Ingebrandt, Biosens. Bioelectron. 2018, submitted.

[5] R. Meng, X. Lu, S. Ingebrandt, X. Chen, Adv. Mater. Interfaces 2017, 4, 1.

[6] I. Tzouvadaki, P. Jolly, X. Lu, S. Ingebrandt, G. De Micheli, P. Estrela, S. Carrara, Nano Lett. 2016, 16, 4472.

[7] W.-M. Munief, F. Heib, F. Hempel, X. Lu, M. Schwartz, V. Pachauri, R. Hempelmann, M. Schmitt, S. Ingebrandt, Langmuir 2018.

[8] F. Hempel, J. K. Y. Law, T. C. Nguyen, W. Munief, X. Lu, V. Pachauri, A. Susloparova, X. T. Vu, S. Ingebrandt, Biosens. Bioelectron. 2017, 93, 132.

Conferences, Summer Schools, and Workshops

[1] X. Lu, A. Miodek, W.-M. Munief, V. Pachauri, M. Eickhoff, P. Estrela, S. Ingebrandt. (2017). Reduced graphene-oxide based in-line impedimetric biosensor for detecting prostate cancer specific antigen. Nanocongress. Brussels, Belgium. (Poster presentation).

[2] X. Lu, P. Damborsky, W.-M. Munief, V. Pachauri, J. Katrlik, S. Ingebrandt. (2017). Highly Sensitive Performance of SPR Platform with Reduced Graphene-Oxide as Functional Layer. Meeting Point Functional Layers (MPFL). Zweibrucken, Germany. (Award of best oral presentation).

[3] X. Lu, A. Miodek, W.-M. Munief, V. Pachauri, M. Eickhoff, P. Estrela, S. Ingebrandt (2017). Reduced graphene-oxide based in-line impedimetric biosensor. Engineering of Functional Interfaces (EnFi), Marburg, Germany. (Oral and poster presentation)

[4] X. Lu, W.-M. Munief, A. Miodek, P. Jolly, V. Pachauri, P. Estrela, S. Ingebrandt. (2016). Sensing molecules at rGO thin-films: A scalable label-free electrical biodetector for PSA. Engineering of Functional Interfaces (EnFi), Wildau, Germany. (Poster presentation).

[5] X. Lu, W.-M. Munief, A. Miodek, P. Jolly, V. Pachauri, P. Estrela, S. Ingebrandt. Reduced graphene-oxide based biosensor platform. (2016). PROSENSE Winter School on "New nano-bio-sensing tools for theragnostics", Lausanne, Switzerland. (Oral and poster presentation).

[6] X. Lu, W.-M. Munief, V. Pachauri, N. Hey, T. Welsch, J. Ka-Yan Law, D. Rani, S. Ingebrandt. Reduced graphene-oxide based biosensor platform for the detection of prostate cancer biomarkers. (2015). PROSENSE workshop on "Biosensor construction" Cardiff, United Kingdom (oral and poster presentation).

[7] X. Lu, W.-M. Munief, V. Pachauri, J. Ka-Yan Law, T. Welsch, S. Ingebrandt. Reduced graphene-oxide based biosensor platform for the detection of prostate cancer biomarkers. (2014). PROSENSE workshop on "Clinical perspectives and commercial forces on biosensor devices", Bath, United Kingdom (oral and poster presentation).

[8] X. Lu, V. Pachauri, W.-M. Munief, J. Ka-Yan Law, S. Ingebrandt. Graphene-based biosensor platform for detecting prostate cancer biomarkers. (2014). PROSENSE

workshop on “Application of lectins in various format of analysis for glycoprofiling”, Bratislava, Slovakia (oral and poster presentation).

[9] X. Lu, W.-M. Munief, V. Pachauri, N. Hey, D. Rani, S. Ingebrandt. (2015). Reduced graphene-oxide based biosensor platform. ICREA WORKSHOP ON GRAPHENE NANOBIOSENSORS, Barcelona, Spain. (Poster presentation).

[10] X. Lu, W.-M. Munief, V. Pachauri, J. Ka-Yan Law, T. Welsch, S. Ingebrandt. (2014). Reduced graphene-oxide based biosensor platform for the detection of prostate cancer biomarkers. EAU Section of Urological Research (ESUR), Glasgow, UK. (Poster presentation).

[11] X. Lu, V. Pachauri, W.-M. Munief, S. Ingebrandt. (2014). All-printing process for optically transparent and flexible biosensors based on graphene oxide. Engineering of Functional Interfaces, Jülich, Germany. (Poster presentation).

Acknowledgments

This thesis is accomplished thanks to the efforts of many lovely people. First of all, I would like to thank Prof. Sven Ingebrandt. He gave me a great opportunity and research platform to work as a Marie Curie fellow in the Biomedical Signaling group of the University of Applied Sciences Kaiserslautern, campus Zweibrücken, Germany. I was able to carry out my Ph.D. work at the interdisciplinary research frontier to explore the application capability of carbon-based materials towards cancer diagnosis. I highly appreciate the efforts and time Prof. Ingebrandt offered me for scientific discussions and the corrections of the thesis. I am also thankful to Prof. Martin Eickhoff, who supervised me at the Justus Liebig University Giessen, Germany. His suggestions and comments for my thesis correction were quite inspiring. Besides, I would like to thank Dr. Vivek Pachauri for his patience, guidance and timely scientific discussions. I believe their serious and cautious scientific attitude is an excellent example for me on my future academic road.

Many thanks to my colleague Walid-Madhat Munief for his academic support during my Ph.D. study. We experienced a great collaboration to explore this new research field. We shared ideas, discussed technical problems, debated scientific issues, communicated closely to design and execute experiments and supported each other to reach our project milestones. I also sincerely thank Dr. Jessica Ka-Yan Law, Dr. Xuan Thang Vu, Felix Hempel, Dr. Ruben Lanche, Dr. Dipti Rani and Dr. Miriam Schwartz for their constructive comments and careful corrections of my thesis. I am also thankful to other members of the biomedical signaling group: Dr. Maryam Weil, Dr. Anette Britz, Dr. Lotta Emilia Delle, Achim Müller, Dr. Thanh Chien Nguyen, Dr. Anna Susloparova, Dr. Dieter Koppenhöfer, and Natascha Hey for their collaboration and the delightful time together. Additionally, I am very grateful for the technical support offered by Detlev Cassel, Rainer Lilischkis, and Erik Engelmann, in relation to the device fabrication in the cleanroom, the device characterizations and the mechanical component processing at the University of Applied Sciences Kaiserslautern, Germany.

I would like to thank the Marie Curie Initial Training Network PROSENSE (Cancer Diagnosis: Parallel Sensing of Prostate Cancer Biomarkers) project (grant no. 317420, 2012-2016). It offered me a superior research platform to collaborate with experts in diverse fields and valuable resources to carry out my Ph.D. project. Different ideas collide and blend to generate innovations. I am very thankful to Dr. Pedro Estrela and all of the PROSENSE members for the valuable communications, discussions and pleasant time together.

In particular, I sincerely appreciate Mikeal Bottemanne for his respect, strong support, consistent and passionate love in many aspects throughout my study time abroad.

In the end, I am deeply thankful to my beloved family members: my father, Renguang Lu, my mother, Shuying Liu, my cute brother Tongling Lu, my cousins, uncle, and aunt who supported me and provided me with warmness selflessly.